

DIGITAL COMMUNICATIONS IN FADING CHANNELS: COMLINK VALIDATION

Approved for public release; distribution is unlimited.

September 2000



Prepared for:
Defense Threat Reduction Agency
45045 Aviation Drive
Dulles, VA 20166-7517

DNA 001-96-C-0040

Roger A. Dana and
Robert L. Bogusch

Prepared by: Mission Research Corporation
P.O. Drawer 719
Santa Barbara, CA 93102-0719
And

Mission Research Corporation
P.O. Box 2256
Atascadero, CA 93423-2256

20010420 072

Technical Report

DESTRUCTION NOTICE:

Destroy this report when it is no longer needed. Do not return to sender.

PLEASE NOTIFY THE DEFENSE THREAT REDUCTION AGENCY, ATTN: ADM, 45045 AVIATION DRIVE, DULLES, VA 20166-7517, IF YOUR ADDRESS IS INCORRECT, IF YOU WISH IT DELETED FROM THE DISTRIBUTION LIST, OR IF THE ADDRESSEE IS NO LONGER EMPLOYED BY YOUR ORGANIZATION.

DISTRIBUTION LIST UPDATE

This mailer is provided to enable DTRA to maintain current distribution lists for reports. (We would appreciate you providing the requested information.)

- ☐ Add the individual listed to your distribution list.
- ☐ Delete the cited organization/individual.
- ☐ Change of address.

Note:

Please return the mailing label from the document so that any additions, changes, corrections or deletions can be made easily. For distribution cancellation or more information call DTRA/ADM (703) 325-1036.

NAME: _____

ORGANIZATION: _____

OLD ADDRESS

NEW ADDRESS

TELEPHONE NUMBER: () _____

DTRA PUBLICATION NUMBER/TITLE

CHANGES/DELETIONS/ADDITIONS, etc.)

(Attach Sheet if more Space is Required)

DTRA or other GOVERNMENT CONTRACT NUMBER: _____

CERTIFICATION of NEED-TO-KNOW BY GOVERNMENT SPONSOR (if other than DTRA):

SPONSORING ORGANIZATION: _____

CONTRACTING OFFICER or REPRESENTATIVE: _____

SIGNATURE: _____

CUT HERE AND RETURN

DEFENSE THREAT REDUCTION AGENCY
ATTN: ADM
45045 AVIATION DRIVE
DULLES, VA 20156-7517

DEFENSE THREAT REDUCTION AGENCY
ATTN: ADM
6801 TELEGRAPH ROAD
ALEXANDRIA, VA 22310-3398



Defense Threat Reduction Agency

8725 John J. Kingman Road, MS 6201
Fort Belvoir, VA 22060-6201

SEP 12 2001

MEMORANDUM FOR PRINTING AND REPRODUCTION BRANCH (ADSR)

SUBJECT: The printing of, **DSWA-TR-98-61**, "Digital Communications in Fading Channels:
COMLNK Validation"

Referenced subject report was printed with missing text in Block 3 of the Standard Form 298. The report has been determined to be Unclassified. The text should appear as follows:

Technical

961001 - 980630

Request you distribute an errata with adhesive backing for easy installation. A distribution list and labels have been provided for your use. Your point-of-contact in this office is Miss Suzie Ballif, (703) 767-4725.

Sincerely,

Linda M. Powell
Chief, Administrative Services
Division

Technical 961001 - 980630

Technical 961001 - 980630

REPORT DOCUMENTATION PAGE

Form Approved
OMB No. 0704-0188

Public reporting burden for this collection of information is estimated to average 1 hour per response, including the time for reviewing instructions, searching existing data sources, gathering and maintaining the data needed, and completing and reviewing the collection of information. Send comments regarding this burden estimate or any other aspect of this collection of information, including suggestions for reducing this burden, to Washington Headquarters Services, Directorate for Information Operations and Reports, 1215 Jefferson Davis Highway, Suite 1204, Arlington, VA 22202-4302, and to the Office of Management and Budget, Paperwork Reduction Project (0704-0188), Washington, DC 20503.

1. AGENCY USE ONLY (Leave blank)		2. REPORT DATE		3. REPORT TYPE AND DATES COVERED	
4. TITLE AND SUBTITLE Digital Communications in Fading Channels: COMLNK Validation				5. FUNDING NUMBERS C - DNA001-96-C-0040 PE - 62715H PR - AF TA - B1 WU- DHRJCOM	
6. AUTHOR(S) Roger A. Dana (MRC-SB) and Robert L. Bogusch (MRC-ATS)					
7. PERFORMING ORGANIZATION NAME(S) AND ADDRESS(ES) Mission Research Corporation P. O. Drawer 719 Santa Barbara, CA 93102-0719				8. PERFORMING ORGANIZATION REPORT NUMBER MRC-R-1531	
9. SPONSORING/MONITORING AGENCY NAME(S) AND ADDRESS(ES) Defense Threat Reduction Agency 45045 Aviation Drive Dulles, VA 20166-7517 CPWP/Schwartz				10. SPONSORING/MONITORING AGENCY REPORT NUMBER DSWA-TR-98-61	
11. SUPPLEMENTARY NOTES This work sponsored by the Defense Threat Reduction Agency under RDT&E RMC Code: B 4662 D B1 3200 A AF 25904D.					
12a. DISTRIBUTION/AVAILABILITY STATEMENT Approved for public release; distribution is unlimited.				12b. DISTRIBUTION CODE	
13. ABSTRACT (Maximum 200 words) This report presents validation results for the DSWA communications link simulation code COMLNK. Simulation results are compared with theoretical demodulation error rates for frequency shift keying (FSK) and phase shift keying (PSK) modulation with a wide range of disturbed channel conditions. Our results show excellent agreement of COMLNK simulation results with theoretical error rates. The propagation channels are characterized by the channel impulse response function (CIRF) that has either Rician or Rayleigh first order statistics. The second order statistics of Rayleigh fading channels vary from slow to fast fading and are either flat or frequency selective fading. New results for the demodulation performance of PSK or FSK links in fast, frequency selective fading are given in the Appendices. The effects of sampling the CIRF, which is necessary in either a simulation such as COMLNK or in hardware channel simulators, are included in fast, frequency selective fading demodulation performance calculations.					
14. SUBJECT TERMS Channel Impulse Response Function Fast, Frequency Selective Fading Rician and Rayleigh Fading Digital Communications Modulation Techniques Signal Scintillation				15. NUMBER OF PAGES	
				16. PRICE CODE	
17. SECURITY CLASSIFICATION OF REPORT UNCLASSIFIED	18. SECURITY CLASSIFICATION OF THIS PAGE UNCLASSIFIED	19. SECURITY CLASSIFICATION OF ABSTRACT UNCLASSIFIED	20. LIMITATION OF ABSTRACT SAR		

UNCLASSIFIED

SECURITY CLASSIFICATION OF THIS PAGE

CLASSIFIED BY:

N/A since Unclassified

DECLASSIFY ON:

N/A since Unclassified

7. PERFORMING ORGANIZATION NAME(S) AND ADDRESS(ES) (Continued)

Mission Research Corporation
P. O. Box 2256
Atascadero, CA 93423-2256

SECURITY CLASSIFICATION OF THIS PAGE

UNCLASSIFIED

CONVERSION TABLE

Conversion factors for U.S. Customary to metric (SI) units of measurement

MULTIPLY \longrightarrow BY \longrightarrow TOGET
 TOGET \longleftarrow BY \longleftarrow DIVIDE

angstrom	1.000000 x E -10	meters (m)
atmosphere (normal)	1.01325 x E +2	kilo pascal (kPa)
bar	1.000000 x E +2	kilo pascal (kPa)
barn	1.000000 x E -28	meter ² (m ²)
British thermal unit (thermochemical)	1.054350 x E +3	joule (J)
calorie (thermochemical)	4.184000	joule (J)
cal (thermochemical) /cm ²	4.184000 x E -2	mega joule/m ² (MJ/m ²)
curie	3.700000 x E +1	*giga becquerel (GBq)
degree (angle)	1.745329 x E -2	radian (rad)
degree Fahrenheit	$t_K = (t_F + 459.67)/1.8$	degree kelvin (K)
electron volt	1.60219 x E -19	joule (J)
erg	1.000000 x E -7	joule (J)
erg/second	1.000000 x E -7	watt (W)
foot	3.048000 x E -1	meter (m)
foot-pound-force	1.355818	joule (J)
gallon (U.S. liquid)	3.785412 x E -3	meter ³ (m ³)
inch	2.540000 x E -2	meter (m)
jerk	1.000000 x E +9	joule (J)
joule/kilogram (J/kg) (radiation dose absorbed)	1.000000	Gray (Gy)
kilotons	4.183	terajoules
kip (1000 lbf)	4.448222 x E +3	newton (N)
kip/inch ² (ksi)	6.894757 x E +3	kilo pascal (kPa)
ktap	1.000000 x E +2	newton-second/m ² (N-s/m ²)
micron	1.000000 x E -6	meter (m)
mil	2.540000 x E -5	meter (m)
mile (international)	1.609344 x E +3	meter (m)
ounce	2.834952 x E -2	kilogram (kg)
pound-force (lbs avoirdupois)	4.448222	newton (N)
pound-force inch	1.129848 x E -1	newton-meter (N-m)
pound-force/inch	1.751268 x E +2	newton/meter (N/m)
pound-force/foot ²	4.788026 x E -2	kilo pascal (kPa)
pound-force/inch ² (psi)	6.894757	kilo pascal (kPa)
pound-mass (lbm avoirdupois)	4.535924 x E -1	kilogram (kg)
pound-mass-foot ² (moment of inertia)	4.214011 x E -2	kilogram-meter ² (kg-m ²)
pound-mass/foot ³	1.601846 x E +1	kilogram/meter ³ (kg/m ³)
rad (radiation dose absorbed)	1.000000 x E -2	**Gray(Gy)
roentgen	2.579760 x E -4	coulomb/kilogram (C/kg)
shake	1.000000 x E -8	second(s)
slug	1.459390 x E +1	kilogram (kg)
torr (mm Hg, O° C)	1.333220 x E -1	kilo pascal (kPa)

*The becquerel (Bq) is the SI unit of radioactivity; 1 Bq = 1 event/s.

**The Gray (Gy) is the SI unit of absorbed radiation.

TABLE OF CONTENTS

Section	Page
CONVERSION TABLE.....	iii
FIGURES.....	vii
1 INTRODUCTION.....	1
2 THE FADING RADIO CHANNEL.....	8
2.1 FLAT FADING CHANNELS.....	9
2.1.1 First-Order Statistics.....	10
2.1.2 Second-Order Statistics.....	13
2.2 FREQUENCY SELECTIVE CHANNELS.....	17
2.3 CHANNEL MODELING TECHNIQUES.....	20
2.3.1 Flat Fading Channels.....	21
2.3.2 Frequency Selective Fading Channels.....	24
3 EFFECT OF CHANNEL TAP SPACING ON DELAY TRACKING AND AUTOMATIC GAIN CONTROL OPERATION.....	29
3.1 IDEAL DELAY OFFSET AND SIGNAL LOSS.....	30
3.1.1 Direct Sequence Spread Spectrum Delay Tracking.....	32
3.1.2 Frequency Hopped Spread Spectrum Delay Tracking.....	35
3.2 COMLNK DLL TRACKING AND SIGNAL LOSS.....	39
3.2.1 Raw Data From COMLNK.....	39
3.2.2 Comparison of COMLNK Delay Tracking with Theory.....	45

TABLE OF CONTENTS (Continued)

Appendix		Page
4	COMLNK DEMODULATION PERFORMANCE.....	51
4.1	SLOW RICIAN AND RAYLEIGH FADING CHANNELS.....	51
4.1.1	Error Rate Expressions.	52
4.1.2	<i>M</i> -ary FSK Sampling Loss.....	54
4.1.3	COMLNK Results in Slow Fading Channels.	55
4.2	FAST RAYLEIGH FADING CHANNELS.	61
4.2.1	DPSK Performance.	62
4.2.2	BFSK Performance.	65
4.2.3	<i>M</i> -ary FSK Performance.	67
4.3	FREQUENCY SELECTIVE FADING CHANNELS.	80
4.3.1	DPSK Performance.	80
4.3.2	BFSK Performance with Hopping.	86
4.3.3	BFSK Performance without Hopping.	95
4.4	SUMMARY.	99
5	REFERENCES.....	103
Appendix		
A	DEMODULATION PERFORMANCE OF COHERENT PSK (ΔPSK).....	A-1
B	DEMODULATION PERFORMANCE OF DIFFERENTIALLY COHERENT PSK (DPSK) WITH AN UNDERLYING SPREAD SPECTRUM CODE	B-1

TABLE OF CONTENTS (Continued)

Appendix		Page
C	DEMODULATION PERFORMANCE OF DIFFERENTIALLY COHERENT PSK (DPSK) WITHOUT AN UNDERLYING SPREAD SPECTRUM CODE	C-1
D	DEMODULATION ERROR RATE FOR DPSK AND BFSK	D-1
E	DIFFERENTIAL PHASE-SHIFT KEYING WITH DIVERSITY COMBINING	E-1
F	DEMODULATION PERFORMANCE OF NON-COHERENT <i>M</i> -ary FREQUENCY SHIFT KEYING IN FAST FADING	F-1
G	DEMODULATION PERFORMANCE OF BINARY FREQUENCY SHIFT-KEYING IN FREQUENCY SELECTIVE FADING WITH HOPPING	G-1
H	DEMODULATION PERFORMANCE OF BINARY FREQUENCY SHIFT-KEYING IN FREQUENCY SELECTIVE FADING WITHOUT HOPPING	H-1
	DOCUMENT DISTRIBUTION	DL-1

FIGURES

Figure		Page
1-1	Example complex communications system simulated with COMLNK.	5
1-2	Example frequency hopped, frequency-shift keying (FH/FSK) receiver.....	7
2-1	Propagation through a striated ionosphere.....	9
2-2	Cumulative distribution of received signal power in Rayleigh fading channels.	11
2-3	Cumulative distribution of received signal power in a Rician fading channel.....	14
2-4	Comparison of Gaussian, f^{-6} and f^{-4} fading signal power spectra.	17
2-5	Flat fading channel simulator.	23
2-6	Tapped delay line frequency selective channel simulator.	26
3-1	Block diagram of a direct sequence PSK receiver with early and late code correlators for DLL tracking.....	31
3-2	Block diagram of a frequency hopped M -ary FSK receiver.	36
3-3	AGC gain of DS receiver in a frequency selective fading channel with $f_0 / R_C = 1.0$	40
3-4	DLL tracking error of DS receiver in a frequency selective fading channel with $f_0 / R_C = 1.0$	40
3-5	AGC gain of DS receiver in a frequency selective fading channel with $f_0 / R_C = 0.2$	41
3-6	DLL tracking error of DS receiver in a frequency selective fading channel with $f_0 / R_C = 0.2$	41
3-7	AGC gain of DS receiver in a frequency selective fading channel with $f_0 / R_C = 0.1$	42

FIGURES (Continued)

Figure	Page
3-8	DLL tracking error of DS receiver in a frequency selective fading channel with $f_0 / R_C = 0.1$42
3-9	AGC gain of DS receiver in a frequency selective fading channel with $f_0 / R_C = 0.08$43
3-10	DLL tracking error of DS receiver in a frequency selective fading channel with $f_0 / R_C = 0.08$43
3-11	AGC gain of DS receiver in a frequency selective fading channel with $f_0 / R_C = 0.06$44
3-12	DLL tracking error of DS receiver in a frequency selective fading channel with $f_0 / R_C = 0.06$44
3-13	Comparison of COMLNK and ideal direct sequence delay tracking errors in frequency selective fading channels.46
3-14	Comparison of COMLNK, L_3P test results, and ideal direct sequence code correlator loss in frequency selective fading channels.47
3-15	Comparison of COMLNK and ideal frequency hopped delay offset in frequency selective fading channels.49
3-16	Comparison of COMLNK and ideal frequency hopped tone filter signal loss in frequency selective fading channels.49
4-1	Channel bit error rates of Δ PSK, DPSK, and 8-ary FSK in slow Rician fading channels.56
4-2	Diversity combining of DPSK decision metrics from two and three slow Rayleigh fading channels.60
4-3	DPSK channel bit error rate in fast Rayleigh fading.63
4-4	Required E_{cb} / N_0 for Δ PSK and DPSK to achieve a ten-percent channel bit error rate in fast Rayleigh fading64

FIGURES (Continued)

Figure	Page
4-5	Comparison of test and COMLNK results for the DPSK demodulation error rate of the prototype L_3P receiver.66
4-6	BFSK channel bit error rate for the minimum tone spacing in fast Rayleigh fading.68
4-7	QFSK channel bit error rate for the minimum tone spacing in fast Rayleigh fading.71
4-8	8-ary FSK channel symbol error rate for the minimum tone spacing in fast Rayleigh fading.72
4-9	8-ary FSK channel symbol error rate for three times the minimum tone spacing in fast Rayleigh fading.73
4-10	16-ary FSK channel symbol error rate for the minimum tone spacing in fast Rayleigh fading.74
4-11	16-ary FSK channel symbol error rate for three times the minimum tone spacing in fast Rayleigh fading.75
4-12	COMLNK results for the ratio of the channel bit error rate to the demodulated symbol error rate for 16-ary FSK.76
4-13	Required E_{cb} / N_0 for 8-ary FSK to achieve a ten-percent channel bit error rate in fast Rayleigh fading.78
4-14	Required E_{cb} / N_0 for 16-ary FSK to achieve a ten-percent channel bit error rate in fast Rayleigh fading.79
4-15	DPSK channel bit error rates in slow, frequency selective fading.84
4-16	Required E_{cb} / N_0 for DPSK to achieve a ten-percent channel bit error rate in slow, frequency selective fading.85
4-17	BFSK channel bit error rates with hopping and an active DLL in fast, frequency selective fading.92

FIGURES (Continued)

Figure	Page
4-18	BFSK channel bit error rates with hopping and ideal delay offset in fast, frequency selective fading.94
4-19	BFSK channel bit error rates with hopping and zero delay offset in fast, frequency selective fading.96
4-20	BFSK channel bit error rates without hopping and zero delay offset in slow, frequency selective fading.....100
4-21	Comparison of measured and simulated Viterbi decoder transfer functions for the prototype L_3P receiver.....102
A-1	Block diagram of a coherent PSK receiver..... A-2
A-2	Δ PSK channel bit error rate for slow Rician fading. A-5
A-3	PSK channel bit error rate for fast Rayleigh fading..... A-6
A-1	Block diagram of a coherent PSK receiver..... A-2
A-2	Δ PSK channel bit error rate for slow Rician fading. A-5
A-3	PSK channel bit error rate for fast Rayleigh fading..... A-6
B-1	Block diagram of a spread spectrum DPSK receiver.....B-2
B-2	Mean energy of early and late code correlator output for continuous and sampled (four samples per chip) CIRF.....B-10
B-3	Ideal delay offset for continuous and sampled CIRFs.....B-11
B-4	Code correlator loss in frequency selective fading channels.B-12
B-5	DPSK channel bit error rate for Rician fading channels.....B-19
B-6	DPSK demodulation error rate for fast, Rayleigh fading channels.B-24
B-7	DPSK irreducible channel bit error rate for fast Rayleigh fading channels.B-25

FIGURES (Continued)

Figure	Page
B-8	Fast fading DPSK demodulation error rate for continuous and time sampled channel impulse response functions.B-28
B-9	Channel bit signal loss for fast Rayleigh fading and time-sampled and continuous CIRFs.B-28
C-1	Block diagram of a DPSK receiver.....C-2
C-2	Ideal delay offset of DPSK receiver in frequency selective fading.C-7
C-3	On-time, ISI, and total signal energy for ideal and zero delay offsets.....C-7
C-4	DPSK irreducible channel bit error rate in slow, frequency selective fading with a continuous CIRF.C-23
C-5	DPSK irreducible error rate in fast, frequency selective fading with a Gaussian Doppler frequency spectrum.C-24
C-6	DPSK irreducible channel bit error rate in slow, frequency selective fading with sampled CIRFs and $P_r = 0.975$C-30
C-7	DPSK irreducible channel bit error rate in slow, frequency selective fading with sampled CIRFs and $P_r = 0.999$C-31
E-1	Channel bit error rate versus single channel signal-to-noise ratio after combining DPSK decision metrics from N_C non-fading channels.E-9
E-2	Channel bit error rate versus total signal-to-noise ratio after combining DPSK decision metrics from N_C non-fading channels.E-11
E-3	Channel bit error rate after combining DPSK decision metrics from two Rician-fading channels.....E-14
E-4	Channel bit error rate after combining DPSK decision metrics from two correlated Rayleigh-fading channels.....E-17

FIGURES (Continued)

Figure		Page
E-5	Channel bit error rate after one-, two- and three-channel combining of DPSK decision metrics versus single channel signal-to-noise ratio E_{cb}/N_0 for uncorrelated Rayleigh fading.	E-19
E-6	Channel bit error rate after one-, two- and three-channel combining of DPSK decision metrics versus total user signal-to-noise ratio E_{ub}/N_0 for uncorrelated Rayleigh fading.	E-20
F-1	Block diagram of an M -ary FSK receiver.	F-2
F-3	8-ary FSK demodulation error rate for slow Rician fading channels.	F-11
F-4	BFSK demodulation error rate for minimum tone spacing in fast Rayleigh fading channels.	F-16
F-5	BFSK demodulation error rate for three times minimum tone spacing in fast Rayleigh fading channels.	F-17
F-6	Irreducible BFSK demodulation error rate for three tone spacings in fast Rayleigh fading channels.	F-18
F-7	BFSK filter output signal energy in fast Rayleigh fading channels.	F-19
F-8	8-ary FSK tone filters.	F-23
F-9	FSK filter output signal energy in fast Rayleigh fading channels.	F-27
F-10	FSK filter cross correlation coefficient in fast Rayleigh fading channels.	F-27
F-11	8-ary FSK demodulation error rate in fast Rayleigh fading channels for minimum tone spacing.	F-29
F-12	8-ary FSK demodulation error rate in fast Rayleigh fading channels for three times minimum tone spacing.	F-30
F-13	Irreducible BFSK and 8-ary FSK demodulation error rates in fast Rayleigh fading channels.	F-32

FIGURES (Continued)

Figure	Page
F-14	8-ary FSK channel bit error rate in fast Rayleigh fading channels for continuous and time-sampled cases. F-37
G-1	Block diagram of a binary FSK receiver with frequency hopping. G-2
G-2	Early, on-time, and late sample energy versus delay for a continuous CIRF. G-10
G-3	Early and late sample energy versus delay for a sampled CIRF with two samples per symbol period. G-11
G-4	Early and late sample energy versus delay for a sampled CIRF with four samples per symbol period. G-11
G-5	Ideal delay offset for sampled and continuous CIRFs. G-12
G-6	Mean signal energy and cross correlation coefficient versus delay for a continuous CIRF, $f_0 T = 0.1$, and $\Delta f T = 3$ G-19
G-7	Mean energy and cross correlation coefficient versus delay for a sampled CIRF ($N_D = 2$), $f_0 T = 0.1$, and $\Delta f T = 3$ G-19
G-8	BFSK irreducible demodulation error rate versus delay for continuous and sampled CIRFs, $f_0 T = 0.1$, and $\Delta f T = 3$ G-20
G-9	BFSK irreducible demodulation error rate with frequency hopping and with and without delay offset. G-20
G-10	BFSK irreducible demodulation error rate with frequency hopping for three tone spacings. G-21
G-11	BFSK demodulation error rate in slow, frequency selective fading with ideal delay offset. G-23
G-12	BFSK irreducible demodulation error rate with frequency hopping in fast fading channels. G-39
G-13	BFSK irreducible demodulation error rate in sampled ($P_r = 0.975$) and continuous frequency selective fading. G-41

FIGURES (Continued)

Figure	Page
G-14	BFSK irreducible demodulation error rate in sampled ($P_r = 0.999$) and continuous frequency selective fading..... G-42
H-1	Ideal delay offset that maximizes the correct filter output amplitude for BFSK modulation with and without hopping. H-11
H-2	BFSK irreducible demodulation error rate in slow, frequency selective fading with and without hopping. H-17
H-3	BFSK irreducible demodulation error rate without hopping for several tone spacings in slow, frequency selective fading..... H-17
H-4	BFSK channel bit error rate without hopping for the optimum tone spacing in slow, frequency selective fading..... H-18
H-5	BFSK irreducible demodulation error rate in slow, frequency selective fading with sampled CIRFs and $P_r = 0.975$ H-22
H-6	BFSK irreducible demodulation error rate in slow, frequency selective fading with sampled CIRFs and $P_r = 0.999$ H-23
H-7	BFSK irreducible demodulation error rate in slow, frequency selective fading for sampled CIRFs with $N_D = 2$ H-26
H-8	BFSK irreducible demodulation error rate in slow, frequency selective fading for sampled CIRFs with $N_D = 64$ H-26

SECTION 1

INTRODUCTION

The high fidelity simulation COMLNK [Bogusch, 1989, 1990, 1996; Bogusch and Michelet, 1993] is intended to facilitate the design, development, specification, testing, and evaluation of digital communications links operating in fading channels. For example, COMLNK allows the link designer to quickly evaluate the relative merits of various signal processing algorithms or tracking loop parameters or many of the myriad design details in modern digital modems. Accuracy is very important because selection of the best algorithm for a particular function may be based on slight differences, sometimes a fraction of a decibel, in performance.

During the hardware development process, implementation choices can be evaluated with COMLNK. For example, the difference in the performance of a Viterbi decoder using three or four bits of soft decision amplitude information can be measured with the code. Another issue that faces the hardware designer is the following: Given an input signal-to-noise ratio, does the design meet its performance requirements? Here a fraction of a decibel can make the difference between a design that is acceptable and one that requires further refinement.

The development of link specifications is another area where accuracy is critically important. Real hardware has real implementation losses. If such losses are inaccurately specified, two things can happen and both can be bad. If the specified loss is too large, a sloppy design that wastes precious power resources may result. If the specified loss is too small, the design may either be more expensive than necessary or simply may not be possible with existing technology.

Hardware testing is yet another application of simulation results where accuracy is very important. When wiring together a complex communications system and test equipment to measure link performance in fading channels, any number of things can be wrong. Thus the prudent tester often will use simulation results as the "truth" against which the efficacy of test results is determined. If the "truth" is in error, then good test results can be rejected because they vary too much from expected results.

Eventually, a good hardware test engineer will get valid results whether or not he or she has accurate predictions of performance. However, there are inherent limitations of such tests because of real limitations in hardware channel simulators. Generally, one cannot test a communications link over all possible variations in the fading

channel. When such limitations occur, the comparison of hardware test results and simulation results for the channels that can be tested is a practical method of validating the simulation, provided the two results agree to within an acceptable margin.

Once validated against test data (or theoretical performance curves when test data are not available), the simulation can then be used confidently to measure link performance under channel conditions that cannot be tested or to evaluate the performance of similar communications links. Indeed, a simulation may be the only way to understand and mitigate link disruptions that occur infrequently in the actual operating environment. The key to using the simulation with confidence for any of these purposes is accuracy.

The COMLNK code has been designed from the beginning to do two things well. First, it is designed to be as accurate as possible, and second, it is designed to be as fast as possible. Sometimes these two goals conflict, particularly in the simulation of the fading channel. An example is the number of delay samples that defines the tap spacing in a frequency selective fading channel simulator. COMLNK uses two delay samples per modulation period. Our validation results show that this choice may be too coarse for some applications, and the number may become a user input in the future. However, it may not be desirable to increase the number of delay samples in all cases. For example, hardware channel simulators also employ sampled channels, and one would like the software and hardware to exhibit similar fidelity.

The purpose of this work is to assess the accuracy of COMLNK in performing the most basic of communications link functions—demodulating the received signal. It is in the simulation of the demodulator that additive white Gaussian noise (AWGN), the transmitted modulation, and the fading channel come together when constructing the received signal.

To assess the accuracy of COMLNK we found that simple “textbook” error rate curves for demodulation performance are inadequate because, in general, they do not include fast fading or frequency selective fading effects nor do they include the effects of carrier tracking. Furthermore, such curves do not address channel delay sampling, and channel sampling is the primary source of the differences we observed between theoretical and simulated demodulation performance.

Thus much of the theoretical work on demodulation performance in fading channels reported here is new and is not yet in the literature. A notable exception is the work of *Bello and Nelin* [1962a, 1962b, 1963], now over 35 years old, which develops

the performance of differentially coherent phase-shift keying (DPSK) and binary frequency-shift keying (BFSK) in fast or frequency selective fading channels. However their results do not include the fading spectra that represent the transionospheric propagation channel and do not include delay sampling effects.

The new analytic delay error and demodulation error rate results in this report, that to our knowledge have not yet been reported in the literature with the exception of ideal delay tracking results [*Dana, Bogusch, and Milner, 1995*], include:

- Ideal direct sequence spread spectrum (DS/SS) delay offset and code correlator loss in continuous and sampled frequency selective fading
- Ideal delay offset for DPSK without an underlying spread spectrum code in frequency selective fading
- DPSK demodulation error rate in fast, frequency selective fading with sampled and continuous channels
- DPSK demodulation error rates in slow fading with two- and three-channel diversity combining
- M -ary FSK demodulation error rates in fast, transionospheric fading excluding tone filter cross correlation
- Ideal delay offset for M -ary FSK with and without hopping in frequency selective fading
- BFSK demodulation error rates with hopping in slow, frequency selective fading with sampled and continuous channels and ideal delay offset
- BFSK demodulation error rates with hopping in fast, frequency selective fading with sampled and continuous channels
- BFSK demodulation error rates without hopping in slow, frequency selective fading with sampled and continuous channels

These theoretical delay offsets and demodulation error rates are discussed in the appendices to this report. Our goal in outlining the often tedious mathematics is to allow the interested reader to follow the theoretical developments and use the results for simulation validation or for use in analytic models of communication links.

While the initial purpose of developing these analytic results was COMLNK validation, in the process we learned a great deal about the simulation of fading chan-

nels that we probably would not have known without the theory together with the simulation. Much of this understanding is related to the effects of delay sampling of the channel. But we also investigated the effects of temporal sampling of the channel and verified that time sampling in COMLNK accurately represents the effects of the channel Doppler frequency spectrum on the demodulation process.

A natural question is why not extend this work to include other processes within a communications link. One part of the answer is that many of the other processes are highly nonlinear and not amenable to analytic solution. The other reason is that it is not really necessary because most of the other processes are emulated, rather than simulated, using the same algorithms as in a microprocessor-based receiver.

An example of a complex link, taken from a COMLNK display, is shown in Figure 1-1. This link includes cyclic redundancy check (CRC) error detection encoding, convolutional encoding for error correction, a convolutional interleaver (IL), binary to M -ary conversion, a chip repeater, synchronization multiplexer, frequency hopping, and frequency-shift keying (FH/FSK) modulation at the data source. There is then an uplink channel to a processing satellite, for example, where the received signal is demodulated and converted back to bits so it can be combined with data from other satellite users. Then the satellite data are converted back to M -ary and again FH/FSK modulated and sent over a downlink channel to the receiver. Here all the signal processing functions performed at the transmitter are undone to form the received message.

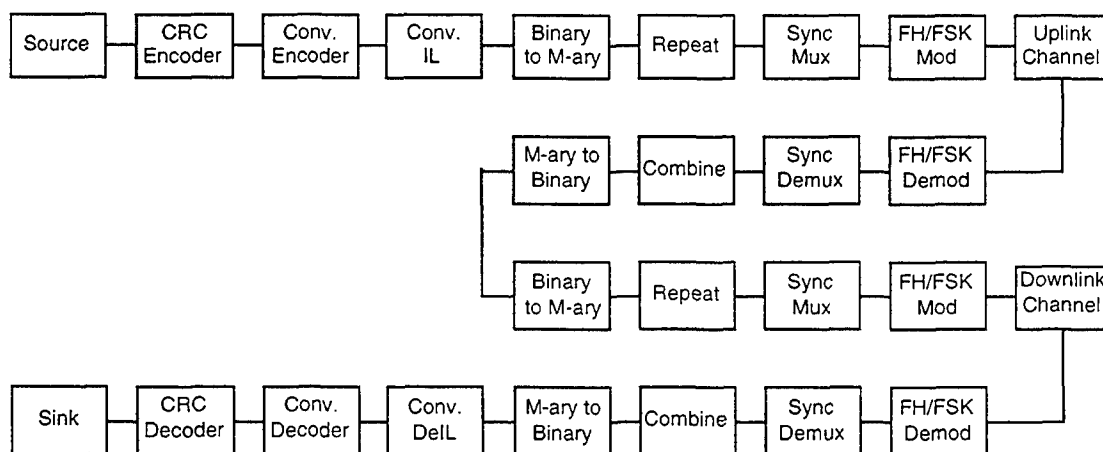


Figure 1-1. Example complex communications system simulated with COMLNK.

In a modern digital communications system the only analog parts are the modulator, the channel, and the demodulator. Indeed, even the demodulation process is often performed using digital samples out of an analog-to-digital (A/D) converter. Thus the only *simulation* in COMLNK is in the generation of the A/D samples. After this point, the receiver is digital and COMLNK is an *emulation* of the digital signal processing that occurs. Validation of the digital signal processing within COMLNK is done by comparing bit by bit and sample by sample the processing with the digital signal processing algorithms within actual receivers.

Most of the signal processing is highly nonlinear and defies analytic analysis that is possible for demodulation. Whenever possible, results from COMLNK are compared with analytic theory, results from other simulations, and test results. This is an ongoing validation effort.

Although in this report we consider only the output of a demodulator after a communications signal has propagated once through a fading channel, we believe that this is sufficient to validate the modulation, demodulation, channel model, and AWGN generation processes within COMLNK. Indeed, a good comparison of the simulated demodulation error rate with theory validates a number of other related processes, as indicated in Figure 1-2 which shows a FH/FSK demodulator in more detail. This block diagram shows the tracking loops necessary for data demodulation, including automatic gain control (AGC), delay-lock loop (DLL), and automatic frequency control (AFC).

A major result of this work is that COMLNK does indeed accurately demodulate DPSK and M -ary FSK signals in fast, frequency selective fading channels. The differences we observe between ideal performance, as defined by the analytic results, and COMLNK results are the result of channel model sampling. When we then compare COMLNK results with ideal performance that includes sampling, we get excellent agreement.

To demonstrate the validation process and to provide the interested reader with useful theoretical results, this report is organized as follows. First, we outline in Section 2 the time and frequency selective fading channel model used in COMLNK and in our theoretical developments. This model is based on official Defense Special Weapons Agency (DSWA) transionospheric channel models with the turbulent approximation to separate time and frequency selective fading effects.

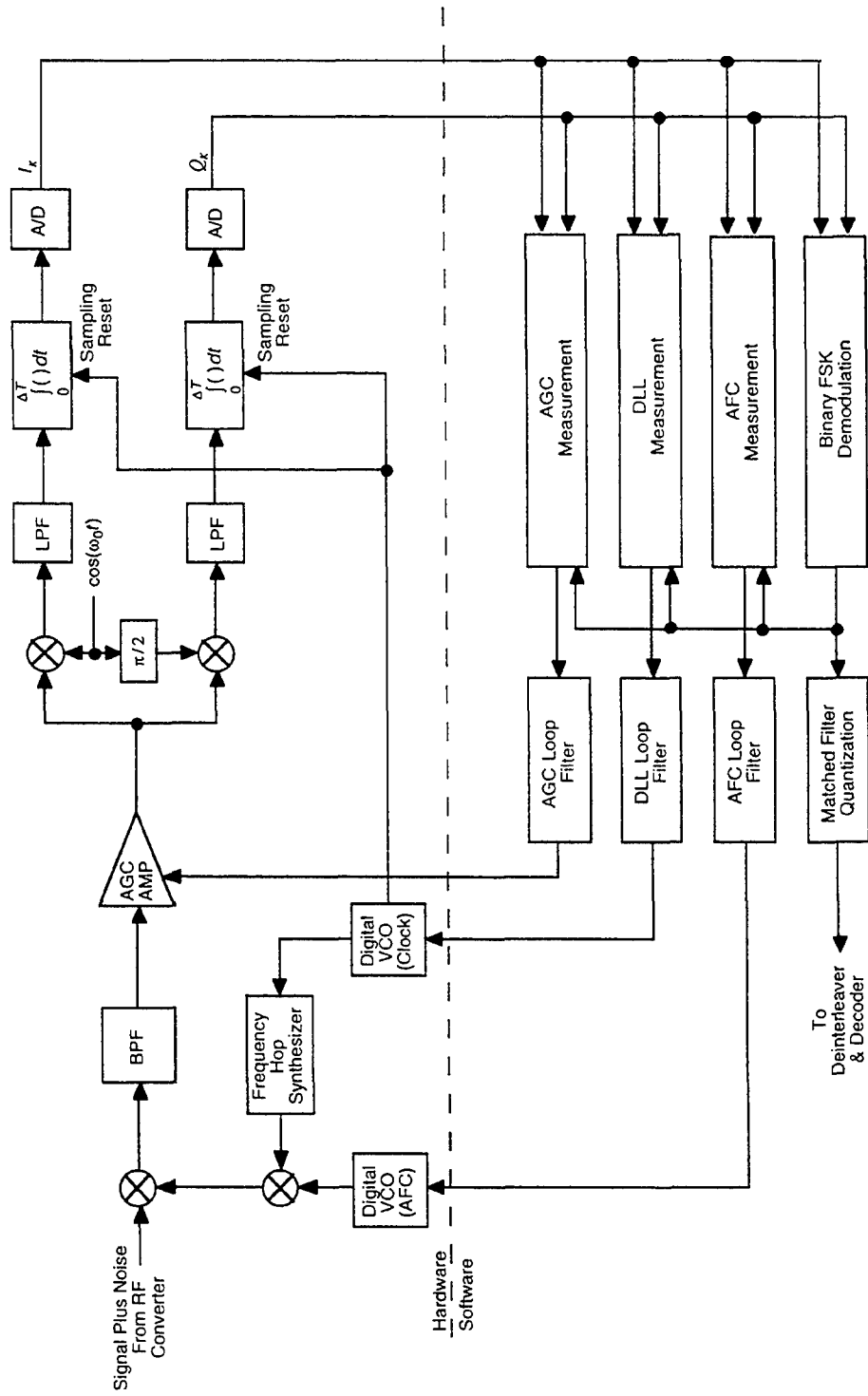


Figure 1-2. Example frequency hopped, frequency-shift keying (FH/FSK) receiver.

In Sections 3 and 4 we compare COMLNK delay tracking and demodulation error rate results, respectively, with theory for all of cases listed above. These two chapters contain all the COMLNK validation results in this report. The rest is analysis.

Theoretical developments are reported in appendices for interested readers. Appendix A, included primarily for completeness, contains a brief discussion of coherent PSK demodulation. This modulation format generally performs poorly in fading channels and is a poor choice for analytic validation because its performance is dependent on that of a highly nonlinear phase-lock loop (PLL). The PLL cannot be treated analytically, although it is readily handled in a simulation.

In Appendix B we discuss DPSK performance with an underlying pseudonoise (PN) code in fast, frequency selective fading channels. This appendix is a summary of work reported earlier [Dana, 1995c], and includes delay offset and code correlator loss for continuous and sampled channel impulse response functions (CIRFs). The performance of DPSK without an underlying PN code in fast, frequency selective fading with sampled and continuous CIRFs is developed in Appendix C. This work, to our knowledge, is new. A short derivation of the basic demodulation error rate formula for DPSK and BFSK is given in Appendix D. A new calculation of the DPSK demodulation error rate with diversity combining in slow fading channels is reported in Appendix E.

Approximate (upper bound) expressions for the demodulation performance of M -ary FSK in fast, flat Rayleigh fading are derived in Appendix F. Because M -ary FSK demodulators are often implemented using discrete Fourier transforms (DFTs), the effects of time sampling are also considered. The question investigated here is whether or not the sampling is sufficient to capture the full Doppler frequency spectrum of the fading channel and what effect, if any, time sampling has on demodulation performance relative to that possible with analog demodulation (*i.e.*, using continuous Fourier transforms). The final two Appendices, G and H, cover BFSK performance, with and without frequency hopping, respectively, in frequency selective fading. These calculations are sufficiently complex that we have not attempted to extend them to M -ary FSK, although such extensions are possible in principle. To our knowledge, all of these FSK results are essentially new and have not been published elsewhere.

SECTION 2

THE FADING RADIO CHANNEL

Scintillation of radio frequency signals propagating through the ionosphere or the troposphere arises from random variations in the index of refraction. Tropospheric index of refraction variations result from atmospheric turbulence, rain, or dust. Ionospheric index of refraction variations result from ionization irregularities produced by plasma instabilities, which cause the ionization to form long filaments, or striations, aligned with the earth's magnetic field. One can visualize such striations as long sheets or rods of relatively high electron density embedded in a background of lower electron density, as shown schematically in Figure 2-1 [Bogusch, *et al.*, 1981].

Consider for a moment an unmodulated wave traversing a region of random fluctuations in the index of refraction. The wave first suffers random phase perturbations due to the variations in phase velocity. As the wave propagates farther, diffractive effects introduce fluctuations in amplitude as well as phase, resulting in undesired complex modulation of the carrier.

In the ionosphere, the index of refraction and phase velocity depend on the frequency of the propagating electromagnetic wave. A communications or radar signal encompasses a spectrum of frequencies because of the transmitted modulation. The frequency-dependent index of refraction causes each spectral component of the signal to experience different phase and amplitude scintillation when propagating along a transionospheric path. If the resulting differences are minor (*i.e.*, if the scintillations are highly correlated across the signal bandwidth), the propagation channel is said to be non-frequency selective, or *flat fading*. When significant statistical decorrelation is observed across the signal bandwidth, the channel is said to be *frequency selective*.

Radio wave propagation through regions of index of refraction fluctuations has been studied for many years by numerous researchers. An extensive body of data has been accumulated from a variety of field experiments. Recordings of signal amplitude and phase scintillation have been made in the natural equatorial and polar regions of the earth's ionosphere [*e.g.*, Fremouw, *et al.*, 1978], and in experiments involving the release of barium chemical compounds at high altitudes [*e.g.*, Davis, *et al.*, 1974; Wolcott, *et al.*, 1978]. The various data have been subjected to considerable analysis to determine the statistical characteristics of scintillation [*e.g.*, Dana, 1992b; De Raad and Grover, 1990; Fremouw, Livingston, and Miller, 1980; Whitney, *et al.*, 1972].

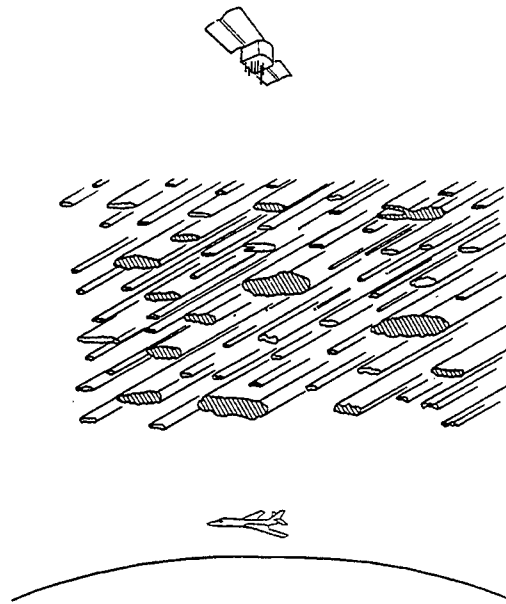


Figure 2-1. Propagation through a striated ionosphere.

The resulting distributions of signal amplitude and phase are described by the first-order scintillation statistics. Temporal, spatial, and spectral correlation properties are described by the second-order statistics.

2.1 FLAT FADING CHANNELS.

As noted above, when the random fluctuations of each spectral component of the received signal exhibit essentially identical behavior in time, scintillation is said to be flat or non-selective over the signal bandwidth. Note that, in this context, the term non-selective refers to frequency selectivity only. Fading channels always exhibit time variation, which is sometimes called time selectivity.

Flat fading is often a good approximation in cases where the signal modulation bandwidth is small, or where index of refraction fluctuations are weak. A monochromatic (CW) signal is a clear example of a situation where the channel is flat or non-selective. In flat fading conditions, the effect of the propagation channel can be represented mathematically by a complex multiplicative factor on the transmitted signal. Thus, if the real transmitted signal is written as

$$S_T(t) = \text{Re}\{m(t)\exp(j\omega_c t)\}$$

where $m(t)$ is the transmitted modulation, ω_c is the carrier angular frequency, and $\text{Re}(\cdot)$ denotes the real part of the argument, then the received signal in a flat fading channel can be written as

$$S_R(t) = r \text{Re}\{a(t)m(t)\exp[j\theta(t) + j\omega_c t]\} \quad (2.1)$$

where r is the nominal received signal amplitude (*i.e.*, the received signal amplitude in the absence of fading), $a(t)$ is the time-varying amplitude modulation imposed by the propagation channel, and $\theta(t)$ is the corresponding channel-imposed phase modulation. The in-phase (I) and quadrature-phase (Q) components of the channel modulation are $a(t)\cos[\theta(t)]$ and $a(t)\sin[\theta(t)]$, respectively. The first-order statistics of the fading channel therefore can be defined either in terms of the amplitude and phase fluctuations, or in terms of the in-phase and quadrature components.

2.1.1 First-Order Statistics.

Statistical analysis of experimental and theoretical results, encompassing many measurements and calculations, reveal that when scintillation is intense or fully developed, the random signal amplitude is Rayleigh distributed, and the random channel phase is uniformly distributed over 2π radians. Thus in a Rayleigh fading channel, the phase function θ is uniformly distributed over the interval $[0, 2\pi]$, and the amplitude function a is described by the Rayleigh probability density function:

$$f_{Ray}(a) = \frac{a}{\sigma^2} \exp\left[-\frac{a^2}{2\sigma^2}\right] \quad a \geq 0 ,$$

where σ^2 is the variance of each of the in-phase and quadrature-phase components of the scattered signal voltage. In terms of received signal power $S = a^2$, the value of σ^2 is equal to one-half the mean power, and the Rayleigh distribution becomes

$$f_{Ray}(S) = \frac{1}{S_0} \exp[-S/S_0] \quad S \geq 0 ,$$

where $S_0 = 2\sigma^2$ is the mean fading signal power. [The quantity S_0 is often set to unity so that amplitude r in Equation (2.1) is determined by the signal-to-noise ratio of the received signal.] The cumulative distribution of the fading signal power S in a Rayleigh fading channel is then

$$F_{Ray}(S) = \int_0^S f_{Ray}(S') dS' = 1 - \exp[-S/S_0] \quad S \geq 0$$

This cumulative distribution is plotted in Figure 2-2. It is seen that in a Rayleigh fading channel, the received signal exhibits fades below 10 dB about 10 percent of the time, below 20 dB one percent of the time, and below 30 dB one-tenth of one percent on the time.

This strong scattering limit can also be obtained by applying the central limit theorem to the superposition of many randomly scattered waves. The I and Q components of the resulting electric field are found to be zero-mean Gaussian random variables, statistically independent, with equal variances of one-half the mean signal power. These conditions are both necessary and sufficient for Rayleigh statistics, which describe the envelope of a narrowband Gaussian noise process. Thus, when scintillation has saturated at a Rayleigh fading condition, the first-order signal statistics are the same as those for narrowband Gaussian noise.

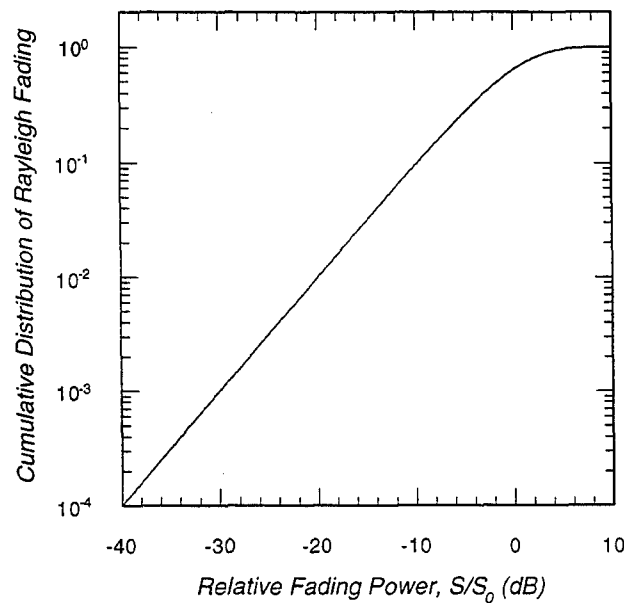


Figure 2-2. Cumulative distribution of received signal power in Rayleigh fading channels.

One measure of the intensity of scintillation is the scintillation index, S_4 , which is the normalized standard deviation of signal power. In terms of the signal voltage a or the fading power S , the scintillation index is defined as

$$S_4 = \left[\frac{\langle a^4 \rangle - \langle a^2 \rangle^2}{\langle a^2 \rangle^2} \right]^{\frac{1}{2}} = \left[\frac{\langle S^2 \rangle - S_0^2}{S_0^2} \right]^{\frac{1}{2}},$$

where angular brackets denote ensemble averages.

In intense scintillation conditions the value of S_4 saturates at unity, which is a necessary (but not sufficient) condition for Rayleigh statistics¹. The value of S_4 is zero in the case of no fading. Values of S_4 between zero and unity correspond to relatively weak scattering conditions where signal fading is less severe than Rayleigh. Values of S_4 somewhat greater than unity are occasionally measured; such values are associated with focusing effects that often accompany multipath conditions.

When the scintillation is not intense or fully developed, the first-order statistics are not neatly described by a single mathematical expression, as is the case for Rayleigh fading. However, two distributions that describe the amplitude fading statistics of non-Rayleigh fading are in common use. These are the Nakagami- m [Nakagami, 1960] and Rician [Rice, 1948] distributions.

There is some evidence that the Rician distribution represents a reasonable worst-case distribution for non-Rayleigh fading [De Raad and Grover, 1990; Dana, 1992b]. This distribution has the added advantage of being as easily implemented in a channel model as is Rayleigh fading since a Rician distributed random process can be obtained by adding a constant component to a Rayleigh distributed process.

The Rician probability density function for the fading power S is

$$f_{Rice}(S) = \frac{1}{S_0(1-R)} \exp\left[-\frac{S/S_0 + R}{1-R}\right] I_0\left[\frac{2\sqrt{RS/S_0}}{1-R}\right], \quad (2.2a)$$

where $I_0(\cdot)$ is the modified Bessel function, and R is the “Rician index,” which is defined as

¹ Sufficient conditions for Rayleigh fading are that the in-phase and quadrature-phase components of the signal be independent, zero-mean, Gaussian random processes with equal variance.

$$R = \sqrt{1 - S_4^2} \quad . \quad (2.2b)$$

The cumulative distribution of the Rician fading power is

$$F_{Rice}(S) = 1 - Q \left[\frac{\sqrt{2R}}{\sqrt{1-R}}, \frac{\sqrt{2S/S_0}}{\sqrt{1-R}} \right] ,$$

where Marcum's Q function [Marcum, 1960] is

$$Q(a, b) = \int_b^{\infty} x \exp \left[-\frac{1}{2}(x^2 + a^2) \right] I_0(ax) dx \quad .$$

The Rician cumulative distribution is plotted in Figure 2-3 for a few values of the scintillation index. The Rician distribution is Rayleigh when S_4 is unity and R is zero. Note that RS_0 is the mean power in the constant component of S , and $(1-R)S_0$ is the mean power of the fluctuating part of S .

2.1.2 Second-Order Statistics.

Relative motion between the propagation path and scattering region, due to movement of the path or scattering region or both, causes the signal propagation channel to vary with time. The resulting time-varying amplitude and phase modulation imposed by the channel is sometimes referred to as time-selective fading. The rate at which the signal amplitude and phase vary with time can range from very slow to quite fast. The fading rate is a function of the relative path velocity, intensity of the scattering irregularity structure, and wave frequency. A precise measure of the fading rate is provided by the signal decorrelation time, which is a parameter involved in the second-order statistics.

The signal decorrelation time is denoted by τ_0 and is defined as the $1/e$ point on the time autocorrelation function of the fluctuating part of complex channel modulation. Writing the complex modulation as

$$E(t) = E_0 + a(t) \exp[j\theta(t)] \quad ,$$

where E_0 is a constant component (E_0 is zero for Rayleigh fading), the autocovariance function² is defined by

² The time autocovariance function is equal to the time autocorrelation function for Rayleigh fading where the constant component E_0 of $E(t)$ is zero.

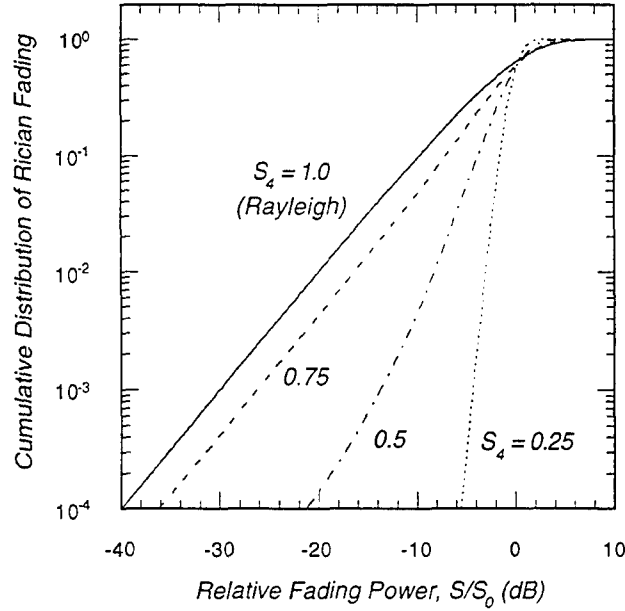


Figure 2-3. Cumulative distribution of received signal power in a Rician fading channel.

$$C(\tau) = \left\langle [E(t) - E_0]^* [E(t + \tau) - E_0] \right\rangle ,$$

where the asterisk denotes complex conjugation. The autocorrelation function of the fluctuating part of $E(t)$ is

$$\rho(\tau) = C(\tau)/C(0) ,$$

and the decorrelation time is defined as $\rho(\tau_0) = 1/e$.

Because small values of τ_0 correspond to fast fading while large values correspond to slow fading, the decorrelation time is an inverse measure of the fading rate. Thus the fading rate can be defined as $1/\tau_0$. Another measure of fading rate that is in use, particularly in the HF community, is the Doppler spread. In this context, Doppler spread refers to the spectral spreading of the signal resulting from the time variation of the undesired amplitude and phase modulation imposed by the propagation channel. The more rapid the scintillation, the greater the Doppler spread. Thus, small values of τ_0 correspond to large values of Doppler spread, and conversely. Doppler spread is de-

finer by the bandwidth of the signal scintillation Doppler frequency power spectrum $S_D(\omega_D)$, which is the Fourier transform of the autocorrelation function:

$$S_D(\omega_D) = \int_{-\infty}^{\infty} \rho(\tau) e^{-j\omega_D \tau} d\tau .$$

The Doppler radian frequency ω_D is measured relative to the signal carrier frequency.

Measurements of the fading power spectrum have been made with experimental data from satellite transmissions and with signal realizations from multiple phase screen (MPS) calculations [Knepp, 1983a]. The spectrum has also been investigated analytically. In slow fading conditions the spectrum is generally found to exhibit a power-law dependence on Doppler frequency, with an f^{-4} dependence being representative of the observed spectra. In fast fading conditions the fall-off with Doppler frequency is more rapid, limiting to a Gaussian spectrum when the fading is quite fast.

A Gaussian spectrum, which is often employed in analytical investigations because of its mathematical tractability, is

$$S_D(\omega_D) = \sqrt{\pi} \tau_0 \exp\left[-\frac{1}{4}(\tau_0 \omega_D)^2\right] . \quad (\text{Gaussian Spectrum}) \quad (2.3)$$

The Fourier transform of a Gaussian function retains the Gaussian form, and the autocorrelation function corresponding to Equation 2.2 is found to be

$$\rho(\tau) = \exp\left[-\frac{\tau^2}{\tau_0^2}\right] . \quad (\text{Gaussian Spectrum})$$

An f^{-4} form for the fading power spectrum is particularly convenient for channel simulation because it can be synthesized using two-pole filters, which are easily implemented in hardware or software. When the two-pole filters are formed using pairs of cascaded single-pole RC filters, the f^{-4} spectrum is given by

$$S_D(\omega_D) = \frac{4\tau_0/\alpha_4}{[1 + (\tau_0 \omega_D/\alpha_4)^2]^2} , \quad (f^{-4} \text{ Spectrum}) \quad (2.4)$$

where τ_0/α_4 is the time constant of each of the single-pole RC filters. The value of α_4 is obtained from the autocorrelation function, given by the Fourier transform of Equation (2.4):

$$\rho(\tau) = \left(1 + \frac{\alpha_4 |\tau|}{\tau_0}\right) \exp\left(-\frac{\alpha_4 |\tau|}{\tau_0}\right) . \quad (f^{-4} \text{ Spectrum})$$

Upon setting $\rho(\tau_0) = 1/e$ and solving the resulting equation numerically, one obtains $\alpha_4 = 2.146193\dots$.

A channel with a Gaussian Doppler frequency spectrum also can be synthesized approximately using multiple-pole filters with suitable weights. However, *Dana* [1994] has shown that temporal statistics (*i.e.*, the mean fade duration and separation) of an f^{-6} spectrum are a close approximation to those of the Gaussian form. The f^{-6} form can be synthesized using three-pole filters, and when the three-pole filters are formed using three cascaded single-pole RC filters the resulting f^{-6} spectrum is

$$S_D(\omega_D) = \frac{16\tau_0/\alpha_6}{[1 + (\tau_0 \omega_D/\alpha_6)^2]^3}, \quad (f^{-6} \text{ Spectrum}) \quad (2.5)$$

where again τ_0/α_6 is the time constant of each of the single-pole RC filters. The value of α_6 is obtained from the autocorrelation function:

$$\rho(\tau) = \left[1 + \frac{\alpha_6|\tau|}{\tau_0} + \frac{1}{3} \left(\frac{\alpha_6|\tau|}{\tau_0} \right)^2 \right] \exp \left(-\frac{\alpha_6|\tau|}{\tau_0} \right). \quad (f^{-6} \text{ Spectrum})$$

Upon setting $\rho(\tau_0) = 1/e$ and solving the resulting equation numerically, one obtains $\alpha_6 = 2.904630\dots$. The use of multiple, uncorrelated f^{-6} flat fading realizations to construct a realization of the frequency selective channel impulse response function is described later in the subsection on channel modeling.

The f^{-4} and f^{-6} spectra given by Equations (2.4) and (2.5) fall off less rapidly at high Doppler frequencies than does the Gaussian spectrum given by Equation (2.3). These three Doppler spectra are compared in Figure 2-4. The greater high frequency content of random amplitude and phase modulation makes the f^{-4} spectrum a more stressing case for most communications systems. Demodulation and tracking functions tend to degrade more rapidly in the presence of “noisier” signal fluctuations corresponding to this power-law spectrum. The fact that the f^{-4} spectrum represents a reasonable worst case, coupled with its ease of implementation in hardware and software, has made it the standard for use in flat fading channel simulators. As can be seen from the figure, the f^{-6} spectrum lies between the Gaussian and f^{-4} spectra.

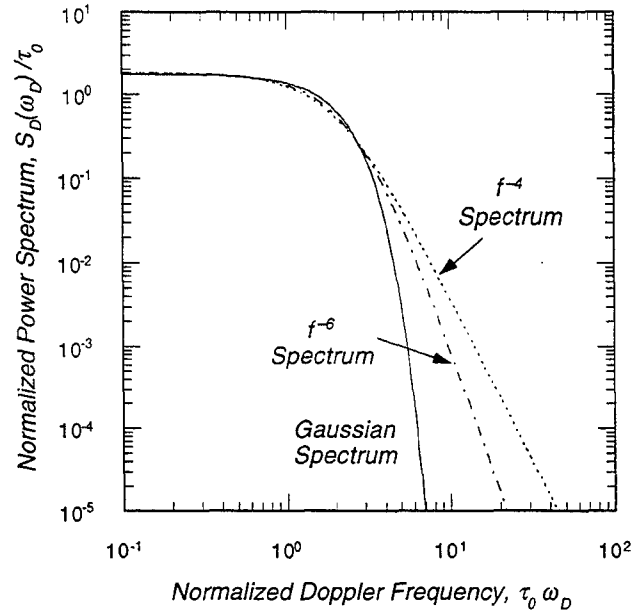


Figure 2-4. Comparison of Gaussian, f^{-6} and f^{-4} fading signal power spectra.

2.2 FREQUENCY SELECTIVE CHANNELS.

When the signal modulation bandwidth is large and the propagation channel is highly disturbed, frequency selective fading becomes important. No longer can the effect of the channel be represented by a multiplicative factor on the transmitted signal. Instead, the channel is represented by a time-varying linear filter, and the received signal is given by the convolution of the transmitted signal and the channel impulse response function:

$$S_R(t) = \text{Re} \left[u(t) \exp(-j\omega_c t) \right]$$

$$u(t) = r \int_0^{\infty} m(t - \tau) h(t, \tau) d\tau \quad , \quad (2.6)$$

where r is the amplitude of the received signal in the absence of propagation effects. The quantity $u(t)$ is the complex envelope of the received signal, and $h(t, \tau)$ is the time-varying impulse response function of the propagation channel. As before, $m(t)$ is the transmitted modulation, and ω_c is the carrier angular frequency.

The primary measure of the level of frequency selectivity is the frequency selective bandwidth, denoted by f_0 . This is another parameter involved in the second-order signal statistics. The relationship between f_0 and the standard deviation of signal time delay jitter σ_τ arising from angular scattering is

$$f_0 = \frac{1}{2\pi\sigma_\tau} .$$

The value of f_0 is commensurate with the maximum modulation rate that the channel will support with little intersymbol interference. Small values of f_0 therefore correspond to severe frequency selectivity, while large values are associated with flat fading or undisturbed channels. Depending on the level of disturbance in the propagation medium, the frequency selective bandwidth can range from very large to quite small values.

Another measure of frequency selectivity that is in common use is the multipath delay spread of the signal. The delay spread is related to the angular scatter-induced time delay jitter and hence is inversely related to the frequency selective bandwidth. Thus small values of f_0 (severe frequency selectivity) correspond to large values of multipath delay spread, and conversely.

Determination of the statistical properties of a frequency selective propagation channel encompasses the relationship between the statistics of the scattering region and those of the received signal. Significant progress has been made in recent years in analytically establishing this link between environmental descriptions and signal statistics [Knepp, 1983b; Dana, 1986; Dana, 1991].

As shown in Equation (2.6), the frequency selective propagation channel is conveniently represented in terms of the time-varying channel impulse response function $h(t, \tau)$. An equivalent representation may be cast in terms of the Fourier dual, the time-varying channel transfer function $H(t, \omega)$. The former is the channel response at time t to an impulse transmitted at $t - \tau$. The latter is the channel response to a sinusoidal excitation at frequency ω .

Propagation theory can be used to compute specific realizations of the channel impulse response function, but these calculations must be performed numerically. What can be obtained analytically is the statistical description of the channel response. This relationship is formulated in terms of the generalized power spectral density (GPSD) of the received signal.

The derivation of the GPSD starts with Maxwell's equations, from which the parabolic wave equation is derived. A necessary condition for the parabolic wave equation to be valid is that the phase perturbation over a distance comparable to a wavelength be small relative to one radian. A sufficient condition is that the angular deviation of the wave relative to the principal propagation path be small relative to one radian. These conditions are generally satisfied whenever attenuation of the propagating wave is not significant in the scattering medium.

The parabolic wave equation can be solved to give the received electric field for a specific distribution of the index of refraction. The difficulty lies in the fact that the index of refraction is a random process, so the received electric field is also a random process. The parabolic wave equation is therefore used to derive an equation for the two-time, two-frequency, two-position mutual coherence function. The solution of the differential equation for the mutual coherence function provides a description of the second-order statistics of the received electric field. The Fourier transform of the mutual coherence function is the GPSD of the received signal. Two of the parameters involved in the GPSD are the decorrelation time, τ_0 , and the frequency selective bandwidth, f_0 .

The GPSD has a particularly simple form in the limit that spatial and temporal fluctuations of the scintillation are decoupled (the so called turbulent model). In this limit, the GPSD can be written as product of the Doppler frequency power spectrum $S_D(\omega_D)$ and the power impulse response function $G(\tau)$:

$$S(\omega_D, \tau) = S_D(\omega_D) G(\tau) , \quad (2.7)$$

where τ is the time delay. In the limit that the scattering is isotropic about the propagation direction, the power impulse response function is exponential:

$$G(\tau) = \begin{cases} \omega_{coh} \exp(-\omega_{coh} \tau) & \tau \geq 0 \\ 0 & \tau < 0 \end{cases} , \quad (2.8)$$

where the coherence bandwidth ω_{coh} is related to f_0 :

$$\omega_{coh} = 2\pi f_0 .$$

The quantity $G(\tau) d\tau$ is the mean signal power arriving in the delay interval τ to $\tau + d\tau$ relative to the nominal propagation time.

The Fourier transform of the power impulse response function is the two-frequency mutual coherence function, which describes the correlation in the fading at two frequencies in the signal bandwidth:

$$\Gamma(\omega) = \langle H^*(t, \omega_1) H(t, \omega_2) \rangle = \int_0^\infty G(\tau) e^{-j\omega\tau} d\tau = \frac{1}{1 + j(\Delta f / f_0)} ,$$

where ω is the difference between two radian frequencies ($\omega = \omega_1 - \omega_2$), and $\Delta f = 2\pi\omega$. As indicated in the expression for $\Gamma(\omega)$, this function is also equal to the expectation of the channel transfer function at two frequencies.

The fact that $\Gamma(\omega)$ is complex indicates that there is correlation between the real part of the channel impulse response function at one frequency and the imaginary part at another frequency. As a consequence, for example, the correlation in the outputs of the two binary frequency-shift keying (BFSK) tone filters in frequency selective fading is complex. A more interesting observation is that the magnitude of $\Gamma(\omega)$,

$$|\Gamma(\omega)| = \frac{1}{\sqrt{1 + (\Delta f / f_0)^2}} ,$$

varies as $f_0 / \Delta f$ for small values of the ratio. Thus the fading measured at one time on two frequencies separated by f_0 or larger exhibits a higher degree of correlation than does the fading on one frequency measured at two times separated by τ_0 or larger.

In conjunction with Rayleigh first order statistics, the GPSD provides a complete statistical description of the frequency selective scattering channel. Given values of the signal decorrelation time and frequency selective bandwidth, the GPSD can be used to generate specific realizations of the channel impulse response function. The channel impulse response function then enables specific realizations of the received signal to be generated for uses in analysis and testing. The procedure for simulating the channel is described in *Dana* [1991, 1994] and is summarized in *Bogusch and Michelet* [1993].

2.3 CHANNEL MODELING TECHNIQUES.

Design, testing and evaluation of digital communications and radar equipment in fading channels are areas in which there is an increasing utilization of channel models to simulate the effects of propagation disturbances. The design process is greatly facilitated and made quite precise by the use of software channel models in conjunction with detailed computer simulations of the receivers. Once a design is selected, verification that it has been properly translated into hardware relies heavily on hardware

channel models that perturb transmitted signals either at RF or after downconversion to IF. Channel models have been developed for both the flat fading channel and the frequency selective fading channel, and these models have been implemented in software and in hardware. This subsection summarizes two techniques that have proven useful in modeling the fading radio channel.

2.3.1 Flat Fading Channels.

Simulation of flat fading channels is readily accomplished in either software or hardware. The basis for a flat fading channel simulator is the fact that the effect of non-selective scintillation is to impose a multiplicative complex modulation (amplitude and phase) on the transmitted signal. In other words, the channel transfer function is independent of frequency over the signal bandwidth, and the channel impulse response function is a Dirac delta function in delay:

$$\begin{aligned} H(t, \omega) &= a(t) e^{j\theta(t)} \\ h(t, \tau) &= a(t) e^{j\theta(t)} \delta(\tau) \end{aligned} \quad (\text{Flat Fading})$$

With these relationships, it is readily seen that the convolution in Equation (2.6) reduces to a multiplication of the transmitted signal times the complex modulation $a(t) e^{j\theta(t)}$, which yields the expression for the received signal given in Equation (2.1). When the transmitted data modulation is real, Equation (2.1) can be rewritten as

$$S_R(t) = a(t) m(t) \cos[\theta(t)] \cos(\omega_c t) - a(t) m(t) \sin[\theta(t)] \sin(\omega_c t) \quad (2.9)$$

Implicit in this representation is the usual assumption that both the data modulation and the fading power spectra are narrowband with respect to the carrier frequency. Equation (2.9) can be rewritten in terms of two quadrature modulating waveforms:

$$S_R(t) = I(t) [m(t) \cos(\omega_c t)] + Q(t) [m(t) \cos(\omega_c t + \pi/2)] ,$$

where

$$\begin{aligned} I(t) &= a(t) \cos[\theta(t)] \\ Q(t) &= a(t) \sin[\theta(t)] \end{aligned}$$

These equations show that the flat fading received signal can be generated by passing the transmitted signal through a power splitter, shifting the phase of one of the outputs by 90 degrees, and then passing the signal and its phase-shifted version through two product modulators. The quadrature modulating waveforms, $I(t)$ and $Q(t)$, repre-

sent the fading channel. These waveforms can have any statistical descriptions; hence the simulator is not limited to any particular type of channel as long as it can be adequately represented as narrowband and non-selective over the signal bandwidth.

One way of generating specific realizations of the quadrature modulating waveforms, applicable to Rayleigh or Rician fading channels, is to invoke the signal statistical approach. In this case the I and Q waveforms are each represented by zero-mean Gaussian random processes, statistically independent of each other, with equal variances. A specular or constant component is included for Rician channels. Given the fading power spectrum, white Gaussian noise can be appropriately filtered to produce the desired second-order statistics of the fluctuating component.

The f^{-4} fading power spectrum defined in Equation (2.4) has become the standard for use in ionospheric flat fading simulators, because it represents a reasonable worst case and is easily synthesized [Wittwer, 1980]. This spectrum can be realized by passing white Gaussian noise through two cascaded single-pole RC lowpass filters in each of the two quadrature channels. Figure 2-5 illustrates the functional configuration of the resulting channel simulator. The relationship between the time constant of each of the RC filters τ_{RC} and the scintillation decorrelation time τ_0 is $\tau_{RC} = \tau_0 / \alpha_4$ [see Eqn. (2.4)], and the relationship between the "Rician index" R and the scintillation index S_4 is given by Equation (2.2).

This flat fading channel simulator can be implemented in software or in analog or digital hardware³. In a digital implementation, the two white Gaussian noise sources are simply two independent sequences from a Gaussian random number generator. Such sequences can be easily generated using uniformly distributed random numbers:

$$\begin{aligned} g_1 &= \sqrt{-2\sigma^2 \ln(u_1)} \cos(2\pi u_2) \\ g_2 &= \sqrt{-2\sigma^2 \ln(u_1)} \sin(2\pi u_2) \end{aligned} ,$$

³ Care must be exercised in a hardware implementation to ensure that no measurable amount of unmodulated signal inadvertently leaks through the output in Rayleigh fading. Because flares to nearly +10 dB and fades to below -30 dB relative to the mean signal level are common in Rayleigh fading channels, the quadrature modulators must operate over at least a 40-dB dynamic range, and there should be at least 50-dB of isolation between the input and output in Rayleigh fading ($R = 0$). If some unmodulated signal leaks through, the resulting specular component yields Rician fading, which may be significantly less stressing than Rayleigh.

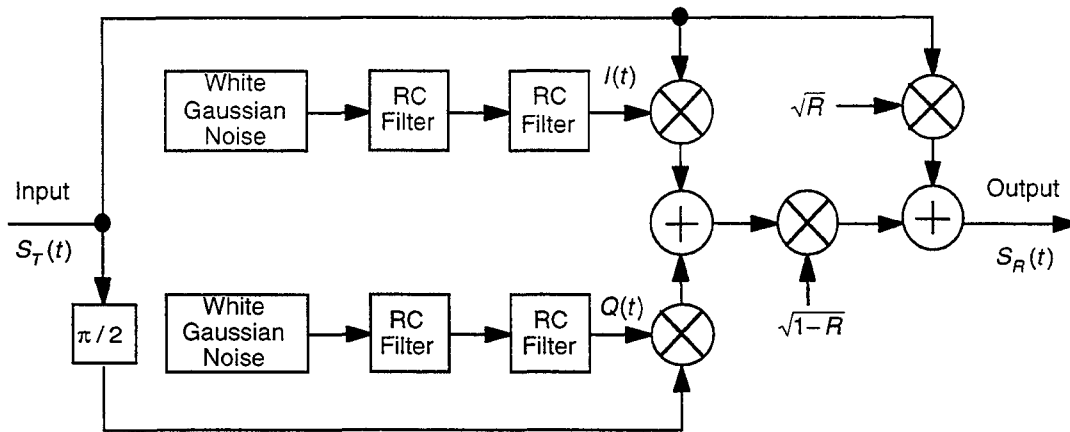


Figure 2-5. Flat fading channel simulator.

where u_1 and u_2 are random numbers drawn from a uniform distribution over the interval $(0,1)$, and g_1 and g_2 are independent, zero-mean, Gaussian random numbers, each with variance σ^2 .

Each single-pole RC filter can be implemented digitally using the recursive relation

$$\xi_k = a\xi_{k-1} + b\zeta_k, \quad (2.10)$$

where ξ_k is the current output of the filter, ζ_k is the current input, and k is the sampling index. The quantities a and b are filter coefficients, where a is determined by the filter time constant, and b is determined by the filter gain. When the filter gain is set to unity, the values of a and b are given by [Bogusch, 1989]

$$a = \exp(-\alpha_4 \Delta t / \tau_0)$$

$$b = \left[\frac{(1-a^2)^3}{1+a^2} \right]^{1/4},$$

where Δt is the sampling time interval. Note that, as in any digital filter implementation, the sampling rate must be rapid enough to minimize spectral aliasing. Because of the stochastic nature of the fading channel, there is no precise definition of the required sampling rate. The sampling rate must be high enough to ensure that the portion of the fading spectrum that will be aliased contains an insignificant fraction of the total

power. Experience has shown that choosing $\Delta t \leq \tau_0 / 10$ is usually sufficient. To accurately represent the statistics of the duration of fades to -30 dB or so, sampling intervals $\Delta t \leq \tau_0 / 40$ are required [Dana, 1982; Dana, 1993].

If the filter coefficients are held constant, the statistics of the flat fading channel will be stationary. On occasion one may wish to simulate a non-stationary channel. This can be done by changing the filter coefficients sufficiently slowly that the channel is quasi-stationary insofar as the sampling process is concerned. Thus a channel whose statistical properties change slowly compared to the fading rate can be readily simulated by variation of filter coefficients in the channel simulator [Dana, 1994].

2.3.2 Frequency Selective Fading Channels.

Simulation of frequency selective channels is straightforward, albeit more complicated than flat fading channel simulation. Two methods of implementing frequency selective channel simulators are in use. These are the Fourier synthesis method (frequency domain) and the convolution synthesis method (time domain). Up to now, the choice between the two methods has been largely dictated by the selection of software or hardware implementation. The Fourier synthesis method has been extensively applied in previous software channel simulations. The convolution synthesis method is used extensively in hardware channel simulators. However, convolution synthesis has also been implemented in software (*e.g.*, COMLNK), and with modern digital signal processing technology Fourier synthesis can be implemented in hardware.

The basis for the Fourier synthesis technique is provided by Equation (2.6) with the convolution rewritten in terms of the signal spectrum and channel transfer function:

$$\begin{aligned} S_R(t) &= \text{Re}[u(t)e^{j\omega_c t}] \\ &= \text{Re}[u(t)]\cos(\omega_c t) - \text{Im}[u(t)]\sin(\omega_c t) \quad , \quad (2.11) \\ u(t) &= \frac{1}{2\pi} \int_{-\infty}^{\infty} M(\omega) H(t, \omega) e^{j\omega t} d\omega \end{aligned}$$

where $M(\omega)$ is the Fourier transform of the transmitted modulation waveform $m(t)$.

Once values of the channel transfer function $H(t, \omega)$ have been computed at a set of discrete frequencies within the signal bandwidth, the complex envelope $u(t)$ is computed from the integral in Equation (2.11) using a discrete Fourier transform. The ex-

pression for the received signal in this equation shows that $S_R(t)$ can be generated using the same type of quadrature modulator as shown in Figure 2-5, except that here the I and Q modulating waveforms are given by $\text{Re}[u(t)]$ and $\text{Im}[u(t)]$, respectively.

The convolution synthesis method of simulating a frequency selective channel is the time domain dual of the Fourier synthesis method. The convolution integral in Equation (2.6) is applied directly here. Thus both methods of synthesizing a frequency selective signal require an integration to be performed at each time that the signal is to be sampled. The Fourier synthesis method implements the integration (Eqn. 2.11) using a discrete Fourier transform. The convolution synthesis method implements the integration (Eqn. 2.6) using a transversal filter. Perhaps the primary difference is that in the convolution synthesis method the transmitted modulation waveform $m(t)$ is input directly rather than in spectral form. This is often convenient in hardware and software implementations of the channel simulator, and is the reason for using convolution synthesis in COMLNK.

A discrete version of the convolution integral (Eqn. 2.6), suitable for implementation in a tapped delay line transversal filter, is given by

$$u(t) = \sum_{i=0}^{N_\tau-1} m(t - i\Delta\tau) h(t, i\Delta\tau) \Delta\tau \quad , \quad (2.12)$$

where N_τ is the number of taps on the delay line, and $\Delta\tau$ is the delay spacing between each tap. The complex tap weights $h(t, i\Delta\tau) \Delta\tau$ are given by the sampled values of the channel impulse response function at delays $i\Delta\tau$. Figure 2-6 illustrates the functional implementation of a tapped delay line frequency selective channel simulator. This configuration is implemented in hardware in the Defense Special Weapons Agency Nuclear Effects Link Simulator (NELS II) [Hsiung, 1997], which operates at 700 MHz intermediate frequency (IF) and employs 48 taps on a coaxial tapped delay line. The tapped delay line configuration is also implemented in software in COMLNK. The number of taps used in COMLNK depends on the ratio of signal bandwidth to the channel frequency selective bandwidth.

With either the tapped delay line or the Fourier synthesis approach, samples of the channel impulse response function (or its Fourier transform) must be generated to simulate the frequency selective channel. This can be accomplished using either the MPS method or the GPSD statistical method. The latter approach is convenient in the limit of strong scattering (Rayleigh fading).

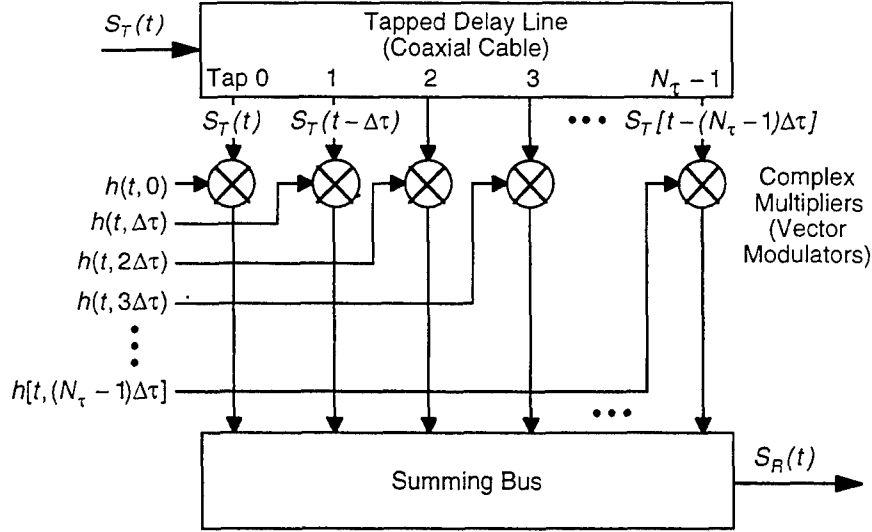


Figure 2-6. Tapped delay line frequency selective channel simulator.

Under strong scattering conditions where the GPSD is valid, the real and imaginary parts of the channel impulse response function are independent, zero-mean, Gaussian random variables. Specific realizations of the impulse response function can be generated using the CIRF [Wittwer, 1980] or ACIRF [Dana, 1992a] codes. This approach enables properly correlated realizations of the received signal to be generated at the outputs of multiple antennas with arbitrary aperture sizes, locations, and orientations with respect to the scattering directions.

A particularly simple special case arises when one considers the turbulent model with isotropic scattering, a small antenna aperture (no spatial filtering), and diffractive effects dominate. In this case, the GPSD takes the form given in Equation (2.7). Specific realizations of the channel impulse response function are generated by choosing a discrete delay grid defined by

$$\tau_i = i \Delta\tau \quad (i = 0, 1, 2, \dots, N_\tau - 1) \quad .$$

The total delay spread depends on the signal bandwidth, determined by the modulation period T , and the channel bandwidth, determined by the frequency selective bandwidth f_0 . The delay spread is proportional to the reciprocal of the product $f_0 T$. The delay spacing and the number of delay samples needed to represent the channel are therefore functions of these parameters. If P_τ denotes the fraction of the total signal

power that is to be contained in the delay grid, then integration of Equation (2.8) yields the following expression for the number of delay taps, N_τ :

$$N_\tau = 1 - \frac{\ln(1 - P_\tau)}{2\pi f_0 \Delta\tau} . \quad (2.13)$$

The mean signal power at each tap is obtained by integrating Equation (2.8) over the corresponding delay interval:

$$P_i = \int_{i\Delta\tau}^{(i+1)\Delta\tau} G(\tau) d\tau = \exp[-i\omega_{coh}\Delta\tau] - \exp[-(i+1)\omega_{coh}\Delta\tau] . \quad (2.14)$$

The sampled channel impulse response function for the i^{th} delay tap is then

$$h(t, i\Delta\tau)\Delta\tau = (x_i + jy_i)\sqrt{P_i} , \quad (2.15)$$

where x_i and y_i are independent, zero-mean, Gaussian random numbers with equal variance of 1/2. The complex Gaussian factor provides the Rayleigh fading time history for each delay sample. It is important to remember that the channel impulse response function is delta-correlated in delay, and hence x_i and y_i are independent for different values of i corresponding to different delay taps.

At times it is desirable to generate frequency selective realizations by time-domain filtering of white Gaussian noise, whereupon it is again convenient to assume that the Doppler spectrum can be represented by a power-law form with an even spectral index. The f^{-6} Doppler spectrum produces realizations with temporal statistics (i.e., mean fade duration and separation) that are close to that produced by a Gaussian spectrum. Realizations of x_k and y_k with an f^{-6} spectrum can be generated directly in the time domain using three cascaded RC filters [Dana, 1994].

Each single-pole RC filter can be implemented digitally using the recursive relation in Equation (2.10), where $\xi_{i,k}$ is the current output of the filter, $\zeta_{i,k}$ is the current input, i is the delay index and k is the sampling index. The filter coefficients a and b for a unity gain filter are given by the expressions

$$a = \exp(-\alpha_6 \Delta t / \tau_0)$$

$$b = \left[\frac{(1 - a^2)^5}{1 + 4a^2 + a^4} \right]^{\frac{1}{6}} .$$

Separate filters with independent noise sources are used for each tap. The resulting samples of the channel impulse response from Equation (2.15) are used directly in the tapped delay line model of Equation (2.12). Alternatively, these samples can be Fourier transformed to yield samples of the channel transfer function and then used in the Fourier synthesis channel model, Equation (2.11).

SECTION 3

EFFECT OF CHANNEL TAP SPACING ON DELAY TRACKING AND AUTOMATIC GAIN CONTROL OPERATION

Generally, when developing analytic demodulation error rates, one assumes that the receiver has negligible tracking errors so it is perfectly locked up on the signal in time-of-arrival, frequency, and phase (if the signal is coherently demodulated). Thus the integration period of the analog-to-digital (A/D) converter is assumed to be perfectly aligned with the modulation boundaries in the received signal, and the phase of the signal is assumed to be constant or varying in a prescribed manner during the sample period. Given that the receiver has well-designed tracking loops, these may be reasonable assumptions if the propagation channel is either slow, flat fading or non-fading. In benign or flat fading propagation environments the ideal delay offset is zero so the receiver sampling time is exactly aligned with the modulation period of the received signal. However, in a frequency selective fading environment, where the signal energy from a transmitted symbol may arrive at the receiver over several symbol periods, the ideal delay offset is not zero. To assume otherwise is to miss an essential part of the problem. This is particularly true in spread spectrum receivers.

In this section we develop the ideal delay tracking offset and the resulting signal loss of direct sequence (DS) and frequency hopped (FH) receivers operating in frequency selective fading channels. This section is primarily concerned with the question of channel model simulation accuracy, rather than COMLNK validation per se. The issue addressed here is the effect of delay sample spacing in a tapped delay line representation of the frequency selective channel.

For both link simulations and hardware channel simulators, the channel impulse response function (CIRF) is necessarily generated with a finite number of delay samples, and the performance of a delay-lock loop (DLL) is found to be quite sensitive to the coarseness of the sampling. Thus we calculate ideal delay offset and the resulting signal loss for both continuous and sampled CIRFs¹ and then compare these results to measurements from COMLNK and actual hardware tests.

¹ By "continuous CIRF" we mean that the delay variable is continuous and by "sampled CIRF" we mean that the delay variable is defined only at discrete values. Because the CIRF is delta correlated in delay, the function itself is "infinitely discontinuous" in either case.

Measurement of the signal energy and tracking errors in COMLNK is done in much the same way that such measurements could be made in an actual receiver². To measure signal energy we monitor the operation of the automatic gain control (AGC) which produces a control value that is roughly proportional to the signal level. This measurement is rough because the input to the AGC is *signal plus noise*, not just signal, and because the AGC is a non-linear tracking loop with start-up transients and dynamically varying output as the input signal plus noise fluctuates sample-by-sample. The significance of this will become apparent when we compare average signal energy in COMLNK with theoretical results. Time and frequency tracking errors are measured by comparing the tracking loop output with the "truth." An important advantage of a simulation over actual hardware in this regard is that the truth is known, so tracking errors can be measured accurately.

In Section 3.1 we summarize the calculation of the ideal delay offset in frequency selective fading. The details of the theoretical calculations are presented in Appendices B and G for DS and FH spread spectrum receivers, respectively. These results are compared with COMLNK and selected test results in Section 3.2.

3.1 IDEAL DELAY OFFSET AND SIGNAL LOSS.

Direct sequence and frequency hopped spread spectrum receivers have different mathematical descriptions for the early and late samples that are inputs to a delay-lock loop tracking filter. Thus we must treat them separately.

A functional block diagram of a direct sequence, phase-shift keying (DS/PSK) receiver with a separate code correlator for DLL tracking is shown in Figure 3-1. An adaptive automatic frequency/phase control (AFC/Costas) loop is used to track phase when possible or to track frequency when phase lock is lost. The differentially encoded PSK signal is then coherently demodulated (Δ PSK) or differentially coherently demodulated (DPSK) when the AFC/Costas loop is in phase lock or not, respectively.

² COMLNK allows monitoring of most internal parameters that could *in principle* be monitored in a receiver. However, there is usually very limited access, if any, to such parameters in an actual receiver, unless it is specifically designed to include a variety of test points.

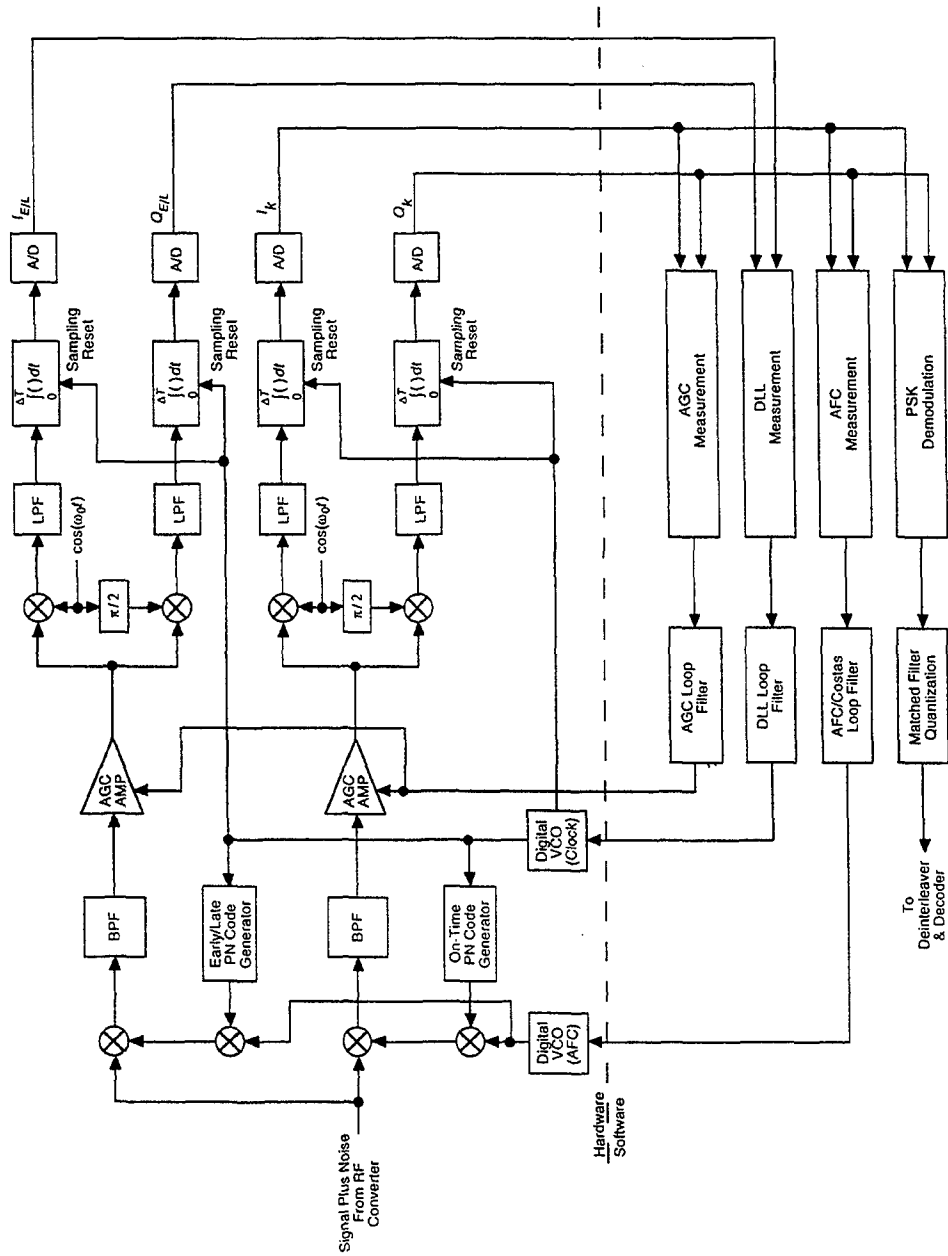


Figure 3-1. Block diagram of a direct sequence PSK receiver with early and late code correlators for DLL tracking.

3.1.1 Direct Sequence Spread Spectrum Delay Tracking.

In a direct sequence spread spectrum (DS/SS) receiver, early and late voltages are formed with a code correlator³ using early and late versions of the locally generated pseudo-noise (PN) code. The DLL error measurement is proportional to the difference in the energy between the early and late samples, and the ideal delay offset is that for which the mean energy difference is zero. To analyze ideal delay offset we must construct the early and late code correlator output voltages in terms of the transmitted PN sequence and the channel impulse response function.

The transmitted DS/SS modulation is⁴

$$m(t) = \sum_k m_k \Pi \left[\frac{t}{T_C} - k \right]$$

where $m_k = \pm 1$ randomly is the PN code, and T_C is the chip period of the code ($R_C = 1/T_C$ is the code rate). The symbol $\Pi(\cdot)$ denotes the rectangular function that is defined as

$$\Pi(x) = \begin{cases} 1 & \text{if } |x| \leq \frac{1}{2} \\ 0 & \text{otherwise} \end{cases}.$$

As described in Section 2, the received signal is the convolution of the channel impulse response function and the transmitted modulation:

$$u(t) = r \int_0^{\infty} m(t - \tau) h(t, \tau) d\tau, \quad (3.1)$$

³ The early and late voltages are usually generated by the same code correlator, which is time-shared between the two measurements.

⁴ We have ignored the data modulation in this theoretical analysis because we assume that the number of PN chips per channel symbol is large and that the delay error tracking measurements are all made within single symbol periods. Because we consider non-coherent tracking where early and late energy samples are compared, the ideal delay offset is independent of the data modulation. This is only one of several design configurations available in COMLNK, wherein effects of data modulation are treated in detail.

where r is the mean received signal amplitude, and $h(t, \tau)$ is the CIRF which is a function of time t and delay or time-of-arrival τ . When the CIRF is sampled the integral in this equation is replaced by a summation:

$$u(t) = r \sum_{i=0}^{N_\tau-1} m(t - i\Delta\tau) h_i(t) ,$$

where $\Delta\tau$ is the delay sample size, N_τ is the number of delay samples (Eqn. 2.13), and $h_i(t)$ is the time-varying channel response for the i^{th} delay bin.

If we assume that the receiver advances or retards its locally generated PN code to match that of the received signal and integrates over a fixed sample period T_S , then the signal contributions to the early, on-time, and late voltage samples are represented by the expressions

$$\begin{aligned} S_E &= \frac{1}{T_S} \int_{-T_S/2}^{T_S/2} m^*(t - \tau_D + T_C / 2) u(t) dt \\ S_O &= \frac{1}{T_S} \int_{-T_S/2}^{T_S/2} m^*(t - \tau_D) u(t) dt , \\ S_L &= \frac{1}{T_S} \int_{-T_S/2}^{T_S/2} m^*(t - \tau_D - T_C / 2) u(t) dt \end{aligned}$$

where $m^*(t)$ is the locally generated PN code, τ_D is the delay offset, and $u(t)$ is the received signal. Note that the early voltage is formed by correlating the received voltage with the local PN code advanced in time by one-half chip period, and the late voltage is formed by correlating the received signal with the local PN code delayed by one-half chip relative to the on-time code.

It is shown in Appendix B that the signal contributions to the average energy of the early, on-time, and late code correlator outputs for a continuous channel impulse response function are

$$\begin{aligned} \langle E_E \rangle &= \langle S_E S_E^* \rangle = r^2 \int_0^\infty T_C G(T_C \xi) \Lambda^2 [\hat{\tau}_D - \xi - \frac{1}{2}] d\xi \\ \langle E_O \rangle &= \langle S_O S_O^* \rangle = r^2 \int_0^\infty T_C G(T_C \xi) \Lambda^2 [\hat{\tau}_D - \xi] d\xi \quad (\text{Continuous CIRF}) \end{aligned}$$

$$\langle E_L \rangle = \langle S_L S_L^* \rangle = r^2 \int_0^\infty T_C G(T_C \xi) \Lambda^2 \left[\hat{\tau}_D - \xi + \frac{1}{2} \right] d\xi$$

where $\hat{\tau}_D = \tau_D / T_C$ is the normalized delay error, and $G(\cdot)$ is the power impulse response function defined in Section 2. The triangle function $\Lambda(\cdot)$ is the autocorrelation of the rectangular function:

$$\Lambda(x) = \begin{cases} 1 - |x| & \text{if } |x| \leq 1 \\ 0 & \text{otherwise} \end{cases}$$

When the CIRF is sampled the integrals are replaced by sums:

$$\begin{aligned} \langle E_E \rangle &= r^2 \sum_{i=0}^{N_\tau-1} P_i \Lambda^2 \left[\hat{\tau}_D - i/N_D - \frac{1}{2} \right] \\ \langle E_O \rangle &= r^2 \sum_{i=0}^{N_\tau-1} P_i \Lambda^2 \left[\hat{\tau}_D - i/N_D \right] \\ \langle E_L \rangle &= r^2 \sum_{i=0}^{N_\tau-1} P_i \Lambda^2 \left[\hat{\tau}_D - i/N_D + \frac{1}{2} \right] \end{aligned} \quad (\text{Sampled CIRF})$$

where $N_D = T_C / \Delta\tau$ is the number of delay samples per chip period, and P_i is the average fading power in the delay samples (Eqn. 2.14).

A non-coherent DLL attempts to equalize the energy in the early and late samples, so the DLL error signal is proportional to the measured difference in the early and late samples, $E_E - E_L$. The ideal delay offset is then found by solving the equation

$$\langle E_E(\hat{\tau}_D) \rangle = \langle E_L(\hat{\tau}_D) \rangle$$

for the normalized delay error $\hat{\tau}_D$. For frequency selective fading channels, the ideal delay offset is a function of the ratio of the frequency selective bandwidth to the chip rate, f_0 / R_C .

The signal energy at the output of the on-time code correlator is just $\langle E_O(\hat{\tau}_D) \rangle$. This quantity is less than r^2 (its maximum value in a benign propagation environment) in frequency selective fading channels because signal energy arriving either early or late relative to τ_D by more than one chip period is severely attenuated by the code correlation process. Stated in another way, the received signal spectrum is distorted by the channel, and the code correlator is no longer matched to the signal.

3.1.2 Frequency Hopped Spread Spectrum Delay Tracking.

A functional block diagram of a FH M -ary frequency-shift keying (FH/FSK) receiver is shown in Figure 3-2. The tracking loops in this example receiver are the DLL, automatic gain control (AGC), and automatic frequency control (AFC)⁵.

In Appendix G of this report we show that the demodulation performance of a FH/FSK receiver is sensitive to the delay offset as are all digital demodulators. Thus it is critical that a simulation of any communications link get the delay offset right as well as frequency error and perhaps phase error. A brief summary of the mathematical developments in Appendix G follows.

For the purpose of computing theoretical delay offset and demodulation performance of FH/FSK systems, we assume a single FSK modulation symbol per hop. An isolated rectangular pulse then approximates the transmitted FSK signal⁶:

$$m(t) = \exp[jn_0\pi\Delta f t] \Pi\left[\frac{t}{T}\right],$$

where n_0 is the transmitted tone ($n_0 = \pm 1$ randomly⁷ for BFSK, $n_0 = \pm 1, \pm 3$ randomly for QFSK, $n_0 = \pm 1, \pm 3, \pm 5, \pm 7$ randomly for 8-ary FSK, and so on), and Δf is the tone spacing. The product $\Delta f T$ is equal to a positive integer for orthogonal signaling⁸.

⁵ Here M -ary FSK demodulation is indicated, but frequency-hopped phase-shift keying (FH/PSK) receivers have similar functional diagrams.

⁶ COMLNK does not make these assumptions. All waveforms involve a sequence of modulation symbols that may have any frequency offset from one symbol to the next. Thus COMLNK can treat any number of FSK modulation symbols per hop.

⁷ In theoretical developments we assume that zeros and ones are equally likely and randomly distributed in the transmitted data stream. Thus each FSK tone is equally likely. In COMLNK, as in an actual system, the user specifies the transmitted data stream, which may undergo a series of coding, interleaving, and alphabet translation operations prior to reaching the modulator.

⁸ Note that this entire development assumes conventional M -ary FSK, wherein each transmitted tone has a fixed offset from the center carrier frequency. This is only one option available in COMLNK, which also implements independent tone M -ary FSK and FH/PSK receivers.

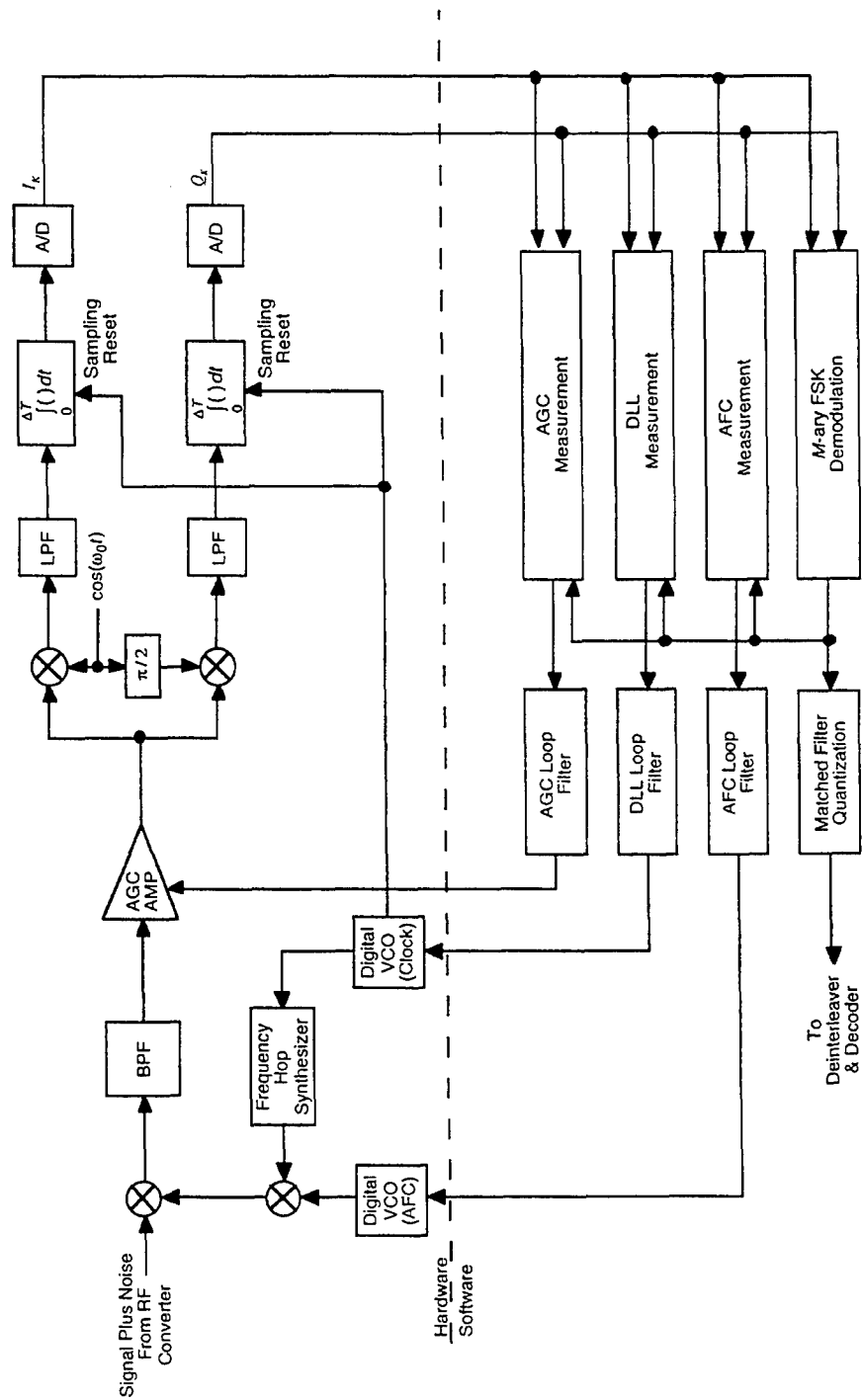


Figure 3-2. Block diagram of a frequency hopped M -ary FSK receiver.

The symbols preceding and following this "on-time" pulse are transmitted at different carrier frequencies determined by the pseudo-random hop pattern. During the on-time pulse period the receiver is set to the transmitted carrier frequency assuming that the receiver is synchronized to the hop pattern. Prior to forming the FSK tone filters, the received signal is band-pass filtered so signal energy from other tones at different carrier frequencies is severely attenuated and is ignored in this analysis.

Separate filters are formed in the receiver for each of the possible M transmitted tones. For non-coherent demodulation considered here, the filter with the largest output amplitude is chosen as corresponding to the transmitted tone. For suppressed-carrier tracking which is tacitly assumed here, the filter with the largest output determines the frequency offset at which two more filters are formed. These two filters provide samples for delay tracking during the first and second halves of the detected symbol.

For this calculation we assume that the DLL tracking threshold (*i.e.*, the signal-to-noise ratio above which the DLL can maintain lock on the signal) is well below the demodulation threshold (*i.e.*, the signal-to-noise ratio above which an "incorrect" filter rarely has the largest output energy). Thus at signal-to-noise ratios where the demodulation error rate is small (say below about 10–20 percent), the DLL should be tracking with nearly the ideal error, and the effect of demodulation errors on the DLL input error signals can be ignored in the analysis⁹.

The on-time signal contribution to the output of the correct tone filter is

$$S_O = \frac{1}{T} \int_{-T/2+\tau_D}^{T/2+\tau_D} u(t) \exp[-jn_0\pi\Delta f t] dt ,$$

where τ_D is the delay offset, and T is the symbol period (also the hop period in this analysis). To perform delay tracking, early and late samples are formed at the frequency offset of the correct filter:

⁹ COMLNK does not involve any such assumption. If suppressed-carrier tracking is selected (sync symbol tracking is another option), data demodulation errors degrade tracking loop operation, especially when the demodulation error rate is large. Thus the suppressed-carrier tracking threshold coincides with the demodulation threshold in COMLNK, as in a real receiver.

$$S_E = \frac{1}{T} \int_{\tau_D - T/2}^{\tau_D} u(t) \exp[-jn_0 \pi \Delta f t] dt$$

$$S_L = \frac{1}{T} \int_{\tau_D}^{\tau_D + T/2} u(t) \exp[-jn_0 \pi \Delta f t] dt .$$

The on-time signal used for demodulation is equivalent to $S_E + S_L$.

In Appendix G it is shown that for a continuous CIRF the signal contribution to early, on-time, and late energy is

$$\begin{aligned} \langle E_E \rangle &= \langle S_E S_E^* \rangle = \frac{1}{4} r^2 \int_0^\infty T G(T\xi) \Xi^2 \left[2(\xi - \hat{\tau}_D) + \frac{1}{2} \right] d\xi \\ \langle E_O \rangle &= \langle S_O S_O^* \rangle = r^2 \int_0^\infty T G(T\xi) \Lambda^2 [\xi - \hat{\tau}_D] d\xi \\ \langle E_L \rangle &= \langle S_L S_L^* \rangle = \frac{1}{4} r^2 \int_0^\infty T G(T\xi) \Xi^2 \left[2(\xi - \hat{\tau}_D) - \frac{1}{2} \right] d\xi \end{aligned} \quad (\text{Continuous CIRF})$$

where $\Xi(\cdot)$ is the trapezoid function defined as

$$\Xi(x) = \begin{cases} 1 & \text{if } |x| \leq \frac{1}{2} \\ \frac{3}{2} - |x| & \text{if } \frac{1}{2} < |x| \leq \frac{3}{2} \\ 0 & \text{otherwise} \end{cases} .$$

For sampled CIRFs these equations become

$$\begin{aligned} \langle E_E \rangle &= \frac{1}{4} r^2 \sum_{i=0}^{N_\tau-1} P_i \Xi^2 \left[2(1/N_D - \hat{\tau}_D) + \frac{1}{2} \right] \\ \langle E_O \rangle &= r^2 \sum_{i=0}^{N_\tau-1} P_i \Lambda^2 [i/N_D - \hat{\tau}_D] \\ \langle E_L \rangle &= \frac{1}{4} r^2 \sum_{i=0}^{N_\tau-1} P_i \Xi^2 \left[2(1/N_D - \hat{\tau}_D) - \frac{1}{2} \right] . \end{aligned} \quad (\text{Sampled CIRF})$$

The ideal delay offset is found by solving the equation $\langle E_E \rangle = \langle E_L \rangle$ for $\hat{\tau}_D$.

In a frequency selective fading channel, the on-time signal energy $\langle E_O(\hat{\tau}_D) \rangle$ is less than its maximum value (r^2) in a benign environment because transmitted energy

arriving early (at times before $\tau_D - T/2$) arrives before the receiver has hopped to the on-time carrier frequency and transmitted energy arriving late (at times after $\tau_D + T/2$) arrives after the receiver has hopped to the carrier frequency for the next transmitted tone. Only signal energy arriving in the period $\tau_D - T/2 \leq t \leq \tau_D + T/2$ contributes to the output of the on-time tone filter.

3.2 COMLNK DLL TRACKING AND SIGNAL LOSS.

In this section we compare measured values of the DLL tracking error and received signal energy from COMLNK with the ideal values computed above. However, before making these comparisons, a few comments on fidelity of such measurements, whether from a simulation or from actual hardware, are in order.

3.2.1 Raw Data From COMLNK.

COMLNK is a faithful emulation of a modern digital communications link. Thus measurements of received signal energy and DLL tracking errors are always corrupted by noise and transients just as they are in an actual receiver. Furthermore, analysis provides ensemble average values, whereas measurements from a simulation or from hardware are averages over a limited time span using specific realizations of the signal and noise processes.

To illustrate the implication of this point we show in Figures 3-3 through 3-12, for five values of the ratio f_0/R_C , the simulated AGC gains (in decibels) and the DLL tracking errors (in units of the PN chip period T_C) of a DS/DPSK receiver as a function of time over the 100-second period of each case (zero time corresponds to the start of the simulation). The channel bit energy-to-noise spectral density ratio E_{cb}/N_0 is 30 dB for each case, and the frequency selective channel in COMLNK is sampled with tap spacing equal to one-half the chip period, so $N_D = T_C/\Delta\tau = 2$. For each plot, the channel decorrelation time (τ_0) is 0.03 seconds, the AGC time constant is 3 seconds, and the DLL and frequency lock-loop (FLL) bandwidths (B_L) are 0.1 Hz.

Two mean values of AGC gain and DLL tracking error are given in the plots. The values labeled "100 sec" are computed by COMLNK and represent time averages over the entire simulation period. (A mean value of the AGC gain of 0 dB corresponds to no loss in signal energy at the output of the on-time code correlator.)

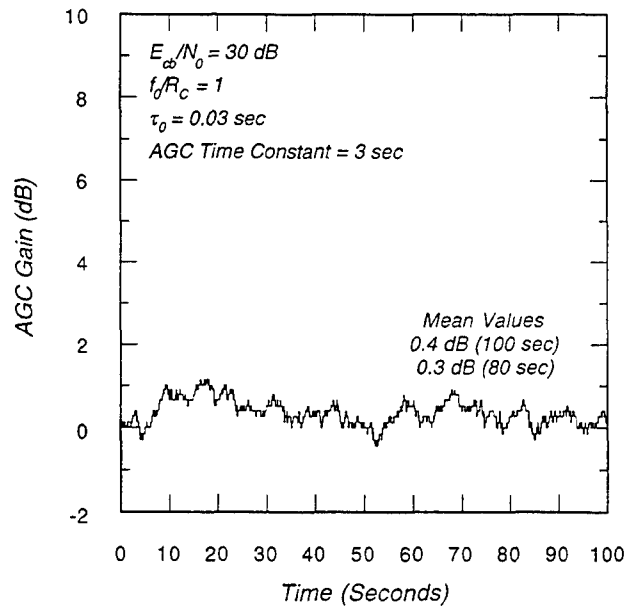


Figure 3-3. AGC gain of DS receiver in a frequency selective fading channel with $f_0 / R_C = 1.0$.

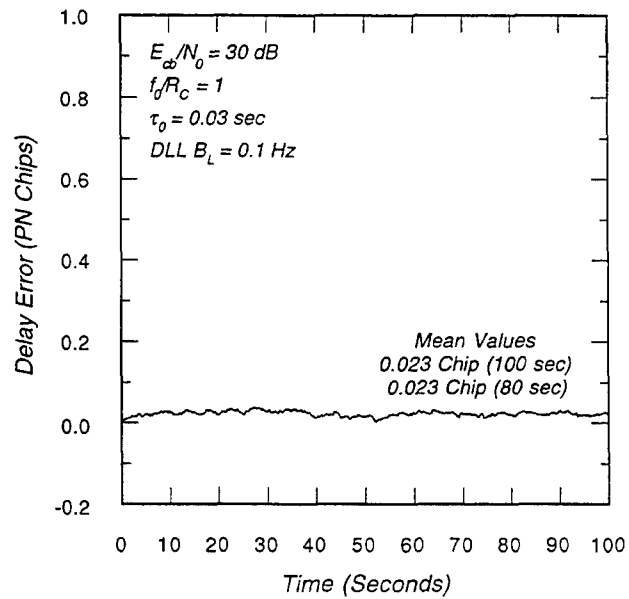


Figure 3-4. DLL tracking error of DS receiver in a frequency selective fading channel with $f_0 / R_C = 1.0$.

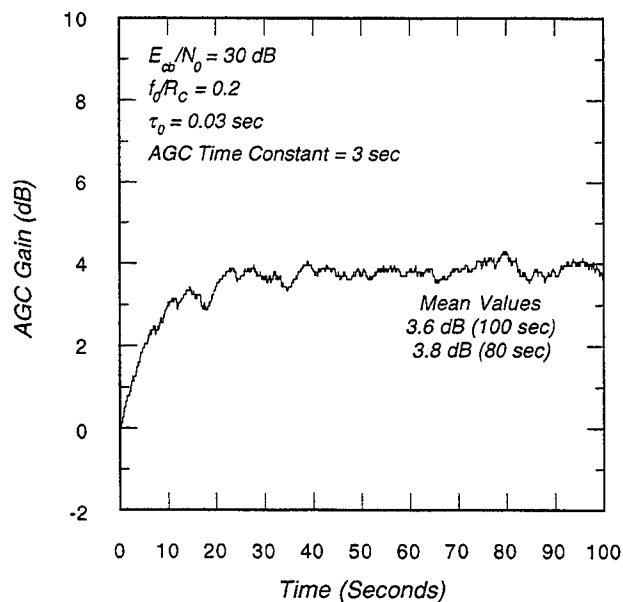


Figure 3-5. AGC gain of DS receiver in a frequency selective fading channel with $f_0 / R_C = 0.2$.

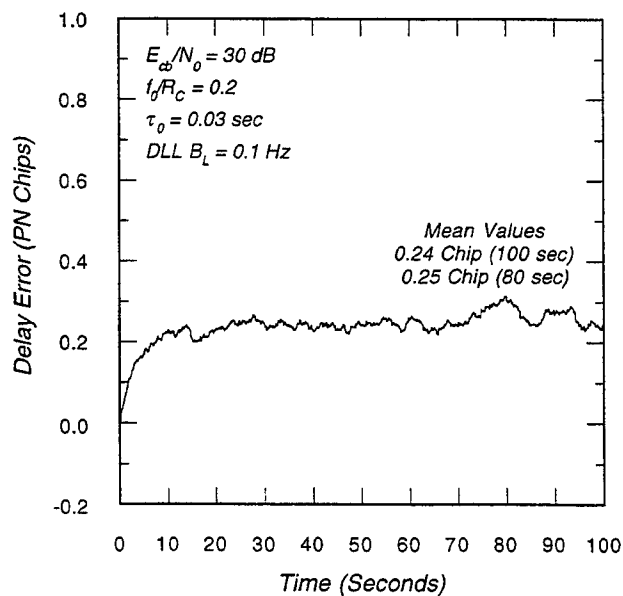


Figure 3-6. DLL tracking error of DS receiver in a frequency selective fading channel with $f_0 / R_C = 0.2$.

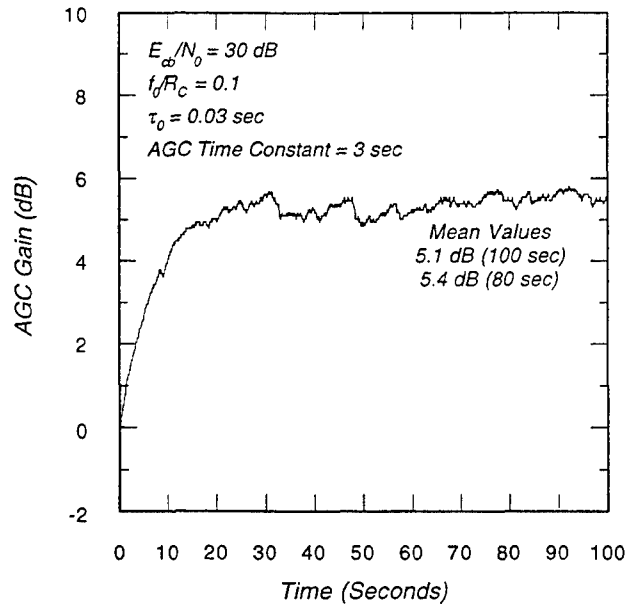


Figure 3-7. AGC gain of DS receiver in a frequency selective fading channel with $f_0 / R_C = 0.1$.

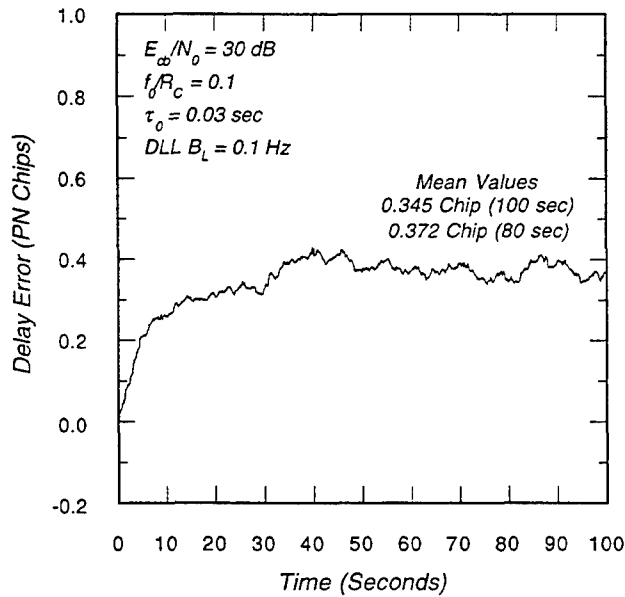


Figure 3-8. DLL tracking error of DS receiver in a frequency selective fading channel with $f_0 / R_C = 0.1$.

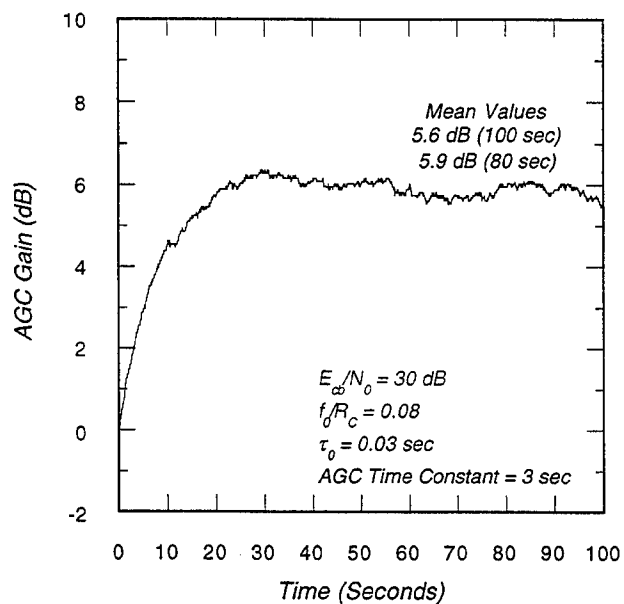


Figure 3-9. AGC gain of DS receiver in a frequency selective fading channel with $f_0 / R_C = 0.08$.

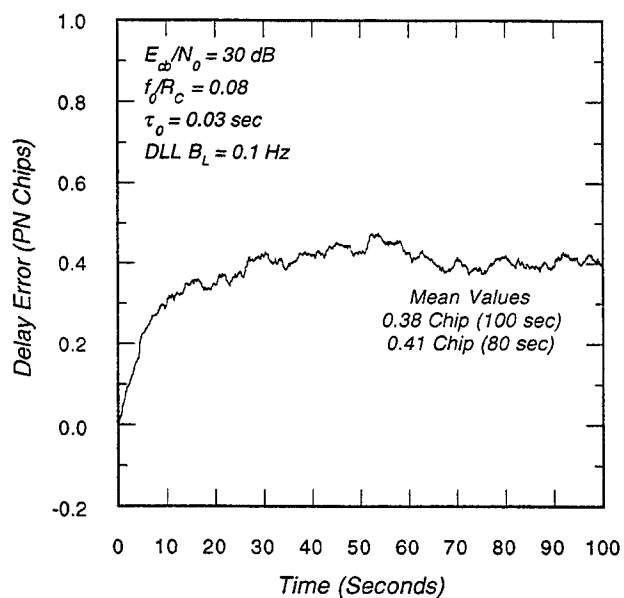


Figure 3-10. DLL tracking error of DS receiver in a frequency selective fading channel with $f_0 / R_C = 0.08$.

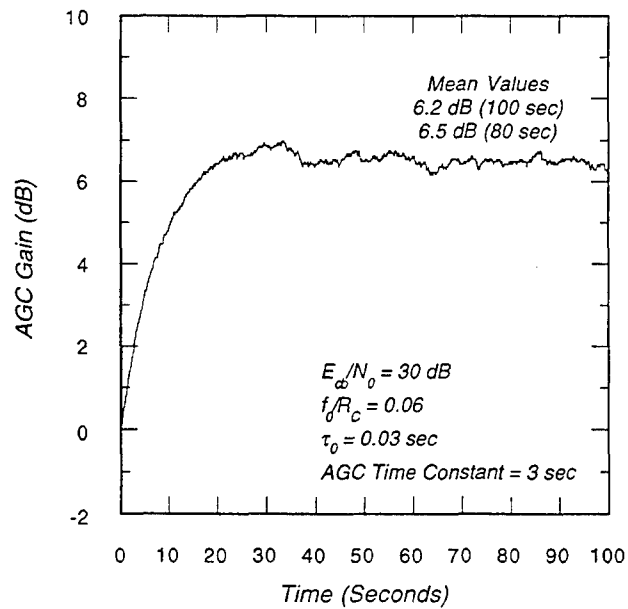


Figure 3-11. AGC gain of DS receiver in a frequency selective fading channel with $f_0 / R_C = 0.06$.

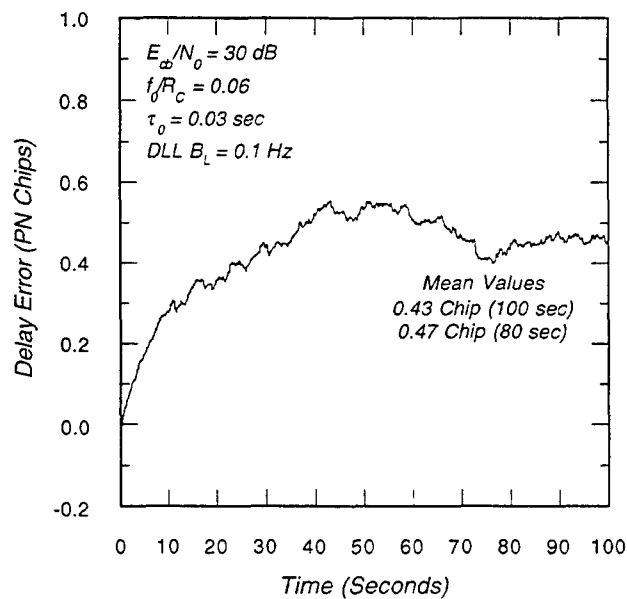


Figure 3-12. DLL tracking error of DS receiver in a frequency selective fading channel with $f_0 / R_C = 0.06$.

Even if the track histories were smooth, these mean values would tend to understate the tracking errors and signal loss because of the initial transient. For the delay and frequency tracking loops we use a rather small bandwidth of 0.1 Hz and for the AGC we use a rather long time constant of 3 seconds to minimize the variation with signal strength fluctuations. This, of course, causes a rather slow response to the mean loss and mean delay of the received signal. Larger loop bandwidths would result in much larger fluctuations in the AGC gain and DLL tracking error than are observed in these plots.

When the initial transient is removed by deleting the first 20 seconds of data from the time averages, it is evident that these measurements labeled "80 sec" still can exhibit significant statistical fluctuation, particularly at small values of f_0/R_C . This is a real-world phenomenon and illustrates the difficulty in accurately measuring the mean signal loss and delay error in real or simulated systems. Nevertheless, the tracking loop transients at the beginning of the simulation appear to have only a small effect on the mean AGC gain and DLL error, on the order of a few tenths of a decibel and a few hundredths of a chip, respectively.

3.2.2 Comparison of COMLNK Delay Tracking with Theory.

A comparison between DLL tracking errors (in units of the PN chip period, T_C) from averaging COMLNK measurements and the theoretical delay offset in frequency selective fading is shown in Figure 3-13 for a direct sequence spread spectrum receiver. Other than Rayleigh fading, no other signal dynamics are applied here such as occur from slant range or total electron content dynamics, although they are implemented in the simulation program. The COMLNK data plotted with solid circles are from the simulation runs discussed in the previous subsection (100 second averages are plotted), and the COMLNK data plotted with open circles are from *Dana, Milner, and Bogusch* [1995].

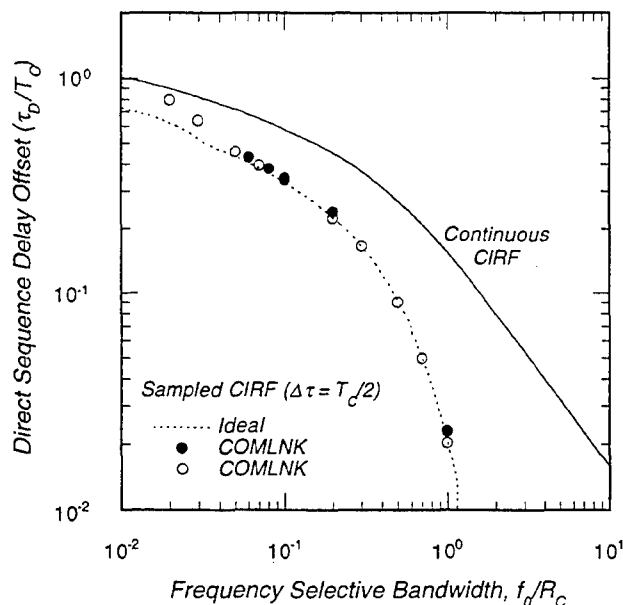


Figure 3-13. Comparison of COMLNK and ideal direct sequence delay tracking errors in frequency selective fading channels.

The ideal curves in Figure 3-13, taken from results presented in Appendix B, are for a continuous CIRF and for a sampled CIRF with two samples per PN chip, which is the tap spacing currently used in COMLNK¹⁰.

There is excellent agreement between the COMLNK results and the ideal sampled CIRF curve for f_0/R_C values above 0.05 or so. This agreement does break down for values of f_0/R_C less than about 0.05, as expected. For channels with such small values of frequency selective bandwidth, the early and late energy are nearly equal and slowly varying with delay for values of τ_D greater than zero. At smaller values of delay the late energy rapidly approaches zero so there is good discrimination in the delay error measurement, $E_E - E_L$. Thus an actual DLL tends to wander on a very flat error

¹⁰ On the basis of results shown here, a future version of COMLNK may allow the number of delay samples per chip to be selectable by user input. This will enable users to obtain delay tracking performance results that are closer to the continuous CIRF curve at the expense of additional computation time. When comparisons with hardware test results are to be made, however, the delay spacing in COMLNK should correspond to the delay spacing employed in the hardware channel simulator.

surface under these conditions, except when the delay approaches zero. Then the error measurement gives the DLL a strong push to larger delays. Hence an actual DLL is biased towards larger delays than the theoretical value when f_0/R_C is small. The departure of the measurements from theory at low signal levels, resulting here from small f_0/R_C , is typical of the tracking threshold observed in any nonlinear tracking loop.

The corresponding code correlator loss is plotted in Figure 3-14. COMLNK results for the five cases discussed above are plotted with solid circles. The solid triangles with error bars are prototype L_3P receiver test results generated using the DSWA NELS II channel simulator [Bogusch and Guigliano, 1982; Dana, 1995c]¹¹. Again there is good agreement between the COMLNK results and the ideal curve, and for the code

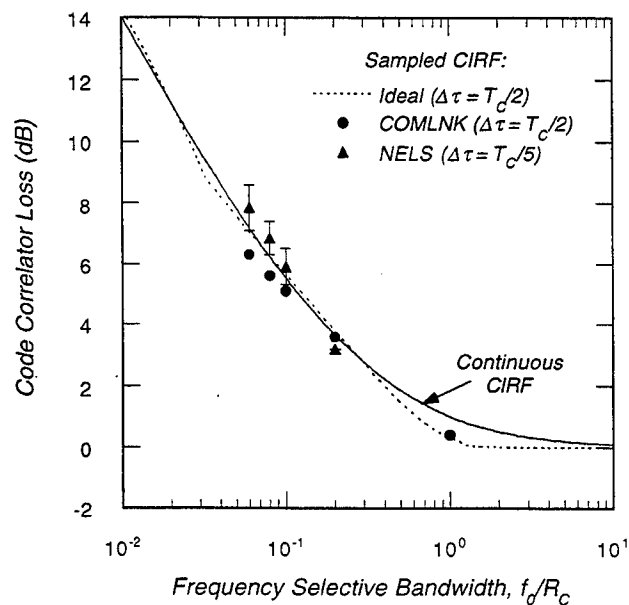


Figure 3-14. Comparison of COMLNK, L_3P test results, and ideal direct sequence code correlator loss in frequency selective fading channels.

¹¹ This prototype receiver, which uses the Global Positioning System (GPS) P-code, was tested with the NELS II 20 nsec tapped delay line. The GPS P-code has a 10.23 MHz chip rate so the number of NELS taps per chip is about 5.

correlator loss, there is also excellent agreement between COMLNK results and actual hardware measurements. Note again that both the COMLNK and actual hardware test results are obtained from AGC operation, which as shown earlier can easily introduce a measurement uncertainty of several tenths of a decibel at small values of f_0 / R_C .

These results show that the signal energy loss at the output of the on-time code correlator is relatively insensitive to the number of delay samples per chip. For communications links this may be all that is necessary for COMLNK to accurately reproduce the error rate performance of an actual receiver operating in a channel with a continuous CIRF. However, if COMLNK is used to simulate the navigation performance of a Global Positioning System (GPS) receiver in frequency selective channels for example, then the discrepancy between the delay offset with a sampled CIRF and that which would occur with a continuous CIRF may indeed be very significant, assuming that the GPS receiver could maintain code lock in such cases. Note that this also applies to an actual GPS receiver that is being tested with a hardware channel simulator.

The ideal delay offset for a frequency hopped FSK spread spectrum receiver is plotted in Figure 3-15. The corresponding signal energy loss at the output of the correct tone filter is plotted in Figure 3-16. The delay offset is plotted for a continuous CIRF and for a sampled CIRF with two delay samples per symbol period, T . There is excellent agreement between the delay offset from COMLNK and the ideal results.

Again there is a discrepancy between the delay offset for a coarsely sampled CIRF and that for a continuous CIRF.

Note that the number of channel delay samples per modulation symbol period makes little difference in the signal energy at the output of the correct tone filter. The solid line in Figure 3-16 is the ideal loss in signal energy for a continuous CIRF, and the dashed line is the loss for a CIRF with two samples per modulation period. The solid circles are losses measured with a COMLNK simulation of a FH link using two channel delay samples per symbol and a finite signal-to-noise ratio. These measurements were obtained by measuring the average AGC gain, a measurement that could also be made using an actual receiver. The effect of the initial transient in the AGC gain has been minimized by deleting the first 20 seconds of data from the time averages.

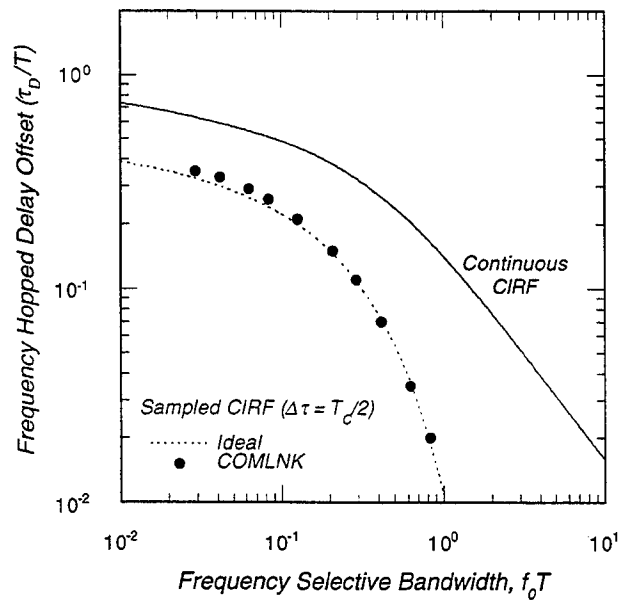


Figure 3-15. Comparison of COMLNK and ideal frequency hopped delay offset in frequency selective fading channels.

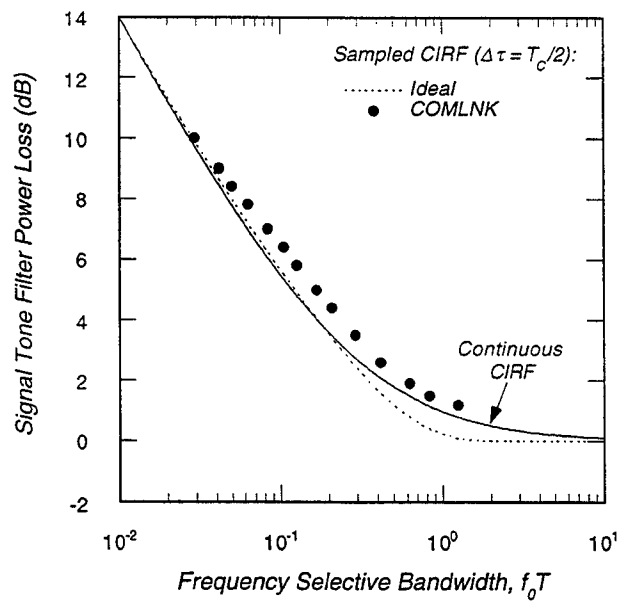


Figure 3-16. Comparison of COMLNK and ideal frequency hopped tone filter signal loss in frequency selective fading channels.

For either a DS or FH system, there probably is little measurable difference in communications link performance for continuous and sampled CIRFs when both have delay errors less than a tenth of a chip or so. However, for small values of f_0 / R_C this difference can be several tenths of a chip. Under these conditions and when the received signal is also undergoing time-of-arrival dynamics, such differences in delay tracking may determine whether or not the receiver maintains lock on the signal, although data demodulation will likely be unacceptably bad in either case.

Although we have concentrated here on the effects of channel delay sampling on simulated delay tracking performance, these effects also exist in hardware channel simulators connected to actual receivers. Frequency selective channel simulators such as NELs and the new DSWA Advanced Channel Simulator (ACS) [Dana, 1995a] are implemented using tapped delay lines with some number of taps per chip, just as in COMLNK. With a fixed number of taps, the way one simulates channels with smaller values of frequency selective bandwidth is to increase the tap delay spacing. If the resulting number of taps per chip is small, one needs to be careful that receiver performance is not unduly affected by channel tap spacing. Because of its high degree of accuracy, COMLNK is an excellent tool for investigating the effect of tap spacing on tracking loop operation and data demodulation performance.

SECTION 4

COMLNK DEMODULATION PERFORMANCE

A critical step in the COMLNK validation process involves comparison of measured demodulated error rates with theoretical results. After the demodulator, COMLNK is an *emulation* of a modern digital receiver. It is at the demodulator that the *simulation* of the channel, thermal noise, and transmitted modulation come together, and it is at that point that we compare measured error rates from COMLNK with theoretical curves.

Analytic expressions are available for phase-shift keying (PSK) and frequency-shift keying (FSK) modulation formats for non-fading and slow Rayleigh fading channels (see, for example, *Schwartz, Bennett, and Stein* [1966] or *Bogusch* [1989]). However, the stressing channels for demodulation are fast fading or frequency selective fading or both, and only a limited number of analytic results were previously available for these types of channels (for example *Bello and Nelin* [1962a, 1962b, 1963]). Thus to thoroughly validate the COMLNK simulation we have derived new results for PSK and FSK demodulation performance in fast, frequency selective fading channels including, in some cases, the effects of channel delay sampling and delay offset. These new results are derived in the Appendices to this report and are summarized in the following subsections.

This section is organized as follows. In Section 4.1 we compare simulated and theoretical PSK and FSK demodulation performance in non-Rayleigh (Rician) and slow Rayleigh fading channels. Then COMLNK demodulation performance in fast, flat Rayleigh fading is compared with theory in Section 4.2 for differentially coherent PSK (DPSK) and non-coherent M -ary FSK. Finally, COMLNK frequency selective fading demodulation performance of DPSK and binary FSK (BFSK) with and without frequency hopping is discussed in Section 4.3.

4.1 SLOW RICIAN AND RAYLEIGH FADING CHANNELS.

In the context of demodulation, slow fading means that the channel decorrelation time is long compared to any time scale over which the receiver expects the signal to be coherent. Slow fading demodulation error rates are then given by averaging non-fading expressions over the probability distribution of the fading amplitude and, as such, are independent of the Doppler frequency spectrum of the fading. The time scale

over which the receiver expects the signal to be coherent depends on the transmitted modulation rate and on the approach to demodulation. For coherent demodulation, the receiver must maintain phase-lock on the signal, and the coherence time is inversely related to the bandwidth of the phase-lock loop. For differentially coherent PSK demodulation and non-coherent FSK demodulation, the relevant time scale is that of the channel symbol period.

4.1.1 Error Rate Expressions.

The Δ PSK, DPSK, and M -ary FSK channel bit error rates in AWGN channels are given by the usual formulas:

$$\begin{aligned}
 P_e &= \operatorname{erfc}\left[\sqrt{E_{cb}/N_0}\right] \left\{1 - \frac{1}{2} \operatorname{erfc}\left[\sqrt{E_{cb}/N_0}\right]\right\} & (\text{non-fading } \Delta\text{PSK}) \\
 P_e &= \frac{1}{2} \exp\left[-E_{cb}/N_0\right] & (\text{non-fading DPSK}) \\
 P_e &= \sum_{k=2}^M (-1)^k \frac{(M/2)(M-2)!}{k!(M-k)!} \exp\left[-\frac{(k-1)\log_2 M}{k} \frac{E_{cb}}{N_0}\right] & (\text{non-fading } M\text{-ary FSK})
 \end{aligned}$$

where E_{cb}/N_0 is the channel bit energy-to-noise spectral density ratio, and $\operatorname{erfc}(\cdot)$ is the complementary error function. Note that there are $\log_2 M$ channel bits per symbol in M -ary FSK.

Theoretical formulas for slow fading channel bit error rates are given by averaging these expressions over the distribution of fading amplitude. Although there is not a single probability distribution that describes non-Rayleigh fading, the Rician distribution appears to represent a reasonable worst-case [Dana, 1993]. This distribution has the added advantage of being easily implemented as Rayleigh fading plus a constant component. The Rician probability density function of the fading power is given in Equation 2.2 of this report, and is reproduced here:

$$f_{\text{Rice}}(S) = \frac{1}{1-R} \exp\left[-\frac{R+S}{1-R}\right] I_0\left[\frac{2\sqrt{RS}}{1-R}\right],$$

where $I_0(\cdot)$ is the modified Bessel function of order zero, and the average fading power $\langle S \rangle$ is unity. The quantity R is the ‘‘Rician Index’’ which is defined in terms of the scintillation index S_4 :

$$R = \sqrt{1 - S_4^2}.$$

For non-fading channels ($S_4 = 0$ and $R = 1$) the Rician power probability density function behaves as the delta-function $\delta(S - 1)$, and for Rayleigh fading channels ($S_4 = 1$ and $R = 0$) the Rician power probability density function reduces to the Rayleigh exponential form.

Theoretical slow Rician fading PSK and FSK channel bit error rates are given by averaging the non-fading results over the probability density function of the instantaneous received channel bit energy-to-noise spectral density ratio:

$$\langle P_e \rangle = \int_0^{\infty} P_e(\gamma S) f_{Rice}(S) dS ,$$

where $\gamma = E_{cb}/N_0$ is the average channel bit energy-to-noise spectral density ratio. For Δ PSK the resulting integral cannot be obtained in closed form to the authors' knowledge, so the indicated integral must be done numerically. For the other two modulation techniques, the Rician fading channel bit error rates are

$$\langle P_e \rangle = \frac{1}{2 + 2(1 - R)\gamma} \exp \left[-\frac{R\gamma}{1 + (1 - R)\gamma} \right] \quad (\text{Slow, Rician-fading DPSK})$$

$$\langle P_e \rangle = \sum_{k=2}^M (-1)^k \frac{(M/2)(M-2)!}{k!(M-k)!} \frac{1}{1 + (1 - R)\gamma_k} \exp \left[-\frac{R\gamma_k}{1 + (1 - R)\gamma_k} \right] \quad (\text{Slow, Rician-fading } M\text{-ary FSK})$$

where $\gamma_k = (1 - 1/k)(\log_2 M) E_{cb}/N_0$. The Δ PSK error rate can be obtained in closed form for Rayleigh fading, so the Rayleigh fading channel bit error rate expressions for the three modulation-demodulation techniques are

$$\langle P_e \rangle = \frac{1}{2} - \frac{\pi - 2 \tan^{-1}(\sqrt{1 + \gamma^{-1}})}{\pi \sqrt{1 + \gamma^{-1}}} \quad (\text{Slow, Rayleigh-fading } \Delta\text{PSK})$$

$$\langle P_e \rangle = \frac{1}{2 + 2\gamma} \quad (\text{Slow, Rayleigh-fading DPSK})$$

$$\langle P_e \rangle = \sum_{k=2}^M (-1)^k \frac{(M/2)(M-2)!}{k!(M-k)!} \frac{1}{1 + \gamma_k} \quad (\text{Slow, Rayleigh-fading } M\text{-ary FSK})$$

4.1.2 *M*-ary FSK Sampling Loss.

In an actual receiver or in COMLNK, the tone filters of an *M*-ary FSK receiver are often implemented using discrete Fourier transforms (DFTs) of multiple samples per symbol. This results in a sampling loss that must be included in the comparison between the analytic results presented above and results from COMLNK.

To compute the sampling loss consider an isolated transmitted *M*-ary FSK symbol. Before up-conversion to RF, the transmitted signal as a function of time is

$$m(t) = \exp(jn_0\pi\Delta f t) \Pi\left(\frac{t}{T}\right)$$

where T is the symbol period, n_0 is the modulation index (\pm an odd integer), Δf is the modulation tone spacing, and $\Pi(\cdot)$ is the rectangular function. In the absence of fading, the signal contribution to the k^{th} discrete sample used in an N_T -point DFT is

$$S_k = \frac{1}{\Delta t} \int_{k\Delta t}^{(k+1)\Delta t} m(t) dt ,$$

where $\Delta t = T / N_T$ is the time duration of each sample. Sampling loss occurs because the down-converted and sampled signal is never actually at baseband, but rather has a radian frequency offset of $n_0\pi\Delta f$. Thus the sampled signal has a time-varying phase during the integration period Δt with a loss in output power as a result.

Upon substituting the expression for the transmitted symbol into the expression for the discrete samples, the signal contribution to the samples reduces to

$$S_k = \exp\left[jn_0\pi\left(k + \frac{1}{2}\right)\Delta f\Delta t\right] \frac{\sin\left[\frac{1}{2}n_0\pi\Delta f\Delta t\right]}{\frac{1}{2}n_0\pi\Delta f\Delta t} .$$

The $\sin(x)/x$ factor in this expression is the signal amplitude sampling loss given that the n_0 tone was transmitted. Assuming that all *M*-ary symbols are equally likely, the average sampling signal power loss is

$$L_S = \frac{2}{M} \sum_{i=1}^{M/2} \frac{\sin^2\left[\frac{1}{4}(2i-1)\omega_M / N_T\right]}{\left[\frac{1}{4}(2i-1)\omega_M / N_T\right]^2}$$

where $\omega_M = 2\pi\Delta f T$ is the normalized tone spacing. For orthogonal signaling $\Delta f T$ is a positive integer.

4.1.3 COMLNK Results in Slow Fading Channels.

Perhaps the most basic requirement of a communications link simulation in fading channels is that it reproduces the correct non-fading and slow fading channel bit error rates. Once this requirement is verified, then we can proceed to performance verification in more complex fast, frequency selective fading channels.

Δ PSK, DPSK, and 8-ary FSK channel bit error rates in slow Rician fading channels are presented in Figure 4-1 versus the scintillation index, S_4 . For each modulation type the channel bit energy-to-noise spectral density ratio E_{cb}/N_0 is 10 dB. No phase variations from slant range or total electron content dynamics are imposed on the simulated signal. The solid lines in the figure are theoretical performance curves generated from the expressions given previously in this section, and the symbols are COMLNK simulation points. The 8-ary FSK results in Figure 4-1 are for minimum tone spacing ($\Delta f T = 1$) using a 16-point DFT for demodulation. Thus there is a 0.29 dB sampling loss [Bogusch, 1989] in this case, giving an effective value of E_{cb}/N_0 of 9.71 dB for the theoretical results.

The most striking feature of the results in this figure is the severe degradation of the channel bit error rate as the channel varies from non-fading ($S_4 = 0$) to full Rayleigh fading ($S_4 = 1$). The error rates vary from between 1.6×10^{-6} (8-ary FSK) and 2.3×10^{-5} (DPSK) for the non-fading channel to about 4–5 percent, essentially independent of the modulation format, in the Rayleigh fading channel. Thus while one can obtain significant improvement in non-fading channels by using 8-ary or higher order FSK modulation, slow Rayleigh fading is a great equalizer of modulation techniques. As will be seen, there are distinct differences in the performance of the modulation types in fast or frequency selective fading.

There is excellent agreement between the COMLNK and theoretical results plotted in Figure 4-1. The COMLNK results lie above theory as they should, but closely follow the theoretical curves as the scintillation index varies. The most noticeable variation between COMLNK results and theory occurs with 8-ary FSK in a non-fading channel. This difference is due in part to the finite precision of the sine and cosine tables in used to perform the DFT demodulation in COMLNK. Finite precision results in a quantization loss in addition to the sampling loss already included in the theoretical results. This is one of the many implementation considerations faced by designers of digital communications equipment.

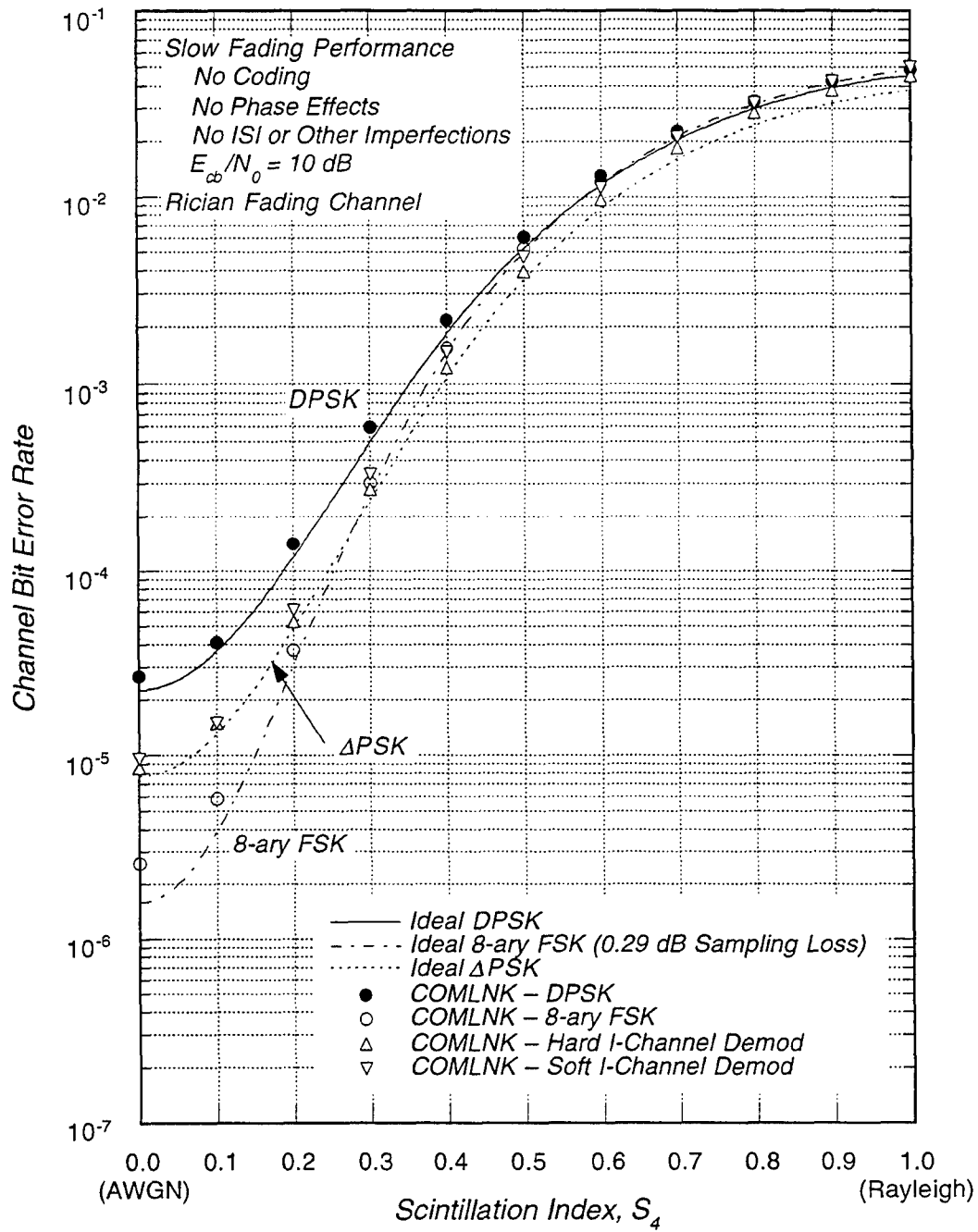


Figure 4-1. Channel bit error rates of Δ PSK, DPSK, and 8-ary FSK in slow Rician fading channels.

Two sets of COMLNK results for Δ PSK are plotted in Figure 4-1 because there are at least two ways to demodulate this waveform. Coherent PSK demodulation with absolute phase encoding is generally rendered useless in a fading channel (slow or otherwise) by numerous phase slips in the phase-lock loop¹. Thus for fading channel applications, coherent PSK should be implemented using differentially encoding and decoding to resolve the inherent π -phase ambiguity arising from suppressed-carrier phase-lock demodulation. The only meaningful error rates are those after the differential decoder. Another way to implement Δ PSK is to use DPSK modulation directly with coherent phase-lock demodulation. This technique is perhaps best described as *I*-channel DPSK demodulation because the *Q*-channel samples are dropped from the data demodulation algorithm.

The two techniques produce results that are similar, but not identical. The basic distinction is that the first technique performs differential demodulation with hard *I*-channel binary decisions (labeled "Hard *I*-Channel Demod" in the figure), while the second performs differential demodulation with soft *I*-channel samples (labeled "Soft *I*-Channel Demod" in the figure). Both techniques suffer significantly from imperfect phase tracking. The results show a clear, albeit small, advantage of the hard limited version of Δ PSK over *I*-channel DPSK. Apparently the noise statistics that occur when hard limited samples are multiplied are different and slightly more favorable than those that occur when non-limited samples are multiplied. The squared noise in the latter case (*I*-channel DPSK) is slightly worse.

While Δ PSK performs better than DPSK in non-fading channels and about the same as DPSK in slow Rayleigh fading, *Bogusch* [1989] shows that Δ PSK performs significantly worse than DPSK in fast Rayleigh fading channels. Thus DPSK is the preferred PSK technique for communications links that must contend with fading.

A powerful mitigation technique is diversity combining of signals that are independently fading. It is much less likely that two independently fading signals will simultaneously be in deep fades than it is that either one will be in a deep fade. However, simply coherently combining independently fading signals does not improve the signal-

¹ An exception to this generalization arises for very high data rate links that employ exceptionally large phase-lock loop bandwidths. In such cases the occurrence of phase slips may be sufficiently infrequent as to enable coherent PSK demodulation to be used successfully, with CRC or frame synchronization techniques for ambiguity resolution.

to-noise ratio because the signals are non-coherent. Thus non-coherent techniques must be used, and DPSK demodulation produces an ideal quantity for combining.

The basic decision metric for DPSK demodulation is

$$\hat{m} = I_k I_{k-1} + Q_k Q_{k-1}$$

where I_k and Q_k are the in-phase and quadrature-phase voltage samples for the k^{th} symbol period. A positive value for \hat{m} indicates no phase change in the received signal between the $k-1^{st}$ and k^{th} symbol periods, and a negative value indicates a π -phase change. If exactly the same data is available on N_C channels then one can simply sum together the DPSK decision metrics for all the channels:

$$\hat{m} = \frac{1}{N_C} \sum_{i=1}^{N_C} \hat{m}_i .$$

The resulting DPSK demodulation error rate is computed in Appendix E for combining of two and three metrics.

One way to implement diversity combining is take advantage of the time diversity in a Rayleigh fading channel. An example is a link with a block interleaver. To implement diversity combining, one simply uses block repetition (*i.e.*, the data in the block interleaver is repeated multiple times and the DPSK metrics for the same channel bit in each block are combined). Assuming a statistically stationary channel, each individual decision metric has the same average value of E_{cb}/N_0 but fades independently if the interleaver span is chosen to be long compared to the channel decorrelation time.

When the individual DPSK decision metrics fade independently, the combined DPSK demodulation error rates are

$$\langle P_e \rangle = \begin{cases} \frac{1}{2} e^{-\gamma} & 1 \text{ Channel} \\ \frac{1}{8} (4 + \gamma) e^{-\gamma} & 2 \text{ Channels} \\ \frac{1}{64} (32 + 12\gamma + \gamma^2) e^{-\gamma} & 3 \text{ Channels} \end{cases}$$

where γ is the average value of E_{ub}/N_0 .

These theoretical two- and three-channel diversity combining bit error rate results (*i.e.*, the error rate after combining assuming no further processing) are compared with COMLNK simulation results in Figure 4-2. The user bit energy-to-noise spectral density ratio E_{ub}/N_0 is the same for all diversity combining cases. The value of E_{cb}/N_0 then depends on the number of combined channels:

$$E_{cb}/N_0 \text{ (dB)} = E_{ub}/N_0 \text{ (dB)} - 10 \log_{10}(N_C) .$$

This keeps the total user bit energy constant as the number of channels changes.

For comparison, the ideal single-channel DPSK user error rates for non-fading and Rayleigh fading channels are also plotted in the figure. The simulation runs were generated using a block interleaver with a span equal to 240 times the channel decorrelation time without repetition. To keep the user bit rate constant with repetition, the interleaver span is effectively reduced as the number of repetitions increases. Thus the separation between repeated channel symbols is $120\tau_0$ for two repeats and $80\tau_0$ for three repeats. These separations are sufficiently large that the fading from symbol-to-symbol is independent.

Three sets of simulation results are plotted in Figure 4-2. The first set, labeled "COMLNK (AGC, 4 Bits)" was generated first for two-channel combining and plotted with open circles. The second set, labeled "COMLNK (No AGC, 4 bits)" was generated for both two- and three-channel diversity combining using 4 bit quantization of the individual DPSK decision metrics. The third set, consisting of two points labeled "COMLNK (No AGC, 8 bits)," was generated using 8 bit quantization of the individual decision metrics.

The first set of data was generated with the automatic gain control (AGC) tracking loop on because the runs encompassed a large range in signal strengths, and a real receiver would attempt to maintain the signal level near some design value. At large values of E_{cb}/N_0 we observed that the two-channel DPSK demodulator was beginning to depart from theory, with the departure increasing as the signal energy increased. The result is a tendency for the error rate curve to flatten out to an apparent "irreducible" value. However, the channel fading rate is very slow compared to the symbol rate, so phase effects do not explain this data.

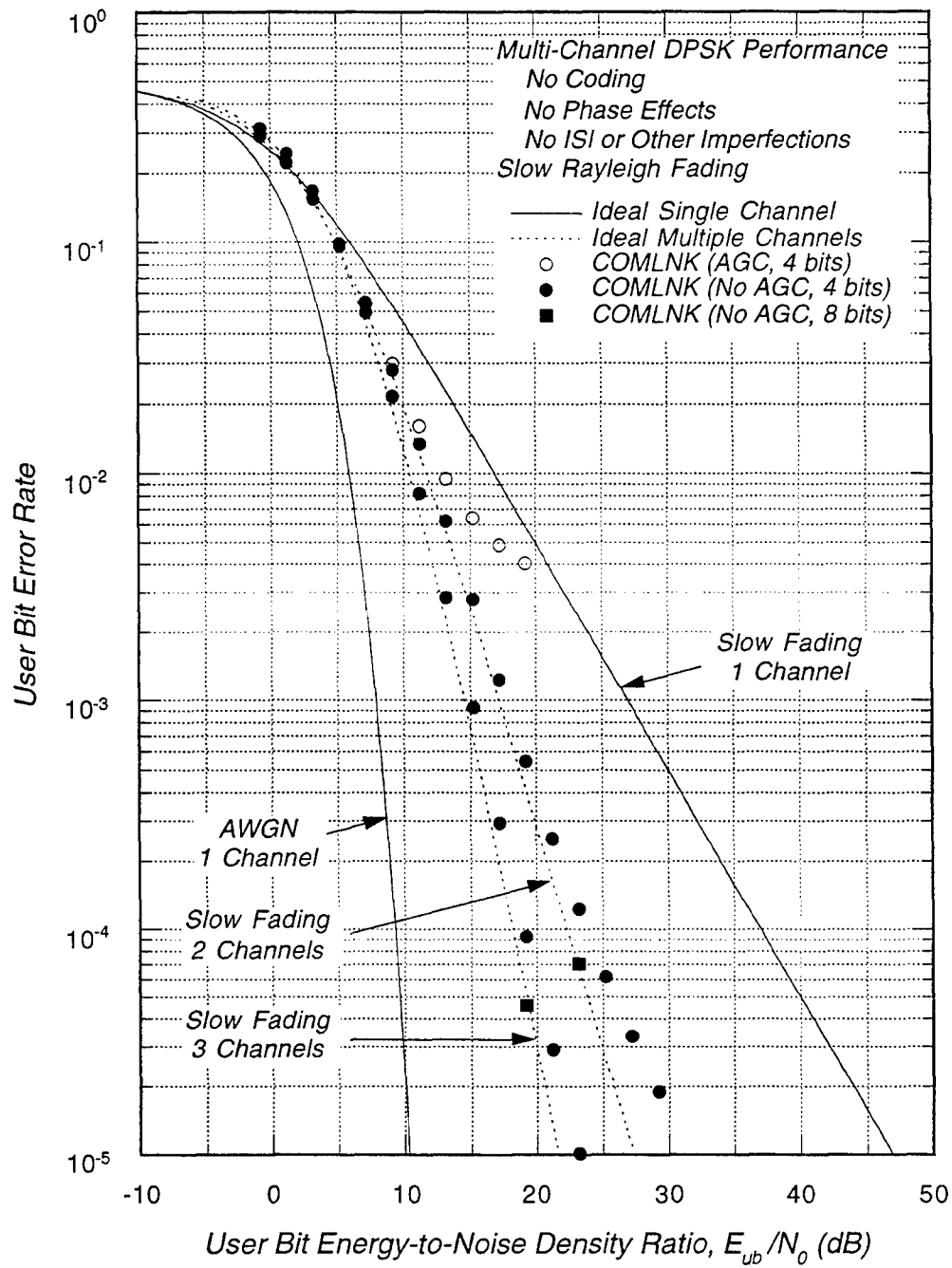


Figure 4-2. Diversity combining of DPSK decision metrics from two and three slow Rayleigh fading channels.

An active signal-based AGC reduces the signal level when E_{cb}/N_0 is above the design value, and small quantized values of signal plus noise in fades results in a loss of precision. At very large mean signal strengths, both the signal and noise voltages can fall off the bottom of the quantizer during deep fades. Thus, while an ideal analog demodulator would likely make correct decision, a real digital demodulator with a signal-based AGC will produce zeros during deep fades, which are correct 50 percent of the time, on the average.

This is a real phenomenon. It normally causes no problem because when it occurs the demodulation error rate is so low that any decent error-correction decoder produces no errors. It is also not a problem in a non-fading channel where the signal remains at its mean level. It is noteworthy that COMLNK exhibits this degree of fidelity. The AGC parameters could have been chosen to provide improved operation. However, to compare COMLNK results with theory we reran the two-channel simulations with the AGC turned off, and observed that the demodulation error rates were close to the theoretical curve over the full range of signal strength. The three-channel case was only run with the AGC off.

Although the COMLNK results with the AGC turned off follow the theoretical curves, the solid circle simulation points do tend to deviate from theory at low error rates. This, we suspected, is due to the finite precision of the individual decision metrics even with the AGC turned off. Most of the cases were run with 4 bits of precision in \hat{m} before combining. To test this hypothesis, we reran both the two- and three-channel cases at one large value of E_{ub}/N_0 using 8 bits of precision in \hat{m} before combining. These results, plotted with solid squares in the figure, fall right on the corresponding theoretical curves. Thus, not only are the DPSK demodulation and combining results verified, it is also seen that COMLNK provides the fidelity to investigate hardware design details such as quantization.

4.2 FAST RAYLEIGH FADING CHANNELS.

Real Rayleigh fading channels are not infinitely slow, and further degradation in the channel bit error rate occurs when fast fading effects are considered. Demodulation error rates for DPSK and binary FSK (BFSK) were derived by *Bello and Noll* [1963b] about 35 years ago. *Rutherford* [1978] extended these results to M -ary FSK by ignoring the tone filter cross correlation terms. We report new fast fading results for DPSK and M -ary FSK in the appendices of this report for the Doppler frequency spectra characteristic of transionospheric scintillation [Wittwer, 1980]. Unfortunately,

these results are not given by simple mathematical expressions as is the case for slow Rayleigh fading, so we leave some details in the appendices.

4.2.1 DPSK Performance.

The single-channel fast fading DPSK demodulation error rate, derived in Appendix B of this report, is

$$\langle P_e \rangle = \frac{\gamma[R_1 - R_2] + 1}{2(\gamma R_1 + 1)} \quad (\text{DPSK, Fast Rayleigh Fading}) ,$$

where

$$R_1 = 2 \int_0^1 (1 - \xi) \rho(T\xi) d\xi ,$$

$$R_2 = \frac{1}{2} \int_0^1 (1 - \xi) \{ \rho[T(1 - \xi)] + \rho[T(1 + \xi)] \} d\xi ,$$

T is the channel bit period ($1/T$ is the channel bit rate), and $\rho(\cdot)$ is the temporal auto-correlation function of the fading. Analytic results are possible for DPSK performance in fast Rayleigh fading for all cases where these integrals have closed form expressions. (R_1 and R_2 for the Gaussian and f^{-4} Doppler frequency are given in Appendix B).

A comparison of COMLNK and theoretical results for the DPSK channel bit error rate in fast Rayleigh fading with an f^{-4} Doppler frequency spectrum is shown in Figure 4-3 for several values of the ratio of the channel decorrelation time to the channel bit period, τ_0/T_{cb} . Excellent agreement is seen in the figure between the simulation and theoretical results.

Another presentation of these data is to consider the channel bit energy-to-noise spectral density ratio necessary to achieve a 10 percent channel bit error rate. This is an interesting error rate because maximum-likelihood, low-rate error correction decoders with uncorrelated input errors at this error rate produce an output error rate of 10^{-5} or less. The required value of E_{cb}/N_0 to achieve the ten percent demodulated error rate is shown in Figure 4-4 for Δ PSK and DPSK modulation. The solid line in the figure is the theoretical curve for DPSK, and the circles are COMLNK simulation points (open circles connected by a dashed line for Δ PSK and solid circles for DPSK). To the authors' knowledge, no fast fading analytic result exists for Δ PSK. Again close agreement is seen between the COMLNK and theoretical DPSK results.

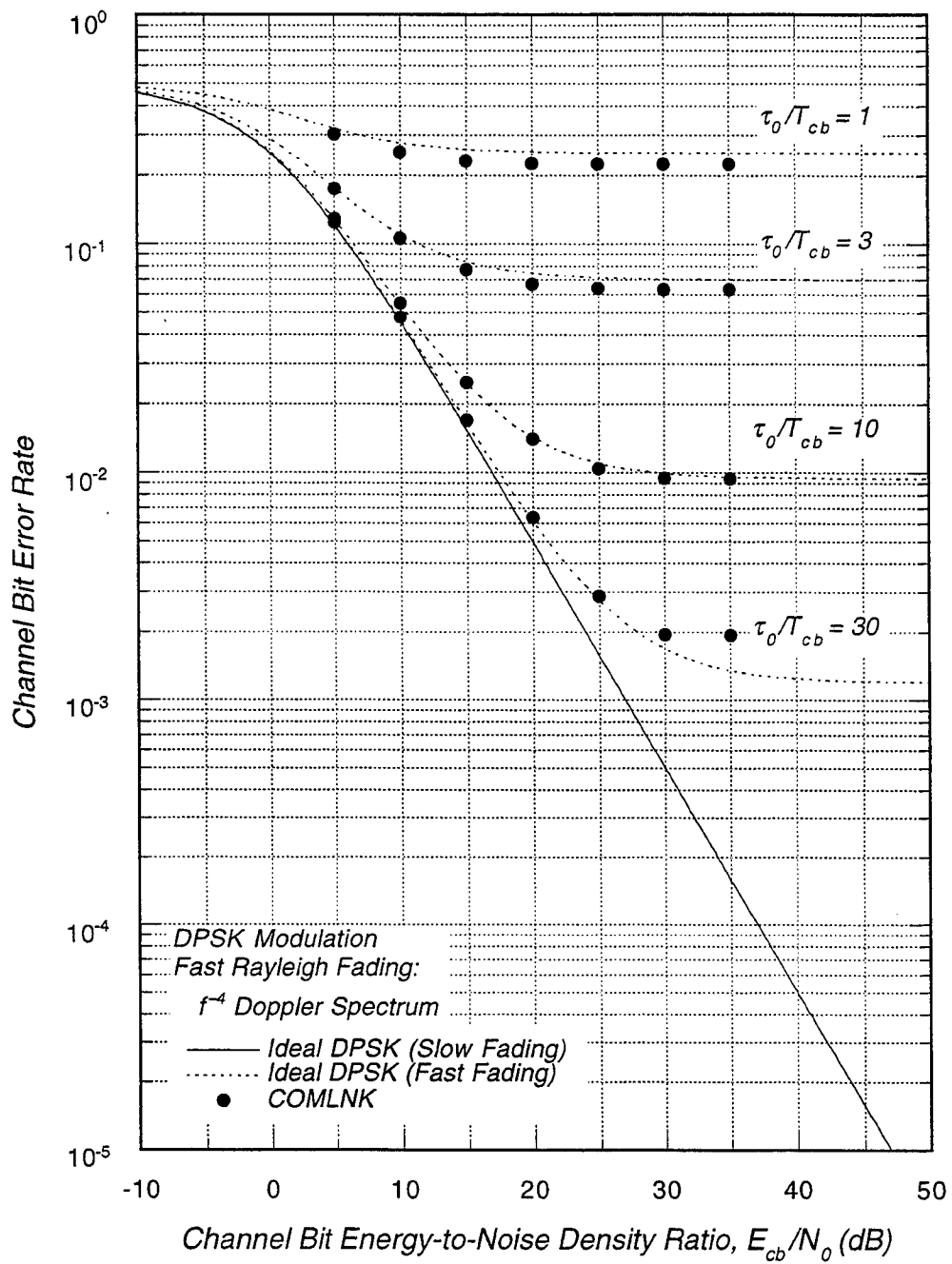


Figure 4-3. DPSK channel bit error rate in fast Rayleigh fading.

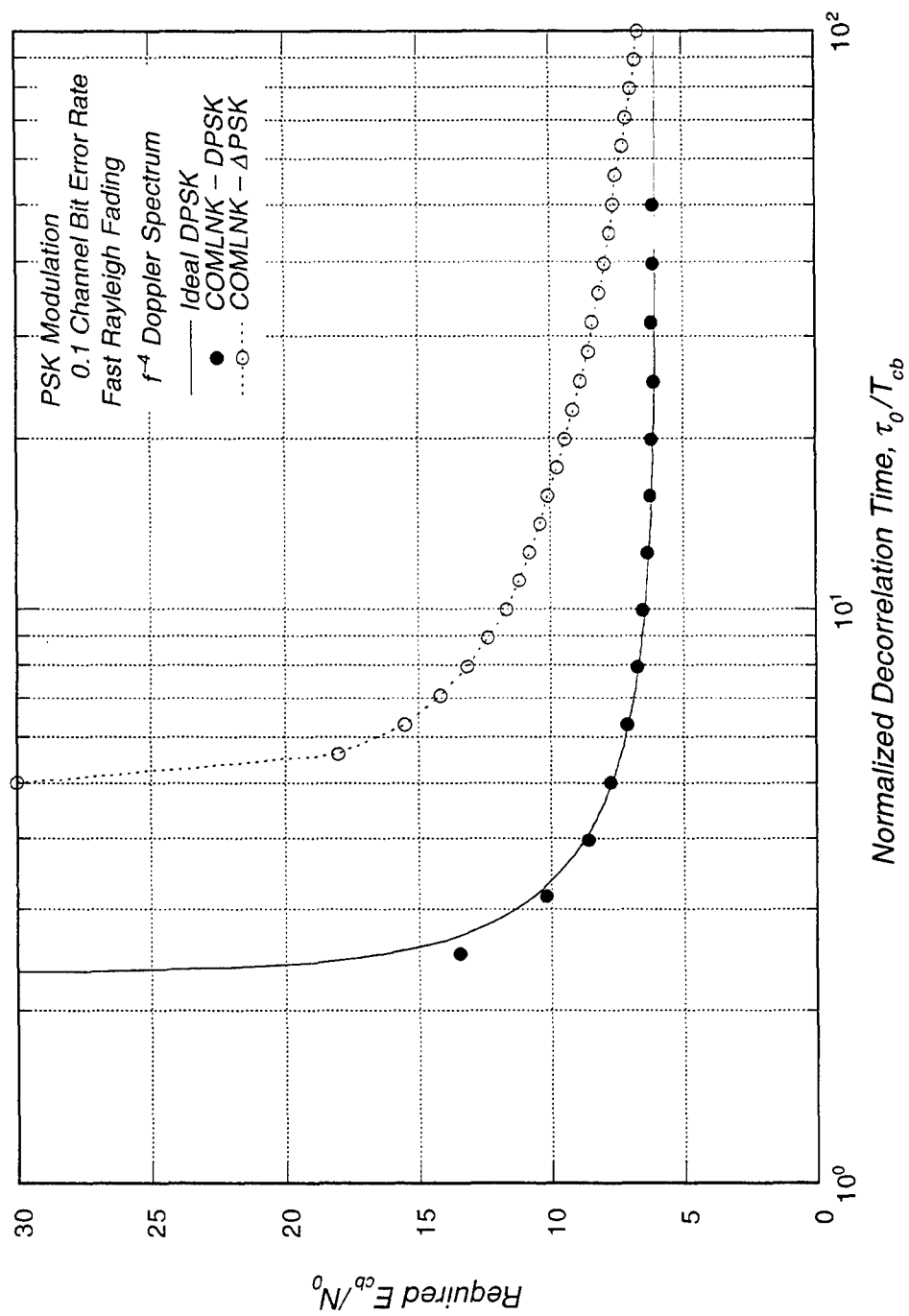


Figure 4-4. Required E_b/N_0 for Δ PSK and DPSK to achieve a ten-percent channel bit error rate in fast Rayleigh fading.

The results in Figure 4-4 illustrate that DPSK has more robust performance in fast fading than does Δ PSK. Indeed for the same channel bit rate, one can operate a DPSK link in faster fading channels (by a factor of 2 or so) with a lower signal-to-noise ratio than is required with Δ PSK.

DPSK test data are available from the prototype L_3P receiver scintillation test program conducted with the NELS channel simulator circa 1982 [Bogusch and Guigliano, 1982; Dana, 1995c]. Channel bit error rate measurements obtained at channel decorrelation times of 5 and 100 msec are compared with recently generated COMLNK results in Figure 4-5².

4.2.2 BFSK Performance.

An exact expression for the binary frequency-shift keying (BFSK) channel bit error rate is derived in Appendix F. This expression is

$$\langle P_e \rangle = \frac{1}{2} \left[1 - \frac{R_1 - R_2}{\sqrt{(R_1 + R_2 + 2\gamma^{-1})^2 - 4R_3^2}} \right] \quad (\text{BFSK, Fast Rayleigh Fading}) ,$$

where

$$R_1 = 2 \int_0^1 \rho(T\xi)(1 - \xi) d\xi \quad (4.1)$$

$$R_2 = 2 \int_0^1 \rho(T\xi)(1 - \xi) \cos(\omega_M \xi) d\xi \quad (4.2)$$

$$R_3 = \frac{2(-1)^{\Delta f T}}{\omega_M} \int_0^1 \rho(T\xi) \sin(\omega_M \xi) d\xi \quad (4.3)$$

² The remarkable agreement to within a small fraction of a decibel between test, theory, and simulation results seen in this figure is achieved by applying an implementation loss to the theoretical and COMLNK results. This loss of 1.5 dB is derived from non-fading test results as described in Dana [1995c]. Nonetheless, the test and simulation results follow the precise shape of the theoretical curves, validating both the theory and COMLNK, as well as the NELS hardware simulator.

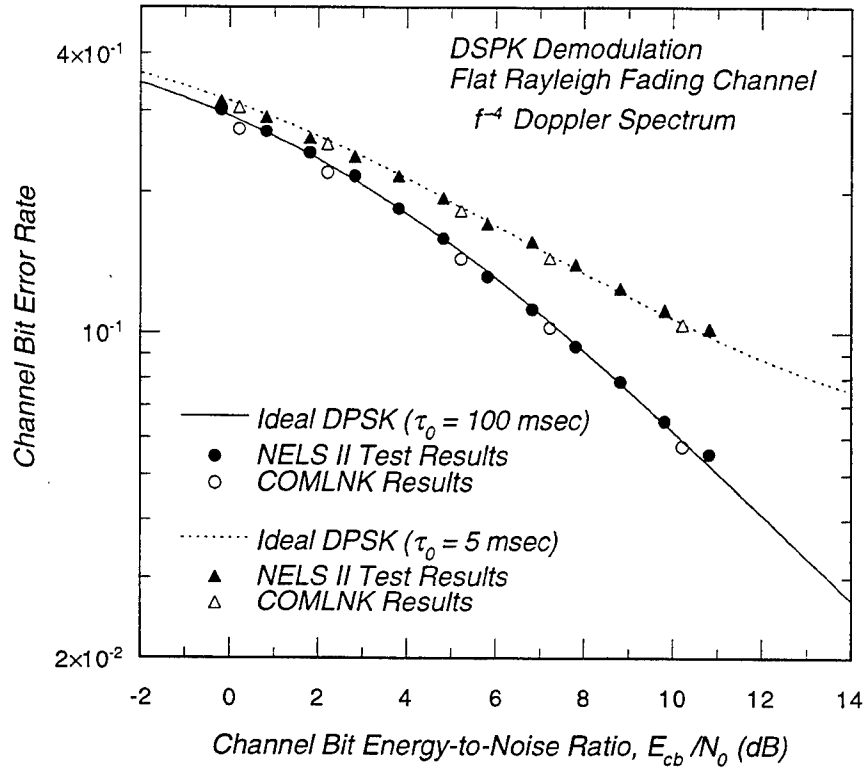


Figure 4-5. Comparison of test and COMLNK results for the DPSK demodulation error rate of the prototype L_3P receiver.

The quantity T in these expressions is the FSK symbol period, which for BFSK is also equal to the channel bit period, T_{cb} (this is not the case for higher order FSK), and the normalized tone spacing radian frequency is $\omega_M = 2\pi \Delta f T$. Expressions for R_1 , R_2 , and R_3 for the f^{-4} Doppler frequency spectrum are given in Appendix F. To the authors' knowledge, closed form expressions for these integrals are not possible for the Gaussian spectrum, although the integrals can be evaluated numerically in this case. In slow Rayleigh fading, R_2 and R_3 are equal to zero, R_1 is equal to unity, and the BFSK fast fading channel bit error rate reduces to the slow fading expression:

$$\langle P_e \rangle = \frac{1}{2 + \gamma} \quad (\text{BFSK, Slow Rayleigh Fading}) .$$

A comparison of these results to COMLNK simulation results is shown in Figure 4-6 for minimum tone spacing ($\Delta f T = 1$), an f^{-4} Doppler frequency spectrum, and three values of the normalized channel decorrelation time, τ_0/T_{cb} . For this case the COMLNK and theoretical results agree perfectly.

4.2.3 *M*-ary FSK Performance.

For Rayleigh fading, the output signal plus noise voltages of the M filters of an M -ary FSK receiver are correlated, complex, zero mean, normally distributed random variables. It is the correlation between the signal contribution to the tone filter outputs that makes the calculation of the non-coherent M -ary FSK demodulation error rate a difficult mathematical problem that may not be tractable. Ignoring the correlation, it is possible to compute the demodulation error rate for the general case from the variance of the outputs of the M filters, as shown in Appendix F and summarized below. We show in the appendix that ignoring the correlation gives an upper bound to the actual demodulation error rate.

We have already calculated the variance of the output voltages of the M filters, although a slight generalization is needed. These results are given in Equations (4.1) and (4.2). The required generalization is that the R_2 integral becomes

$$R_2(k) = 2 \int_0^1 \rho(T\xi)(1-\xi) \cos(\omega_M k \xi) d\xi ,$$

where k is the distance of the other filter from the correct filter [$k = (i-l)/2$ where i and l are odd integers]. To simplify the notation, we rewrite the filter output variances as follows:

$$\begin{aligned} \mu_0 &= r^2 [R_1 + \gamma^{-1}] \\ \mu_k &= r^2 [R_2(k) + \gamma^{-1}] \end{aligned} \quad (4.4)$$

where r is the mean signal amplitude. Formulas for R_1 and $R_2(k)$ for an f^{-4} Doppler frequency spectrum are given in Appendix F with ω_M replaced by $k\omega_M$. The R_1 integral given in the appendix for the signal energy out of the correct tone remains the same in this case.

It is shown in Appendix F that the probability of selecting the correct tone filter is given by the expression

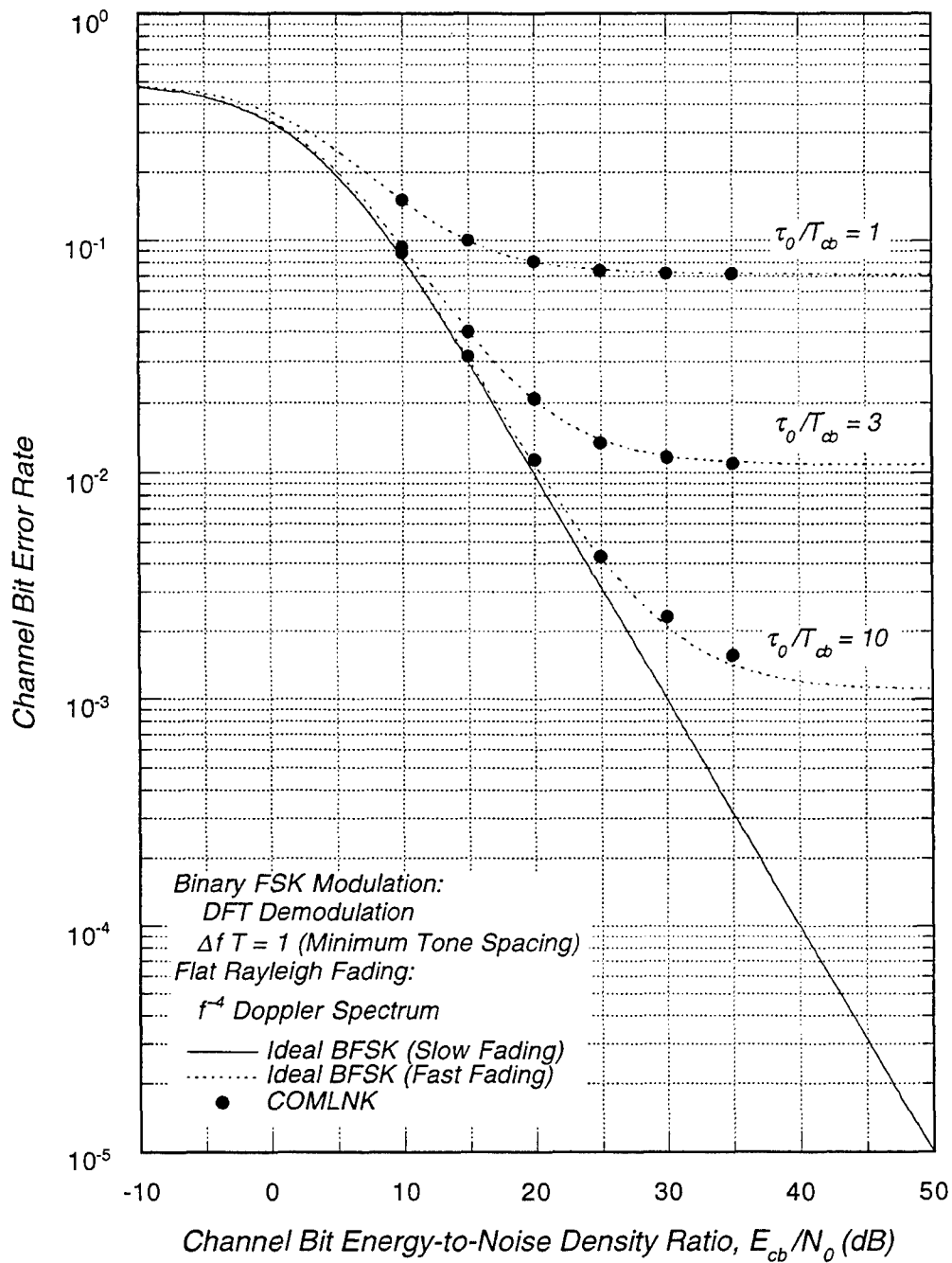


Figure 4-6. BFSK channel bit error rate for the minimum tone spacing in fast Rayleigh fading.

$$P_c = \frac{2}{M} P_M(v_0, v_1, \dots, v_{M-1}) + \frac{2}{M} \sum_{l=1}^{M/2-1} P_M(v_0, v_1, \dots, v_{l-1}, v_0, \dots, v_{M-l-1}) ,$$

where $v_k = \mu_k / \mu_0$ and $v_0 = 1$. The P_M terms are evaluated by recursion:

$$P_M(\bar{v}_M) = P_{M-1}(v_0, v_2, \dots, v_{M-1}) - P_{M-1}\left(\frac{v_0 v_1}{v_0 + v_1}, v_2, \dots, v_{M-1}\right) ,$$

and

$$P_2(v_0, v_1) = \frac{v_0^2}{v_0 + v_1} .$$

In fast fading the relationship between channel symbol error rate and the bit error rate is not given by the AWGN formula $\frac{1}{2} M/(M-1)$. In deriving this expression, it is assumed that when a demodulation error occurs all incorrect tone filters are equally likely to be selected. This is only the case when all incorrect filters have equal output amplitudes on the average. This is not the case with M -ary FSK demodulation in fast fading channels. Rapid variations of signal amplitude and phase cause the received signal spectrum to smear out. This Doppler spreading causes the receiver filters to become mis-matched, and some of the signal energy that would otherwise appear at the output of the correct filter instead appears in the outputs of adjacent filters.

Thus, when the channel bit error rate is less than 50 percent in fast fading, M -ary FSK demodulation errors are most likely to be made by choosing a filter adjacent to the correct filter. This changes the average number of channel bit errors per channel symbol error. For example, the AWGN formula predicts this ratio to be $\frac{4}{7}$ for 8-ary FSK, whereas the ratio is $\frac{11}{21}$ when adjacent filters cause all demodulation errors. The difference is even larger for 16-ary FSK where the AWGN formula predicts a ratio of $\frac{8}{15}$ or 0.53, whereas the adjacent filter assumption results in a ratio of $\frac{13}{30}$ or 0.43. Of course the ratio is 1 for BFSK, and one can show that it is $\frac{2}{3}$ for QFSK in either case.

The difficulty here is that this change in the relationship between symbol and bit error rate is not accounted for in our theoretical development, whereas it is treated automatically and properly in COMLNK. We can avoid this difficulty by comparing theoretical and simulation results for channel symbol error rates, rather than bit error rates, for the 8-ary and 16-ary FSK cases.

For QFSK the average channel bit error rate is obtained from the probability P_c that the correct filter has the largest output amplitude as follows:

$$\langle P_e \rangle = \frac{2}{3} (1 - P_c) \quad \text{QFSK} ,$$

where this formula holds whether one assumes that all incorrect tone filters are equally likely to be chosen when a demodulation error occurs (AWGN case), or that the tone filters adjacent to the correct one are most likely to be chosen (fast fading). Comparisons of the fast Rayleigh fading theoretical results with COMLNK simulation results are presented in Figure 4-7 for QFSK with minimum tone spacing ($\Delta f T = 1$) and τ_0/T_{cb} ratios of 1, 3, 10, and 30. As predicted, the simulation results fall slightly below the theoretical curves that are an upper bound because the correlation between the signal components of the tone filter outputs is ignored in the theory.

For 8-ary and 16-ary FSK, the theoretical demodulation symbol error rate is computed from the expression $\langle P_d \rangle = 1 - P_c$. Comparisons between our theoretical results and COMLNK simulation results are shown in Figures 4-8 and 4-9 for 8-ary FSK with $\Delta f T = 1$ and $\Delta f T = 3$, respectively, and in Figures 4-10 and 4-11 for 16-ary FSK with $\Delta f T = 1$ and $\Delta f T = 3$, respectively. In these figures, the channel symbol error rate is plotted against the channel symbol energy-to-noise spectral density ratio, E_{cs}/N_0 , for several values of the ratio of channel decorrelation time to the channel bit period, τ_0/T_{cb} . Note that the symbol error rate limit for small values of E_{cs}/N_0 is $(M-1)/M$ rather than $\frac{1}{2}$, which is the bit error rate limit.

The agreement between the theoretical upper bounds and COMLNK results is generally very good. For large values of τ_0/T_{cb} , the COMLNK results are consistently below the theoretical results, and the discrepancy increases as τ_0/T_{cb} increases. We believe that this is a result of our analytical assumption that the signal contributions to the tone filter outputs are uncorrelated. (Of course the noise contributions are always uncorrelated for orthogonal tone spacing, but noise has no discernible effect at large signal-to-noise ratios.) We show in Appendix F that the signal contributions to the incorrect filter outputs are correlated, with the correlation coefficient approaching unity for $\tau_0/T_{cb} \geq \frac{1}{2} \log_2 M$ or so. The correlation between the filter outputs reduces the error probability. This correlation is inherent in the COMLNK filters, but is neglected in the analysis³.

³ Further evidence that COMLNK results are correct comes from comparison of measured values of the average output power from all tone filters with the theoretical expected values given in Appendix F. The neglect of the filter output correlation has no effect on these theoretical values, and the COMLNK measurements exhibit excellent agreement.

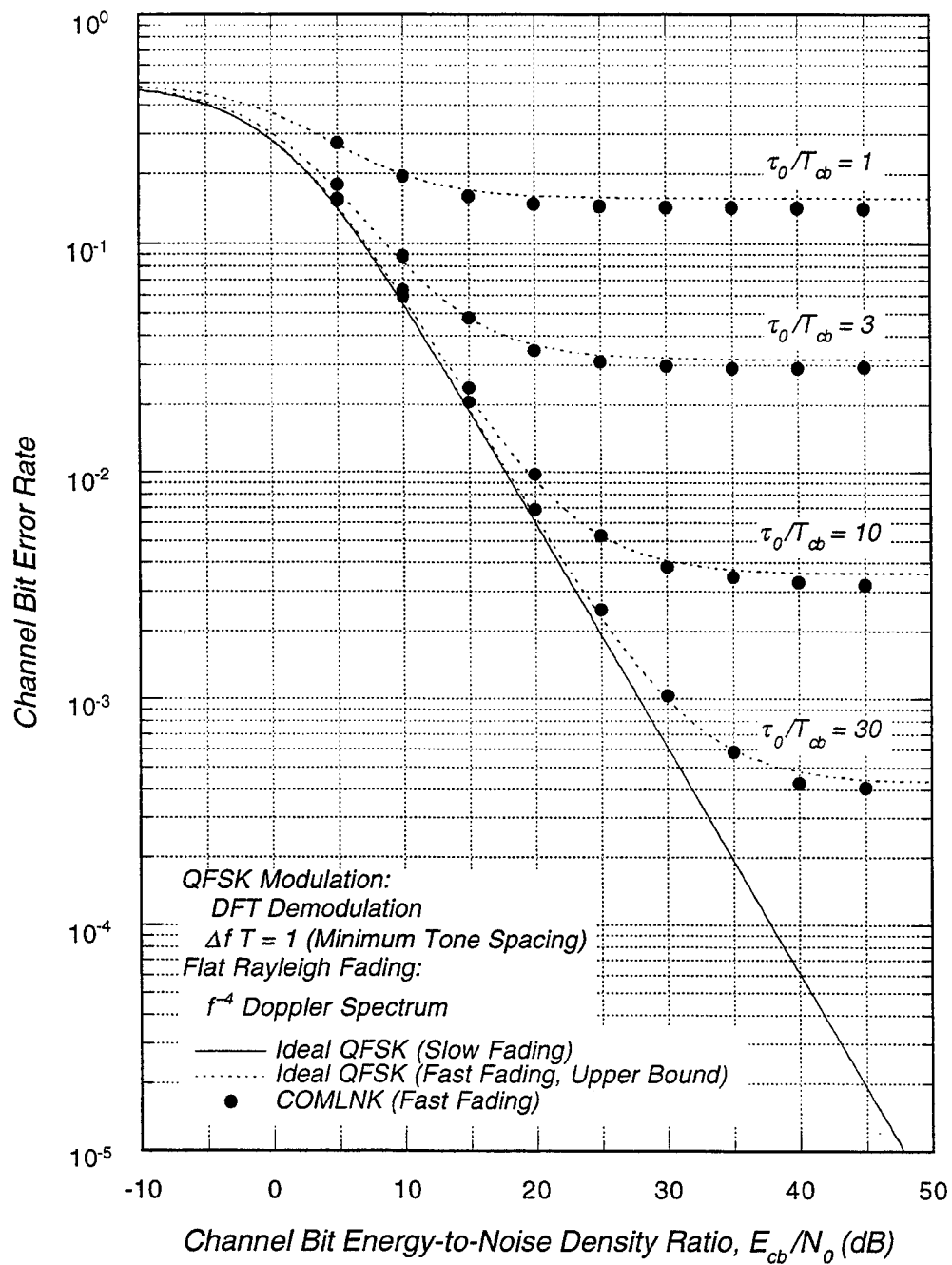


Figure 4-7. QFSK channel bit error rate for the minimum tone spacing in fast Rayleigh fading.

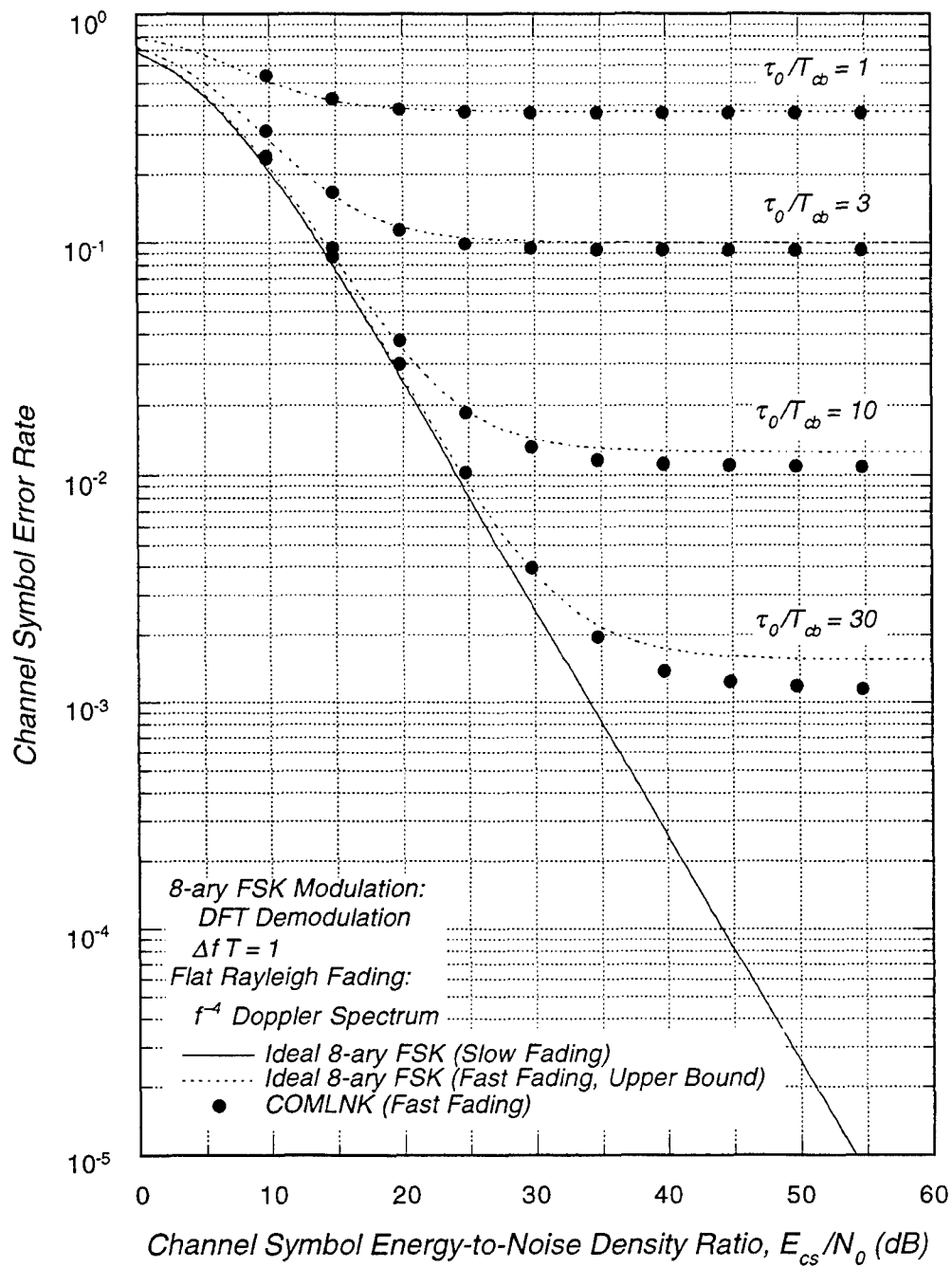


Figure 4-8. 8-ary FSK channel symbol error rate for the minimum tone spacing in fast Rayleigh fading.

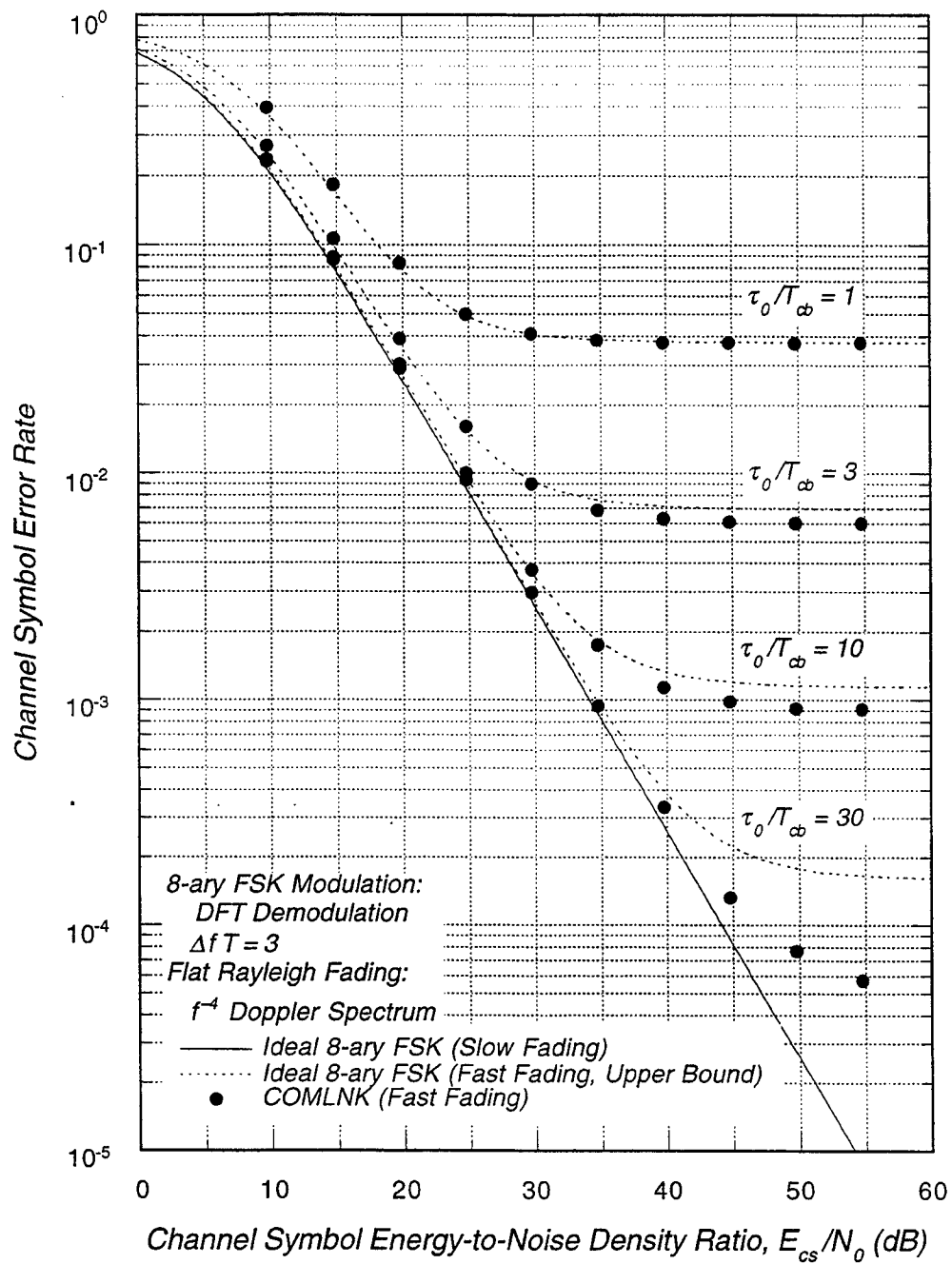


Figure 4-9. 8-ary FSK channel symbol error rate for three times the minimum tone spacing in fast Rayleigh fading.

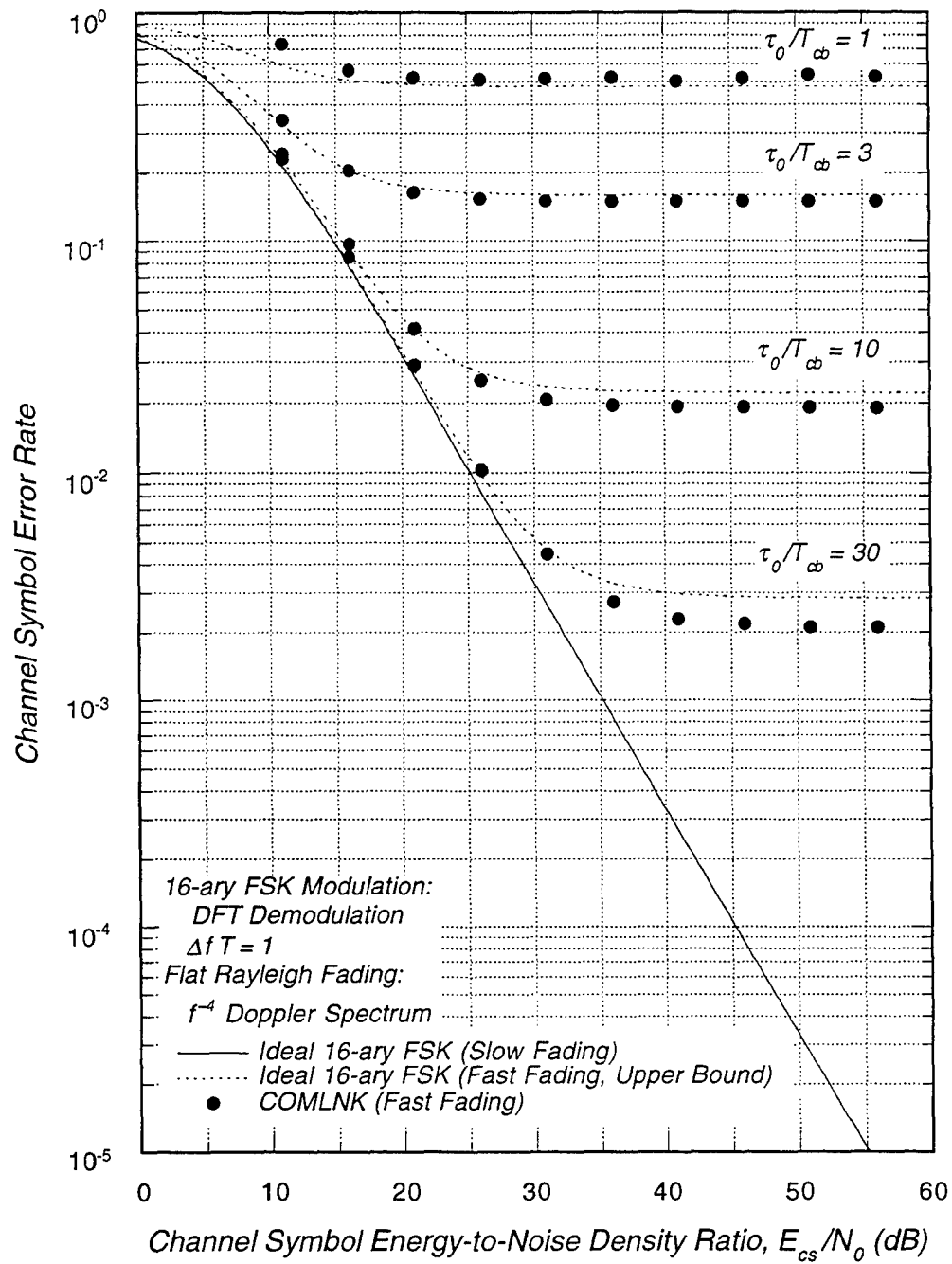


Figure 4-10. 16-ary FSK channel symbol error rate for the minimum tone spacing in fast Rayleigh fading.

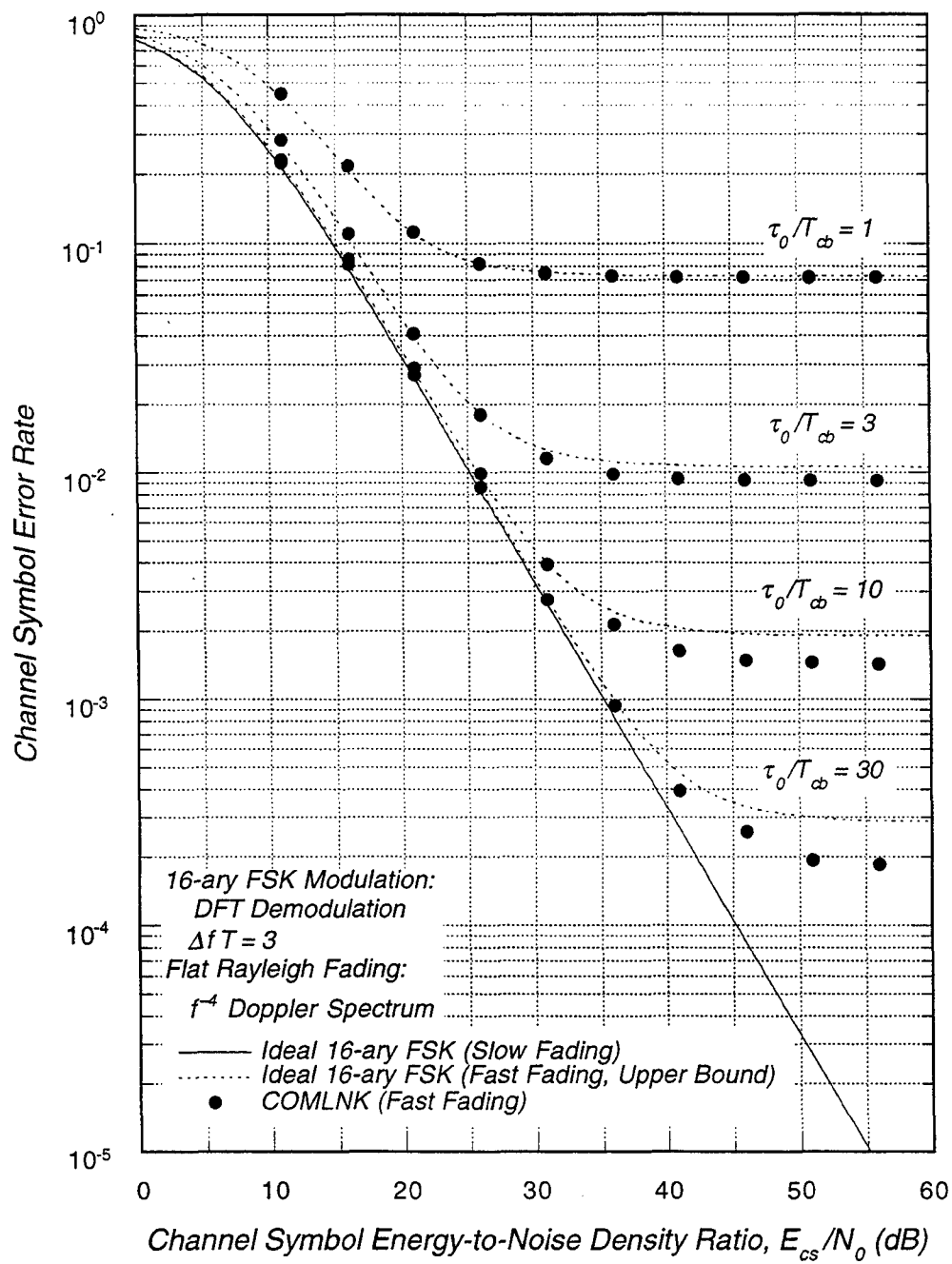


Figure 4-11. 16-ary FSK channel symbol error rate for three times the minimum tone spacing in fast Rayleigh fading.

Thus our theoretical results for $M > 2$, calculated assuming uncorrelated filter outputs, provide an upper limit to the demodulation error rate. The difference between the theoretical results and the true error rate increases as τ_0/T_{cb} increases because the correlation between the filters also increases. Eventually, as τ_0/T_{cb} gets large enough, the signal energy out of filters becomes so small that the correlation is no longer important, and our theoretical results approach the usual slow fading limit for the error rate. For values of τ_0/T_{cb} less than $\frac{1}{2} \log_2 M$, the correlation coefficient rapidly approaches zero, our assumption of uncorrelated outputs is correct, and close agreement is seen between COMLNK results and our theoretical results.

In the discussion above, we point out that the ratio between the demodulated symbol error rate and the channel bit error rate is not the same in fast fading as it is in AWGN because adjacent filter errors are more likely in fast fading. We can predict this ratio in the limits of slow and fast fading, but we do not have a formula for the ratio in the transition regime. We can, however, compute this ratio from COMLNK simulation results, and the ratio is plotted in Figure 4-12 versus symbol error rate for the 16-ary case. The 12 curves plotted in the figure are from 12 different simulation cases ($\tau_0/T_{cb} = 1, 3, 10$, and 30 , and $\Delta f T = 1, 2$ and 3). The 9 points along any one curve are for 9 values of E_{cb}/N_0 (5 dB to 45 dB in 5 dB steps). Note that for some of the curves, there are several simulation points at the minimum value of the ratio.

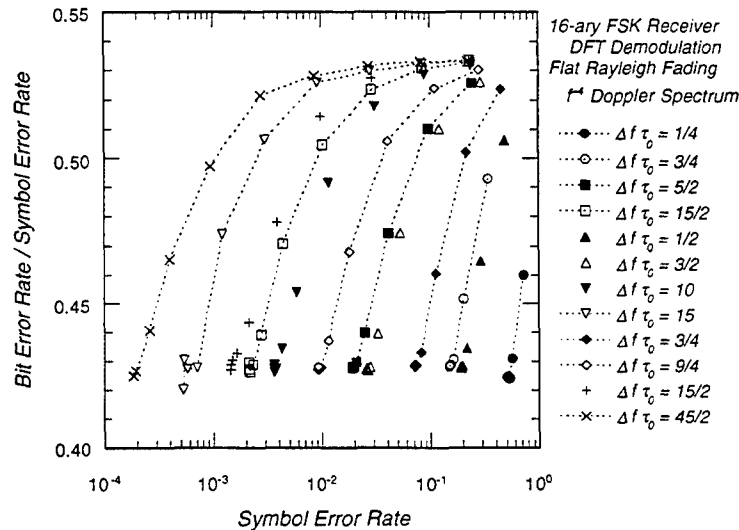


Figure 4-12. COMLNK results for the ratio of the channel bit error rate to the demodulated symbol error rate for 16-ary FSK.

We predicted for this case that the ratio would vary between a maximum of $\frac{1}{2}M/(M-1) = 0.53$ (the value for AWGN, slow fading or when the demodulation error rate is large) and a minimum of $\frac{13}{30}$ or 0.43 (the value when only adjacent filters cause demodulation errors). The COMLNK results fall generally within this predicted range. In principle, one could calculate the ratio of the two error rates for the general case by computing the probability of each incorrect filter being chosen for each of the M correct tone positions. For our validation purposes, however, the close comparison of COMLNK with the theoretical upper bound on the channel symbol error rate and the excellent agreement for the average power are sufficient to validate the M -ary FSK demodulation performance.

The results for 8- and 16-ary FSK are summarized in Figures 4-13 and 4-14, respectively, where the required value of E_{cb}/N_0 to achieve a 10 percent channel bit error rate is plotted versus normalized decorrelation time, τ_0/T_{cb} . The COMLNK results, generated using N_T -point DFTs, agree quite well with the theoretical predictions, which are described in Appendix F. These results show the significant performance gain in fast fading achieved by increasing the spacing of FSK tones.

The discrepancy between the required value of E_{cb}/N_0 in fast fading computed with COMLNK and the theoretical curves is due to the two effects discussed above. The theoretical curve is for the AWGN value of the ratio of the channel bit error rate to the demodulated symbol error rate, and the theory neglects the correlation in the outputs of the tone filters. Thus for most cases the COMLNK results indicate a slightly smaller value for the fast fading limit of τ_0/T_{cb} (*i.e.*, the point where the required E_{cb}/N_0 goes to infinity). In the slow fading limit ($\tau_0/T_{cb} \geq 10$), the required values of E_{cb}/N_0 from the COMLNK results are slightly above the theoretical curves as they should be. In this limit where the error rate ratio is given by the AWGN formula and the correlation between incorrect tone filters is negligible, the theoretical curves give the ideal receiver performance. The COMLNK results are for an actual receiver implementation with finite resolution and dynamic range in the signal plus noise voltage samples, and a small implementation loss is indicated in the simulation results.

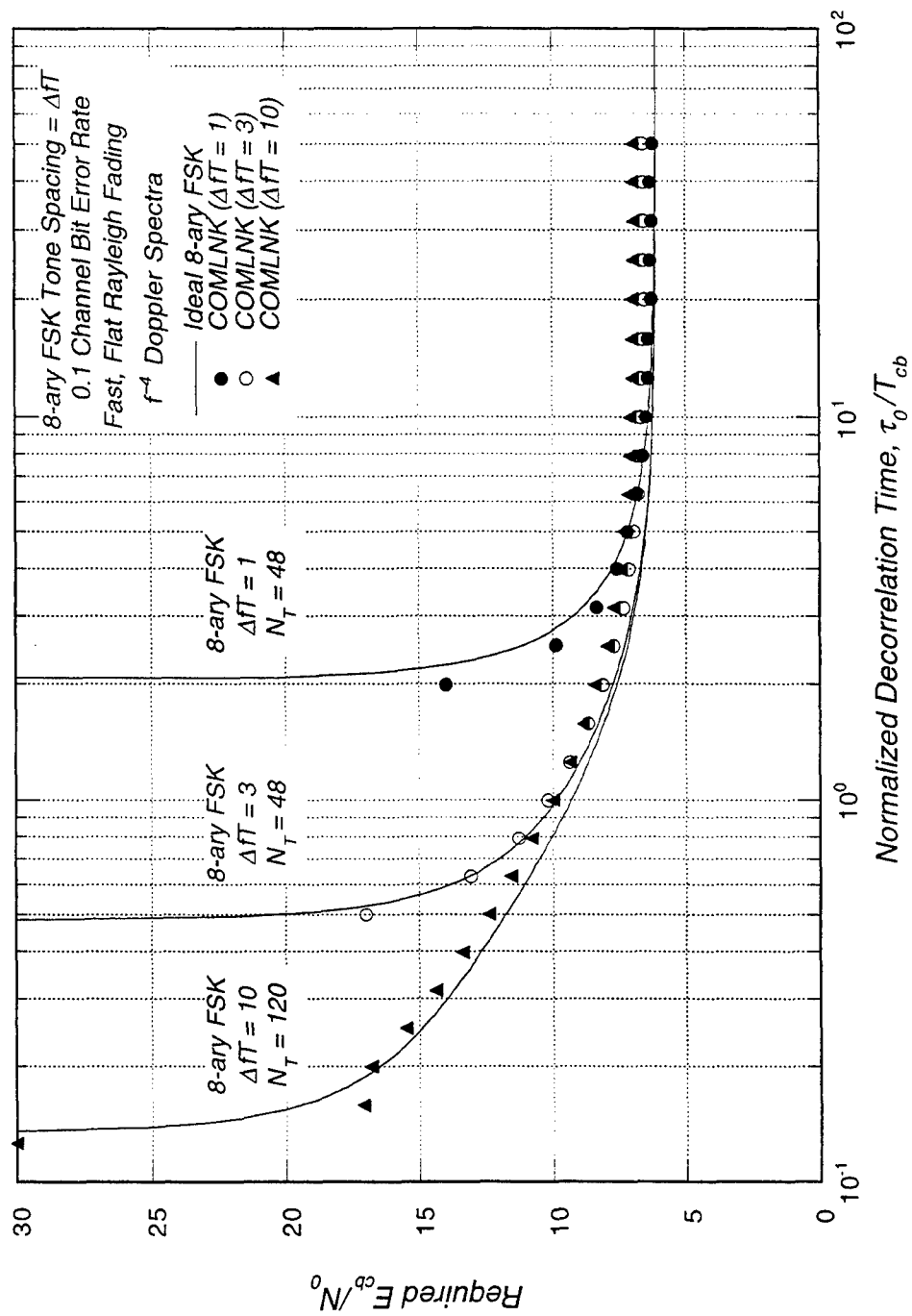


Figure 4-13. Required E_{cb} / N_0 for 8-ary FSK to achieve a ten-percent channel bit error rate in fast Rayleigh fading.

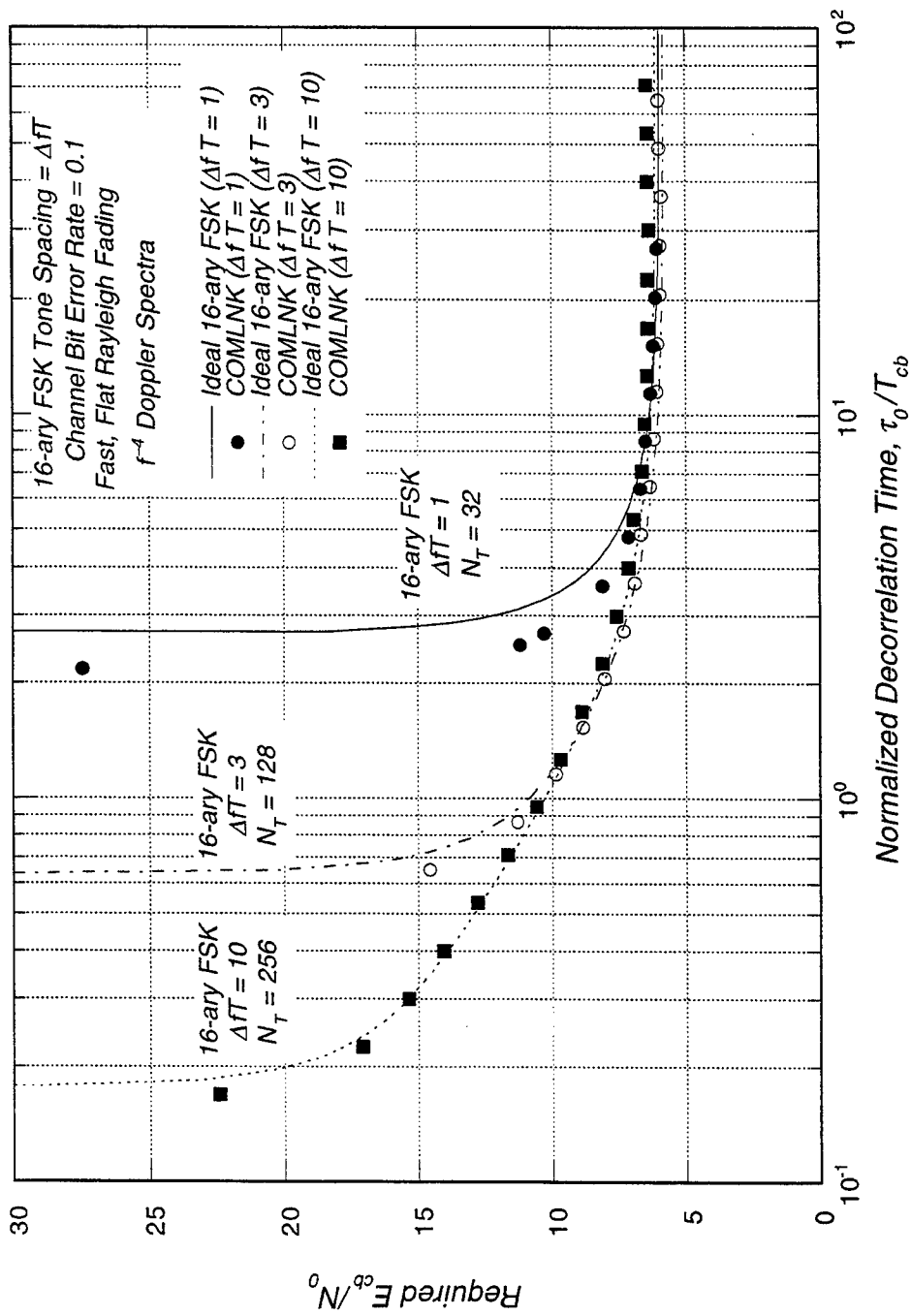


Figure 4-14. Required E_{cb}/N_0 for 16-ary FSK to achieve a ten-percent channel bit error rate in fast Rayleigh fading.

4.3 FREQUENCY SELECTIVE FADING CHANNELS.

Frequency selectivity adds three significant complications to the analysis of ideal demodulation error rates. First is the effect of the delay lock loop (DLL) which ideally tracks with a non-zero offset in such environments. The second complication is that demodulation error rates are quite sensitive to the coarseness of the sampling of the channel impulse response function (CIRF). Ultimately both of these effects were included in the theory because without them there was poor agreement between COMLNK and theoretical results.

The third complication is that the analytic expressions for the demodulation error rates in frequency selective fading channels are very complicated in part due to double integrals over the time and time-of-arrival properties of the channel. Without the use of the program *Mathematica*® [Wolfram, 1996] to perform the necessary integration, the theoretical frequency selective fading results in this report would not be possible, simply because of the large number of terms. COMLNK, of course, takes all of this in stride.

To the authors' knowledge the analytic demodulation error rates presented in this section that include the effects of delay tracking and CIRF sampling have not been published previously. Before these results were developed, the sensitivity of FSK demodulation error rates in particular to delay error and sampling was not well understood, and perhaps never would have been understood to the degree now possible simply by studying simulation results alone.

As in the previous subsection, we will first discuss DPSK performance with intersymbol interference and then discuss BFSK demodulation performance. This latter case is sufficiently complex that we have not attempted to derive analytic results for M -ary FSK performance in frequency selective fading channels, although this requires a straightforward extension of the BFSK formalism. We believe that the BFSK case is sufficient for COMLNK validation in frequency selective channels.

4.3.1 DPSK Performance.

Frequency selective fading does not directly impact DPSK demodulation if there is an underlying direct sequence spread spectrum code. For such a waveform, frequency selectivity only causes a loss in signal energy out of the code correlator to first

order, but the output signal is essentially flat fading⁴. The magnitude of the code correlation loss is given in Section 3, and the fast, flat fading performance of DPSK is given in Section 4.2. Thus we consider only the case of DPSK demodulation without an underlying PN code in this subsection.

In Appendix C we show that the ideal delay offset for DPSK demodulation without a PN code is a small fraction of a channel bit period. Therefore we ignore delay tracking in developing the ideal DPSK demodulation error rate. Thus when we compare our analytic results to those of COMLNK, we run the simulation with the DLL turned off and the delay offset fixed at zero.

With the assumptions of zero delay offset, no PN code, and a continuous channel impulse response function, the DPSK demodulation error rate is

$$\langle P_e \rangle = \frac{1}{2} - \frac{\sigma_1^2}{4\sqrt{\sigma_2^4 - R_4^2}} - \frac{\sigma_3^2}{4\sqrt{\sigma_4^4 - R_4^2}}$$

(DPSK, Continuous Frequency Selective Fading)

where

$$\begin{aligned} \sigma_1^2 &= R_3 + R_4 \left(e^{-\lambda} + \frac{1}{1 - e^{-\lambda}} \right) & \sigma_2^2 &= 2 \frac{R_1 + R_2}{1 - e^{-\lambda}} + R_4 + \gamma^{-1} \\ \sigma_3^2 &= R_3 - R_4 \left(e^{-\lambda} + \frac{1}{1 - e^{-\lambda}} \right) & \sigma_4^2 &= 2 \frac{R_1 + R_2}{1 - e^{-\lambda}} - R_4 + \gamma^{-1} \end{aligned}$$

and $\lambda = 2\pi f_0 T$. The R integrals are

$$\begin{aligned} R_1 &= \int_0^1 d\zeta T G(T\zeta) \int_0^{1-\zeta} d\xi \rho(T\xi) (1 - \zeta - \xi) \\ R_2 &= \int_0^1 d\zeta T G(T\zeta) \int_0^\zeta d\xi \rho(T\xi) (\zeta - \xi) \end{aligned}$$

⁴ Stated another way, frequency selective effects on the PN code correlator occur with much larger values of f_0 because of the much wider signal bandwidth in a PN system. Once the signal is despread, the value of f_0 then is much larger than the data bandwidth. If the value of f_0 were reduced sufficiently to cause frequency selective effects on data demodulation, then the PN code correlator would fail completely.

$$\begin{aligned}
R_3 &= \int_0^1 d\zeta T G(T\zeta) \int_0^{1-\zeta} d\xi \{ \rho[T(1+\xi)] + \rho[T(1-\xi)] \} (1-\zeta-\xi) \\
R_4 &= \int_0^{1/2} d\zeta T G(T\zeta) \left[\int_0^\zeta d\xi \xi \rho(T\xi) + \zeta \int_\zeta^{1-\zeta} d\xi \rho(T\xi) + \int_{1-\zeta}^1 d\xi \rho(T\xi) (1-\xi) \right] \\
&\quad + \int_{1/2}^1 d\zeta T G(T\zeta) \left[\int_0^{1-\zeta} d\xi \xi \rho(T\xi) + (1-\zeta) \int_{1-\zeta}^\zeta d\xi \rho(T\xi) + \int_\zeta^1 d\xi \rho(T\xi) (1-\xi) \right]
\end{aligned}$$

where $G(\cdot)$ is the power impulse response function, and $\rho(\cdot)$ is the temporal autocorrelation function of the channel impulse response function. Closed form expressions for these integrals for f^{-4} and f^{-6} Doppler frequency spectra are given in Appendix C.

As we have discussed before, the CIRF is necessarily sampled in both link simulations such as COMLNK and in hardware channel simulators such as the DSWA Nuclear Effects Link Simulator. To simplify the equations in this case, we consider only the case of slow, sampled frequency selective fading. For such fading the DPSK demodulation error rate is given by the expression

$$\langle P_e \rangle = \frac{1}{2} - \frac{\sigma_1^2}{4\sqrt{\sigma_2^4 - (R_1 - R_2)^2}} - \frac{\sigma_3^2}{4\sqrt{\sigma_4^4 - (R_1 - R_2)^2}} ,$$

(DPSK, Slow Sampled Frequency Selective Fading)

where the sigma terms are

$$\begin{aligned}
\sigma_1^2 &= R_0 + (R_I - 1 + e^{-\lambda})R_1 - (R_I + e^{-\lambda})R_2 \\
\sigma_2^2 &= (1 + R_I)R_0 - (1 + 2R_I)R_1 + R_I(1 + e^\lambda)R_2 + \gamma^{-1} \\
\sigma_3^2 &= R_0 - (3 + R_I + e^{-\lambda})R_1 + (2 + R_I + e^{-\lambda})R_2 \\
\sigma_4^2 &= (1 + R_I)R_0 - (3 + 2R_I)R_1 + (2 + R_I + R_I e^\lambda)R_2 + \gamma^{-1} .
\end{aligned}$$

For a sampled CIRF the R integrals are

$$\begin{aligned}
R_0 &= 1 - e^{-\lambda} \\
R_I &= \frac{e^{-\lambda}(1 - e^{-N_I \lambda})}{1 - e^{-\lambda}}
\end{aligned}$$

$$R_1 = \frac{e^{-\lambda/N_D} - e^{-\lambda} [N_D - (N_D - 1)e^{-\lambda/N_D}]}{N_D(1 - e^{-\lambda/N_D})}$$

$$R_2 = \frac{e^{-\lambda/N_D} (1 + e^{-\lambda/N_D}) - e^{-\lambda} [N_D^2 + (1 + 2N_D - 2N_D^2)e^{-\lambda/N_D} + (N_D - 1)^2 e^{-2\lambda/N_D}]}{N_D^2(1 - e^{-\lambda/N_D})^2}$$

The integer N_D is the number of delay samples per channel symbol, and N_I is the number of channel bits in the total CIRF delay spread ($N_I = N_\tau / N_D$ rounded up to the nearest integer).

These analytic results are compared with COMLNK simulation results in Figure 4-15 for several values of the normalized frequency selective bandwidth, $f_0 T_{cb}$. The COMLNK simulations were run with $\tau_0 / T_{cb} = 300$ to assure slow fading and with two delay samples per channel bit period. The agreement between ideal DPSK demodulation error rate curves for a sampled CIRF ($N_D = 2$) and simulation results is excellent. The reader should note, however, that we first computed the ideal DPSK demodulation error rates for the continuous CIRF case and these theoretical results did not agree at all well with the simulation results. It was this discrepancy that prompted us to consider the effects of channel delay sampling on demodulation error rates.

There is a significant difference between ideal DPSK demodulation error rates with a coarsely sampled CIRF and that for the continuous case. This difference is illustrated in Figure 4-16 where we show the value of the channel bit energy-to-noise spectral density ratio required to achieve a ten-percent demodulation error rate versus $f_0 T_{cb}$ for continuous and sampled CIRFs. Again there is excellent agreement between the COMLNK results and the ideal sampled CIRF curve⁵.

⁵ The COMLNK results in this figure plotted with solid circles only go down to $f_0 T_{cb} = 0.5$ because they were generated before we calculated the DPSK error rate with a sampled CIRF. The minimum frequency selective bandwidth for the set of COMLNK runs from which these results were generated was then determined by the continuous CIRF curve where finite values of E_{cb}/N_0 are only possible for $f_0 T_{cb} \geq 0.5$. The COMLNK results plotted with open circles were generated after the ideal curve for the sampled CIRF case was derived. This is an example of the manner in which detailed analyses and high-fidelity simulations complement each other.

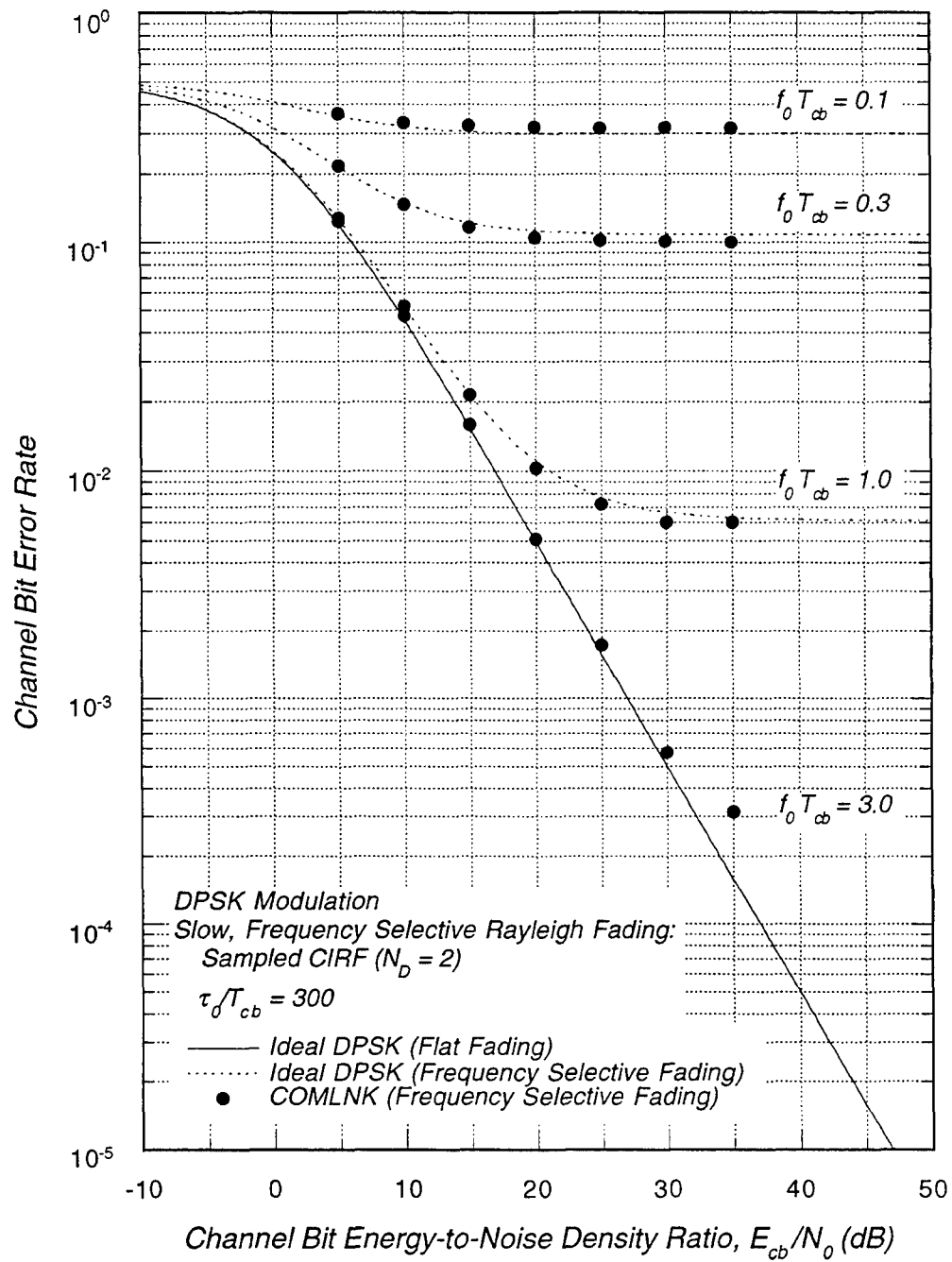


Figure 4-15. DPSK channel bit error rates in slow, frequency selective fading.

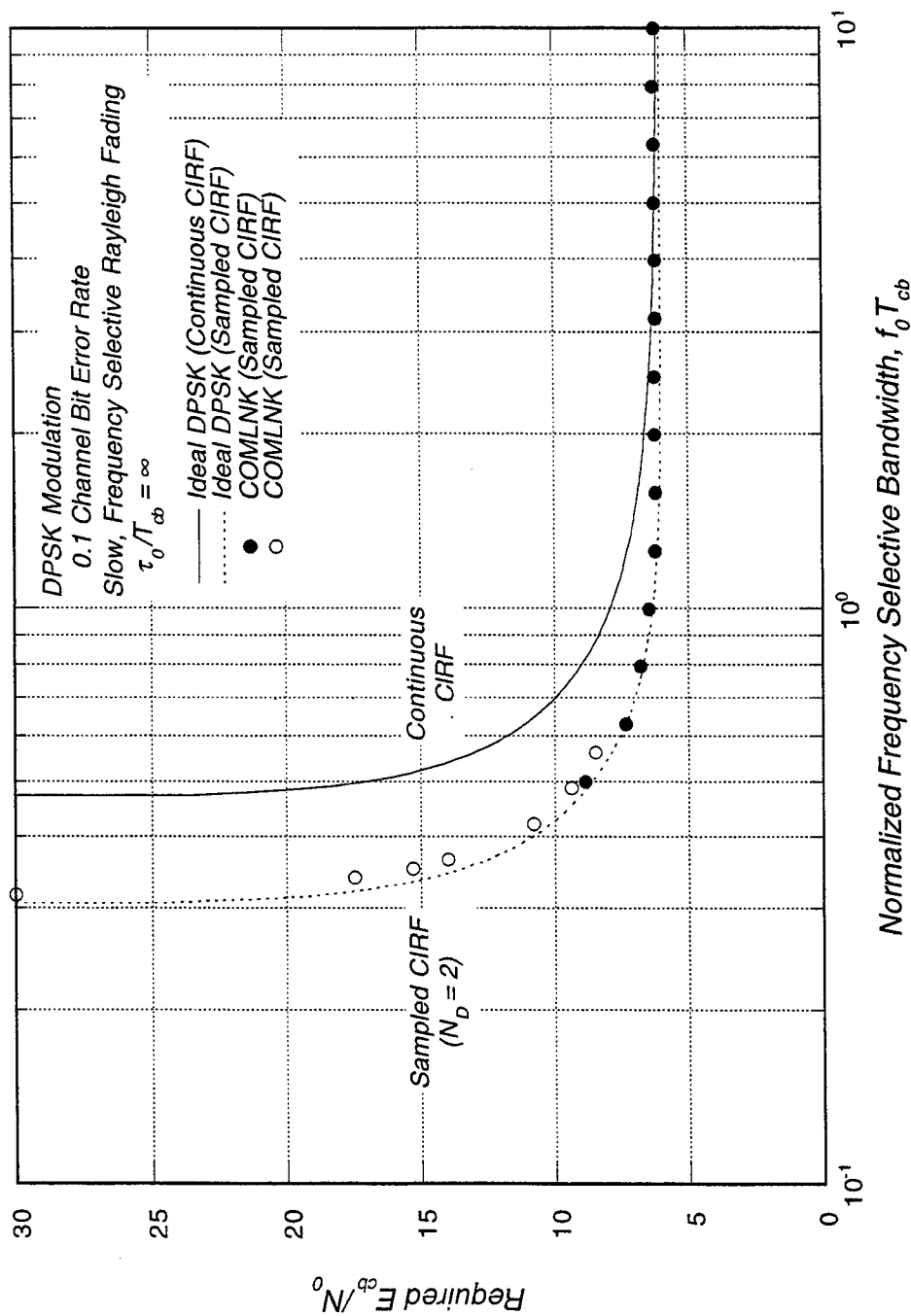


Figure 4-16. Required E_{cb}/N_0 for DPSK to achieve a ten-percent channel bit error rate in slow, frequency selective fading.

These results show that an ideal DPSK link can operate in frequency selective fading channels with $f_0 T_{cb} \geq \frac{1}{2}$. Sampling the CIRF with two samples per channel bit gives the appearance that a DPSK link can operate in frequency selective fading channels with values of $f_0 T_{cb}$ about 1.5 times smaller than the lower limit with a continuous CIRF. Thus both COMLNK simulation results and hardware test results using a frequency selective channel simulator may be somewhat optimistic relative to the performance of a DPSK link in a continuous frequency selective fading channel.

The cure for the difference between demodulation results with continuous and sampled CIRFs is to increase the number of delay samples per channel bit period. The price to be paid for this is increased execution time, primarily in the convolution of the channel with the transmitted modulation.

Rather than indiscriminately increasing the value of N_D in an attempt to achieve COMLNK results (or hardware test results) closer to those for a continuous CIRF, we recommend that users just be aware of the effect of channel delay sampling. Only when considering DPSK link performance near the threshold indicated by the results in Figure 4-16 and only when a factor of 1.5 or so in the minimum value of $f_0 T_{cb}$ makes some difference in conclusions inferred from simulation or test results, should one increase the value of N_D .

4.3.2 BFSK Performance with Hopping.

There are two fundamental characteristics of frequency selective fading that complicate the problem of analytically computing the FSK demodulation error rate. As pointed out in Section 2 of this report, the two-frequency mutual coherence function varies inversely with frequency difference. As a consequence, the correlation between the signal components at the output of the tone filters is not small as is the case for fast fading, and one is left with the problem of dealing with M mutually correlated random variables to compute the error rate. A further complication is that the two-frequency mutual coherence function is complex, so the cross correlation of the tone filter outputs is also complex. This effectively doubles the analytic calculations necessary to compute the correlation coefficients. Thus analytic results are practical only in the case of BFSK modulation. As we will show, the BFSK case is sufficiently tedious mathematically that there is little reason to attempt to develop analytic results for higher-order FSK signaling, although such results could, in principle, be obtained. Furthermore, the BFSK case is sufficient to achieve our goal of COMLNK validation. Note that none of these

analytical difficulties affects COMLNK, which can readily simulate M -ary FSK under fast, frequency selective fading channel conditions.

The block diagram in Figure 3-2 of Section 3 is for FSK with frequency hopping, although hopping can easily be disabled. Frequency hopping provides two key advantages to an FSK communications link. The primary advantage is protection from jamming, whether hostile or inadvertent. A side benefit, if the hopping rate equals or exceeds the modulation symbol rate, is to provide protection from intersymbol interference in frequency selective fading channels. In this section we only consider the case where the hopping rate is equal to the symbol rate. If the hopping rate is faster than the symbol rate, then signal energy from multiple hops per symbol must be non-coherently combined, which adds considerable complexity to the analysis (although readily treated by COMLNK). If the hopping rate is slower than the symbol rate, then signal energy from previous symbols within a hop can interfere with the on-time symbol. This approaches the case without hopping considered in the next subsection.

Even ignoring delay tracking, the BFSK demodulation error rate for general time and frequency selective fading is extraordinarily tedious to calculate analytically⁶. Thus we have chosen to develop analytic demodulation error rate expressions with non-zero delay tracking error only for slow, frequency selective fading and to develop such expressions with zero delay tracking error for fast, frequency selective fading. Results for these two cases are outlined below. The mathematical details are in Appendix G.

The BFSK channel bit error rate is computed analytically from the mean energy at the outputs of the two filters and the voltage cross correlation coefficient. For BFSK, the transmitted frequency is $\pm\Delta f/2$ (relative to the carrier frequency), and without loss of generality we assume that the $+\Delta f/2$ tone is transmitted. The normalized signal contribution E_+ ($E_+ = 1$ in the limit of flat fading) to the mean output energy of the correct filter corresponding to the transmitted tone is, for a slow fading continuous channel impulse response function,

⁶ It is important to distinguish between analysis and simulation when discussing complexity. Analytic results can be obtained only under rather limited conditions due to extraordinary mathematical complexity that must be faced each time that a calculation is performed. For a first-principles simulation such as COMLNK, complexity was faced once in structuring and coding the program. Thereafter, simulations of a wide range of systems and channels are readily performed.

$$E_+ = \int_0^{\infty} T G(T\zeta) \Lambda^2[\zeta - \hat{\tau}_D] d\zeta \quad (\text{Slow Fading, Continuous CIRF})$$

where $\hat{\tau}_D = \tau_D/T$ is the normalized delay offset, T is the modulation symbol period (which is also the channel bit period for BFSK), $\Lambda(\cdot)$ is the triangle function, and $G(\cdot)$ is the power impulse response function (Eqn. 2.8). When the CIRF is sampled, the delay integral reduces to a sum over the delay bins, and the slow fading signal energy at the output of the correct tone filter is

$$E_+ = \sum_{i=0}^{N_\tau-1} P_i \Lambda^2[i/N_D - \hat{\tau}_D] \quad (\text{Slow Fading, Sampled CIRF})$$

where P_i is the mean power in the i^{th} delay bin (Eqn. 2.14), N_D is the number of delay samples per symbol ($N_D = T/\Delta\tau$ where $\Delta\tau$ is the delay bin size), and N_τ is the number of delay samples (Eqn. 2.13). Similarly, the slow fading normalized mean signal energy at the output of the other tone filter (corresponding to a $-\Delta f/2$ tone) for the continuous CIRF case is

$$E_- = \frac{4}{\omega_M^2} \int_0^{\infty} T G(T\zeta) \sin^2\left[\frac{1}{2}\omega_M(\hat{\tau}_D - \zeta)\right] d\zeta \quad |\zeta - \hat{\tau}_D| \leq 1$$

(Slow Fading, Continuous CIRF)

where $\omega_M = 2\pi\Delta f T$ and $\Delta f T$ is the normalized tone spacing (a positive integer). Note that $E_- = 0$ in the limit of flat fading. For a sampled CIRF this equation becomes

$$E_- = \frac{4}{\omega_M^2} \sum_{i=0}^{N_\tau-1} P_i \sin^2\left[\frac{1}{2}\omega_M(\hat{\tau}_D - i/N_D)\right] \quad |i/N_D - \hat{\tau}_D| \leq 1$$

(Slow Fading, Sampled CIRF)

The cross correlation of the voltage out of the two filters is complex because the two-frequency mutual coherence function for trans-ionospheric channels is complex. We show in Appendix F that the noise out of the two filters is uncorrelated for orthogonal signaling and we make the reasonable assumption that the noise is uncorrelated with the fading, so only the signal contributes to the cross correlation. For slow fading, the complex cross correlation coefficient is

$$C = \frac{2(-1)^{\Delta f T + 1}}{\omega_M} \int_0^{\infty} T G(T\zeta) \Lambda[\zeta - \hat{\tau}_D] \sin\left[\frac{1}{2}\omega_M|\zeta - \hat{\tau}_D|\right] e^{-j\Delta f T(\zeta + \hat{\tau}_D)} d\zeta$$

(Slow Fading, Continuous CIRF)

$$C = \frac{2(-1)^{\Delta f T + 1}}{\omega_M} \sum_{i=0}^{N_t-1} P_i \Lambda[i/N_D - \hat{\tau}_D] \sin\left[\frac{1}{2}\omega_M|i/N_D - \hat{\tau}_D|\right] e^{-j\Delta f T(i/N_D + \hat{\tau}_D)} .$$

(Slow Fading, Sampled CIRF)

For the exponential form of the power impulse response function used in this report, the integrals for the continuous CIRF case can be obtained in closed form (see Appendix G for these results). For the sampled CIRF case, the above expressions are evaluated numerically using the expression in Section 2 for P_i .

The BFSK channel bit error rate in slow, frequency selective Rayleigh fading is

$$\langle P_e \rangle = \frac{1}{2} \left[1 - \frac{E_+ - E_-}{\sqrt{(E_+ + E_- + 2/\gamma)^2 - 4(C_R^2 + C_I^2)}} \right] . \quad (4.5)$$

(BFSK, Slow Frequency Selective Fading)

where $\gamma = E_{cb} / N_0$ is the channel bit energy-to-noise spectral density ratio in the absence of fading, and C_R and C_I are the real and imaginary parts of the cross correlation coefficient, respectively.

The expressions for the BFSK demodulation error rate in time and frequency selective fading are sufficiently complex that we have not included delay-tracking effects in this calculation. Without loss of generality, we again assume that the $+\Delta f/2$ tone is transmitted. The normalized signal energy at the output of the filter corresponding to the transmitted tone in time and frequency selective fading is

$$E_+ = 2 \int_0^1 d\zeta TG(T\zeta) \int_0^{1-\zeta} d\xi \rho(T\xi)(1-\zeta-\xi) , \quad (\text{Fast Fading, Continuous CIRF})$$

where $\rho(\cdot)$ is the temporal autocorrelation function of the fading. The signal energy at the output of the other tone filter reduces to the deceptively simple form

$$E_- = 2 \int_0^1 d\zeta TG(T\zeta) \int_0^{1-\zeta} d\xi \rho(T\xi) \cos(\omega_M \xi)(1-\zeta-\xi) .$$

(Fast Fading, Continuous CIRF)

The deception is that closed form expressions for E_- for a continuous CIRF channel with an f^{-6} Doppler frequency spectrum involves a very large number of terms. After considerable manipulation, the real (C_R) and imaginary (C_I) parts of the cross correlation coefficient of the two tone filters reduce to

$$\begin{aligned}
C_R &= -\frac{(-1)^{\Delta f T}}{\omega_M} \int_0^1 TG(T\zeta) R_{CR}(\zeta) d\zeta \\
C_I &= \frac{(-1)^{\Delta f T}}{\omega_M} \int_0^1 TG(T\zeta) R_{CI}(\zeta) d\zeta
\end{aligned}
\tag{Fast Fading, Continuous CIRF}$$

where the time integrals are

$$\begin{aligned}
R_{CR}(\zeta) &= [1 + \cos(\omega_M \zeta)] R_S(\zeta) + \sin(\omega_M \zeta) [R_p(\zeta) + R_C(\zeta)] \\
R_{CI}(\zeta) &= [1 - \cos(\omega_M \zeta)] [R_p(\zeta) + R_C(\zeta)] + \sin(\omega_M \zeta) R_S(\zeta)
\end{aligned}$$

and the integrals $R_S(\zeta)$, $R_C(\zeta)$, and $R_p(\zeta)$ are defined as

$$\begin{aligned}
R_p(\zeta) &= \int_0^{1-\zeta} \rho(T\xi) d\xi \\
R_S(\zeta) &= \int_0^{1-\zeta} \rho(T\xi) \sin(\omega_M \xi) d\xi \quad R_C(\zeta) = \int_0^{1-\zeta} \rho(T\xi) \cos(\omega_M \xi) d\xi
\end{aligned}$$

At this point we have a formal solution to the problem of the BFSK demodulation error rate in fast, frequency selective fading. To obtain an analytic answer, however, one must simply perform the indicated integrals. Therein lies the problem. For the f^{-6} form for the temporal autocorrelation function and the simple exponential form for the power impulse response function, the analytic expression for E_- has *more than 80 terms* unless care is taken to collect together similar factors. The expressions for C_R and C_I are even more unwieldy. The analytic results are given in Appendix G for interested readers.

To compute the BFSK error rate for a sampled CIRF we make the assumption that the channel is sampled with sufficient temporal resolution. In COMLNK the channel is sampled with nominally 40 samples per decorrelation time, which has been shown to accurately reproduce the temporal statistics of the fading [Dana, 1988; Dana, 1993]⁷. When properly sampled in time, the ξ integrals in the expressions above are insensitive to the time sample size, so the difference in these integrals for continuous or sampled CIRFs is the delay variable that is either continuous or discrete.

⁷ The number of samples per decorrelation time is an input to COMLNK via the channel data menu. The default value is 40 samples per τ_0 .

The extension to the sampled CIRF case simply involves replacing the delay integrals with sums over the delay samples. Thus the signal contributions to the tone filter output signal energy are

$$E_+ = 2r^2 \sum_{i=0}^{N_D-1} P_i \int_0^{1-i/N_D} \rho(T\xi) (1 - i/N_D - \xi) d\xi$$

$$E_- = 2r^2 \sum_{i=0}^{N_D-1} P_i \int_0^{1-i/N_D} \rho(T\xi) \cos(\omega_M \xi) (1 - i/N_D - \xi) d\xi$$

(Fast Fading, Sampled CIRF)

where r is the mean signal amplitude, and $N_D = T/\Delta\tau$ is the number of delay samples per symbol. Similarly, the real and imaginary parts of the cross correlation coefficient are

$$C_R = -r^2 \frac{(-1)^M}{2\pi M} \sum_{i=0}^{N_D-1} P_i I_{CR}(i/N_D)$$

$$C_I = r^2 \frac{(-1)^M}{2\pi M} \sum_{i=0}^{N_D-1} P_i I_{CI}(i/N_D)$$

(Fast Fading, Sampled CIRF)

These expressions are evaluated numerically using the analytic expressions for the time integrals derived in Appendix G. Once values for E_+ , E_- , C_R , and C_I are calculated, the expression in Equation (4.5) is used to evaluate the demodulation error rate.

The first set of COMLNK results we generated for comparison with these theoretical results is plotted in Figure 4-17. The ideal BFSK results in the figure are for a sampled CIRF with two delay samples per symbol (the same as COMLNK) and with the indicated ideal delay offset, τ_D/T_{cb} . Because we knew from our theoretical calculations that the ideal delay offset is not zero in frequency selective fading, we generated these simulation results with an *active* delay-lock loop. Indeed the average COMLNK DLL tracking errors for these cases are very close to the ideal delay offsets given in the figure.

The agreement between the COMLNK results and the ideal curves is poor at large values of E_{cb}/N_0 but good at small values. The reason for this discrepancy is the active DLL. In Appendix G we show that the irreducible BFSK error rate is very sensitive to delay offset, and an active DLL with a time-varying delay estimate effectively averages the error rate over a distribution of delay offsets, thereby washing out the dependence of the irreducible error rate on delay offset.

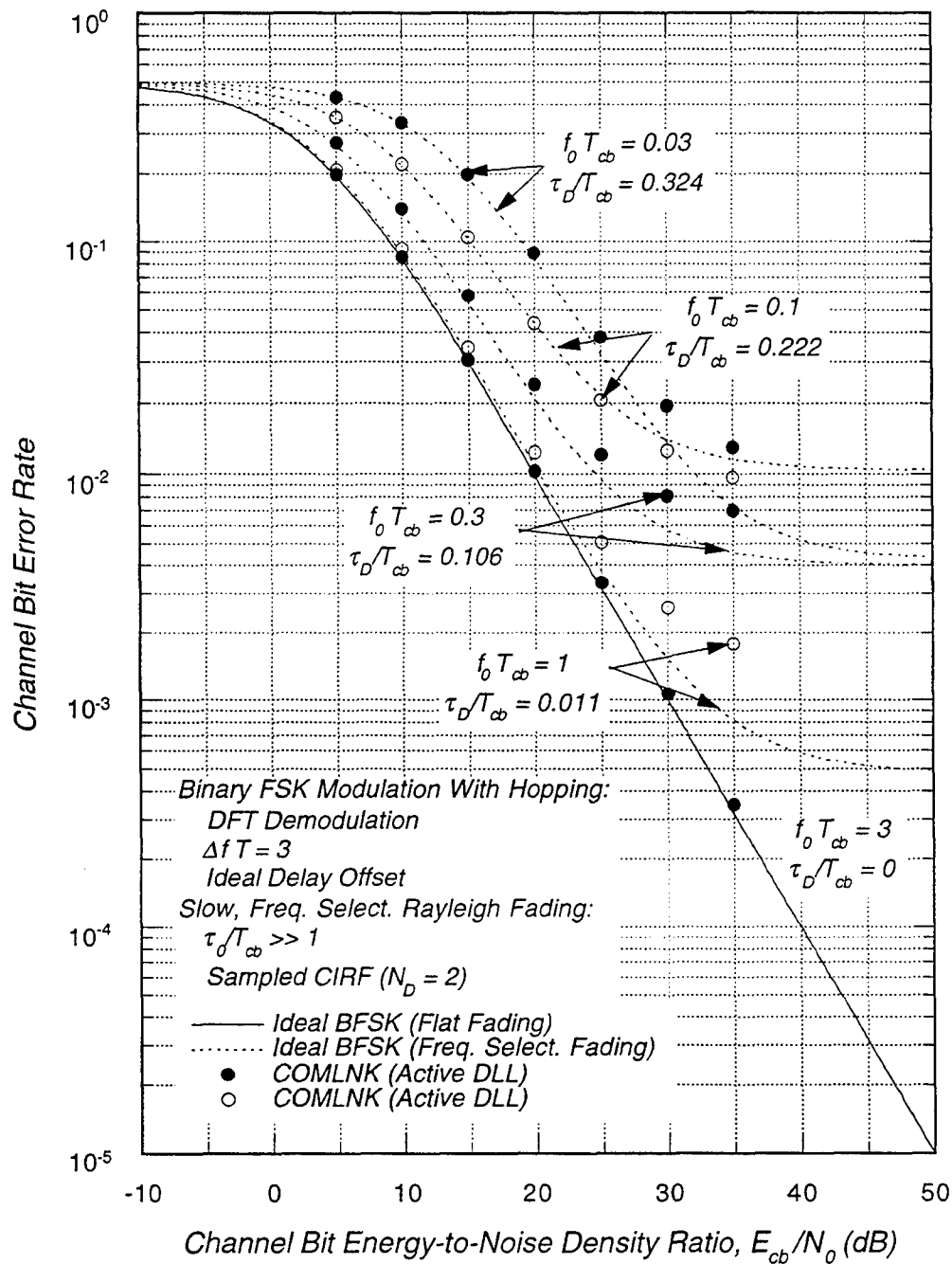


Figure 4-17. BFSK channel bit error rates with hopping and an active DLL in fast, frequency selective fading.

Thus the COMLNK results in Figure 4-17 are monotonically decreasing as $f_0 T_{cb}$ increases whereas the "ideal" results are not monotonic at large signal-to-noise ratios. This is an example of a situation where "ideal" theoretical results will likely never be seen in a real receiver, making these analytic results somewhat of academic interest beyond their utility for simulation validation.

The non-monotonic behavior of the irreducible BFSK error rate with $f_0 T_{cb}$ and ideal delay offset is only seen in the sampled CIRF results given in Appendix G. This behavior results because maximizing the signal energy at the output of the correct tone filter, which is what a DLL is attempting to do, does not necessarily minimize either the signal energy out of the other tone filter or the cross correlation coefficient in frequency selective fading. Thus the ideal delay offset does not necessarily minimize the demodulation error rate.

The problem of comparing COMLNK results with an active DLL to ideal BFSK error rates with a constant delay offset is easily fixed by setting the COMLNK delay offset to a constant value and turning the DLL off. This is accomplished via input, and the results are plotted in Figure 4-18 for several values of $f_0 T_{cb}$.

However, there is yet another problem in comparing ideal and simulation error rate results. The simulation channel model for frequency selective fading and hopped FSK modulation currently limits the decorrelation time to not exceed a value of three times the hop period, so that quasi-independent channel samples will be obtained at different hop frequencies. The channel model reverts to the input value of τ_0 , if it is larger, when the channel is flat fading or when it is selective over the modulation bandwidth. Our theoretical results are either for a slow fading channel with non-zero delay offset, or for a fast fading channel with zero delay offset.

Thus two types of "ideal BFSK" results are plotted in the figure. For $f_0 T_{cb} \leq 0.3$ and for $f_0 T_{cb} = 3$ slow fading ideal results with the indicated delay offsets are plotted. For $f_0 T_{cb} = 1$ the fast fading ideal BFSK result with $\tau_D / T_{cb} = 0$ is plotted. Note that the ideal delay offset for this case is $\tau_D / T_{cb} = 0.011$, which is essentially equal to 0.

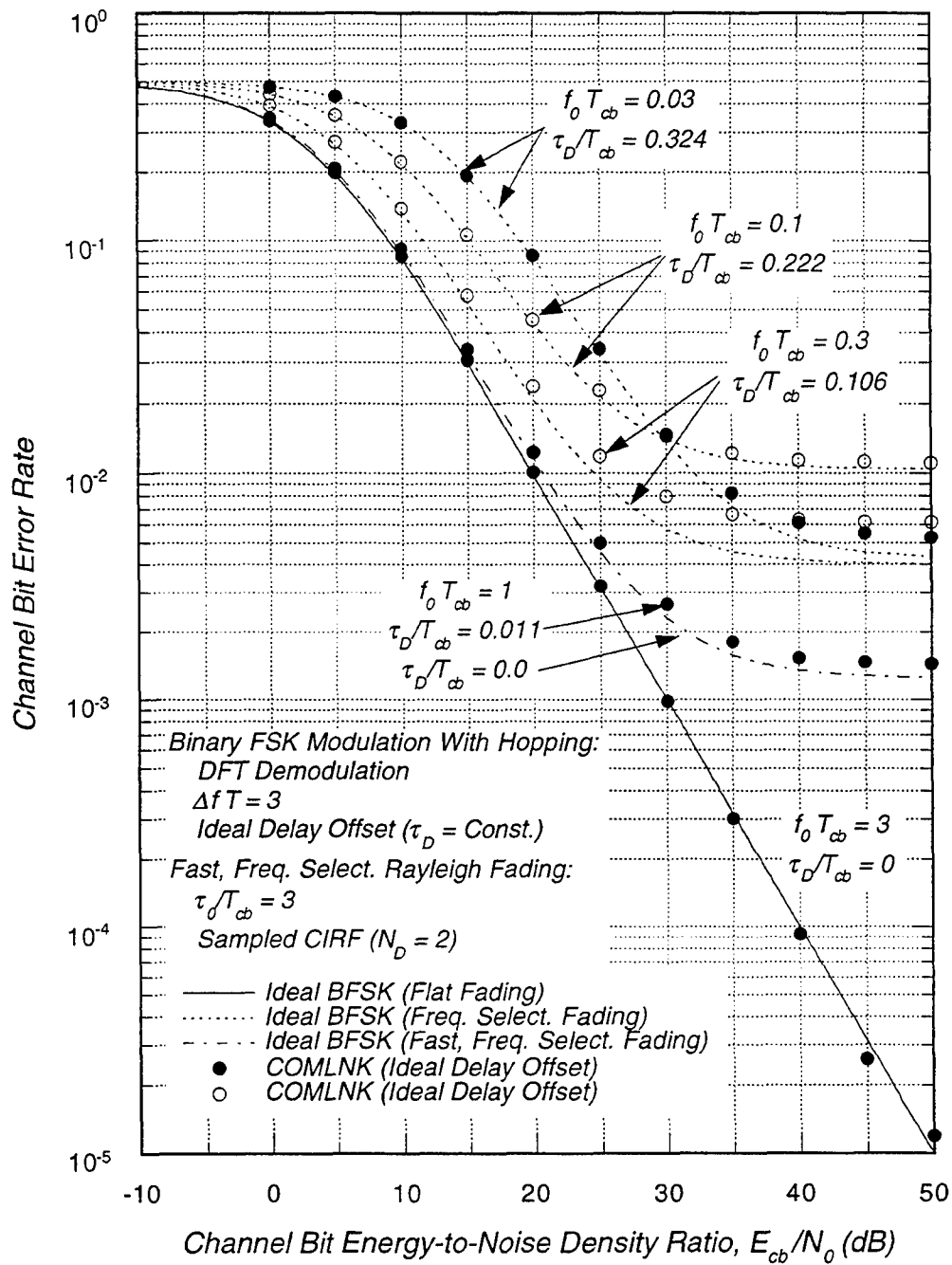


Figure 4-18. BFSK channel bit error rates with hopping and ideal delay offset in fast, frequency selective fading.

When the delay offset in COMLNK is fixed at the ideal value for the sampled CIRF, the agreement between the simulation and ideal results is remarkable. The simulation results for $f_0 T_{cb} = 0.03$ and 0.1 (plotted with open circles to distinguish them from other cases) cross over at large signal-to-noise ratios as do the ideal curves. In addition, the simulation results for $f_0 T_{cb} = 1$ agree very well with the ideal fast fading curve, and the simulation results for $f_0 T_{cb} = 0.03$ and 3 agree very well with the ideal slow fading curves for these cases. Evidently, for a tone spacing of 3 , the effect of fast fading on the demodulation error rate diminishes as f_0 is reduced.

We believe that the small differences between simulation and ideal results for $f_0 T_{cb} = 0.1$ and 0.3 at large values of E_{cb} / N_0 are primarily due to the effects of fast fading that are not in the ideal curves with $\tau_D / T_{cb} > 0$. To verify this conclusion we reran the COMLNK cases with the delay error fixed at zero. These results are plotted in Figure 4-19 and are compared with the ideal fast fading curves. Here the agreement between COMLNK results and the ideal curves is excellent.

For $E_{cb} / N_0 \leq 20$ dB or so, the frequency selective error rate curves in either Figure 4-18 or Figure 4-19 are essentially versions of the flat fading curve shifted to the right by a loss in signal energy at the output of the correct tone filter. Thus for error rates above 0.01 or so, one can estimate the frequency selective BFSK demodulation error rate by applying a matched filter loss to the flat fading error rate curve.

4.3.3 BFSK Performance without Hopping.

The frequency selective fading performance of a BFSK demodulator without frequency hopping differs considerably from the case with frequency hopping. Without hopping, energy from previous symbols is not attenuated by the front-end downconverter and bandpass filters of the receiver because all symbols have the same carrier frequency. Thus there is intersymbol interference (ISI) as energy from previous symbols interferes with the demodulation of the on-time symbol.

A functional block diagram of a non-coherent binary frequency-shift keying (BFSK) receiver is shown in Figure 3-2. The block diagram in this figure is for BFSK with frequency hopping, but the hop synthesizer is disabled here.

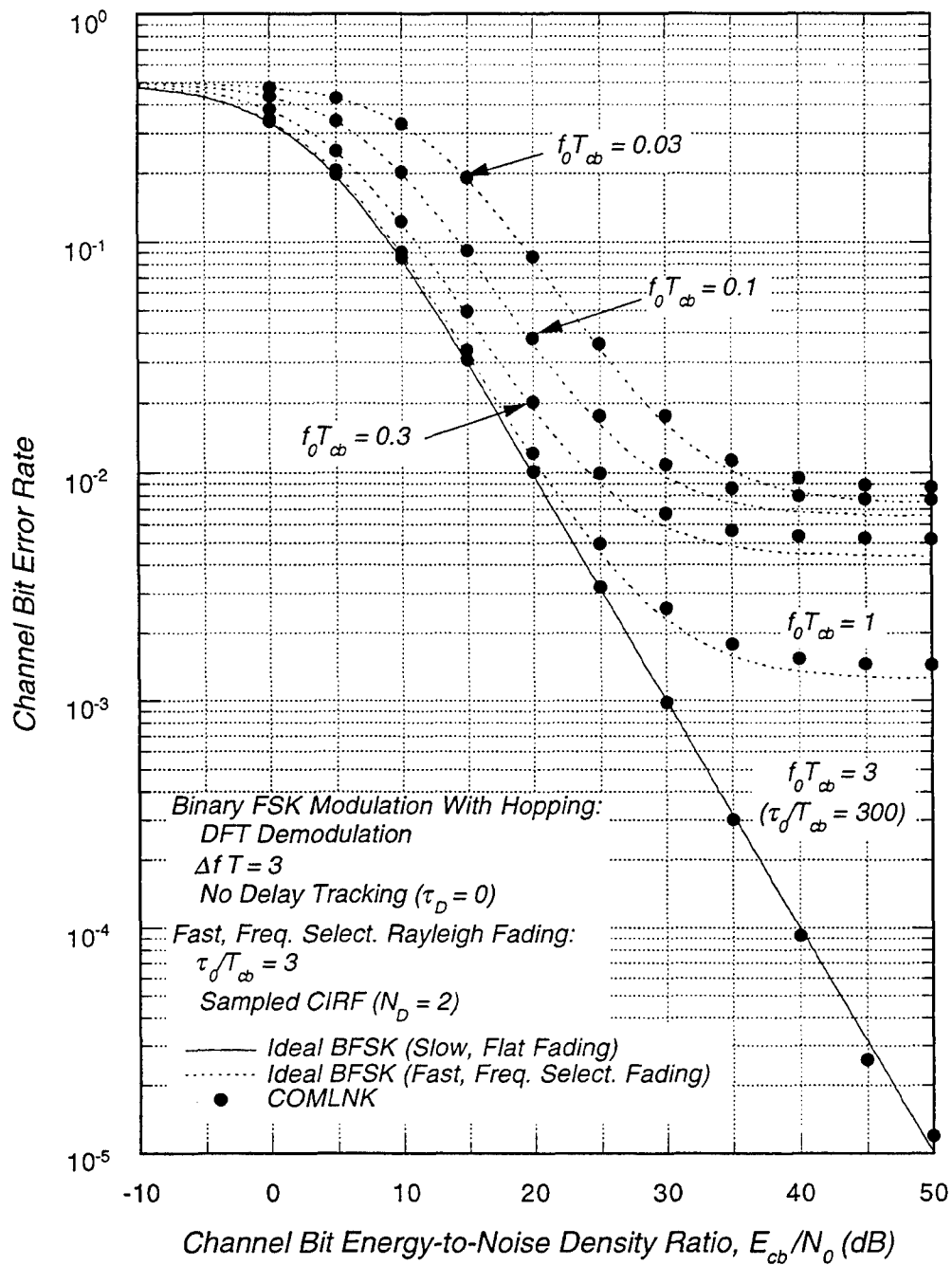


Figure 4-19. BFSK channel bit error rates with hopping and zero delay offset in fast, frequency selective fading.

In Appendix H, we assume that the AGC and AFC tracking loops are operating perfectly and investigate the ideal delay offset in frequency selective fading. Our results show that this ideal offset is a small fraction of a modulation period. Thus we ignore delay tracking in developing expressions for the BFSK demodulation error rate. To simplify the equations somewhat, we also assume slow fading. The resulting BFSK demodulation error rate is sufficient for COMLNK validation, which of course can treat much more complex cases.

Again we assume, without loss of generality, that the $+\Delta f/2$ tone was transmitted during the on-time tone period. The normalized signal contribution to the output energy of the correct tone filter is then given by the following expression derived in Appendix H:

$$E_+ = R_0 - R_1 + \frac{1}{2} R_2 + R_{S,1} + \frac{1}{2} R_{S,2} - R_{S,3} + \frac{1}{2} S_0 (R_0 - R_1 + R_2 + R_{S,1} + R_{S,2} - 2R_{S,3})$$

where

$$S_0 = \frac{e^{-\lambda}}{1 - e^{-\lambda}}.$$

The I integrals in the expression for E_+ and three other integrals that occur in the expressions for the mean signal energy out of the other tone filter and the cross correlation coefficient are

$$\begin{aligned} R_0 &= \int_0^1 TG(T\zeta) d\zeta = 1 - e^{-\lambda} \\ R_1 &= \int_0^1 TG(T\zeta) \zeta d\zeta = \frac{1 - (\lambda + 1)e^{-\lambda}}{\lambda} \\ R_2 &= \int_0^1 TG(T\zeta) \zeta^2 d\zeta = \frac{2 - (\lambda^2 + 2\lambda + 2)e^{-\lambda}}{\lambda^2} \\ R_{S,1} &= \frac{(-1)^{\Delta f T}}{\omega_M} \int_0^1 TG(T\zeta) \sin(\omega_M \zeta) d\zeta = \frac{(-1)^{\Delta f T} \lambda (1 - e^{-\lambda})}{\lambda^2 + \omega_M^2} \\ R_{S,2} &= \frac{4}{\omega_M^2} \int_0^1 TG(T\zeta) \sin^2 \left[\frac{1}{2} \omega_M \zeta \right] d\zeta = \frac{2(1 - e^{-\lambda})}{\lambda^2 + \omega_M^2} \end{aligned}$$

$$R_{S,3} = \frac{(-1)^{\Delta f T}}{\omega_M} \int_0^1 TG(T\zeta) \zeta \sin(\omega_M \zeta) d\zeta = \frac{(-1)^{\Delta f T} \lambda [2\lambda(1 - e^{-\lambda}) - (\lambda^2 + \omega_M^2) e^{-\lambda}]}{(\lambda^2 + \omega_M^2)^2}$$

$$R_{S,4} = \frac{(-1)^{\Delta f T}}{\omega_M} \int_0^1 TG(T\zeta) (1 - 2\zeta) \sin^2\left[\frac{1}{2}\omega_M \zeta\right] d\zeta$$

$$= \frac{(-1)^{\Delta f T} \omega_M [\lambda(\lambda^2 + \omega_M^2)(1 + e^{-\lambda}) - 2(3\lambda^2 + \omega_M^2)(1 - e^{-\lambda})]}{2\lambda(\lambda^2 + \omega_M^2)^2}$$

$$R_{S,5} = \int_0^1 TG(T\zeta) \zeta (1 - \zeta) \sin(\omega_M \zeta) d\zeta$$

$$= \frac{2\lambda \omega_M [\lambda(\lambda^2 + \omega_M^2)(1 + e^{-\lambda}) - (3\lambda^2 - \omega_M^2)(1 - e^{-\lambda})]}{(\lambda^2 + \omega_M^2)^3}$$

$$R_C = \int_0^1 TG(T\zeta) \zeta (1 - \zeta) \cos(\omega_M \zeta) d\zeta$$

$$= \frac{\lambda(\lambda^4 - \omega_M^4)(1 + e^{-\lambda}) - 2\lambda^2(\lambda^2 - 3\omega_M^2)(1 - e^{-\lambda})}{(\lambda^2 + \omega_M^2)^3} ,$$

where closed form expressions for the integrals are obtained using the exponential power impulse response function [Eqn. 2.8]. The latter three integrals are used in subsequent expressions. When the CIRF is sampled, the delay integrals in these expressions are replaced by delay sums, and the R integrals are all of the form

$$R_X = \sum_{i=0}^{N_D-1} P_i I_X(\zeta = i/N_D)$$

where $I_X(\zeta = i/N_D)$ is the function in the continuous CIRF integrals that multiplies the normalized power impulse response function, $TG(T\zeta)$ evaluated as the discrete normalized delay samples i/N_D .

The normalized mean signal energy at the output of the other tone filter is

$$E_- = \frac{1}{2} R_2 + \frac{1}{2} R_{S,2} - R_{S,3} + \frac{1}{2} S_0 (R_0 - R_1 + R_2 + R_{S,1} + R_{S,2} - 2R_{S,3}) ,$$

and, after considerable algebra, the real and imaginary parts of cross correlation of the two tone filters reduce to

$$C_R = \frac{1}{2}(1 + S_0)[R_C - R_{S,1} - R_{S,2} + 2R_{S,3}]$$

$$C_I = \frac{1}{2}(1 + S_0)[2R_{S,4} - R_{S,5}]$$

The BFSK demodulation error rate without hopping in slow, frequency selective Rayleigh fading is again given by the expression in Equation (4.5).

The final comparison of COMLNK results with ideal demodulation error rate curves is shown in Figure 4-20 for BFSK without hopping in slow, frequency selective fading channels. All results in this figure are for the delay offset equal to zero. Without hopping, frequency selective fading produces ISI, and the irreducible demodulation error rate approaches 50 percent for small values of $f_0 T_{cb}$.

Excellent agreement is seen between the simulation results and the ideal error rate curves, validating the frequency selective channel model and BFSK demodulation algorithms within COMLNK.

4.4 SUMMARY.

The process of comparing COMLNK results with ideal demodulation error rate curves has both validated the simulation and produced a number of new insights into the effects of fading on digital communications. In this process, we have generated new analytic results for demodulation error rates in fast and/or frequency selective fading.

The new insights on the performance of digital communications links in fading channels include the following:

- There can be a significant difference between the ideal delay offsets and demodulation error rates in sampled and continuous frequency selective fading;
- The channel delay sampling in the current version of COMLNK may be too coarse for some applications involving small frequency selective bandwidths combined with large signal-to-noise ratios;
- The current DSWA specification for the total signal power in the delay grid should be increased from 97.5 percent to 99.9 percent.

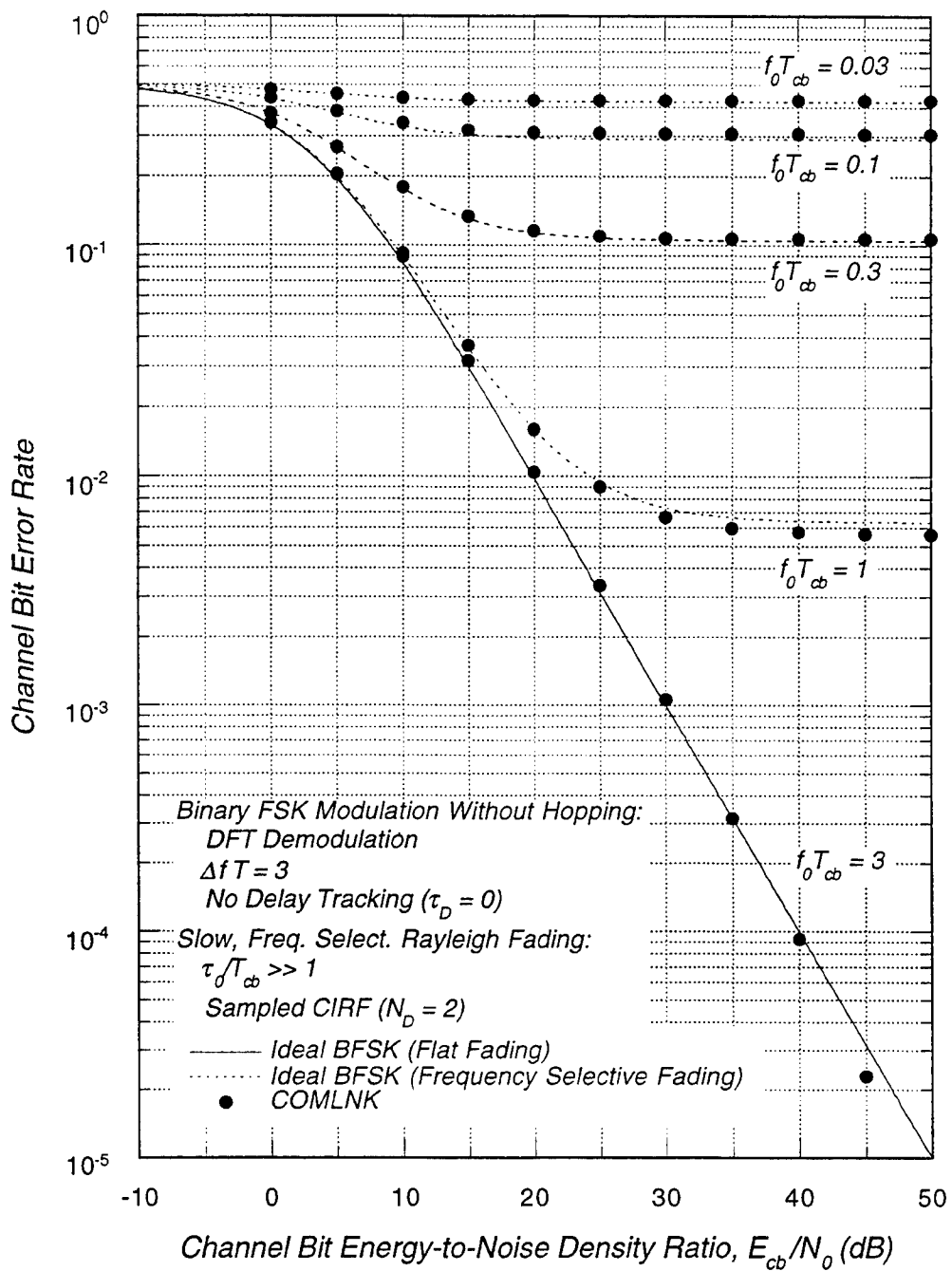


Figure 4-20. BFSK channel bit error rates without hopping and zero delay offset in slow, frequency selective fading.

Now that the demodulation performance of COMLNK has been validated against analytic models and a limited set of test data for phase-shift keying and frequency-shift keying modulation in fast, frequency selective fading channels, the next obvious comparison is that of the output of an error correction decoder with analytic results. Unfortunately, analytic results for Viterbi decoders have been limited to performance bounds, not actual decoded bit error rates. Furthermore, the only *simulation* in COMLNK occurs in constructing the digital samples at the output of the analog-to-digital (A/D) converter, and this part of COMLNK has been verified. After the A/D converter, COMLNK is an *emulation* of a digital communications receiver and is validated by direct comparisons with hardware.

There is a reasonable amount of test data available to compare with COMLNK simulation results for processes that occur after the demodulator. An example is the L_3P receiver scintillation test program conducted with the NELS channel simulator circa 1982 [Bogusch and Guigliano, 1982; Dana, 1995c]. In Figure 4-21 we plot the measured and simulated Viterbi decoder transfer function (*i.e.*, the output decoded bit error rate versus the input demodulated symbol error rate) for two fast fading channels. The demodulated channel bit error rate for these two channels is plotted in Figure 4-21. The solid line in the figure is just a curve fit to the COMLNK data points, generated because it is not possible to analytically describe this transfer function. Again there is remarkable agreement between the COMLNK simulation results and the test data.

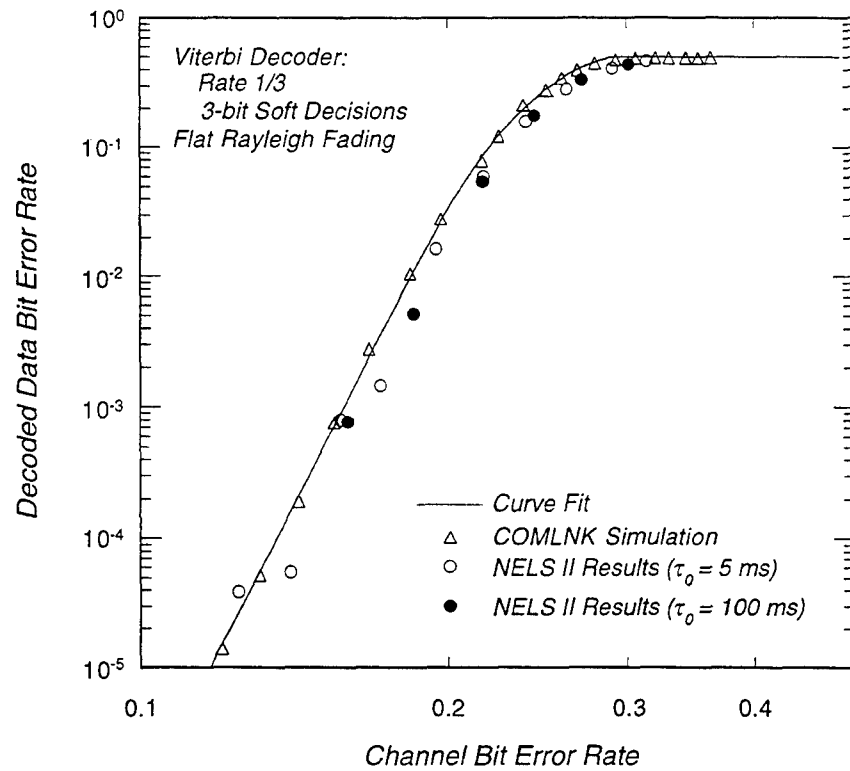


Figure 4-21. Comparison of measured and simulated Viterbi decoder transfer functions for the prototype L_3P receiver.

SECTION 5

REFERENCES

Bello, P., and B. D. Nelin, "Predetection Diversity Combining with Selectively Fading Channels," *IRE Trans. on Communications Systems*, Vol. CS-10, pp. 32-42, March 1962a. (UNCLASSIFIED)

Bello, P., and B. D. Nelin, "The Influence of Fading Spectrum on the Binary Error Probabilities of Incoherent and Differentially Coherent Matched Filter Receivers," *IRE Trans. on Communications Systems*, Vol. CS-10, pp. 160-168, June 1962b. (UNCLASSIFIED)

Bello, P., and B. D. Nelin, "The Effect of Frequency Selective Fading on the Binary Error Probabilities of Incoherent and Differentially Coherent Matched Filter Receivers," *IEEE Trans. on Communications Systems*, Vol. CS-11, pp. 170-186, June 1963. (UNCLASSIFIED)

Bogusch, R. L., F. W. Guigliano, D. L. Knepp, and A. H. Michelet, "Frequency Selective Propagation Effects on Spread-Spectrum Receiver Tracking," *Proc. of the IEEE*, Vol. 69, No. 7, pp. 787-796, July 1981. (UNCLASSIFIED)

Bogusch, R. L., and F. W. Guigliano, *IONDS Receiver Test Briefing*, Mission Research Corporation, unpublished, October 1982. (UNCLASSIFIED)

Bogusch, R. L., *Digital Communications in Fading Channels: Modulation and Coding*, AFWL-TR-87-52, MRC-R-1043, Mission Research Corporation, 1989. (UNCLASSIFIED)

Bogusch, R. L., *Digital Communications in Fading Channels: Tracking and Synchronization*, WL-TR-90-15, MRC-R-1251, Mission Research Corporation, April 1990. (UNCLASSIFIED)

Bogusch, R. L., and A. H. Michelet, *Digital Communications in Fading Channels: Signal Acquisition*, PL-TR-92-1024, MRC-R-1365, Mission Research Corporation, March 1993. (UNCLASSIFIED)

Bogusch, R. L., *Digital Communications in Fading Channels: Computer Aided Design and Evaluation*, DNA-TR-95-120, MRC-R-1504, Mission Research Corporation, May 1996. (UNCLASSIFIED)

Dana, R. A., *Temporal Statistics of Scintillation for Satellite Communication and Radar Systems*, DNA-TR-81-129, MRC-R-692, Mission Research Corporation, April 1982. (UNCLASSIFIED)

Dana, R. A., *Propagation of RF Signals Through Structured Ionization: Theory and Antenna Aperture Effect Applications*, DNA-TR-86-158, MRC-R-976, Mission Research Corporation, May 1986. (UNCLASSIFIED)

Dana, R. A., *Statistics of Sampled Rayleigh Fading*, DNA-TR-89-5, MRC-R-1203, Mission Research Corporation, April 1988. (UNCLASSIFIED)

Dana, R. A., *Propagation of RF Signals Through Structured Ionization: The General Model*, DNA-TR-90-9, MRC-R-1262R, Mission Research Corporation, March 1991 .

Dana, R. A., *ACIRF User's Guide for the General Model (Version 3.5)*, DNA-TR-91-162, MRC-R-1358, Mission Research Corporation, June 1992a. (UNCLASSIFIED)

Dana, R. A., *Temporal Statistics of Non-Rayleigh Fading*, MRC-R-1427, Mission Research Corporation, December 1992b. (UNCLASSIFIED)

Dana, R. A., *Statistics of Sampled Rician Fading*, DNA-TR-92-98, MRC-R-1410, Mission Research Corporation, February 1993. (UNCLASSIFIED)

Dana, R. A., *A Non-Stationary Model for Frequency Selective Channels*, MRC-R-1403R, Mission Research Corporation, September 1994. (UNCLASSIFIED)

Dana, R. A., *Advanced Channel Simulator Qualification Test Plan*, MRC-R-1491, Mission Research Corporation, March 1995a. (UNCLASSIFIED)

Dana, R. A., "Effects of Two-Way Decorrelation on Radar Detection in Scintillation," *IEEE Trans. on Aerospace and Electronic Systems*, Vol. 31, No. 2, pp. 795-804, April 1995b. (UNCLASSIFIED)

Dana, R. A., *A Model of a Direct Sequence Spread Spectrum Differential Phase-Shift Keying Communications Link*, DNA-TR-95-13, MRC-R-1487, Mission Research Corporation, August 1995c. (UNCLASSIFIED)

Dana, R. A., B. R. Milner, R. L. Bogusch, "Effects of Channel Tap Spacing on Delay Lock Tracking," in R. C. Dixon and M. M. Oprysko (Editors), *Wireless Data Transmission*, SPIE Vol. 2601, pp. 197-209, October 1995. (UNCLASSIFIED)

Davis, T. N., G. J. Romick, E. M. Westcott, R. A. Jeffries, D. M. Kerr, and H. M. Peek, "Observations of the Development of Striations in Large Barium Clouds," *Planetary Space Science*, Vol. 22, p.67, 1974. (UNCLASSIFIED)

De Raad, Jr., L. L., and M. K. Grover, *First-Order Intensity Statistics for Non-Rayleigh Fading*, DNA-TR-89-150, R&D Associates, February 1990. (UNCLASSIFIED).

Frasier, S. M., *Private Communication*, Mission Research Corporation, 1996. (UNCLASSIFIED).

Fremouw, E. J., R. L. Leadabrand, R. C. Livingston, M. D. Cousins, C. L. Rino, B. C. Fair, and R. A. Long, "Early Results from the DNA Wideband Satellite Experiment – Complex-Signal Scintillation," *Radio Science*, Vol. 13, pp. 167-187, January-February 1978. (UNCLASSIFIED)

Fremouw, E. J., R. C. Livingston, and D. A. Miller, "On the Statistics of Scintillating Signals," *Journal of Atmospheric and Terrestrial Physics*, Vol. 42, pp. 717-731, 1980 .

Hsiung, C. Y., *Development and Operation of Nuclear Effects Link Simulator*, DSWA-TR-96-84, Lockheed Martin Missiles & Space, September 1997. (UNCLASSIFIED)

Knepp, D. L., "Multiple Phase-Screen Calculation of the Temporal Behavior of Stochastic Waves," *Proc. IEEE*, Vol. 71, pp. 722-737, June 1983a. (UNCLASSIFIED)

Knepp, D. L., "Analytic Solution for the Two-frequency Mutual Coherence Function for Spherical Wave Propagation," *Radio Science*, Vol. 18, No. 4, pp. 535-549, July 1983b. (UNCLASSIFIED)

Marcum, J. L., "A Statistical Theory of Target Detection by Pulsed Radar," *IEEE Transactions on Information Theory*, Vol. IT-6, pp. 59-144, April 1960 .

Nakagami, M., "The m -distribution; A General Formula of Intensity Distribution of Rapid Fading," in W. C. Hoffman (Editor), *Statistical Methods in Radio Propagation*, Pergamon, New York, 1960 .

Nuttall, A. H., *Some Integrals Involving the Q-Function*, NUSC 4297, Naval Underwater Systems Center, April 1972 .

Rice, S. O., "Statistical Properties of a Sine Wave Plus Random Noise," *Bell System Technical Journal*, Vol. 27, pp. 109-1157, January 1948 .

Reinking, T. *Private Communication*, Mission Research Corporation, August 1995 .

Rutherford, R. R., *WEPH-SAT System Models*, GE78TMP-91, General Electric Company, October 1978. (UNCLASSIFIED)

Schwartz, M., W. R. Bennett, and S. Stein, *Communications Systems and Techniques*, McGraw-Hill Book Company, New York, 1966. (UNCLASSIFIED)

Viterbi, A. J., *Principles of Coherent Communication*, McGraw-Hill Book Company, New York, 1966. (UNCLASSIFIED)

Whitney, H. E., J. Aarons, R. S. Allen, and D. R. Seeman, "Estimation of the Cumulative Amplitude Probability Distribution Function of Ionospheric Scintillations," *Radio Science*, Vol. 7, No. 12, pp. 1095-1104, December 1972. (UNCLASSIFIED)

Wittwer, L. A., *A Trans-Ionospheric Signal Specification for Satellite C³ Applications*, DNA 5662D, Defense Nuclear Agency, December 1980. (UNCLASSIFIED)

Wolcott, J. H., D. J. Simons, T. E. Eastman, and T. J. Fitzgerald, "Characteristics of Late-Time Striations Observed During Operation STRESS," in J. M. Goodman (Editor), *Effects of the Ionosphere on Space and Terrestrial Systems*, pp. 602-613, U. S. Government Printing Office, 1978. (UNCLASSIFIED)

Wolfram, S., *The Mathematica Book*, Wolfram Media, Champaign, 1996. (UNCLASSIFIED)

APPENDIX A

DEMODULATION PERFORMANCE OF COHERENT PSK (Δ PSK)

A functional block diagram of a differentially encoded, coherently demodulated phase-shift keying (Δ PSK) receiver is shown in Figure A-1. The data are differentially encoded at the transmitter so that the inherent π -phase ambiguity in suppressed-carrier, coherent PSK demodulation can be resolved at the receiver. A Costas loop is used to track signal phase, so ideally the entire signal is in the in-phase (I) channel. Thus only this channel is used for data demodulation. A delay lock loop (DLL) is used to keep the receiver timing aligned with the bit edges in the received signal. The automatic gain control (AGC) tracking loop keeps the signal within the dynamic range of the analog-to-digital converter and keeps the signal amplitude at the design values of the DLL and Costas tracking loops.

The Δ PSK demodulation metric is

$$\hat{m} = I_k I_{k-1} \quad ,$$

where I_k is the k^{th} sample of the in-phase voltage. When the transmitted signal phase is unchanged from the $k-1$ to k symbol period the sign of \hat{m} should be positive. Conversely, a negative value of \hat{m} indicates a change in the transmitted phase.

After downconversion, the received PSK signal plus noise in a non-fading channel is given by the expression

$$z(t) = [r e^{j(\varphi + \varphi_0)} + n(t)] e^{-j\varphi_c} \quad ,$$

where r and φ are the signal amplitude and phase due to propagation, respectively, φ_0 is transmitted PSK phase ($\varphi_0 = 0$ or π randomly), and φ_c is the phase correction generated by the Costas tracking loop.

The complex voltage $n(t)$ is additive white Gaussian noise (AWGN) with the usual properties:

$$\begin{aligned} \langle n(t) \rangle &= 0 \\ \langle n(t_1) n(t_2) \rangle &= 0 \quad , \\ \langle n(t_1) n^*(t_2) \rangle &= N_0 \delta(t_1 - t_2) \end{aligned}$$

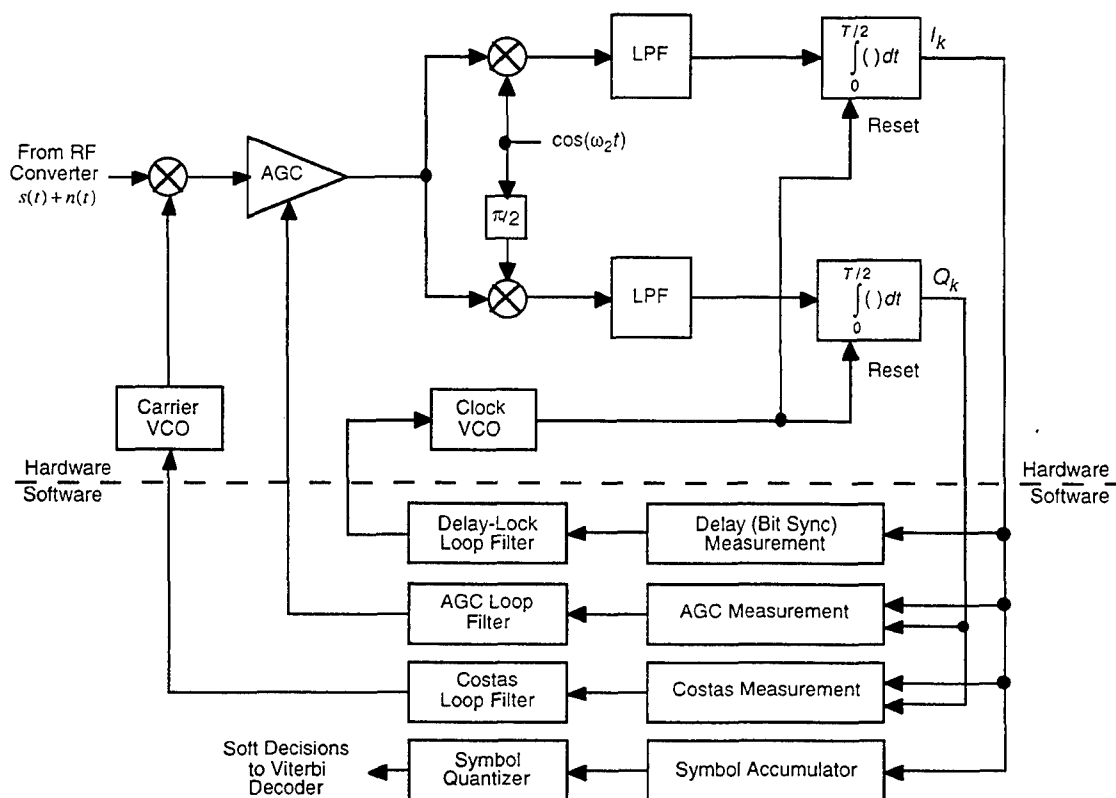


Figure A-1. Block diagram of a coherent PSK receiver.

where N_0 is the one-sided noise power spectral density. The middle of these equations results because the real and imaginary parts of $n(t)$ are uncorrelated. The noise contribution to $z(t)$, $n(t)e^{-j\varphi_c}$, has exactly the same statistical properties as does $n(t)$.

Assuming that the Costas phase tracking loop is operating perfectly (*i.e.*, the loop tracks the signal phase due to propagation but not the transmitted modulation so $\varphi_c = \varphi$), the received signal contribution to $z(t)$ is just $\pm r$.

The voltage $z(t)$ is integrated over a sample period (equal to one-half the symbol period T in this case) to produce the I and Q samples. The two samples per modulation period are coherently summed to give the signal used for demodulation:

$$Z_k = \frac{1}{T} \int_{(k-1/2)T+\tau_D}^{(k+1/2)T+\tau_D} z(t) dt ,$$

where τ_D is the DLL delay tracking error, and I_k and Q_k are the real and imaginary parts of Z_k , respectively. For this calculation we will assume that the delay tracking error is small compared to T and can be ignored¹. The real part of Z_k is then

$$I_k = \pm r + \text{Re}(N_k) , \quad (\text{A.1})$$

where

$$N_k = \frac{1}{T} \int_{(k-1/2)T}^{(k+1/2)T} n(t) e^{-j\phi_c} dt$$

is the sampled noise. The noise contribution to I_k , $\text{Re}(N_k)$, is a zero-mean, normally distributed random variable with variance $N_0 / (2T)$. An expression similar to Equation (A.1) holds for I_{k-1} .

Assuming that the transmitted modulation is unchanged, the channel bit (or demodulation) error rate is given by the probability that \hat{m} is negative. Because the noise from one sample to the next is uncorrelated and independent, the probability density function of \hat{m} can be obtained from the formula for the product of two independent random variables. Integrating the resulting expression over negative values yields the familiar expression for the Δ PSK channel bit error rate in AWGN:

$$P_e = \text{erfc}[\sqrt{E_{cb} / N_0}] \left\{ 1 - \frac{1}{2} \text{erfc}[\sqrt{E_{cb} / N_0}] \right\} ,$$

where E_{cb} / N_0 is the channel bit energy-to-noise spectral density ratio ($r^2 T / N_0$), and $\text{erfc}(\cdot)$ is the complementary error function:

$$\text{erfc}(x) = \frac{2}{\sqrt{\pi}} \int_x^{\infty} e^{-t^2} dt .$$

In very slow fading, slow enough that the Costas loop maintains phase lock on the signal, the average demodulation error rate is

¹ Ideally, the tracking thresholds are well below the data demodulation threshold, so tracking errors are small whenever the demodulation error rate is less than 50 percent. However, when a modified Costas loop is used, as in most modern receivers, then even in a well-designed receiver the tracking loop threshold will be closely related to the demodulation threshold, as discussed by *Bogusch* [1990].

$$\langle P_e \rangle = \int_0^{\infty} P_e(\gamma S) f(S) dS ,$$

where γ is the nominal value of E_{cb} / N_0 , and $f(S)$ is the probability density function of the fading power S (with $\langle S \rangle$ set to unity). For Rician fading, $f(S)$ is given by Equation (2.2b) with S_0 set to unity. The resulting integral must be done numerically. However, a closed form expression is available for Rayleigh fading:

$$\langle P_e \rangle = \frac{1}{2} - \frac{\pi - 2 \tan^{-1}(\sqrt{1 + \gamma^{-1}})}{\pi \sqrt{1 + \gamma^{-1}}} . \quad (\text{Rayleigh Fading})$$

The Δ PSK channel bit error rate for Rician fading is plotted in Figure A-2 for several values of the scintillation index ($S_4 = 0, 0.25, 0.5, 0.75$, and 1). These curves show that an additional 35 dB of signal power is required to maintain a 10^{-5} error rate as the channel varies from non-fading to slow Rayleigh fading.

For Rayleigh fading channels with finite decorrelation times, Δ PSK demodulation performance is limited by the ability of the Costas loop to maintain phase lock on the signal, as shown by COMLNK results plotted in Figure A-3. Here the channel bit period T_{cb} is equal to the symbol period T . For finite values of τ_0 / T_{cb} and large values of E_{cb} / N_0 , the channel bit error rate approaches an irreducible value determined by the frequency of loss-of-lock or phase slip events.

Increasing the bandwidth B_L of the Costas tracking loop, thereby making the loop more responsive to the phase fluctuations caused by fading, can reduce the frequency of phase slips. However, a loop that is too responsive will begin to track the PSK modulation, wiping out the desired data in the process.

Because Δ PSK demodulation performance in fast fading depends on the Costas loop tracking performance, which is highly non-linear, we do not believe that it is possible to compute ideal fast fading performance analytically. This renders Δ PSK modulation useless for analytic validation of any simulation in fading channels. However, differentially coherent PSK demodulation (DPSK) is much more robust in fast fading because it does not require phase tracking, and for this demodulation technique fast fading analytic results are available.

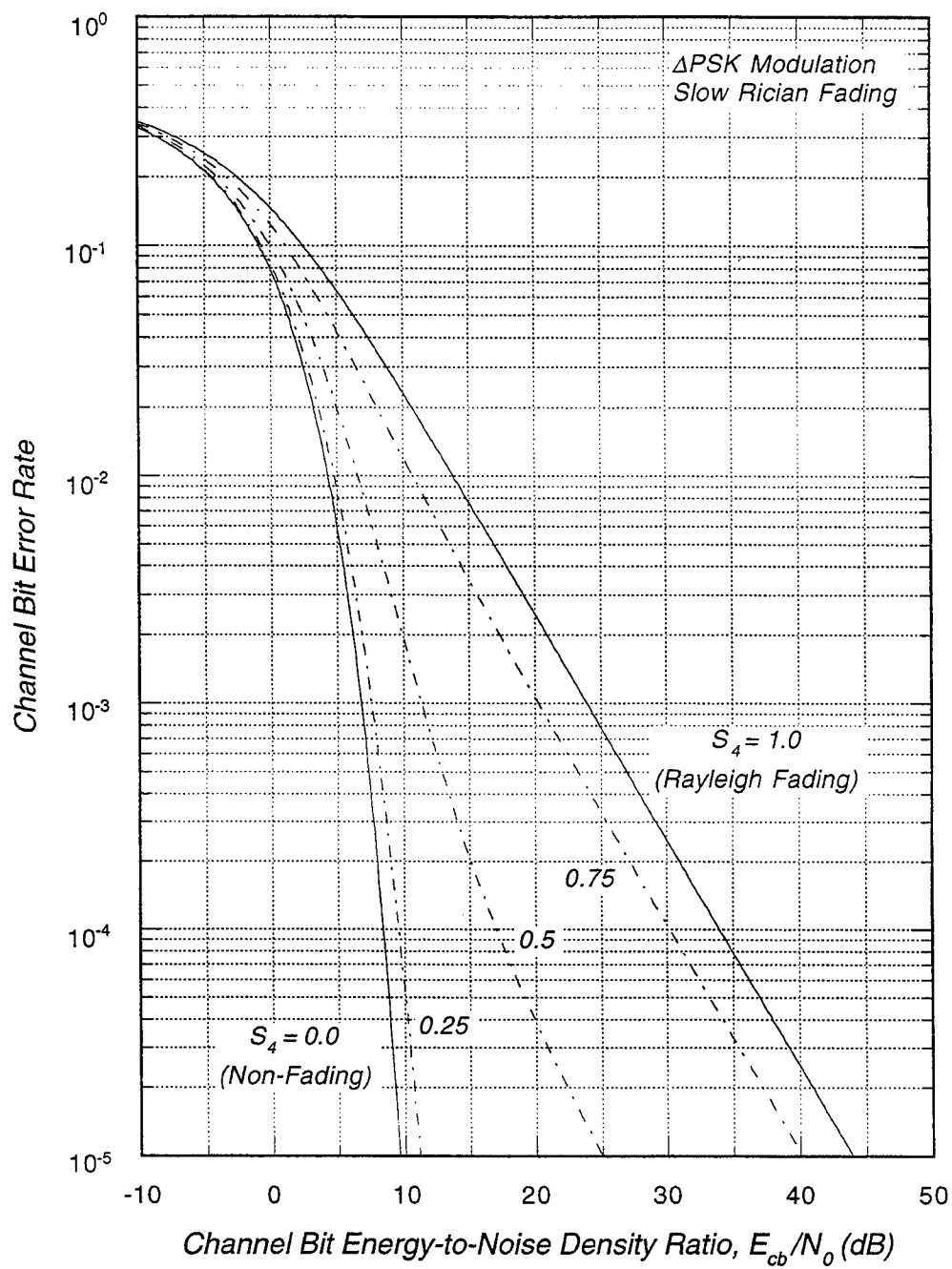


Figure A-2. Δ PSK channel bit error rate for slow Rician fading.

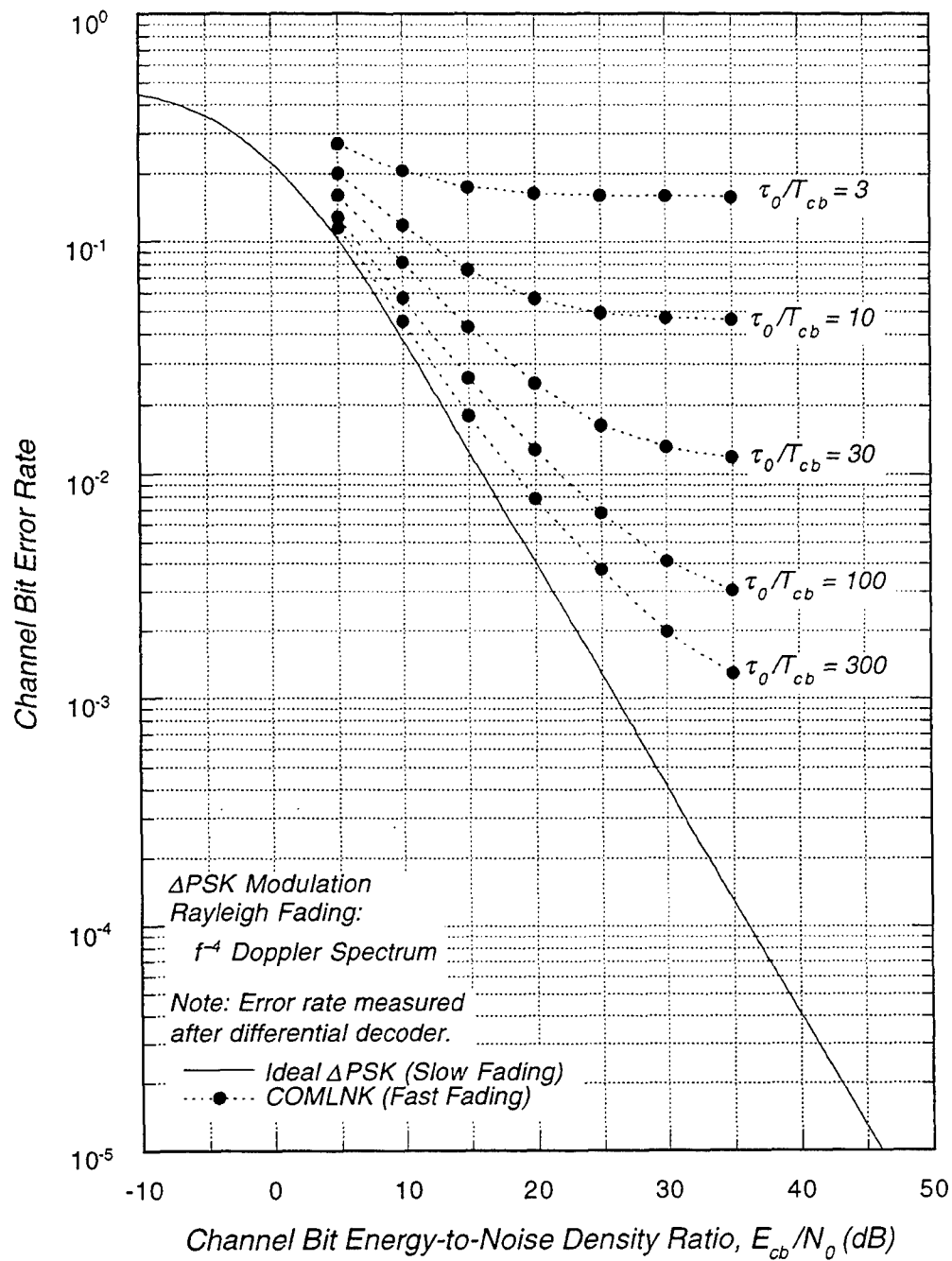


Figure A-3. Δ PSK channel bit error rate for fast Rayleigh fading.

APPENDIX B

DEMODULATION PERFORMANCE OF DIFFERENTIALLY COHERENT PSK (DPSK) WITH AN UNDERLYING SPREAD SPECTRUM CODE

A functional block diagram of a differentially coherent phase-shift keying (DPSK) receiver with an underlying direct sequence (DS) pseudo-noise (PN) code is shown in Figure B-1. The transmitted data are differentially encoded so that differentially coherent demodulation can be used. Thus the frequency but not the phase of the received signal needs to be tracked. This eliminates the primary failure mechanism of a coherent PSK receiver in a fading channel — loss of phase lock.

The receiver has two code correlators (labeled early/late and on-time): one for the delay lock loop (DLL) and one for all other functions. Delay tracking is accomplished by measuring the code correlator output energy with the PN code either one-half chip early or one-half chip late relative to that in the on-time code correlator. The DLL attempts to equalize the energy of the early and late measurements.

In this appendix we show that, because of the underlying PN code, time selective and frequency selective fading effects are decoupled in the output of the code correlator, thereby reducing the demodulation problem to that of DPSK performance in fast fading with a code correlator loss caused by frequency selective fading. The code correlator loss is determined by the severity of the frequency selective fading and the DLL tracking performance.

In COMLNK or in hardware channel simulators the channel impulse response function (CIRF) must be sampled in time and delay. Our results show that if the sampling in time is sufficient to accurately reproduce the temporal statistics of the fading, then the time sampling is also sufficient to accurately measure DPSK demodulation performance. We also show that the optimum delay offset in frequency selective fading is quite sensitive to the delay sampling interval, and in this dimension the channel sampling in either a simulation or a hardware channel simulator can be rather coarse.

In Section B.1 of this appendix we derive the output of the code correlators in terms of the channel impulse response function and the PN code autocorrelation function to show the separation of time and frequency selective fading effects. Next the delay tracking offset of an idealized delay tracking loop is computed for both continuous and sampled channel impulse response functions. The ideal delay offset of the receiver's PN code is between zero and one chip late, depending on the severity of the

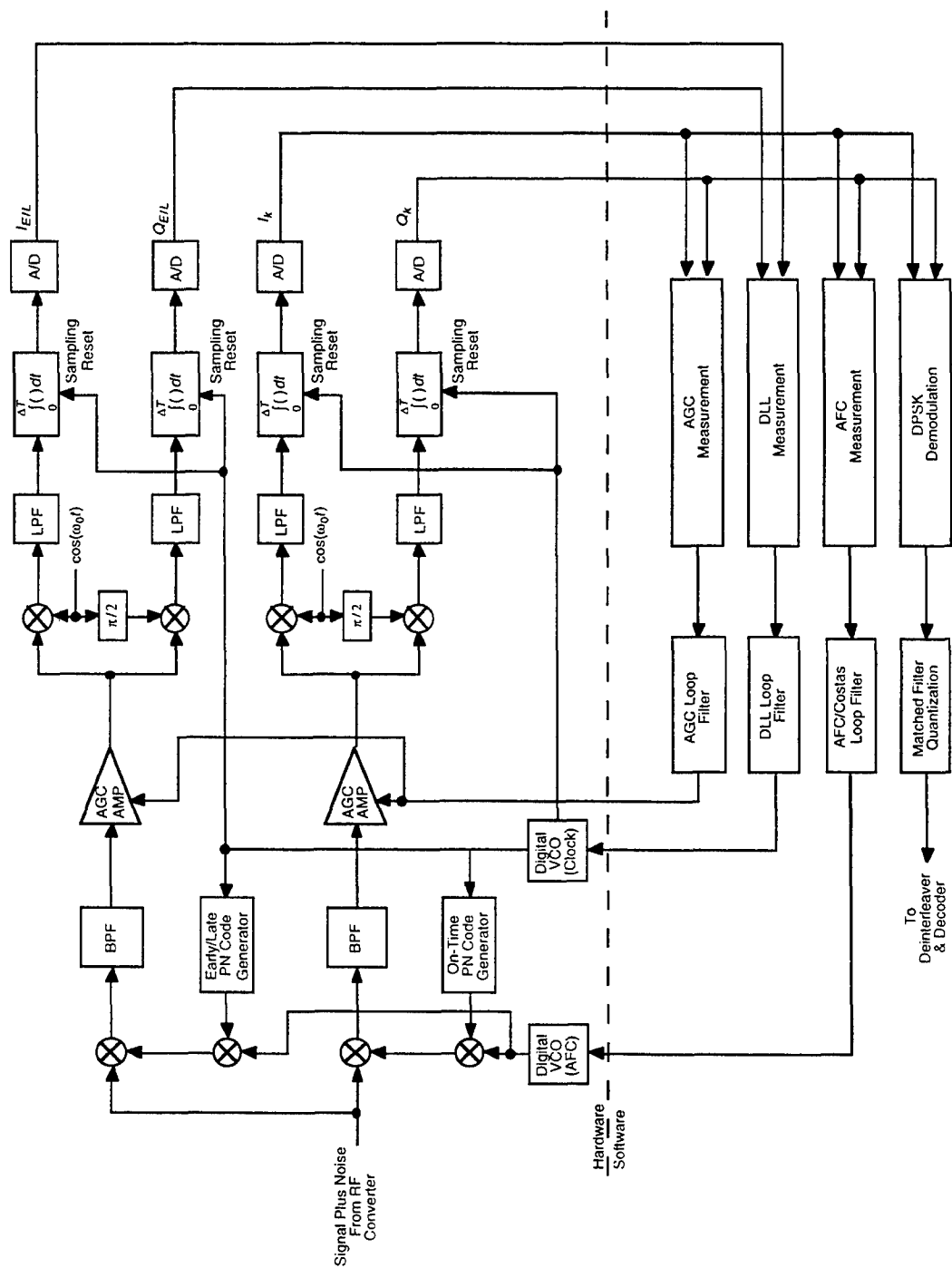


Figure B-1. Block diagram of a spread spectrum DPSK receiver.

frequency selective fading, relative to the ideal position in a non-fading or flat fading channel. Then the loss of signal energy at the output of the code correlator is computed. DPSK demodulation performance in non-fading, slow fading, and fast fading channels is computed in Section B.2. New results on the effect of time sampling of the channel on DPSK demodulation performance and on signal energy at the output of the code correlator are presented in Section B.3. We show that the demodulation performance is insensitive to the "coarseness" of the time sampling. However, the output signal energy is sensitive to the temporal sampling interval, but only for fast fading where the demodulation error rate is near 50 percent.

B.1 CODE CORRELATOR OUTPUT.

Under frequency selective fading conditions, the code correlator in a pseudo-noise direct sequence spread spectrum (DS/SS) receiver loses signal energy because of the time-of-arrival jitter or delay spread of the received signal. Signal energy that arrives more than one chip late relative to the local PN code generator (or more than one chip early if the code delay tracking loop is late by a chip or more) will not correlate with the local PN code and will be severely attenuated.

B.1.1 Fading Signal Out of PN Code Correlator.

Consider a transmitted PN waveform:

$$m(t) = \sum_k m_k \Pi \left[\frac{t}{T_C} - k \right]$$

where $m_k = \pm 1$ pseudo-randomly is the PN chip modulation, and T_C is the chip period. The rectangular function $\Pi(x)$ is defined as

$$\Pi(x) = \begin{cases} 1 & \text{for } |x| < \frac{1}{2} \\ 0 & \text{otherwise} \end{cases}$$

An ideal PN sequence has a triangular autocorrelation function:

$$\lim_{T \rightarrow \infty} \frac{1}{T} \int_{-T/2}^{+T/2} m(t) m^*(t + \tau) dt = \Lambda(\tau / T_C)$$

where

$$\Lambda(x) = \begin{cases} 1-|x| & \text{for } |x| < 1 \\ 0 & \text{otherwise} \end{cases}.$$

For binary phase-shift keying modulation considered in this appendix, the information bearing transmitted signal is $e^{j\varphi_0} m(t)$ where φ_0 is either 0 or π . By writing the transmitted signal as a product of a phasor $e^{j\varphi_0}$ and the PN sequence, it is assumed that the phasor varies slowly relative to the duration of a chip, or equivalently, that the number of chips in a channel bit modulation period is large.

The signal at the input to the PN code correlator is the convolution of the channel impulse response function and the transmitted modulation:

$$u(t) = r e^{j\varphi_0} \int_0^\infty m(t-\tau) h(t,\tau) d\tau$$

where r is the received signal amplitude. This received signal is then correlated with a locally generated version of the transmitted PN sequence and sampled. The complex signal at the output of the code correlator is a function of time and the delay error of the local PN code generator relative to the received signal PN code, τ_D :

$$s(t, \tau_D) = \frac{1}{T_S} \int_{t-T_S/2+\tau_D}^{t+T_S/2+\tau_D} m^*(\xi - \tau_D) u(\xi) d\xi,$$

where T_S is the code correlator sample period, and $m^*(t)$ is the locally generated PN code. Subsequently, we will assume that the delay error is on the order of a chip period or less and thus is a small fraction of the sample period (*i.e.*, $|\tau_D| \ll T_S$). Therefore edge effects can be ignored in the limits of integration. Upon substituting the expression for the input signal, the output signal becomes

$$s(t, \tau_D) = r e^{j\varphi_0} \int_0^\infty d\tau \frac{1}{T_S} \int_{t-T_S/2}^{t+T_S/2} d\xi h(\xi, \tau) m^*(\xi - \tau_D) m(\xi - \tau). \quad (\text{B.1})$$

We are implicitly assuming that the receiver is tracking the frequency of the received signal well enough that any residual frequency error does not result in significant phase rotation during a sample period. This also implicitly assumes a slow fading channel.

The channel impulse response function occurs in the second integral of this equation. Without this term in the integrand, the second integral is just the triangle function. For a moment consider that the channel decorrelation time τ_0 is large compared to the sample period T_S . Then $h(\xi, \tau)$ is slowly varying in time over the sample period and can be pulled out of the second integral. As long as there are a large number of chip periods within a sample period (say 100 or more), then the second integral is essentially the triangle function, and the output signal can be written as

$$s(t, \tau_D) = r e^{j\phi_0} \int_0^{\infty} h(t, \tau) \Lambda(\tau_D - \tau) d\tau \quad (\tau_0 > T_S \gg \tau_D) \quad (\text{B.2})$$

The fading statistics of the sampled signal at the output of the code correlator can now be determined. Under Rayleigh fading conditions, the channel impulse response function is a complex, zero-mean, normally distributed random process. Thus the integrand and the integral are also complex, zero-mean, normally distributed random processes.

For convenience in further developments, the integral in Equation (B.2) is defined as the combined channel and code correlator response function, $h_C(t, \tau_D)$:

$$h_C(t, \tau_D) = \int_0^{\infty} h(t, \tau) \Lambda(\tau_D - \tau) d\tau \quad (\text{B.3})$$

Under the turbulent model, the signal at all delays varies at the same rate, so the fading rate of the code correlator output is independent of the value of τ_D .

Before proceeding with the calculation of the code correlator output energy, we need to consider the effects of fast fading on the output signal. When the decorrelation time is comparable to or less than the modulation period T (also referred to in this report as the channel bit period) of the transmitted DPSK signal, we can imagine super-sampling the output of the code correlator at faster and faster rates until the sample time is less than τ_0 , and Equation (B.3) applies. The number of super-samples per channel bit period is just $n = T/T_S$. These n super-samples are then coherently summed to obtain the code correlator output voltage for the k^{th} channel bit period:

$$S_k(\tau_D) = \frac{1}{n} \sum_{l=k-n/2}^{k+n/2-1} s(l T_S, \tau_D) \quad .$$

In the limit that the number of super-samples per channel bit is large, this summation can be replaced by an integral over the channel bit period:

$$S_k(\tau_D) = r e^{j\varphi_k} \frac{1}{T} \int_{(k-1/2)T}^{(k+1/2)T} h_C(t, \tau_D) dt \quad (\text{B.4})$$

where φ_k is the transmitted DPSK modulation during the k^{th} channel bit period.

When the fading is slow, the decorrelation time is large compared to T . In this case the output signal is just $r e^{j\varphi_0} h_C(kT, \tau_D)$. However, when the fading is fast (*i.e.*, when $\tau_0 \leq T$), the combined channel and code correlator response function will vary within the integral, and the full signal-to-noise ratio gain of the PN code is not realized. The effects of fast fading on DPSK demodulation performance are computed in Sections B.2 and B.3.

The point of this digression is that frequency selective fading effects can be treated separately from fast fading effects as long as the number of chips per decorrelation time is large. This is not a very restrictive limitation because the real question in which we are interested (Does the link operate?) is easy to answer when τ_0 is comparable to T_C . (It does not.) The loss in code correlator output signal energy due to frequency selective fading is computed from Equation (B.3). When there are a sufficient number of chips per sample, this loss does not depend on the integration period of the code correlator *per se*, but only on the time-of-arrival jitter relative to the duration of a chip. The number of chips per sample must be large enough that the autocorrelation of the PN code is essentially a triangle. After the received signal is multiplied by the locally generated PN code to remove the spread spectrum modulation, the resultant “de-spread” voltage is flat fading because signal energy arriving early or late by $\pm 1/2$ chip or more is severely attenuated by the correlation process. This de-spread signal, with mean energy reduced by the code correlator loss, is then coherently integrated over the channel bit period. The fast fading loss of the signal is computed from Equation (B.4), and depends on the decorrelation time of the de-spread signal relative to the channel bit period.

A limitation of separately evaluating the effects of frequency and time selective fading is that we implicitly assume the turbulent model by ignoring the effect of the code correlator on the decorrelation time of the output. This is not a fundamental limitation because one could determine the decorrelation time of $h_C(t, \tau_D)$ as a func-

tion of τ_D and f_0 . However, this level of detail is more appropriate for COMLNK than it is for an analytic model.

B.1.2 Ideal Delay Offset and Code Correlator Loss.

So far, we have considered only continuous channel impulse response functions (CIRFs). However, in COMLNK and in hardware channel simulators the CIRF is sampled in time and delay. For the moment we will assume that the CIRF is sampled in time with sufficient resolution that temporal sampling effects are negligible¹. The sampling in delay, however, can be relatively coarse, and sampling effects can not be neglected in comparing analytic and COMLNK results. For the DS/SS systems considered here, the effects of sampling are seen primarily in the performance of the DLL. Both sampled and continuous CIRFs are considered in calculating the ideal delay offset in frequency selective fading.

In a DS/SS receiver early and late signal samples are generated by code correlators² using an early and late version of the locally generated PN code. If we assume that the receiver advances or retards its locally generated PN code to match that of the received signal and integrates over a fixed sample period T_S , then the early, on-time, and late signal samples out of the code correlators can be written as

$$\begin{aligned} S_E &= \frac{1}{T_S} \int_{t-T_S/2}^{t+T_S/2} m^*(\xi - \tau_D + T_C / 2) u(\xi) d\xi \\ S_O &= \frac{1}{T_S} \int_{t-T_S/2}^{t+T_S/2} m^*(\xi - \tau_D) u(\xi) d\xi \\ S_L &= \frac{1}{T_S} \int_{t-T_S/2}^{t+T_S/2} m^*(\xi - \tau_D - T_C / 2) u(\xi) d\xi \end{aligned}$$

¹ Dana [1988, 1993] discusses the requirements on the temporal sampling necessary to achieve accurate temporal statistics of the fading (e.g., mean duration and separation). The effects of temporal sampling on signal power and DPSK demodulation performance are discussed in Section B.3 of this appendix.

² Usually the early and late voltages are generated by the same code correlator that is time-shared between the two measurements.

Note that the early sample is formed by correlating the received voltage with the local PN code advanced in time by one-half chip period, and the late sample is formed by correlating the received signal with the local PN code delayed by one-half chip relative to the on-time code.

The combined response of a sampled channel and the code correlator can be written as a discrete sum:

$$h_C(t, \tau_D) = \sum_{i=0}^{N_\tau-1} h(t, i\Delta\tau) \Delta\tau \Lambda(\tau_D - i\Delta\tau) ,$$

where $\Delta\tau$ is the delay sample size, and N_τ is the number of delay samples (see Eqn. 2.13). In further developments $h_i(t)$ is used as a short hand notation for $h(t, i\Delta\tau) \Delta\tau$. The channel impulse response function is delta-correlated in delay (*i.e.*, it represents a wide-sense stationary process in frequency), so $h_i(t)$ has the following properties:

$$\begin{aligned} \langle h_i(t) \rangle &= 0 \\ \langle h_i(t) h_k(t) \rangle &= 0 , \\ \langle h_i(t) h_k^*(t) \rangle &= P_i \delta_{i,k} \end{aligned}$$

where P_i is the mean power in each delay sample (see Eqn. 2.14), and $\delta_{i,k}$ is the Kronecker delta symbol:

$$\delta_{i,k} = \begin{cases} 1 & \text{if } i = k \\ 0 & \text{otherwise} \end{cases} .$$

The second of these equations arises because the real and imaginary parts of the channel impulse response function are uncorrelated.

Assuming slow fading (*i.e.*, $\tau_0 \gg T_S$) so the channel impulse response function is time-invariant during the sample period, the early code correlator output sample is

$$S_E = \sum_{i=0}^{N_\tau-1} h_i(t) \frac{1}{T_S} \int_{t-T_S/2}^{t+T_S/2} d\xi m^*(\xi - \tau_D + T_S/2) m(\xi - i\Delta\tau) .$$

Similar expressions hold for the on-time and late samples. If the number of chips per sample period is large ($T_S \gg T_C$), the second integral is just the autocorrelation func-

tion of the PN code which is assumed to be a perfect triangle. Thus the early, on-time, and late signal samples can be written as

$$\begin{aligned} S_E &= \sum_{i=0}^{N_\tau-1} h_i \Lambda \left[\frac{\tau_D - i\Delta\tau}{T_C} - \frac{1}{2} \right] \\ S_O &= \sum_{i=0}^{N_\tau-1} h_i \Lambda \left[\frac{\tau_D - i\Delta\tau}{T_C} \right] \\ S_L &= \sum_{i=0}^{N_\tau-1} h_i \Lambda \left[\frac{\tau_D - i\Delta\tau}{T_C} + \frac{1}{2} \right] \end{aligned}$$

The corresponding mean energy of the early, on-time, and late samples for sampled and continuous channel impulse response function are

$$\left. \begin{aligned} \langle E_E \rangle &= \sum_{i=0}^{N_\tau-1} P_i \Lambda^2 \left[\frac{\tau_D - i\Delta\tau}{T_C} - \frac{1}{2} \right] \\ \langle E_O \rangle &= \sum_{i=0}^{N_\tau-1} P_i \Lambda^2 \left[\frac{\tau_D - i\Delta\tau}{T_C} \right] \\ \langle E_L \rangle &= \sum_{i=0}^{N_\tau-1} P_i \Lambda^2 \left[\frac{\tau_D - i\Delta\tau}{T_C} + \frac{1}{2} \right] \end{aligned} \right\} \quad \text{(Sampled CIRF)}$$

$$\left. \begin{aligned} \langle E_E \rangle &= \int_0^\infty G(\tau) \Lambda^2 \left[\frac{\tau_D - \tau}{T_C} - \frac{1}{2} \right] d\tau \\ \langle E_O \rangle &= \int_0^\infty G(\tau) \Lambda^2 \left[\frac{\tau_D - \tau}{T_C} \right] d\tau \\ \langle E_L \rangle &= \int_0^\infty G(\tau) \Lambda^2 \left[\frac{\tau_D - \tau}{T_C} + \frac{1}{2} \right] d\tau \end{aligned} \right\} \quad \text{(Continuous CIRF)}$$

A DLL attempts to equalize the energy in the early and late measurements, so the ideal delay offset is obtained by solving the equation $\langle E_E \rangle = \langle E_L \rangle$ for τ_D . Plots of the early and late energy for continuous and sampled CIRFs with four samples per chip ($N_D = T_C / \Delta\tau = 4$) are in Figure B-2. The frequency selective bandwidth for these plots is one-tenth of the PN chip rate. The ideal delay offset is the value of τ_D / T_C where the early and late curves cross. It is apparent from the figure that the ideal value for a sampled CIRF is slightly smaller than that for a continuous CIRF.

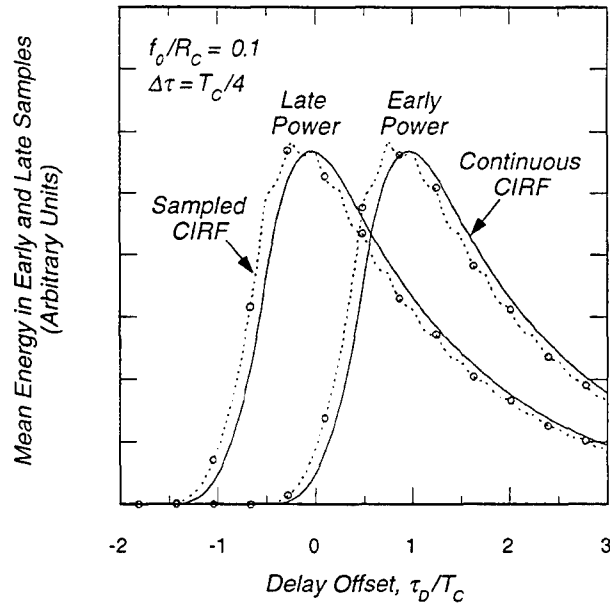


Figure B-2. Mean energy of early and late code correlator output for continuous and sampled (four samples per chip) CIRF.

Ideal values of τ_D are plotted in Figure B-3 for continuous and sampled CIRFs with 2, 4, 8, and 32 delay samples per chip. The sampled CIRF curves have steps that are most apparent for values of f_0/R_C greater than one or so. These steps result from the change in the number of delay samples (Eqn. 2.13), as the ratio f_0/R_C varies. These curves show that the ideal delay offset approaches one chip as the frequency selective fading channel becomes more severe (smaller values of f_0/R_C), and that the delay offset can be significantly smaller with a sampled CIRF than it is for a continuous CIRF. This difference is probably insignificant when the offset is less than one-tenth of a chip or so. However, when f_0/R_C is small and the offset is several tenths of a chip the difference could impact whether or not a DLL maintains lock on the signal³.

³ Reinking [1995] has shown that the bias in delay error can be partially corrected by “adjusting” the relative power in the delay samples and the delay sample size. However, such adjustments are not allowed in the official DSWA channel models. Furthermore, it is the authors’ opinion that the channel model should depend only on the modulation bandwidth of the transmitted signal, and should be independent of the details of the receiver.

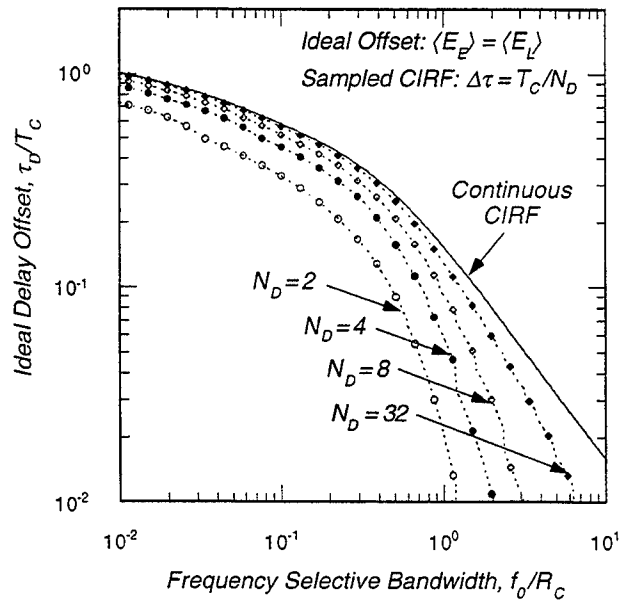


Figure B-3. Ideal delay offset for continuous and sampled CIRFs.

It is seen that the theoretical results for a sampled CIRF approach those for a continuous CIRF only when the number of delay samples per chip is large (greater than 8 or so). Because of computation time or hardware complexity, it may be impractical to achieve the ideal performance of a continuous CIRF in a software simulation or in a hardware simulator. Note that these analytic results neglect noise and are therefore valid for large signal-to-noise ratios.

Once the ideal delay offset is known, the ideal code correlator loss is just the value of $\langle E_O \rangle$ relative to unity, its value for large values of f_0 / R_C . This loss is plotted in Figure B-4 for both continuous and sampled CIRFs. The curves plotted with solid and dashed lines are the losses for continuous CIRFs with and without delay offset, respectively. For $f_0 / R_C = 10^{-2}$, optimally positioning the PN code provides about 3 dB more signal power out of the code correlator than is obtained with no offset ($\tau_D = 0$).

The code correlator loss is relatively insensitive to the delay sampling of the CIRF. The loss curve for eight delay samples per chip (plotted with solid circles) is essentially on top of the continuous CIRF curve. However, for values of f_0 / R_C between 0.3 and 3, the loss curve for two delay samples per chip varies noticeably from that for the continuous case, although the loss is rather small.

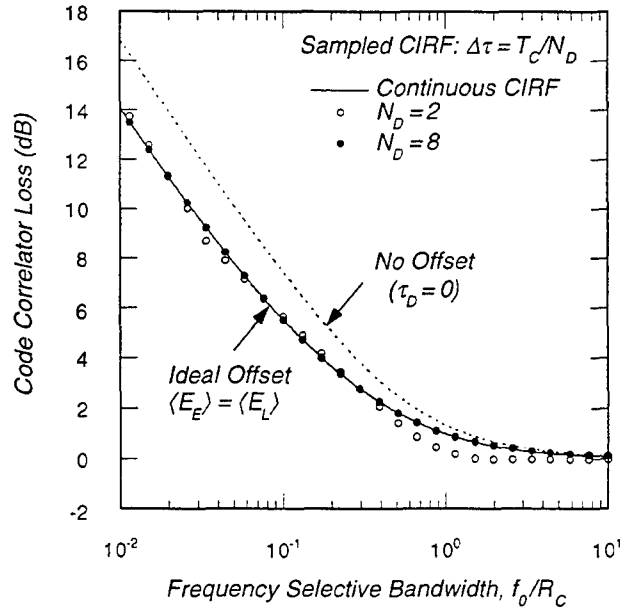


Figure B-4. Code correlator loss in frequency selective fading channels.

B.2 DPSK DEMODULATION ERROR RATE FOR CONTINUOUS CHANNELS.

Error rates for binary differential phase-shift keying (DPSK) demodulation are computed in this section for non-fading additive white Gaussian noise (AWGN) channels, Rician fading channels, and slow and fast Rayleigh fading channels. The channel impulse response function is assumed to be continuous in the time domain. The DPSK error rates for non-fading and slow, flat, Rayleigh fading channels are neatly derived in *Schwartz, Bennett, and Stein* [1966]. A slightly generalized version of their derivation is reproduced here because it is the starting point for the derivation of the DPSK error rate in fast fading. The fast fading DPSK error rate was originally derived by *Bello and Nelin* [1962b]. Their calculation is extended in *Dana* [1995c] to include the Doppler frequency spectra appropriate to transionospheric scintillation.

B.2.1 Additive White Gaussian Noise Channels.

The complex base-band signal plus additive white Gaussian noise (AWGN) at the code correlator output for the k^{th} channel bit can be written as

$$Z_k = \frac{1}{T} \int_{(k-1/2)T}^{(k+1/2)T} \left[r e^{j\phi_k} h_C(t) + n(t) \right] dt ,$$

where $n(t)$ is complex AWGN, and $h_C(t)$ is the combined channel and code correlator response function. This equation is essentially the same as Equation (B.1) with the inclusion of noise. For mathematical convenience in later developments the sample period of the code correlator is assumed to be equal to the channel bit period T . The code correlator loss in frequency selective fading is included in the mean power of $h_C(t)$. The notation τ_D for the delay of the locally generated PN sequence has been deleted because it is assumed that the receiver sets this delay at the optimum value plotted in Figure B-3.

The phase ϕ_k is determined by the transmitted data stream. For binary DPSK modulation, a change in ϕ_k of $\pm\pi$ from one channel bit period to the next indicates a transmitted one, whereas no change in phase indicates a transmitted zero.

Additive white Gaussian noise is assumed to have the usual properties:

$$\begin{aligned} \langle n(t) \rangle &= 0 \\ \langle n(t_1)n(t_2) \rangle &= 0 , \\ \langle n(t_1)n^*(t_2) \rangle &= N_0 \delta(t_1 - t_2) \end{aligned}$$

where N_0 is the one-sided noise spectral density. The second equation results because the real and imaginary components of AWGN are uncorrelated.

In further developments it is convenient to define the real and imaginary parts of the noise voltage and the combined channel and code correlator response function:

$$\begin{aligned} n_R(t) &= \text{Re}[n(t)] & n_I(t) &= \text{Im}[n(t)] \\ h_R(t) &= \text{Re}[h_C(t)] & h_I(t) &= \text{Im}[h_C(t)] \end{aligned}$$

Now, to compute the DPSK demodulation error rate, consider the code correlator output samples for the $k = 0$ and $k = 1$ symbol periods, Z_0 and Z_1 , respectively. The complex output voltages are then given by the expressions

$$\begin{aligned}
Z_0 &= \frac{1}{T} \int_{-T/2}^{T/2} [r \cos \varphi_0 h_R(t) - r \sin \varphi_0 h_I(t) + n_R(t)] dt \\
&\quad + j \frac{1}{T} \int_{-T/2}^{T/2} [r \sin \varphi_0 h_R(t) + r \cos \varphi_0 h_I(t) + n_I(t)] dt \\
&= [r \cos \varphi_0 X_0 - r \sin \varphi_0 Y_0 + N_{R,0}] + j[r \sin \varphi_0 X_0 + r \cos \varphi_0 Y_0 + N_{I,0}] \\
Z_1 &= \frac{1}{T} \int_{T/2}^{3T/2} [r \cos \varphi_1 h_R(t) - r \sin \varphi_1 h_I(t) + n_R(t)] dt \\
&\quad + j \frac{1}{T} \int_{T/2}^{3T/2} [r \sin \varphi_1 h_R(t) + r \cos \varphi_2 h_I(t) + n_I(t)] dt \\
&= [r \cos \varphi_1 X_1 - r \sin \varphi_1 Y_1 + N_{R,1}] + j[r \sin \varphi_1 X_1 + r \cos \varphi_1 Y_1 + N_{I,1}]
\end{aligned}$$

where

$$X_k = \frac{1}{T} \int_{(k-1/2)T}^{(k+1/2)T} h_R(t) dt \quad Y_k = \frac{1}{T} \int_{(k-1/2)T}^{(k+1/2)T} h_I(t) dt, \quad (\text{B.5})$$

and

$$N_{R,k} = \frac{1}{T} \int_{(k-1/2)T}^{(k+1/2)T} n_R(t) dt \quad N_{I,k} = \frac{1}{T} \int_{(k-1/2)T}^{(k+1/2)T} n_I(t) dt.$$

The noise samples N_R and N_I are the integrals of zero-mean, normally distributed random variables, and thus are similarly distributed. Furthermore, because the $n_R(t)$ and $n_I(t)$ components of the noise voltage are uncorrelated, $N_{R,k}$ and $N_{I,k}$ are also uncorrelated. Using these properties, it is easy to show that

$$\begin{aligned}
\langle N_{R,k} N_{R,l} \rangle &= \frac{1}{T^2} \int_{(k-1/2)T}^{(k+1/2)T} dt \int_{(l-1/2)T}^{(l+1/2)T} dt' \langle n_R(t) n_R(t') \rangle = \frac{N_0}{2T} \delta_{k,l} \\
\langle N_{I,k} N_{I,l} \rangle &= \frac{N_0}{2T} \delta_{k,l} \\
\langle N_{R,k} N_{I,l} \rangle &= 0
\end{aligned} \quad (\text{B.6})$$

The DPSK decision metric \hat{m} is [Schwartz, Bennett, and Stein, 1966]

$$\hat{m} = \text{Re}[Z_1 Z_0^*] = \frac{1}{4}|Z_1 + Z_0|^2 - \frac{1}{4}|Z_1 - Z_0|^2 .$$

It is now easy to see that if the phase ϕ_k does not change from symbol 0 to 1, the signal components will add coherently in the $Z_1 + Z_0$ term but will cancel in the $Z_1 - Z_0$ term. Thus \hat{m} should be positive in this case, and the probability of error is just the probability that \hat{m} is negative. Conversely, if there is a $\pm\pi$ phase change from channel bit 0 to 1, then the signal components will add coherently in the $Z_1 - Z_0$ term and will cancel in the other term. Thus \hat{m} should be negative in this case, and an error occurs if it is positive. Assuming that zeros and ones are equally likely and uniformly distributed in the transmitted data, we only need to evaluate the error rate for one of these cases. Without further loss of generality⁴, we can assume that the signal phase remains constant ($\phi_1 = \phi_0$) during these two channel bit periods. The probability of a demodulation error is then equal to the probability that the DPSK decision metric indicates a polarity change.

For convenience we define two new variables w_+ and w_- where

$$w_+ = \frac{1}{2}(Z_1 + Z_0) \quad w_- = \frac{1}{2}(Z_1 - Z_0) .$$

In terms of these new variables, the DPSK metric is

$$\hat{m} = |w_+|^2 - |w_-|^2 = a_+^2 - a_-^2 \quad (\text{B.7})$$

where a_+ and a_- are the amplitudes of w_+ and w_- , respectively. The w_+ and w_- variables, written in terms of signal and noise components, are

⁴ It is shown in Appendix C that the DPSK error rate with intersymbol interference (*i.e.*, when there is no underlying PN code and f_0 is comparable to or smaller than the symbol rate) does depend on whether or not there is a phase change in the transmitted modulation. Only in flat fading is the error rate independent of the modulation. However, the signal at the output of a code correlator is always flat fading, for a properly designed code, because the PN code chips on interfering symbols are uncorrelated with the PN code chips on the on-time symbol.

$$\begin{aligned}
w_+ &= \frac{1}{2} \left[r \cos \varphi_0 (X_1 + X_0) - r \sin \varphi_0 (Y_1 + Y_0) + N_{R,1} + N_{R,0} \right] + \\
&\quad \frac{j}{2} \left[r \sin \varphi_0 (X_1 + X_0) + r \cos \varphi_0 (Y_1 + Y_0) + N_{I,1} + N_{I,0} \right] \\
w_- &= \frac{1}{2} \left[r \cos \varphi_0 (X_1 - X_0) - r \sin \varphi_0 (Y_1 - Y_0) + N_{R,1} - N_{R,0} \right] + \\
&\quad \frac{j}{2} \left[r \sin \varphi_0 (X_1 - X_0) + r \cos \varphi_0 (Y_1 - Y_0) + N_{I,1} - N_{I,0} \right]
\end{aligned}$$

The probability of a demodulation error for the case that the signal phase is constant is the probability that \hat{m} is negative or that a_- is greater than a_+ .

In the absence of fading, the combined channel and code correlator response function is just a complex phasor:

$$h_C(t) = e^{j\theta}.$$

The voltages w_+ and w_- are then given by the expressions

$$\begin{aligned}
w_+ &= \frac{1}{2} \left[2r \cos(\varphi_0 + \theta) + N_{R,1} + N_{R,0} \right] + \frac{j}{2} \left[2r \sin(\varphi_0 + \theta) + N_{I,1} + N_{I,0} \right] \\
w_- &= \frac{1}{2} \left[N_{R,1} - N_{R,0} \right] + \frac{j}{2} \left[N_{I,1} - N_{I,0} \right]
\end{aligned}$$

Thus, for an AWGN channel, w_+ and w_- are complex, uncorrelated (and independent), normally distributed random variables with the properties:

$$\begin{aligned}
\langle w_+ \rangle &= r e^{j(\varphi_0 + \theta)} \\
\langle w_- \rangle &= \langle w_+ w_-^* \rangle = 0 \\
\langle w_+ w_+^* \rangle &= r^2 + N_0/2T \\
\langle w_- w_-^* \rangle &= N_0/2T
\end{aligned}$$

Because w_+ is complex Gaussian with a non-zero mean, the probability density function of the amplitude a_+ is Rician, and because w_- is complex Gaussian with zero mean, the probability density function of the amplitude a_- is Rayleigh:

$$f(a_+) = \frac{2a_+}{N_0/(2T)} \exp\left[-\frac{a_+^2 + r^2}{N_0/(2T)}\right] I_0\left[\frac{2ra_+}{N_0/(2T)}\right]$$

$$f(a_-) = \frac{2a_-}{N_0/(2T)} \exp\left[-\frac{a_-^2}{N_0/(2T)}\right]$$

where $I_0(\cdot)$ is the modified Bessel function.

The DPSK demodulation symbol error rate is, as discussed above, the probability that \hat{m} is negative or that a_- is larger than a_+ :

$$P_e = \text{Prob}[a_- > a_+] = \int_0^\infty da_+ \int_{a_+}^\infty da_- f(a_+, a_-) .$$

Because w_+ and w_- are uncorrelated and normally distributed, they are also independent. Thus the joint probability density function $f(a_+, a_-)$ is equal to the product of the two separate probability density functions. The DPSK channel bit (or demodulation) error rate is then easily computed:

$$P_e = \frac{1}{2} \exp\left[-\frac{r^2 T}{N_0}\right] .$$

The quantity $r^2 T$ is equal to the channel bit energy E_{cb} in a demodulated symbol period. Thus the expression above reduces to the familiar DPSK form:

$$P_e = \frac{1}{2} \exp\left[-\frac{E_{cb}}{N_0}\right] \quad (\text{Non-Fading}) . \quad (\text{B.8})$$

B.2.2 Slow Non-Rayleigh Fading Channels.

Under slow fading conditions, the channel decorrelation time is much longer than a channel bit period, and the average demodulation error rate is equal to the non-fading expression averaged over the fading distribution of power:

$$\langle P_e \rangle = \int_0^\infty \frac{1}{2} e^{-\gamma S} f(S) dS . \quad (\text{B.9})$$

The quantity γS , where $\gamma = E_{cb}/N_0$, is the instantaneous symbol energy-to-noise spectral density ratio.

For Rician fading, the integral in Equation (B.9) can be done in closed form, and the average DPSK demodulation error rate is

$$\langle P_e \rangle = \frac{1}{2 + 2(1 - R)\gamma} \exp \left[-\frac{R\gamma}{1 + (1 - R)\gamma} \right] \quad (\text{Slow Rician Fading}) .$$

In the limit that the scintillation index S_4 is zero and the Rician index R is unity, indicating non-fading, this reduces to the non-fading error rate [Eqn. (B.8)]. In the limit that S_4 is unity ($R = 0$), indicating Rayleigh fading, this reduces to the familiar Rayleigh fading form:

$$\langle P_e \rangle = \frac{1}{2 + 2\gamma} \quad (\text{Slow Rayleigh Fading}) .$$

DPSK channel bit error rates for non-Rayleigh fading are plotted in Figure B-5 for several values of the scintillation index. The top curve in this figure is for a slow Rayleigh fading channel ($S_4 = 1$), and the bottom curve is for a non-fading channel ($S_4 = 0$). DPSK symbol error rates for Rician fading are close to the Rayleigh fading curve for values of S_4 greater than 0.75, and are close to the non-fading curve for values of S_4 less than 0.25. Evidently, the DPSK channel bit error rate makes a transition between non-fading and fading for values of S_4 ranging from 0.25 to 0.75.

B.2.3 Fast Rayleigh Fading Channels.

Assuming that the receiver tracking loops maintain lock on the time-of-arrival and frequency of the received signal, two effects of fast fading degrade PN spread spectrum DPSK demodulation performance. First, when the decorrelation time of $h_C(t)$ is less than the channel bit period, random fluctuations in the de-spread signal phase reduce the gain of the code correlator. The signal does not integrate coherently, and a loss in the signal-to-noise ratio of the output results. This loss depends on the ratio of the decorrelation time to the channel bit period (τ_0/T), and on the Doppler spectrum of the fading⁵. Second, random phase fluctuations in the received signal can cause the DPSK metric to have the wrong sign. The receiver then misinterprets phase fluctuations caused by fading as phase changes in the transmitted signal.

⁵ Here τ_0 is the decorrelation time of $h_C(t)$. This is the same as the decorrelation time of the channel only for the turbulent model. For the general case, the decorrelation time of $h_C(t)$ depends on antenna filtering, if any, and on the relative delay between the local and received PN codes.

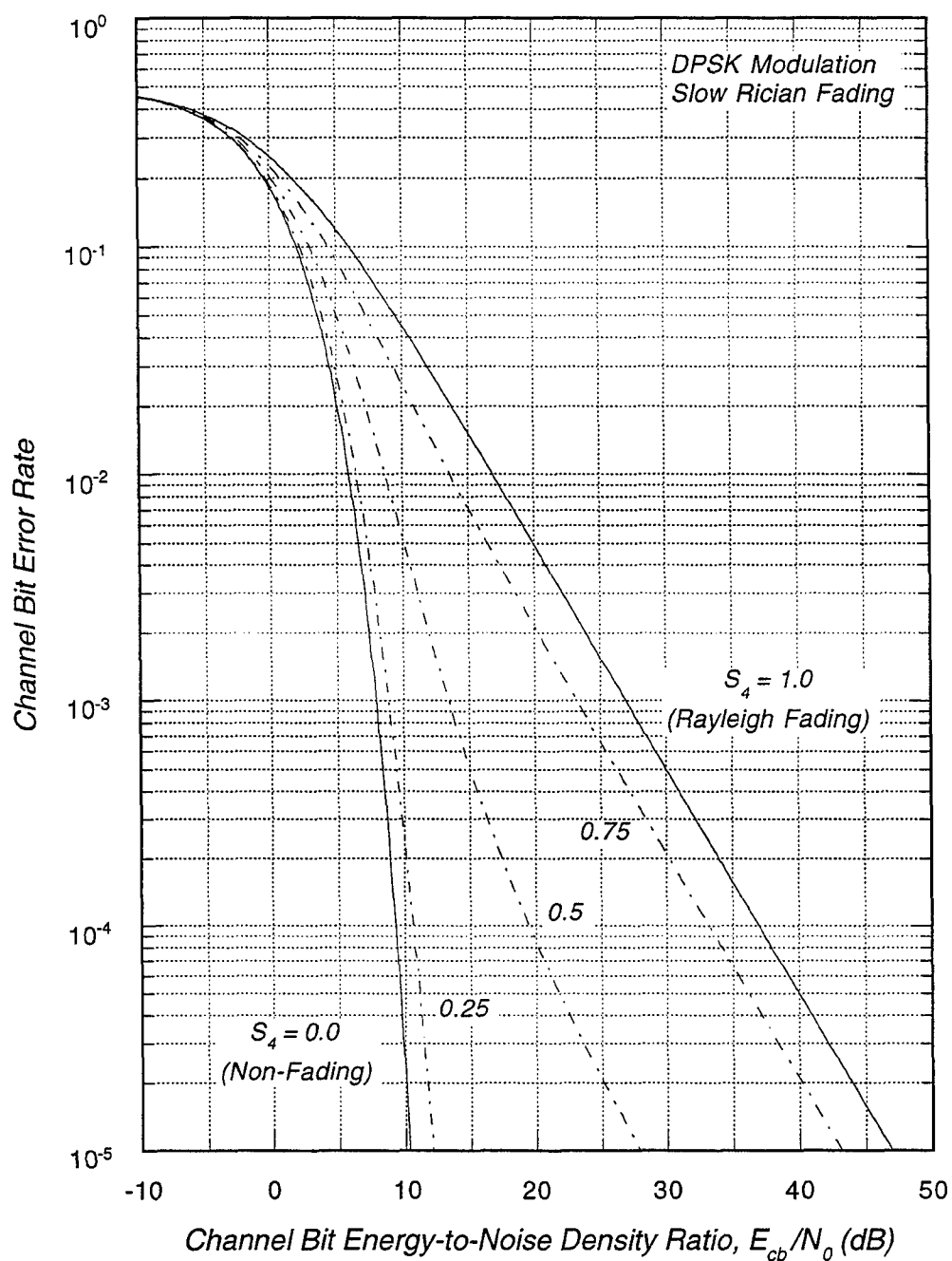


Figure B-5. DPSK channel bit error rate for Rician fading channels.

Both of these effects can be treated simultaneously in a derivation similar to one developed by *Bello and Nelin* [1962b] about 35 years ago. The starting point of the fast fading error rate derivation is the DPSK metric [Eqn. (B.7)] written in terms of the w_+ and w_- variables.

In fast Rayleigh fading, the combined response function $h_C(t)$ is a complex, zero-mean, normally distributed random process, so the amplitude of $h_C(t)$ has a Rayleigh distribution. The X and Y variables in w_+ and w_- are then zero-mean, normally distributed random variables. Thus w_+ and w_- are similarly distributed. The second order moments of w_+ and w_- are then easy to compute:

$$\begin{aligned}\langle w_+ w_+^* \rangle &= \frac{r^2}{4} [\langle X_0^2 \rangle + \langle X_1^2 \rangle + 2\langle X_0 X_1 \rangle + \langle Y_0^2 \rangle + \langle Y_1^2 \rangle + 2\langle Y_0 Y_1 \rangle] \\ &\quad + \frac{1}{4} [\langle N_{R,0}^2 \rangle + \langle N_{R,1}^2 \rangle + \langle N_{I,0}^2 \rangle + \langle N_{I,1}^2 \rangle] \\ \langle w_- w_-^* \rangle &= \frac{r^2}{4} [\langle X_0^2 \rangle + \langle X_1^2 \rangle - 2\langle X_0 X_1 \rangle + \langle Y_0^2 \rangle + \langle Y_1^2 \rangle - 2\langle Y_0 Y_1 \rangle] \\ &\quad + \frac{1}{4} [\langle N_{R,0}^2 \rangle + \langle N_{R,1}^2 \rangle + \langle N_{I,0}^2 \rangle + \langle N_{I,1}^2 \rangle] \\ \langle w_+ w_-^* \rangle &= \frac{r^2}{4} [\langle X_1^2 \rangle - \langle X_0^2 \rangle + \langle Y_1^2 \rangle - \langle Y_0^2 \rangle] \\ &\quad + \frac{1}{4} [\langle N_{R,1}^2 \rangle - \langle N_{R,0}^2 \rangle + \langle N_{I,1}^2 \rangle - \langle N_{I,0}^2 \rangle] = 0\end{aligned}$$

where cross correlation terms of the form channel \times noise or noise \times noise are zero. Because the w_+ and w_- terms are uncorrelated and normally distributed, they are also independent⁶. The second order moments of the noise terms are given in Equation (B.6), and the second order moments of X and Y are

⁶ Note that w_+ and w_- are uncorrelated if and only if there is equal average power in the real and imaginary (or in-phase and quadrature-phase) components of the noise and combined channel and code correlator response function. Evaluating the effects of imbalances in the average power of these components is beyond the scope of this idealized model, but is easy to compute with COMLNK.

$$\begin{aligned}\langle X_0^2 \rangle &= \langle X_1^2 \rangle = \langle Y_0^2 \rangle = \langle Y_1^2 \rangle = \frac{1}{2} R_1 \\ \langle X_0 X_1 \rangle &= \langle Y_0 Y_1 \rangle = \frac{1}{2} R_2\end{aligned}$$

With some computation, R_1 and R_2 can be written in terms of the temporal correlation function $\rho(t)$ of the combined channel and code correlator response function:

$$\begin{aligned}R_1 &= 2 \int_0^1 (1 - \xi) \rho(T\xi) d\xi \\ R_2 &= \frac{1}{2} \int_0^1 (1 - \xi) \{ \rho[T(1 - \xi)] + \rho[T(1 + \xi)] \} d\xi\end{aligned}$$

Once it has been determined that w_+ and w_- are uncorrelated (and thus are independent), complex, zero-mean, normally distributed random variables, it is simple to compute the DPSK error rate. The DPSK metric can be rewritten as

$$\hat{m} = a_+^2 - a_-^2$$

where a_+ and a_- are equal to $|w_+|$ and $|w_-|$, respectively. The amplitudes a_+ and a_- have Rayleigh probability density functions:

$$\begin{aligned}f(a_+) &= \frac{2a_+}{\mu_+} e^{-a_+^2/\mu_+} \\ f(a_-) &= \frac{2a_-}{\mu_-} e^{-a_-^2/\mu_-}\end{aligned}$$

where

$$\begin{aligned}\mu_+ &= \frac{r^2}{2} [R_1 + R_2 + \gamma^{-1}] \\ \mu_- &= \frac{r^2}{2} [R_1 - R_2 + \gamma^{-1}]\end{aligned}$$

The average symbol error rate is then the probability that a_- is larger than a_+ :

$$\langle P_e \rangle = \int_0^\infty da_+ f(a_+) \int_{a_+}^\infty da_- f(a_-) = \frac{\mu_-}{\mu_+ + \mu_-},$$

which reduces to

$$\langle P_e \rangle = \frac{R_1 - R_2 + \gamma^{-1}}{2(R_1 + \gamma^{-1})} \quad (\text{Fast Rayleigh Fading}) \quad . \quad (\text{B.10})$$

One can see from the definition of R_1 that this quantity is equal to the loss in signal energy within a channel bit period⁷, so the quantity γR_1 is the value of the channel bit energy-to-noise spectral density ratio. The quantity $1 - R_2 / R_1$ then represents the degrading effect of channel bit-to-bit phase fluctuations on demodulation performance. In the slow fading limit ($\tau_0 \gg T$), R_1 and R_2 both approach unity, and the fast fading error rate reduces to the expression for slow Rayleigh fading.

When the fading is fast ($\tau_0 < T$), there is a certain probability that channel phase fluctuations will erroneously change the sign of the DPSK decision metric resulting in what *Bello and Nelin* [1962b] call an irreducible error rate. For large values of γ , the DPSK error rate reduces to

$$\langle P_e \rangle = \frac{R_1 - R_2}{2R_1} \quad (\gamma \gg 1) \quad (\text{Fast Fading Irreducible Error Rate}) \quad ,$$

independent of γ . The irreducible error rate depends on the ratio τ_0 / T and on the Doppler frequency spectrum of the fading. This probability is independent of signal-to-noise ratio for large values of γ because it is the *signal* phase that is randomly varying and causing demodulation errors.

For the Doppler frequency spectra defined in Section 2 that are representative of transionospheric propagation, R_1 and R_2 are

⁷ The A/D output signal voltage is proportional to

$$S = \frac{1}{T} \int_{-T/2}^{T/2} h_c(t) dt \quad ,$$

so the power of the output signal can be written as

$$\langle SS^* \rangle = \frac{1}{T} \int_{-T}^T (1 - |t|/T) \rho_c(t) dt \quad .$$

This expression reduces to R_1 with a change in variables.

$$\begin{aligned}
R_1 &= \begin{cases} \frac{2}{T_4^2} [2T_4 - 3 + (T_4 + 3)e^{-T_4}] & f^{-4} \\ \frac{2}{3T_6^2} [8T_6 - 15 + (T_6^2 + 7T_6 + 15)e^{-T_6}] & f^{-6} \\ \frac{\sqrt{\pi} \operatorname{erf}(T_g)}{T_g} - \frac{1 - e^{-T_g^2}}{T_g^2} & \text{Gaussian} \end{cases} \\
R_2 &= \begin{cases} \frac{1}{T_4^2} [3 - 2(T_4 + 3)e^{-T_4} + (2T_4 + 3)e^{-2T_4}] & f^{-4} \\ \frac{1}{3T_6^2} [15 - 2(T_6^2 + 7T_6 + 15)e^{-T_6} + (4T_6^2 + 14T_6 + 15)e^{-2T_6}] & f^{-6} \\ \frac{\sqrt{\pi}}{T_g} [\operatorname{erf}(2T_g) - \operatorname{erf}(T_g)] + \frac{1}{2T_g^2} [1 + e^{-4T_g^2} - 2e^{-T_g^2}] & \text{Gaussian} \end{cases}
\end{aligned}$$

where $T_4 = \alpha_4 T / \tau_0$, $T_6 = \alpha_6 T / \tau_0$, and $T_g = T / \tau_0$, and where α_4 and α_6 are numerical constants defined in Section 2.

Figure B-6 shows the DPSK channel bit error rate in fast Rayleigh fading for several values of the ratio τ_0/T . The Doppler frequency spectrum for these cases has the f^{-4} functional form. As the channel bit energy-to-noise spectral density ratio increase, all curves, except the $\tau_0/T = \infty$ case, eventually flatten out and approach an irreducible error rate. In this respect, DPSK demodulation is quite robust compared to coherent PSK: The decorrelation time can be as small as 10 times the symbol period, and symbol error rates near one percent can still be achieved. For coherent PSK, the decorrelation time must be greater than 30 times the symbol period to achieve demodulation error rates below one percent⁸.

⁸ Even more robust performance in fast fading is obtainable with frequency shift keying (FSK) modulation and non-coherent demodulation. There still is an irreducible error rate because the Doppler frequency spectrum of the fading smears signal energy across the FSK tones, but a binary FSK link can operate at smaller decorrelation times than a DPSK link with the same symbol period. FSK links can be further hardened to fast fading effects by using larger tone spacings [Bogusch, 1989].

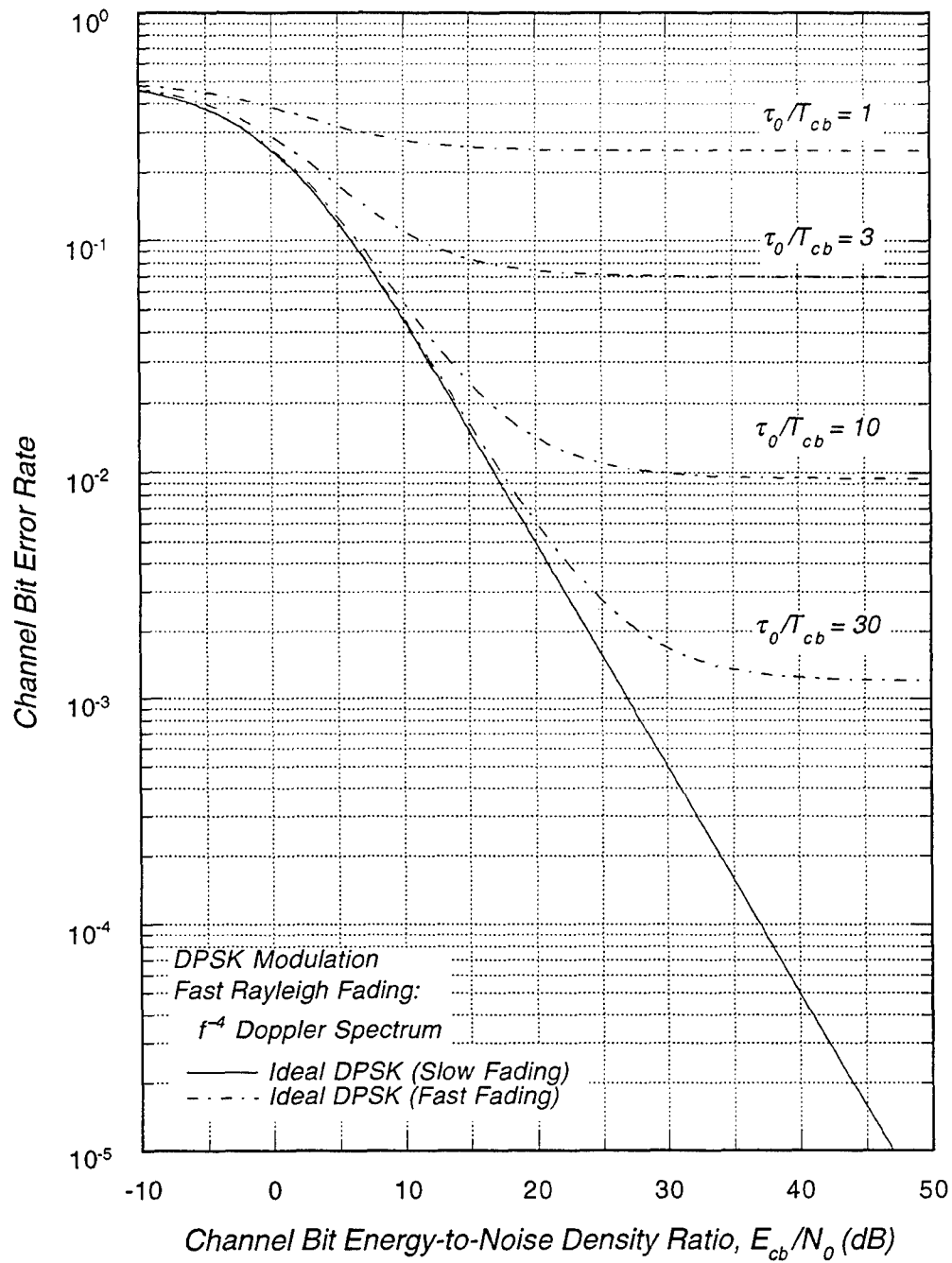


Figure B-6. DPSK demodulation error rate for fast, Rayleigh fading channels.

Another view of the effect of fast fading on DPSK demodulation performance is given in Figure B-7 where the irreducible channel bit error rate is plotted versus normalized decorrelation time (τ_0/T) for the three Doppler frequency spectra. These spectra produce irreducible error rates that are within a factor of 2 or so for a given value of τ_0/T . The normalized decorrelation time must be greater than 2, 3, and 10 to achieve DPSK demodulation error rates less than 0.1, 0.05, and 0.01, respectively.

B.3 DPSK FAST FADING DEMODULATION ERROR RATE FOR SAMPLED CHANNELS.

Although an actual transionospheric channel impulse response function is continuous, the calculation of the CIRF for use in COMLNK or in a hardware channel simulator necessarily involves sampling in both time and delay. Earlier in this Appendix we discussed the effects of delay sampling of the CIRF on code tracking. Here we focus on the effects of time sampling on DPSK demodulation performance.

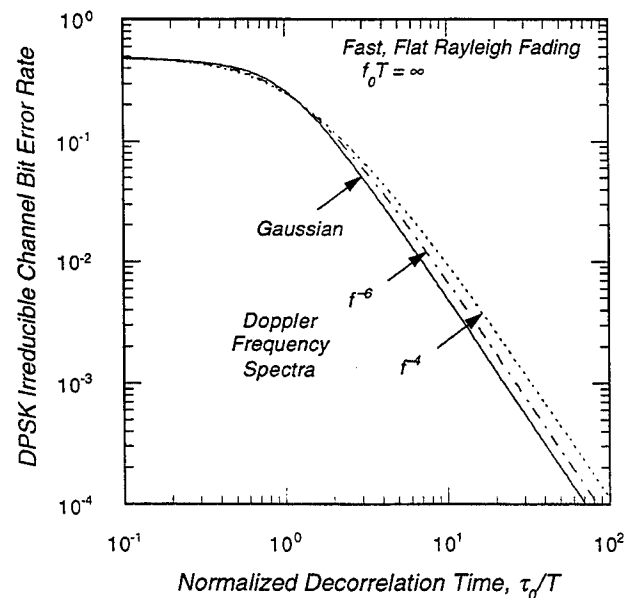


Figure B-7. DPSK irreducible channel bit error rate for fast Rayleigh fading channels.

It has been the practice of the authors to sample the CIRF in time with sufficient resolution that the temporal statistics of fades to -30 dB or so match ensemble values. The requirements on time sampling to achieve such a match are discussed in *Dana* [1988]. Once these requirements have been met, we have assumed that the sampling is also adequate for DPSK demodulation. The purpose of this discussion is to explore the limitations, if any, of this assumption.

In the time domain, the CIRF is sampled at a fixed rate where the sample period is usually an integral fraction of the channel decorrelation time (*i.e.*, $\Delta t = \tau_0 / n_0$ where n_0 is an integer). The signal contributions to the X and Y samples in Equation (B.5) are then constructed as

$$X_k = \frac{1}{T} \sum_{l=k}^{k+N_T-1} \text{Re}[h_C(l\Delta t)] \Delta t_l \quad Y_k = \frac{1}{T} \sum_{l=k}^{k+N_T-1} \text{Im}[h_C(l\Delta t)] \Delta t_l \quad ,$$

where N_T is the number of CIRF time samples per symbol period T , and $h_C(l\Delta t)$ is the time-sampled combined channel and code correlator response. The time sample interval is a function of the index l to account for edge effects (in general, the symbol period begins and ends between channel samples). To simplify this calculation somewhat, but with a slight loss in generality, we assume that there are an integer number of channel samples per symbol and that they are aligned with the symbols. Thus we assume that $\Delta t_l = \Delta t = T / N_T$ for all l .

For Rayleigh fading the sampled CIRF is a zero-mean, normally distributed process with uncorrelated real and imaginary parts. Then, as shown above, the DPSK demodulation error rate depends on the second order moments of X and Y . The variance of X and Y is

$$\langle X_k^2 \rangle = \langle Y_k^2 \rangle = \frac{\Delta t^2}{2T^2} \sum_{l=k}^{k+N_T-1} \sum_{l'=k}^{k+N_T-1} \rho[(l-l')\Delta t] = \frac{1}{2} R_1 \quad ,$$

where $\rho(t)$ is the temporal correlation function of the channel. The leading factor of $1/2$ results because the real and imaginary parts of $h_C(l\Delta t)$ each contain exactly $1/2$ of the signal power. By counting the number of terms with the same value of $l-l'$, the expression for R_1 reduces to

$$R_1 = \frac{1}{N_T} \left\{ 1 + 2 \sum_{l=1}^{N_T} (1 - l/N_T) \rho(l\Delta t) \right\} \quad .$$

Similarly, the cross correlation of X and of Y is

$$C = \langle X_k X_{k+N_T} \rangle = \langle Y_k Y_{k+N_T} \rangle = \frac{\Delta t^2}{2T^2} \sum_{l=k}^{k+N_T-1} \sum_{l'=k+N_T}^{k+2N_T-1} \rho[(l-l')\Delta t] = \frac{1}{2} R_2 .$$

After some manipulation the expression for R_2 reduces to

$$R_2 = \frac{1}{N_T} \left\{ \rho(T) + \sum_{l=1}^{N_T} (1 - l/N_T) [\rho(T + l\Delta t) + \rho(T - l\Delta t)] \right\} .$$

Note that in the limit of slow fading (*i.e.*, when $\rho = 1$) both R_1 and R_2 are unity.

The DPSK channel bit error rate is given in terms of R_1 and R_2 by the expression in Equation (B.10). The error rate is relatively insensitive to the number of temporal channel samples per symbol as illustrated in Figure B-8 where $\langle P_e \rangle$ is plotted versus channel bit energy-to-noise spectral density ratio for three values of the ratio τ_0/T and for continuous and sampled CIRFs. While there are small differences between the sampled and continuous CIRF curves for the $N_T = 1$ case, particularly at small values of τ_0/T , the sampled case curves for N_T greater than one agree well with the continuous CIRF curves. Thus only the $N_T = 1$ and 2 cases are plotted in the figure.

Note that the DSWA requirement is that there be at least 10 samples per decorrelation time [Wittwer, 1980]. For one and two samples per symbol, this requirement is only met when $\tau_0/T \geq 10$ and $\tau_0/T \geq 5$, respectively. Thus for the $\tau_0/T \geq 3$ and $\tau_0/T \geq 1$ cases, the channels are significantly undersampled. We conclude that when the channel is sampled at least 10 times per τ_0 , time sampling effects on DPSK demodulation are negligible.

This does not say that this issue can be ignored entirely. Indeed the signal energy in a channel bit period is very sensitive to the resolution of the time samples, as shown in Figure B-9. Here the signal sample energy loss due to fast fading (which is equal to $1/R_1$) is plotted versus the ratio τ_0/T for continuous CIRFs and sampled CIRFs with 1 through 32 channel samples per channel bit period. In the fast fading limit, R_1 for sampled CIRFs approaches $1/N_T$ rather than zero, as is the case for continuous CIRFs. Thus these results show that there can be significant discrepancy in the fast fading signal loss at small values of τ_0/T with time-sampled CIRFs. However, at values of τ_0/T where the output signal is significantly affected by the resolution of the temporal sampling, the irreducible DPSK demodulation error rate is already 50 percent.

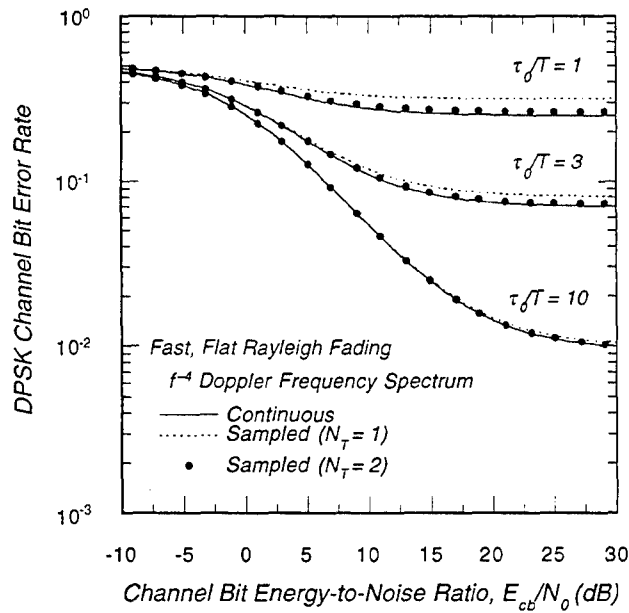


Figure B-8. Fast fading DPSK demodulation error rate for continuous and time sampled channel impulse response functions.

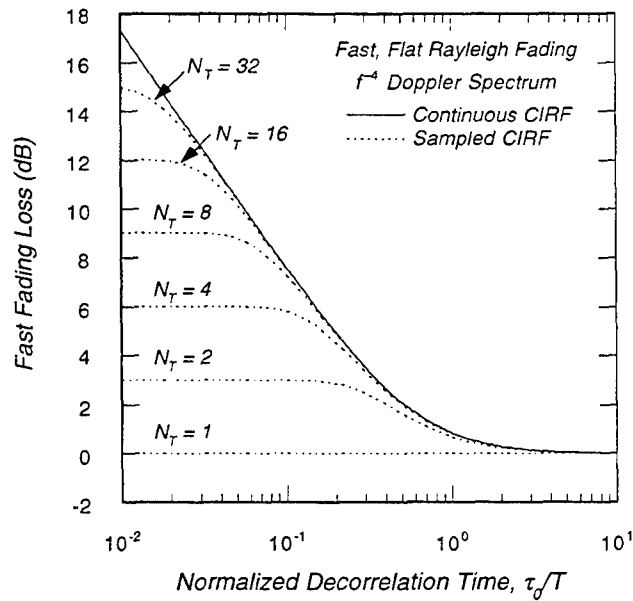


Figure B-9. Channel bit signal loss for fast Rayleigh fading and time-sampled and continuous CIRFs.

APPENDIX C

DEMODULATION PERFORMANCE OF DIFFERENTIALLY COHERENT PSK (DPSK) WITHOUT AN UNDERLYING SPREAD SPECTRUM CODE

A functional block diagram of a differentially coherent phase-shift keying (DPSK) receiver without an underlying spread spectrum code is shown in Figure C-1. The transmitted data are differentially encoded so that differentially coherent demodulation can be used. Thus only the frequency but not the phase of the received signal needs to be tracked. This eliminates the primary failure mechanism of a coherent PSK receiver in a fading channel — loss of phase lock.

Without an underlying pseudo-noise (PN) code, time and frequency selective fading effects are not mathematically separable as they are with a PN code (see Appendix B). Thus the problem of DPSK demodulation in time and frequency selective fading channels is considerably more complex in this case. Because of this we have not developed analytic demodulation error rates with as much detail as is included in the analytic model for DPSK with a PN code. In principle such detailed models could be developed, but would add little to the COMLNK validation process. To simplify the comparison of COMLNK and analytic results we always consider either fast, flat fading or slow, frequency selective fading, although analytic expressions have been developed for fast, frequency selective fading.

Delay tracking can be accomplished in this type of receiver by measuring the signal energy during the first and second halves of the modulation period and equalizing the energy in these two measurements¹. To simplify this calculation we approximate the effects of delay tracking by finding the sampling time that maximizes the received signal energy. We then show that the optimum sampling time in frequency selective fading is a small fraction of a symbol period, even in severe conditions.

In Section C.1 of this appendix we derive the received signal in terms of the channel impulse response function and then investigate the effect of delay tracking by finding the ideal delay offset. The ideal offset is between zero and two-tenths of a symbol period late, depending on the severity of the frequency selective fading, relative to

¹ Actually, several different delay discriminator algorithms can be used, as described in *Bogusch* [1990]. Perhaps the most common PSK technique involves mid-bit sampling.

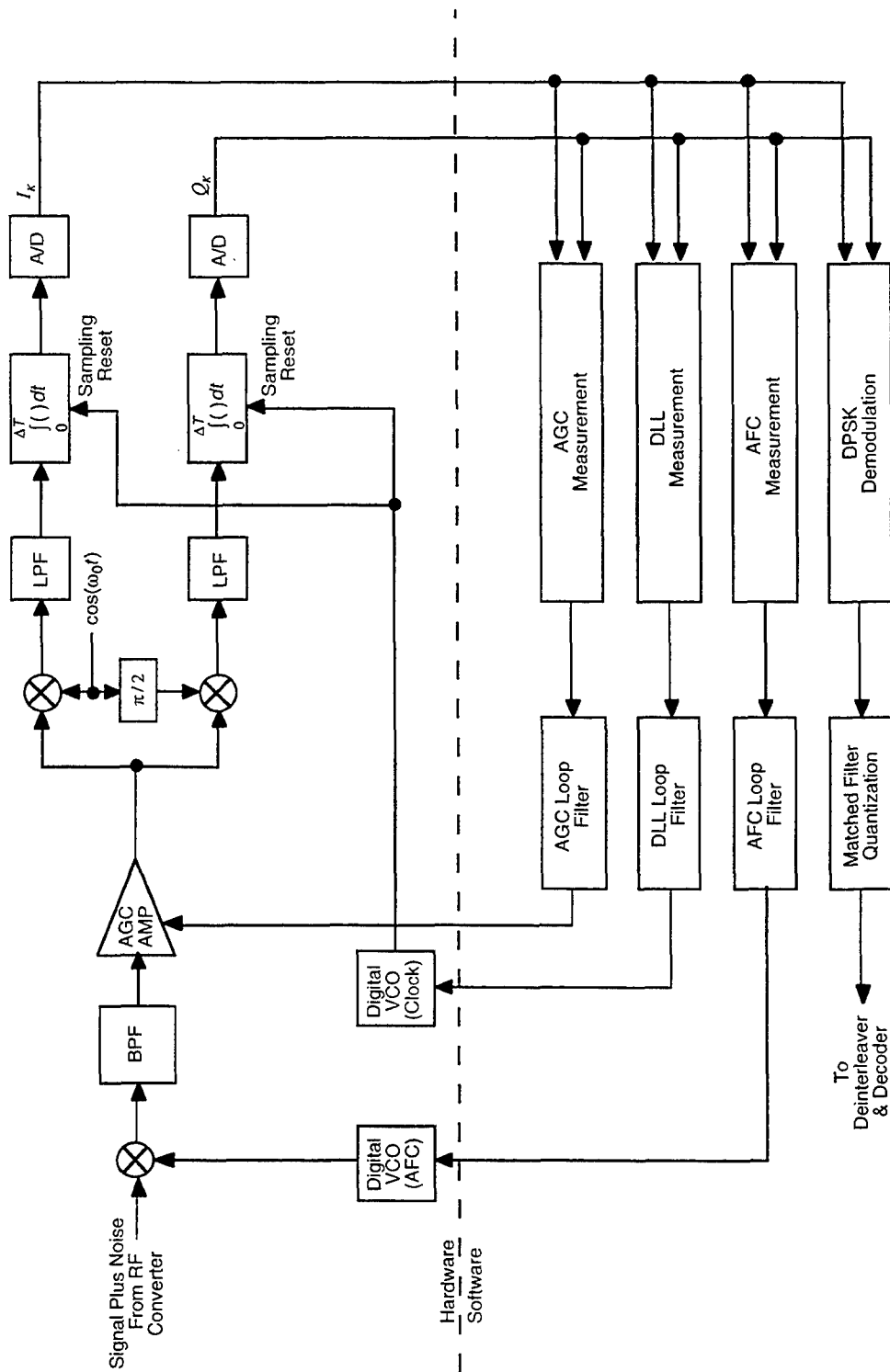


Figure C-1. Block diagram of a DPSK receiver.

the optimum position in a non-fading or flat fading channel. These results are used to compute on-time and intersymbol interference (ISI) signal energy. DPSK demodulation performance in continuous time and frequency selective fading channels and in sampled frequency selective fading channels is computed in Section C.2.

C.1 IDEAL DELAY OFFSET AND OUTPUT SIGNAL ENERGY.

The ideal delay offset is computed in this subsection for a slow, frequency selective fading channel with a continuous channel impulse response function (CIRF). The ideal delay we calculate here is that which maximizes the total received signal energy, including the on-time signal and the ISI. Presumably, a delay-lock loop (DLL) that uses early and late signal samples and attempts to equalize the signal energy in the two will produce a delay offset close to that which maximizes the signal energy.

Consider a transmitted DPSK waveform:

$$m(t) = \sum_l e^{j\varphi_l} \Pi\left[\frac{t}{T} - l\right] \quad (\text{C.1})$$

where $\varphi_l = 0, \pi$ randomly is the data modulation, and T is the channel bit period. The rectangular function $\Pi(\cdot)$ is defined as

$$\Pi(x) = \begin{cases} 1 & \text{for } |x| < \frac{1}{2} \\ 0 & \text{otherwise} \end{cases}.$$

The output of the channel is the convolution of the transmitted modulation and the CIRF. This convolution is

$$u(t) = r \int_0^{\infty} m(t - \tau) h(t, \tau) d\tau \quad (\text{C.2})$$

for a continuous CIRF, where r is the received signal amplitude.

The received signal is then sampled in an A/D converter. The sampled signal used for data demodulation is integrated over the channel bit period, so the complex voltage sample during the k^{th} bit period that is converted to a digital representation by the A/D can be written as:

$$Z_k = \frac{1}{T} \int_{(k-1/2)T+\tau_D}^{(k+1/2)T+\tau_D} [u(t) + n(t)] dt, \quad (\text{C.3})$$

where τ_D is the delay offset. In subsequent developments we calculate the ideal delay offset assuming that the channel is slow fading ($\tau_0 \gg T$), so the time dependence of the CIRF can be ignored when Z_k is evaluated.

The voltage $n(t)$ is complex additive white Gaussian noise (AWGN) with the usual properties:

$$\begin{aligned}\langle n(t) \rangle &= 0 \\ \langle n(t_1)n(t_2) \rangle &= 0 \\ \langle n(t_1)n^*(t_2) \rangle &= N_0 \delta(t_1 - t_2)\end{aligned}$$

where N_0 is the two-sided noise spectral density ratio. The second equation results because the real and imaginary components of AWGN are uncorrelated.

It is convenient to separate the complex signal samples into contributions from the on-time signal and the ISI. Assuming that the delay offset is limited to the range $0 < \tau_D < T$, the on-time signal contribution to Z_k is

$$S_O = r e^{j\phi_k} \int_0^{T+\tau_D} h(\tau) \Lambda\left(\frac{\tau - \tau_D}{T}\right) d\tau,$$

where we have suppressed the time dependence of the CIRF for this slow fading calculation. The triangle function in this equation is defined as

$$\Lambda(x) = \begin{cases} 1 - |x| & \text{for } |x| < 1 \\ 0 & \text{otherwise} \end{cases}.$$

The ISI contribution is

$$S_I = r \sum_{l=1}^{\infty} e^{j\phi_{k-l}} \int_{\tau_D}^{T+\tau_D} \left\{ h[\tau + (l-1)T] \left(\frac{\tau - \tau_D}{T} \right) + h[\tau + lT] \left(1 - \frac{\tau - \tau_D}{T} \right) \right\} d\tau.$$

Rather than computing early and late voltages to find the ideal delay offset, we will assume that the offset is close to the delay that gives the maximum mean *signal* energy. That is, we will find the value of τ_D that maximizes

$$E = \langle |S_O + S_I|^2 \rangle,$$

ignoring the effects of AWGN. In computing the expectation in this expression, we make the reasonable assumptions that the transmitted modulation is uncorrelated with the channel impulse response function and that the modulation is uncorrelated from symbol-to-symbol. The two resulting expectations are

$$\begin{aligned}\langle h(\tau) h^*(\tau') \rangle &= G(\tau) \delta(\tau - \tau') , \\ \langle e^{j(\varphi_k - \varphi_l)} \rangle &= \delta_{k,l} ,\end{aligned}\tag{C.4}$$

where $G(\cdot)$ is the power impulse response function, $\delta(\cdot)$ is the Dirac delta function, and $\delta_{k,l}$ is the Kronecker delta symbol:

$$\delta_{k,l} = \begin{cases} 1 & \text{if } k = l \\ 0 & \text{otherwise} \end{cases} .$$

With these assumptions and definitions, the mean output energy of the on-time and ISI contributions, respectively, is

$$\begin{aligned}E_O &= \langle S_O S_O^* \rangle = r^2 \int_0^{T+\tau_D} G(\tau) \Lambda^2\left(\frac{\tau - \tau_D}{T}\right) d\tau \\ E_I &= \langle S_I S_I^* \rangle = r^2 \int_0^{T+\tau_D} G(\tau) \left(\frac{\tau - \tau_D}{T}\right)^2 d\tau \\ &\quad + r^2 \sum_{l=1}^{\infty} \int_{\tau_D}^{T+\tau_D} G(\tau + lT) \left[1 - 2\left(\frac{\tau - \tau_D}{T}\right) + 2\left(\frac{\tau - \tau_D}{T}\right)^2 \right] d\tau\end{aligned}$$

When $G(\cdot)$ has an exponential form [Eqn. (2.8)], the on-time and ISI terms reduce to

$$\begin{aligned}E_O &= r^2 \left[\left(\frac{\tau_D}{T} - 1\right)^2 + 2 \frac{1 - e^{-\lambda(1+\tau_D/T)} + \lambda(1 - 2e^{-\lambda\tau_D/T} - \tau_D/T)}{\lambda^2} \right] \\ E_I &= 2r^2 \frac{e^{-\lambda\tau_D/T} (1 - e^{-2\lambda} - 2\lambda e^{-\lambda})}{(1 - e^{-\lambda}) \lambda^2} ,\end{aligned}$$

where $\lambda = 2\pi f_0 T$.

The ideal value of τ_D/T that maximizes $E_O + E_I$ is plotted in Figure C-2 versus normalized frequency selective bandwidth, $f_0 T$. When $f_0 T$ is less than 0.1 or so, τ_D/T approaches 0.182. The on-time, ISI, and total signal power for the ideal value of τ_D/T (solid and dashed lines) and for τ_D/T equal to zero are plotted in Figure C-3.

In the limit of severe frequency selective fading, the total signal energy approaches $2/3$. The loss of $1/3$ of the energy is often attributed to the "mismatch" of the received signal and the rectangular pulse shape assumed in the receiver. However, the missing $1/3$ of the signal energy (in the limit that $f_0 T \ll 1$) is actually contained in the cross correlation of the on-time signal and interfering signal voltages, which is identically zero in this calculation only because we assume that the DPSK modulation is uncorrelated from bit-to-bit. If long sequences of zeros or ones are transmitted, then the signal modulation is perfectly correlated from bit-to-bit, the cross term is no longer zero, and the total energy is unity for all values of $f_0 T$, as it should be.

The signal energy for the zero offset case ($\tau_D = 0$) is shown in Figure C-3 because in later developments we are going to ignore the delay offset to simplify the tedious algebra somewhat. These results show that the total signal energy is relatively insensitive to the value of τ_D/T . However, using the ideal delay offset increases the on-time signal energy by a factor of $3/2$ or so and decreases the ISI energy by a factor of about 2. Thus we expect there to be some impact of delay tracking on the DPSK demodulation error rate in frequency selective fading.

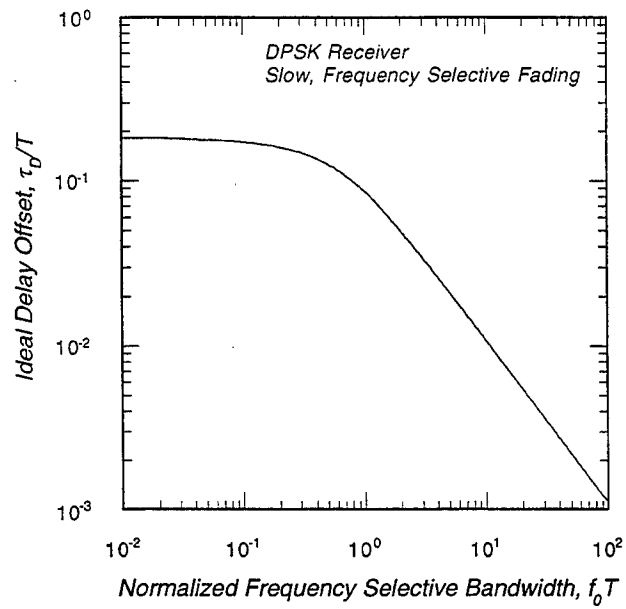


Figure C-2. Ideal delay offset of DPSK receiver in frequency selective fading.

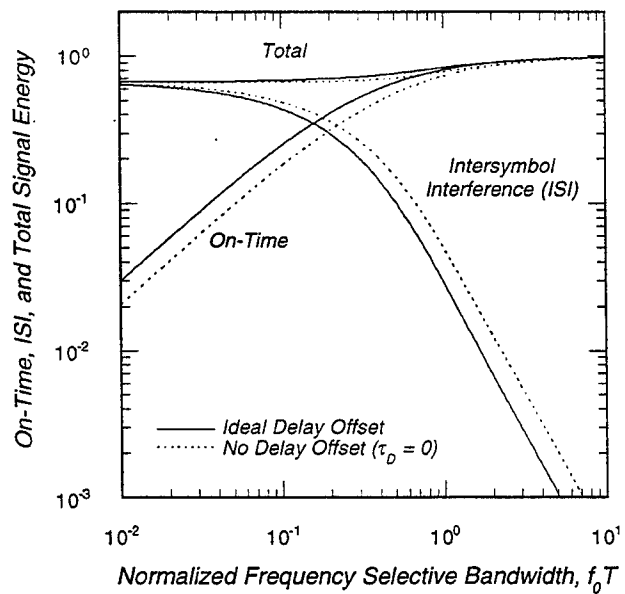


Figure C-3. On-time, ISI, and total signal energy for ideal and zero delay offsets.

C.2 DPSK DEMODULATION ERROR RATE IN FAST, FREQUENCY SELECTIVE FADING WITH CONTINUOUS CIRF.

Error rates for binary differential phase-shift keying (DPSK) demodulation are computed in Appendix B for non-fading additive white Gaussian noise (AWGN) channels, Rician fading channels, and slow and fast, flat Rayleigh fading channels. In this appendix the calculation is extended to fast, frequency selective fading. The DPSK error rates for fast fading or frequency selective fading was originally derived by *Bello and Nelin* [1962b]. To our knowledge this is the first time this calculation has been extended to *simultaneous* fast and frequency selective fading. To simplify the calculation somewhat we assume that the CIRF is continuous and that the delay offset is zero.

By combining Equations (C.1), (C.2) and (C.3) the complex signal plus noise voltage, sampled over a channel bit period T , is

$$Z_k = r \sum_{l=0}^{\infty} e^{j\varphi_{k-l}} \int_{(l-1)T}^{(l+1)T} d\tau \frac{1}{T} \int_{-T/2}^{T/2} dt h(t+kT, \tau) \Pi\left(\frac{t-\tau}{T} + l\right) + N_k ,$$

where the delay offset has been set to zero, and the CIRF is identically zero for negative values of delay. The AWGN contribution to Z_k ,

$$N_k = \frac{1}{T} \int_{(k-1/2)T}^{(k+1/2)T} n(t) dt ,$$

has the following properties:

$$\begin{aligned} \langle N_k \rangle &= \langle N_k N_l \rangle = 0 \\ \langle N_k N_l^* \rangle &= \frac{N_0}{T} \delta_{k,l} \end{aligned} \quad (C.5)$$

It is convenient to separate the k^{th} voltage sample Z_k into on-time and ISI contributions:

$$Z_k = r e^{j\varphi_k} \hat{S}_1(k) + r \sum_{l=1}^{\infty} e^{j\varphi_{k-l}} \hat{S}_2(k, l) + N_k ,$$

where

$$\hat{S}_1(k) = \int_0^T d\tau \frac{1}{T} \int_{-T/2}^{T/2} dt h(t + kT, \tau) \Pi\left(\frac{t - \tau}{T}\right)$$

and

$$\hat{S}_2(k, l) = \int_0^{2T} d\tau \frac{1}{T} \int_{-T/2}^{T/2} dt h[t + (k - l + 1)T, \tau + (l - 1)T] \Pi\left(\frac{t - \tau}{T} + 1\right) .$$

Similarly, the $k + 1^{st}$ voltage sample is

$$Z_{k+1} = r e^{j\varphi_{k+1}} \hat{S}_1(k + 1) + r \sum_{l=1}^{\infty} e^{j\varphi_{k+1-l}} \hat{S}_2(k + 1, l) + N_{k+1} .$$

Following the derivation in *Schwartz, Bennett and Stein* [1966], the DPSK decision metric is

$$\hat{m} = |w_+|^2 - |w_-|^2 ,$$

where

$$w_+ = \frac{1}{2}(Z_{k+1} + Z_k)$$

$$w_- = \frac{1}{2}(Z_{k+1} - Z_k)$$

Upon substituting the expressions for Z_k and Z_{k+1} into the expression for \hat{m} , we get

$$w_{\pm} = \frac{1}{2} \left\{ \underbrace{r e^{j\varphi_{k+1}} \hat{S}_1(k + 1)}_1 + \underbrace{r e^{j\varphi_k} \hat{S}_2(k + 1, 1)}_2 + \underbrace{r \sum_{l=2}^{\infty} e^{j\varphi_{k+1-l}} \hat{S}_2(k + 1, l)}_3 + \underbrace{N_{k+1}}_4 \right. \\ \left. \pm \underbrace{r e^{j\varphi_k} \hat{S}_1(k)}_5 \pm \underbrace{r e^{j\varphi_{k-1}} \hat{S}_2(k, 1)}_6 \pm \underbrace{r \sum_{l=2}^{\infty} e^{j\varphi_{k-l}} \hat{S}_2(k, l)}_7 \pm \underbrace{N_k}_8 \right\} . \quad (C.6)$$

The terms in this equation have been numbered as a short hand way of referring to them in further developments.

C.2.1 Statistics of w_+ and w_- .

In Rayleigh fading, whether flat or frequency selective, the first-order statistics of the channel impulse response function are complex normal with zero mean. Of course the noise is also complex normal with zero mean. Because the integral of a zero mean, normally distributed random process is similarly distributed, w_+ and w_- are also zero mean, normally distributed random processes. Thus the statistics of w_+ and w_- are completely determined once the second order moments of the eight terms are computed.

For the steady state channel and AWGN random processes considered here, the variances of the terms in Equation (C.6) must be independent of the index k . Thus the variances of terms 1 and 5, terms 2 and 6, terms 3 and 7, and terms 4 and 8 are all pair-wise equal. The variance of terms 4 and 8 is given in Equation (C.5). Furthermore, because the channel fluctuations are uncorrelated with the AWGN, all channel \times noise cross terms necessarily have zero mean.

The variance of term 1 in Equation (C.6) is

$$\begin{aligned}\sigma_1^2 &= \frac{r^2}{4} \langle \hat{S}_1(k+1) \hat{S}_1^*(k+1) \rangle \\ &= \frac{r^2}{4T^2} \int_0^T d\tau \int_0^T d\tau' \int_{-T/2}^{T/2} dt \int_{-T/2}^{T/2} dt' \langle h(t+kT, \tau) h^*(t'+kT, \tau') \rangle \Pi\left(\frac{t-\tau}{T}\right) \Pi\left(\frac{t'-\tau'}{T}\right)\end{aligned}$$

The turbulent model is assumed so that the expectation of the channel impulse response function is equal to the power impulse response $G(\cdot)$ times the temporal autocorrelation function of the channel:

$$\langle h(t, \tau) h^*(t', \tau') \rangle = \rho(t-t') G(\tau) \delta(\tau - \tau') \quad .$$

After some manipulations of the two time integrals, the expression for σ_1^2 can be reduced to a single time integral with the result

$$\sigma_1^2 = \frac{r^2}{2} \int_0^1 d\zeta T G(T\zeta) \int_0^{1-\zeta} d\xi \rho(T\xi) (1-\zeta-\xi) \quad ,$$

where $\zeta = \tau/T$ and $\xi = t/T$ are normalized delay and time variables, respectively.

The variance of term 2 in Equation (C.6) is

$$\begin{aligned}\sigma_2^2 &= \frac{r^2}{4} \langle \hat{S}_2(k+1,1) \hat{S}_2^*(k+1,1) \rangle \\ &= \frac{r^2}{4T^2} \int_0^{2T} d\tau \int_0^{2T} d\tau' \int_{-T/2}^{T/2} dt \int_{-T/2}^{T/2} dt' \langle h[t+(k+1)T, \tau] h^*[t'+(k+1)T, \tau'] \rangle \\ &\quad \times \Pi\left(\frac{t-\tau}{T}+1\right) \Pi\left(\frac{t'-\tau'}{T}+1\right)\end{aligned}$$

Similar manipulations as were performed in the expression for σ_1^2 reduce this variance to the following

$$\begin{aligned}\sigma_2^2 &= \frac{r^2}{2} \int_0^1 d\zeta T G(T\zeta) \int_0^\zeta d\xi \rho(T\xi) (\zeta - \xi) \\ &\quad + \frac{r^2}{2} \int_0^1 d\zeta T G[T(\zeta+1)] \int_0^{1-\zeta} d\xi \rho(T\xi) (1 - \zeta - \xi)\end{aligned}$$

The variance of term 3 in Equation (C.6) is

$$\sigma_3^2 = \frac{r^2}{4} \sum_{l=2}^{\infty} \sum_{l'=2}^{\infty} \langle e^{j\Phi_{k+1-l} - j\Phi_{k+1-l'}} \rangle \langle \hat{S}_2(k+1, l) \hat{S}_2^*(k+1, l') \rangle .$$

We assume that the transmitted modulation is uncorrelated with the channel impulse response function and is uncorrelated from symbol-to-symbol². Thus the expectation of the modulation is given by the expression in Equation (C.4), and the double summation in this equation reduces to a single sum. After some algebra,

$$\begin{aligned}\sigma_3^2 &= \frac{r^2}{2} \sum_{l=1}^{\infty} \left\{ \int_0^1 d\zeta T G[T(\zeta+l)] \int_0^\zeta d\xi \rho(T\xi) (\zeta - \xi) \right. \\ &\quad \left. + \int_0^1 d\zeta T G[T(\zeta+l+1)] \int_0^{1-\zeta} d\xi \rho(T\xi) (1 - \zeta - \xi) \right\} .\end{aligned}$$

² The first of these assumptions is reasonable because the transmitted data and the channel fading are completely unrelated. The second assumption implies that the transmitted data are random and do not contain long sequences of zeros, ones, or alternating zeros and ones.

The two terms within the curly brackets are equal to σ_2^2 when $l = 0$. Thus $\sigma_2^2 + \sigma_3^2$ and $\sigma_6^2 + \sigma_7^2$ are equal to this expression with the lower summation limit set to zero.

Fortunately (because they are quite tedious to calculate), there are only five signal \times signal cross correlation terms that are non-zero. The other 10 signal \times signal cross correlation terms are equal to zero because the transmitted modulation is uncorrelated from symbol-to-symbol [*i.e.*, because of Equation (C.4)]. All 12 signal \times noise cross correlation terms and the one noise \times noise cross correlation term are equal to zero. The non-zero terms are C_{12} , C_{15} , C_{25} , C_{36} , and C_{37} where C_{kl} denotes the cross correlation of the k^{th} and l^{th} terms in Equation (C.6). The 1-2 cross correlation is

$$\begin{aligned} C_{12} &= \frac{r^2}{4} \langle \hat{S}_1(k+1) \hat{S}_2^*(k+1, 1) \rangle \\ &= \frac{r^2}{4T^2} \int_0^T d\tau \int_0^T d\tau' \int_{-T/2}^{T/2} dt \int_{-T/2}^{T/2} dt' \langle h[t + (k+1)T, \tau] h^*[t' + (k+1)T, \tau'] \rangle \\ &\quad \times \Pi\left(\frac{t-\tau}{T}\right) \Pi\left(\frac{t'-\tau'}{T} + 1\right) \end{aligned}$$

After considerable manipulation this expression reduces to

$$\begin{aligned} C_{12} &= \frac{r^2}{4} \int_0^{1/2} d\zeta T G(T\zeta) \left[\int_0^\zeta d\xi \xi \rho(T\xi) + \zeta \int_\zeta^{1-\zeta} d\xi \rho(T\xi) + \int_{1-\zeta}^1 d\xi \rho(T\xi) (1-\xi) \right] \\ &\quad + \frac{r^2}{4} \int_{1/2}^1 d\zeta T G(T\zeta) \left[\int_0^{1-\zeta} d\xi \xi \rho(T\xi) + (1-\zeta) \int_{1-\zeta}^\zeta d\xi \rho(T\xi) + \int_\zeta^1 d\xi \rho(T\xi) (1-\xi) \right] \end{aligned}$$

The 1-5 cross correlation is

$$\begin{aligned} C_{15} &= \pm \frac{r^2}{4} \langle \hat{S}_1(k+1) \hat{S}_1^*(k) \rangle \\ &= \pm \frac{r^2}{4T^2} \int_0^T d\tau \int_0^T d\tau' \int_{-T/2}^{T/2} dt \int_{-T/2}^{T/2} dt' \langle h[t + (k+1)T, \tau] h^*[t' + kT, \tau'] \rangle \\ &\quad \times \Pi\left(\frac{t-\tau}{T}\right) \Pi\left(\frac{t'-\tau'}{T}\right) \end{aligned}$$

which reduces to

$$C_{15} = \pm \frac{r^2}{4} \int_0^1 d\zeta T G(T\zeta) \int_0^{1-\zeta} d\xi \{ \rho[T(\xi+1)] + \rho[T(1-\xi)] \} (1-\zeta-\xi) .$$

Next, the 2-5 cross correlation term is

$$\begin{aligned} C_{25} &= \pm \frac{r^2}{4} \langle \hat{S}_2(k+1,1) \hat{S}_1^*(k) \rangle \\ &= \pm \frac{r^2}{4T^2} \int_0^{2T} d\tau \int_0^T d\tau' \int_{-T/2}^{T/2} dt \int_{-T/2}^{T/2} dt' \langle h[t+(k+1)T, \tau] h^*[t'+kT, \tau'] \rangle \\ &\quad \times \Pi\left(\frac{t-\tau}{T}+1\right) \Pi\left(\frac{t'-\tau'}{T}\right) \end{aligned}$$

After some manipulation it can be seen that this expression is equal to C_{12} , except for the leading sign.

The 3-6 cross correlation is

$$C_{36} = \pm \frac{r^2}{4} \sum_{l=2}^{\infty} \langle e^{j\Phi_{k-1}-j\Phi_{k+1-l}} \rangle \langle \hat{S}_2(k,1) \hat{S}_2^*(k+1,l) \rangle .$$

The expectation of the modulation is non-zero only for the $l=2$ term, so this expression collapses to

$$\begin{aligned} C_{36} &= \pm \frac{r^2}{4} \langle \hat{S}_2(k,1) \hat{S}_2^*(k+1,2) \rangle \\ &= \pm \frac{r^2}{4T^2} \int_0^{2T} d\tau \int_0^{2T} d\tau' \int_{-T/2}^{T/2} dt \int_{-T/2}^{T/2} dt' \langle h[t+kT, \tau] h^*[t'+kT, \tau'+T] \rangle \\ &\quad \times \Pi\left(\frac{t-\tau}{T}+1\right) \Pi\left(\frac{t'-\tau'}{T}+1\right) \end{aligned}$$

After considerable algebra, this reduces to an expression similar to that for C_{12} except for the sign:

$$C_{36} = \pm \frac{r^2}{4} \int_0^{1/2} d\zeta T G[T(\zeta+1)] \left[\int_0^\zeta d\xi \xi \rho(T\xi) + \zeta \int_\zeta^{1-\zeta} d\xi \rho(T\xi) + \int_{1-\zeta}^1 d\xi \rho(T\xi)(1-\xi) \right] \\ \pm \frac{r^2}{4} \int_{1/2}^1 d\zeta T G[T(\zeta+1)] \left[\int_0^{1-\zeta} d\xi \xi \rho(T\xi) + (1-\zeta) \int_{1-\zeta}^\zeta d\xi \rho(T\xi) + \int_\zeta^1 d\xi \rho(T\xi)(1-\xi) \right] .$$

For the exponential form of the power impulse response function [Eqn. (2.8)],

$$G[T(\zeta+1)] = e^{-\lambda} G(T\zeta) ,$$

where $\lambda = 2\pi f_0 T$. Thus

$$C_{36} = \pm e^{-\lambda} C_{12} \quad (\text{exponential power impulse response function}) .$$

The final cross correlation (3-7) to be evaluated is

$$C_{37} = \pm \frac{r^2}{4} \sum_{l=2}^{\infty} \sum_{l'=2}^{\infty} \langle e^{j\varphi_{k+1-l} - j\varphi_{k-l'}} \rangle \langle \hat{S}_2(k+1, l) \hat{S}_2^*(k, l') \rangle .$$

The expectation of the modulation is non-zero only if $l' = l - 1$, so a single sum results:

$$C_{37} = \pm \frac{r^2}{4T^2} \sum_{l=2}^{\infty} \int_0^{2T} d\tau \int_0^{2T} d\tau' \int_{-T/2}^{T/2} dt \int_{-T/2}^{T/2} dt' \\ \times \langle h[t + (k+2)T, \tau + (l-1)T] h^*[t' + (k+2)T, \tau' + (l-2)T] \rangle . \\ \times \Pi\left(\frac{t-\tau}{T} + 1\right) \Pi\left(\frac{t'-\tau'}{T} + 1\right)$$

Again after considerable manipulation, C_{37} reduces to

$$C_{37} = \pm \frac{r^2}{4} \sum_{l=1}^{\infty} \int_0^{1/2} d\zeta T G[T(\zeta+l)] \left\{ \int_0^\zeta d\xi \xi \rho(T\xi) + \zeta \int_\zeta^{1-\zeta} d\xi \rho(T\xi) + \int_{1-\zeta}^1 d\xi \rho(T\xi)(1-\xi) \right\} \\ \pm \frac{r^2}{4} \sum_{l=1}^{\infty} \int_{1/2}^1 d\zeta T G[T(\zeta+l)] \left\{ \int_0^{1-\zeta} d\xi \xi \rho(T\xi) + (1-\zeta) \int_{1-\zeta}^\zeta d\xi \rho(T\xi) + \int_\zeta^1 d\xi \rho(T\xi)(1-\xi) \right\}$$

When $G(\cdot)$ exponential, C_{37} reduces further to

$$C_{37} = \pm C_{12} \sum_{l=1}^{\infty} e^{-l\lambda} = \pm C_{12} \frac{e^{-\lambda}}{1 - e^{-\lambda}} \quad (\text{exponential power impulse response function}) .$$

These second order moments of the terms in Equation (C.6) now can be written in terms of four double integrals:

$$\begin{aligned} R_1 &= \int_0^1 d\zeta T G(T\zeta) \int_0^{1-\zeta} d\xi \rho(T\xi) (1 - \zeta - \xi) \\ R_2 &= \int_0^1 d\zeta T G(T\zeta) \int_0^{\zeta} d\xi \rho(T\xi) (\zeta - \xi) \\ R_3 &= \int_0^1 d\zeta T G(T\zeta) \int_0^{1-\zeta} d\xi \{ \rho[T(1 + \xi)] + \rho[T(1 - \xi)] \} (1 - \zeta - \xi) \\ R_4 &= \int_0^{1/2} d\zeta T G(T\zeta) \left[\int_0^{\zeta} d\xi \xi \rho(T\xi) + \zeta \int_{\zeta}^{1-\zeta} d\xi \rho(T\xi) + \int_{1-\zeta}^1 d\xi \rho(T\xi) (1 - \xi) \right] \\ &\quad + \int_{1/2}^1 d\zeta T G(T\zeta) \left[\int_0^{1-\zeta} d\xi \xi \rho(T\xi) + (1 - \zeta) \int_{1-\zeta}^{\zeta} d\xi \rho(T\xi) + \int_{\zeta}^1 d\xi \rho(T\xi) (1 - \xi) \right] \end{aligned}$$

With these definitions and the exponential form for $G(\cdot)$,

$$\sigma_1^2 = \sigma_5^2 = \frac{r^2}{2} R_1$$

$$\sigma_2^2 + \sigma_3^2 = \sigma_6^2 + \sigma_7^2 = \frac{r^2}{2} \left[\frac{R_2 + e^{-\lambda} R_1}{1 - e^{-\lambda}} \right]$$

$$C_{12} = C_{25} = \frac{r^2}{4} R_4$$

$$C_{15} = \frac{r^2}{4} R_3$$

$$C_{36} = \frac{r^2}{4} e^{-\lambda} R_4$$

$$C_{37} = \frac{r^2}{4} \frac{e^{-\lambda}}{1 - e^{-\lambda}} R_4$$

The variances of the noise terms (4 and 8) are given by Equation (C.5).

We note in passing that the on-time (E_O), ISI (E_I), and total energy (E_T) of the signal can also be written in terms of R_1 and R_2 :

$$E_O = 2r^2 R_1$$

$$E_I = 2r^2 \frac{R_2 + e^{-\lambda} R_1}{1 - e^{-\lambda}}$$

$$E_T = 2r^2 \frac{R_1 + R_2}{1 - e^{-\lambda}}$$

C.2.2 Evaluation of Integrals.

The R_1 , R_2 , R_3 and R_4 integrals can be done in closed form for the exponential form of the power impulse response function and for the temporal correlation functions given in Chapter 2. The results are tabulated in this subsection for Gaussian, f^{-6} and f^{-4} Doppler spectra and for the slow fading limit ($\tau_0 \gg T$).

Gaussian Doppler Spectrum

$$R_1 = \frac{\sqrt{\pi}}{2T_g \lambda} \exp \left[-\lambda + \frac{\lambda^2}{4T_g^2} \right] \left\{ \operatorname{erf} \left[\frac{\lambda}{2T_g} \right] + \operatorname{erf} \left[T_g - \frac{\lambda}{2T_g} \right] \right\} + \frac{\sqrt{\pi}(\lambda - 1)}{2T_g \lambda} \operatorname{erf} [T_g] - \frac{1}{2T_g^2} [1 - e^{-T_g^2}]$$

$$R_2 = \frac{\sqrt{\pi}}{2T_g \lambda} \exp \left[\frac{\lambda^2}{4T_g^2} \right] \left\{ \operatorname{erf} \left[T_g + \frac{\lambda}{2T_g} \right] - \operatorname{erf} \left[\frac{\lambda}{2T_g} \right] \right\} - \frac{\sqrt{\pi}(1 + \lambda)}{2T_g \lambda} e^{-\lambda} \operatorname{erf} [T_g] + \frac{1}{2T_g^2} e^{-\lambda} [1 - e^{-T_g^2}]$$

$$\begin{aligned}
R_3 &= \frac{\sqrt{\pi}}{2T_g\lambda} \exp\left[-2\lambda + \frac{\lambda^2}{4T_g^2}\right] \left\{ \operatorname{erf}\left[2T_g - \frac{\lambda}{2T_g}\right] - \operatorname{erf}\left[T_g - \frac{\lambda}{2T_g}\right] \right\} \\
&\quad + \frac{\sqrt{\pi}}{2T_g\lambda} \exp\left[\frac{\lambda^2}{4T_g^2}\right] \left\{ \operatorname{erf}\left[T_g + \frac{\lambda}{2T_g}\right] - \operatorname{erf}\left[\frac{\lambda}{2T_g}\right] \right\} \\
&\quad - \frac{\sqrt{\pi}}{T_g} \left\{ \operatorname{erf}[T_g] - \left(1 - \frac{1}{2\lambda}\right) \operatorname{erf}[2T_g] \right\} + \frac{1}{2T_g^2} \left[1 + e^{-4T_g^2} - 2e^{-T_g^2} \right] \\
R_4 &= \frac{\sqrt{\pi}}{2T_g\lambda} \exp\left[\frac{\lambda^2}{4T_g^2}\right] \left\{ \operatorname{erf}\left[\frac{\lambda}{2T_g}\right] - \operatorname{erf}\left[T_g + \frac{\lambda}{2T_g}\right] \right\} + \frac{\sqrt{\pi}}{2T_g\lambda} (1 + e^{-\lambda}) \operatorname{erf}[T_g] \\
&\quad - \frac{\sqrt{\pi}}{2T_g\lambda} \exp\left[-\lambda + \frac{\lambda^2}{4T_g^2}\right] \left\{ \operatorname{erf}\left[\frac{\lambda}{2T_g}\right] + \operatorname{erf}\left[T_g - \frac{\lambda}{2T_g}\right] \right\}
\end{aligned}$$

where $\operatorname{erf}(\cdot)$ is the error function and $T_g = T / \tau_0$.

f^{-6} Doppler Spectrum

$$\begin{aligned}
R_1 &= \frac{8T_6^2 - 9T_6\lambda + 3\lambda^2}{3\lambda(T_6 - \lambda)^3} e^{-\lambda} - \frac{8T_6 + 15\lambda - 8T_6\lambda}{3T_6^2\lambda} \\
&\quad - \lambda \frac{T_6^2(24 + 9T_6 + T_6^2) - \lambda T_6(37 + 16T_6 + 2T_6^2) + \lambda^2(15 + 7T_6 + T_6^2)}{3T_6^2(T_6 - \lambda)^3} e^{-T_6} \\
R_2 &= \frac{8T_6^2 + 9T_6\lambda + 3\lambda^2}{3\lambda(T_6 + \lambda)^3} - \frac{8T_6 - 15\lambda + 8T_6\lambda}{3T_6^2\lambda} e^{-\lambda} \\
&\quad - \lambda \frac{T_6^2(24 + 9T_6 + T_6^2) + \lambda T_6(37 + 16T_6 + 2T_6^2) + \lambda^2(15 + 7T_6 + T_6^2)}{3T_6^2(T_6 + \lambda)^3} e^{-T_6 - \lambda}
\end{aligned}$$

$$\begin{aligned}
R_3 = & \lambda \frac{24T_6^2 + 37T_6\lambda + 15\lambda^2}{3T_6^2(T_6 + \lambda)^3} - \frac{2(15 + 7T_6 + T_6^2)}{3T_6^2} e^{-T_6} \\
& - \lambda \frac{2T_6^2(12 + 9T_6 + 2T_6^2) - \lambda T_6(37 + 32T_6 + 8T_6^2) + \lambda^2(15 + 14T_6 + 4T_6^2)}{3T_6^2(T_6 - \lambda)^3} e^{-2T_6} \\
& + 2 \frac{T_6^4(15 + 7T_6 + T_6^2) - 2(\lambda T_6)^2(5 + 5T_6 + T_6^2) + \lambda^4(3 + 3T_6 + T_6^2)}{3(T_6^2 - \lambda^2)^3} e^{-T_6 - \lambda} \\
R_4 = & \frac{15T_6^2 + 21T_6\lambda + 8\lambda^2}{3T_6(T_6 + \lambda)^3} - \frac{15T_6^2 - 21T_6\lambda + 8\lambda^2}{3T_6(T_6 - \lambda)^3} e^{-\lambda} \\
& + \frac{T_6^2(15 + 7T_6 + T_6^2) - \lambda T_6(21 + 12T_6 + 2T_6^2) + \lambda^2(8 + 5T_6 + T_6^2)}{3T_6(T_6 - \lambda)^3} e^{-T_6} \\
& - \frac{T_6^2(15 + 7T_6 + T_6^2) + \lambda T_6(21 + 12T_6 + 2T_6^2) + \lambda^2(8 + 5T_6 + T_6^2)}{3T_6(T_6 + \lambda)^3} e^{-T_6 - \lambda}
\end{aligned}$$

where $T_6 = \alpha_6 T / \tau_0$, and α_6 is a numerical constant ($\alpha_6 = 2.904630\dots$) defined in Section 2.1.

f^{-4} Doppler Spectrum

$$\begin{aligned}
R_1 = & \frac{2T_4\lambda - 2T_4 - 3\lambda}{T_4^2\lambda} + \frac{2T_4 - \lambda}{(T_4 - \lambda)^2\lambda} e^{-\lambda} - \lambda \frac{T_4(4 + T_4) - \lambda(3 + T_4)}{T_4^2(T_4 - \lambda)^2} e^{-T_4} \\
R_2 = & \frac{2T_4 + \lambda}{(T_4 + \lambda)^2\lambda} - \frac{2T_4 - 3\lambda + 2T_4\lambda}{T_4^2\lambda} e^{-\lambda} - \lambda \frac{T_4(4 + T_4) + \lambda(3 + T_4)}{T_4^2(T_4 + \lambda)^2} e^{-T_4 - \lambda} \\
R_3 = & \lambda \frac{4T_4 + 3\lambda}{T_4^2(T_4 + \lambda)^2} - \frac{2(3 + T_4)}{T_4^2} e^{-T_4} - \lambda \frac{2T_4(2 + T_4) - \lambda(3 + 2T_4)}{T_4^2(T_4 - \lambda)^2} e^{-2T_4} \\
& + 2 \frac{T_4^2(3 + T_4) - \lambda^2(1 + T_4)}{(T_4^2 - \lambda^2)^2} e^{-T_4 - \lambda}
\end{aligned}$$

$$R_4 = \frac{3T_4 + 2\lambda}{T_4(T_4 + \lambda)^2} - \frac{3T_4 - 2\lambda}{T_4(T_4 - \lambda)^2} e^{-\lambda} + \frac{T_4(3 + T_4) - \lambda(2 + T_4)}{T_4(T_4 - \lambda)^2} e^{-T_4} - \frac{T_4(3 + T_4) + \lambda(2 + T_4)}{T_4(T_4 + \lambda)^2} e^{-T_4 - \lambda}$$

where $T_4 = \alpha_4 T / \tau_0$ and α_4 is a numerical constant ($\alpha_4 = 2.146193 \dots$) defined in Section 2.1.

Slow Fading Limit ($\tau_0 \gg T$)

All of the above expressions for R_1 , R_2 , R_3 , and R_4 reduce to the same set of equations in the limit that the decorrelation time is much larger than the symbol period. The slow fading limits for these equations are

$$R_1 = \frac{2(1 - e^{-\lambda}) - \lambda(2 - \lambda)}{2\lambda^2}$$

$$R_2 = \frac{2 - (2 + 2\lambda + \lambda^2)e^{-\lambda}}{2\lambda^2}$$

$$R_3 = \frac{2 - 2\lambda + \lambda^2 - 2e^{-\lambda}}{\lambda^2}$$

$$R_4 = \frac{4(\lambda - 2) + (8 - \lambda^2)e^{-\lambda/2}}{4\lambda^2}$$

C.2.3 DPSK Channel Bit Error Rate.

In general, the DPSK channel bit error rate (*i.e.*, the demodulation error rate) is

$$P_e = P[\hat{m} < 0 | \varphi_{k+1} = \varphi_k] P[\varphi_{k+1} = \varphi_k] + P[\hat{m} > 0 | \varphi_{k+1} = \varphi_k + \pi] P[\varphi_{k+1} = \varphi_k + \pi] \quad (C.7)$$

where $P[\hat{m} < 0 | \varphi_{k+1} = \varphi_k]$ is the probability that \hat{m} is negative given that there was no phase change between the k^{th} and the $k+1^{st}$ transmitted bits (*i.e.*, that $\varphi_{k+1} = \varphi_k$), $P[\varphi_{k+1} = \varphi_k]$ is the probability that there was no phase change in the transmitted modulation, $P[\hat{m} > 0 | \varphi_{k+1} = \varphi_k + \pi]$ is the probability that \hat{m} is positive given that there was a phase change between the k^{th} and the $k+1^{st}$ transmitted bits (*i.e.*, that

$\varphi_{k+1} = \varphi_k + \pi$), and $P[\varphi_{k+1} = \varphi_k + \pi]$ is the probability that there was a phase change in the transmitted modulation.

For non-fading or flat fading channels the probabilities $P[\hat{m} < 0 | \varphi_{k+1} = \varphi_k]$ and $P[\hat{m} > 0 | \varphi_{k+1} = \varphi_k + \pi]$ are equal, so only one of these needs to be computed. Thus the channel bit error rate is independent of the exact distribution of zeros and ones in the transmitted data stream. For frequency selective fading these two probabilities are not equal so both must be computed, and the channel bit error rate depends on the transmitted data. In further developments we will assume that phase changes or no phase changes are equally likely in the transmitted modulation. Thus we assume that

$$P[\varphi_{k+1} = \varphi_k] = P[\varphi_{k+1} = \varphi_k + \pi] = \frac{1}{2} . \quad (\text{C.8})$$

This may not always be the case. For example, one could imagine a fixed message or a preamble that contains more ones than zeros or *vice versa* or a long sequence of alternating zeros and ones. We will show that in the limit of severe frequency selective fading ($f_0 T \ll 1$) and large signal-to-noise ratio, the irreducible DPSK channel bit error rates for the two cases are

$$\begin{aligned} P[\hat{m} < 0 | \varphi_{k+1} = \varphi_k] &\rightarrow \frac{3}{8} \\ P[\hat{m} > 0 | \varphi_{k+1} = \varphi_k + \pi] &\rightarrow \frac{5}{8} \end{aligned} \quad (\text{C.9})$$

Obviously the linear average of these two limits is 50 percent, but if Equation (C.8) does not hold, the average irreducible error rate could be greater than 50 percent. However, because these two probabilities differ by a measurable amount only at large error rates and large signal-to-noise ratios, this may be of little practical significance.

With the above assumption about the distribution of phase changes in the transmitted modulation, the channel bit error rate reduces to

$$P_e = \frac{1}{2} P[\hat{m} < 0 | \varphi_{k+1} = \varphi_k] + \frac{1}{2} P[\hat{m} > 0 | \varphi_{k+1} = \varphi_k + \pi] . \quad (\text{C.10})$$

Case 1. $\varphi_{k+1} = \varphi_k$. In this case the probability of a demodulation error is the probability that the amplitude of w_- is greater than that of w_+ . Assuming Rayleigh fading so w_+ and w_- are both zero-mean, normally distributed, complex random process, the DPSK channel bit error rate is given by the expression derived in Appendix D:

$$P[\hat{m} < 0 | \varphi_{k+1} = \varphi_k] = \frac{1}{2} \left[1 - \frac{\sigma_+^2 - \sigma_-^2}{\sqrt{(\sigma_+^2 + \sigma_-^2)^2 - 4\sigma_+^2\sigma_-^2\rho_R^2}} \right], \quad (C.11)$$

where

$$\sigma_+^2 = \langle w_+ w_+^* \rangle \quad \sigma_-^2 = \langle w_- w_-^* \rangle \quad \rho_R = \frac{\langle w_+ w_-^* \rangle}{\sigma_+ \sigma_-}.$$

The cross correlation of w_+ and w_- is real for DPSK waveforms.

The variances and cross correlation of w_+ and w_- can be written in terms of variances and cross correlations of the individual terms calculated in Section B.2.1. Being careful to keep track of the sign of each term, we get

$$\begin{aligned} \sigma_+^2 &= \sigma_1^2 + \sigma_2^2 + \sigma_3^2 + \sigma_4^2 + \sigma_5^2 + \sigma_6^2 + \sigma_7^2 + \sigma_8^2 \\ &\quad + 2C_{12} + 2C_{15} + 2C_{25} + 2C_{36} + 2C_{37} \\ \sigma_-^2 &= \sigma_1^2 + \sigma_2^2 + \sigma_3^2 + \sigma_4^2 + \sigma_5^2 + \sigma_6^2 + \sigma_7^2 + \sigma_8^2 \\ &\quad + 2C_{12} - 2C_{15} - 2C_{25} - 2C_{36} - 2C_{37} \\ \sigma_+ \sigma_- \rho_R &= 2C_{12}. \end{aligned} \quad (C.12)$$

Writing these expressions in terms of the R integrals and assuming the exponential form for the power impulse response gives the following:

$$\begin{aligned} \sigma_+^2 + \sigma_-^2 &= r^2 \left[\frac{2(R_1 + R_2)}{1 - e^{-\lambda}} + R_4 + \frac{1}{\gamma} \right] \\ \sigma_+^2 - \sigma_-^2 &= r^2 \left[\left(e^{-\lambda} + \frac{1}{1 - e^{-\lambda}} \right) R_4 + R_3 \right] \\ \sigma_+ \sigma_- \rho_R &= \frac{1}{2} r^2 R_4 \end{aligned}$$

where $\gamma = r^2 T / N_0$ is the channel bit energy-to-noise spectral density ratio, E_{cb} / N_0 , in the absence of propagation effects.

In the limit of slow ($\tau_0 / T \gg 1$), severe frequency selective fading ($f_0 T \ll 1$), the irreducible error rate (*i.e.*, lower limit of the channel bit error rate when $\gamma \gg 1$) when the modulation is unchanged ($\varphi_{k+1} = \varphi_k$) is 3/8.

Case 2. $\varphi_{k+1} = \varphi_k + \pi$. In this case the probability of a channel bit error is the probability that the amplitude of w_- is less than that of w_+ . Again assuming Rayleigh fading, this error rate is given by the expression in Appendix D:

$$P[\hat{m} > 0 | \varphi_{k+1} = \varphi_k + \pi] = \frac{1}{2} \left[1 - \frac{\sigma_-^2 - \sigma_+^2}{\sqrt{(\sigma_+^2 + \sigma_-^2)^2 - 4\sigma_+^2\sigma_-^2\rho_R^2}} \right]. \quad (\text{C.13})$$

We get the following expressions for the variances and cross correlation of w_+ and w_- when the modulation has changed:

$$\begin{aligned} \sigma_+^2 &= \sigma_1^2 + \sigma_2^2 + \sigma_3^2 + \sigma_4^2 + \sigma_5^2 + \sigma_6^2 + \sigma_7^2 + \sigma_8^2 \\ &\quad - 2C_{12} - 2C_{15} + 2C_{25} + 2C_{36} + 2C_{37} \\ \sigma_-^2 &= \sigma_1^2 + \sigma_2^2 + \sigma_3^2 + \sigma_4^2 + \sigma_5^2 + \sigma_6^2 + \sigma_7^2 + \sigma_8^2 \\ &\quad - 2C_{12} + 2C_{15} - 2C_{25} - 2C_{36} - 2C_{37} \\ \sigma_+\sigma_-\rho_R &= -2C_{12}. \end{aligned} \quad (\text{C.14})$$

Writing these expressions in terms of the R integrals and assuming the exponential form for the power impulse response function gives the following:

$$\begin{aligned} \sigma_+^2 + \sigma_-^2 &= r^2 \left[\frac{2(R_1 + R_2)}{1 - e^{-\lambda}} - R_4 + \frac{1}{\gamma} \right] \\ \sigma_-^2 - \sigma_+^2 &= r^2 \left[R_3 - \left(e^{-\lambda} + \frac{1}{1 - e^{-\lambda}} \right) R_4 \right] \\ \sigma_+\sigma_-\rho_R &= \frac{1}{2} r^2 R_4. \end{aligned}$$

In the limit of slow severe frequency selective fading, the irreducible error rate when the modulation is changed ($\varphi_{k+1} = \varphi_k + \pi$) is 5/8.

General Case. The DPSK irreducible channel bit error rate in slow, frequency selective fading with a continuous CIRF is plotted in Figure C-4 for three cases: when the modulation is unchanged ($\varphi_{k+1} = \varphi_k$), when it is changed ($\varphi_{k+1} = \varphi_k + \pi$), and the linear average of the two. One can see from the figure that the difference between the irreducible error rate for the two cases is negligible for error rates below 0.01 or so. In further developments we will assume that the two cases are equally likely, and we will plot the average of the error rates for the two cases.

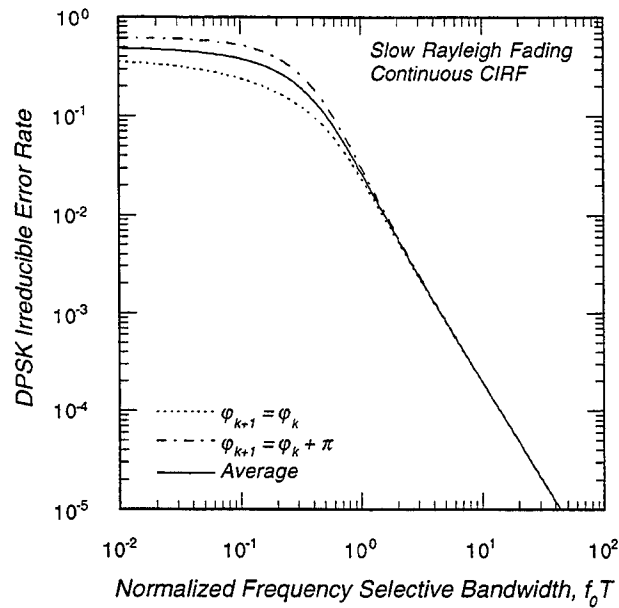


Figure C-4. DPSK irreducible channel bit error rate in slow, frequency selective fading with a continuous CIRF.

The DPSK irreducible error rate in fast, frequency selective fading with a continuous CIRF and a Gaussian Doppler frequency spectrum is plotted in Figure C-5. Here the error rate is plotted versus the product $f_0 T$ for parametric values of the ratio τ_0 / T . These results show that the effect of fast fading is to increase the irreducible error rate above that for slow fading, as is expected.

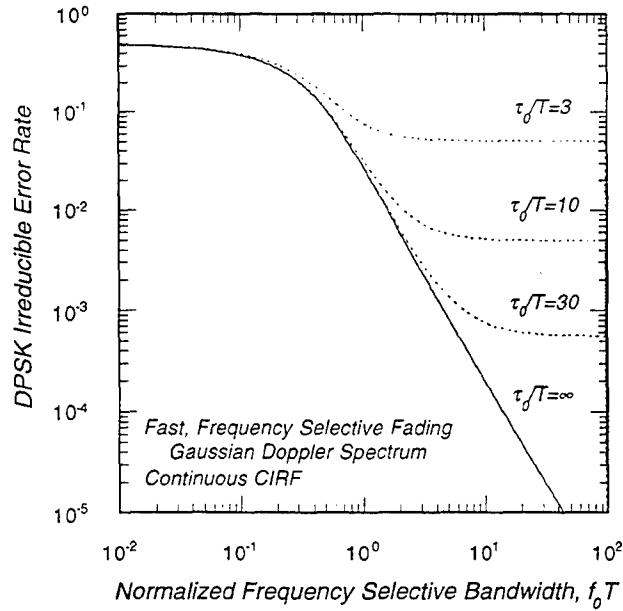


Figure C-5. DPSK irreducible error rate in fast, frequency selective fading with a Gaussian Doppler frequency spectrum.

C.3 DPSK DEMODULATION ERROR RATE IN SLOW, FREQUENCY SELECTIVE FADING WITH A SAMPLED CIRF.

So far the results in this appendix have been developed for a continuous channel impulse response function (CIRF)³. Thus the effect of the channel on the transmitted modulation is given by the convolution integral in Equation (C.2). However, to actually generate a realization of the CIRF for use in either a simulation or a hardware channel simulator, the channel must be discretely sampled in time and delay. In the time domain, the sampling is usually done to accurately reproduce the mean duration and separation of fades, say down to -30 or -40 dB. This requires something on the order of 40 samples per decorrelation time [Dana, 1988]. It is shown in Appendix B that such fine time sampling is more than adequate to minimize time sampling effects on DPSK demodulation performance.

³ By continuous CIRF we mean that the delay variable is continuous. The function itself is delta correlated, and hence is "infinitely discontinuous".

Sampling effects are more significant in the delay domain where the sample size often is coarser. With delay sampling, Equation (C.2) becomes

$$u(t) = r \sum_{i=0}^{N_\tau-1} m(t - i\Delta\tau) h(t, i\Delta\tau) \Delta\tau$$

where $m(t)$ is the transmitted DPSK modulation, $\Delta\tau$ is the delay sample size, N_τ is the number of delay samples [see Equation (2.13)], and $h(t, i\Delta\tau) \Delta\tau$ is the sampled CIRF. In subsequent developments, we use $h_i(t)$ as a short-hand notation for $h(t, i\Delta\tau) \Delta\tau$. Upon substituting the expression for the transmitted modulation [Equation (C.1)], the complex voltage sample in Equation (C.3) becomes

$$Z_k = r \sum_{l=0}^{\infty} e^{j\varphi_{k-l}} \sum_{i=0}^{N_\tau-1} \frac{1}{T} \int_{-T/2}^{T/2} dt h_i(t + kT) \Pi \left[\frac{t - i\Delta\tau}{T} + l \right] + N_k ,$$

where N_k is an AWGN sample with properties given in Equation (C.5). After a few changes in variables and assuming slow fading so $h_i(t + kT)$ can be pulled out of the time integral, the complex voltage sample can be written as

$$Z_k = r e^{j\varphi_k} \hat{S}_1 + r \sum_{l=1}^{\infty} e^{j\varphi_{k-l}} \hat{S}_2(l) + N_k .$$

Assuming that the number of delay samples per channel bit period $N_D = T/\Delta\tau$ is an integer, the \hat{S} terms are

$$\hat{S}_1 = \sum_{i=0}^{N_D-1} (1 - i/N_D) h_i$$

$$\hat{S}_2(l) = \sum_{i=0}^{N_\tau-1} \left[(i/N_D) h_{i+(l-1)N_D} + (1 - i/N_D) h_{i+lN_D} \right] .$$

The time argument of the sampled CIRF has been suppressed because of the assumption of slow fading.

With these definitions, the w_{\pm} terms in the DPSK decision metric are

$$w_{\pm} = \frac{1}{2} \left\{ \underbrace{re^{j\varphi_{k+1}} \hat{S}_1}_1 + \underbrace{re^{j\varphi_k} \hat{S}_2(1)}_2 + \underbrace{r \sum_{l=2}^{\infty} e^{j\varphi_{k+1-l}} \hat{S}_2(l)}_3 + \underbrace{N_{k+1}}_4 \right. \\ \left. \pm \underbrace{re^{j\varphi_k} \hat{S}_1}_5 \pm \underbrace{re^{j\varphi_{k-1}} \hat{S}_2(1)}_6 \pm \underbrace{r \sum_{l=2}^{\infty} e^{j\varphi_{k-l}} \hat{S}_2(l)}_7 \pm \underbrace{N_k}_8 \right\}$$

Again the terms are numbered as a short-hand way of referring to them below.

C.3.1 Statistics of w_+ and w_- .

As is the case for a continuous CIRF, the first order statistics of a sampled CIRF in Rayleigh fading are complex normal with zero mean. Thus the statistics of w_{\pm} are completely determined once the second order moments of the eight terms are computed. The second order moments of the noise terms are given in Equation (C.5), and all channel \times noise terms all have zero mean.

The variances of terms 1 and 5 are equal and are

$$\sigma_1^2 = \sigma_5^2 = \langle \hat{S}_1 \hat{S}_1^* \rangle = \frac{r^2}{4} \sum_{i=0}^{N_D-1} \sum_{i'=0}^{N_D-1} \langle h_i h_{i'}^* \rangle (1 - i/N_D)(1 - i'/N_D) .$$

Because the CIRF represents a stationary process in frequency, it is delta correlated in delay. Thus the delay correlation of the sampled CIRF is

$$\langle h_i h_{i'}^* \rangle = P_i \delta_{i,i'} ,$$

where P_i is the mean power of the i^{th} delay sample of the CIRF [Eqn. (2.14)]. The double sum in the variance expression then collapses to a single sum to give

$$\sigma_1^2 = \sigma_5^2 = \frac{r^2}{4} \sum_{i=0}^{N_D-1} P_i (1 - i/N_D)^2 .$$

Similarly,

$$\sigma_2^2 = \sigma_6^2 = \frac{r^2}{4} \sum_{i=0}^{N_D-1} \left[P_i (i/N_D)^2 + P_{i+N_D} (1 - i/N_D)^2 \right] ,$$

and

$$\sigma_3^2 = \sigma_7^2 = \sum_{l=2}^{\infty} \sum_{i=0}^{N_D-1} \left[P_{i+(l-1)N_D} (i/N_D)^2 + P_{i+lN_D} (1-i/N_D)^2 \right] .$$

Although the upper limit of the first sum in the expression for σ_3^2 is infinity, there are only a finite number (N_τ) of non-zero P_i terms, as determined by Equation (2.13).

The non-zero cross correlation terms are C_{12} , C_{15} , C_{25} , C_{36} , and C_{37} . These terms are

$$C_{12} = C_{25} = \frac{r^2}{4} \sum_{i=0}^{N_D-1} P_i (i/N_D)(1-i/N_D)$$

$$C_{15} = \sigma_1^2$$

$$C_{36} = \frac{r^2}{4} \sum_{i=0}^{N_D-1} P_{i+N_D} (i/N_D)(1-i/N_D)$$

$$C_{37} = \frac{r^2}{4} \sum_{l=1}^{\infty} \sum_{i=0}^{N_D-1} P_{i+lN_D} (i/N_D)(1-i/N_D) .$$

C.3.2 Evaluation of Sampled CIRF Sums.

Some care must be taken in evaluating the sums that occur in the expressions for the demodulation error rate with a sampled CIRF so that the delay grid in the analytic error rate expression contains exactly the same total signal energy as is contained in the COMLNK grid. The mean energy of the sampled CIRF in each delay bin (P_i) in terms of the normalized frequency selective bandwidth ($\lambda = 2\pi f_0 T$) and the number of delay samples per modulation period N_D is, from Equation 2.14,

$$P_i = (1 - e^{-\lambda/N_D}) e^{-i\lambda/N_D} .$$

The total number of delay samples N_τ in the grid is related to the total signal energy P_τ in the delay grid by the expression

$$N_\tau = 1 - \frac{\ln(1 - P_\tau)N_D}{\lambda} .$$

The current DSWA specification for the *minimum* total signal energy in the delay grid is 0.975 for which the factor $-\ln(1 - P_\tau)$ is equal to 3.7. We show later in this Appendix and in Appendix G for BFSK without hopping that this may be inadequate for ISI applications and should be increased to 0.999. For this new value of P_τ , the factor $-\ln(1 - P_\tau)$ is equal to 6.9, increasing the required number of delay samples by a factor of 1.9 for small values of λ .

The sums that occur in the sampled CIRF expressions for mean signal energy can be written in one of two forms:

$$E_X = \sum_{i=0}^{N_D-1} P_i R_X(i/N_D)$$

$$E_Y = \sum_{l=1}^{\infty} \sum_{i=0}^{N_D-1} P_{i+lN_D} R_Y(i/N_D)$$

where $R_X(i/N_D)$ and $R_Y(i/N_D)$ are expressions that result from the integrals over the sample time T . The l sum in the second expression results from evaluating the contribution of the intersymbol interference. The upper limit in the delay sums, $N_D - 1$, must be replaced by $N_\tau - 1$ when $N_\tau < N_D$. Equivalently, one could evaluate these expressions by setting $P_i = 0$ for $i \geq N_\tau$.

Because the sampled CIRF has an exponential fall-off for the delay bin energy,

$$P_{i+lN_D} = e^{-l\lambda} P_i ,$$

and the ISI sum can be separated from the delay sum:

$$E_Y = \left[\sum_{l=1}^{N_\tau/N_D-1} e^{-l\lambda} \right] \left[\sum_{i=0}^{N_D-1} P_i R_Y(i/N_D) \right] ,$$

where N_τ / N_D is the number of delayed modulation periods in the sampled CIRF. There are two cases to consider. When $N_\tau < N_D$, only signal energy from the immediately preceding modulation period contributes to the energy received during the on-time modulation period, and

$$E_Y = 0 \quad N_\tau < N_D .$$

When the delay spread equals or exceeds one modulation period ($N_\tau \geq N_D$), the ISI sum is

$$E_Y = \left[\sum_{l=1}^{N_\tau / N_D - 1} e^{-l\lambda} \right] \left[\sum_{i=0}^{N_D - 1} P_i R_Y(i / N_D) \right] + e^{-\lambda N_\tau / N_D} \left[\sum_{i=0}^{N_{\tau D} - 1} P_i R_X(i / N_D) \right] \quad N_\tau \geq N_D ,$$

where the sums are equal to zero when the upper limit is less than the lower limit. The second term is the contribution from the "leftover" delay samples, where

$$N_{\tau D} = \text{Mod}(N_\tau, N_D) ,$$

and $\text{Mod}(\cdot, \cdot)$ is the remainder of the first argument divided by the second.

C.3.3 DPSK Channel Bit Error Rate.

As is the case for a continuous CIRF, the demodulation error rate in frequency selective fading for a sampled CIRF depends on the transmitted modulation. Thus Equation (C.7) again gives the channel bit error rate. To simplify this calculation with little loss in generality, we will make the reasonable assumption that zeros and ones are equally likely and uniformly distributed in the transmitted data stream, so Equations (C.8) and (C.10) hold. The demodulation error rate for the case where the transmitted modulation is unchanged ($\varphi_{k+1} = \varphi_k$) is then given by Equations (C.11) and (C.12) using the sampled CIRF expressions for the variances and cross correlation coefficients. Similarly, the demodulation error rate for the case where the transmitted modulation is changed ($\varphi_{k+1} = \varphi_k + \pi$) is given by Equations (C.13) and (C.14), again using the sampled CIRF expressions. The average DPSK demodulation error rate is the linear average of the two error rates for the two cases.

The DPSK irreducible channel bit error rate in slow, frequency selective fading is plotted in Figure C-6 for sampled CIRFs with 2, 4, 8, and 32 delay samples per channel bit period. The total signal energy in the delay grid is 0.975 for these curves. For comparison, the irreducible error rate is also plotted for a continuous CIRF. The discontinuous jumps in the sampled CIRF curves occur as the number of delay samples in the grid changes. For small values of $f_0 T$ there are many delay samples and the discontinuities are less obvious in the curves. As $f_0 T$ increases, the number of delay samples eventually decreases to one, and the irreducible error rate is zero for flat fading (*i.e.*, for $N_\tau = 1$). Of course the value of $f_0 T$ where flat fading is reached depends on the number of delay samples per modulation period, N_D .

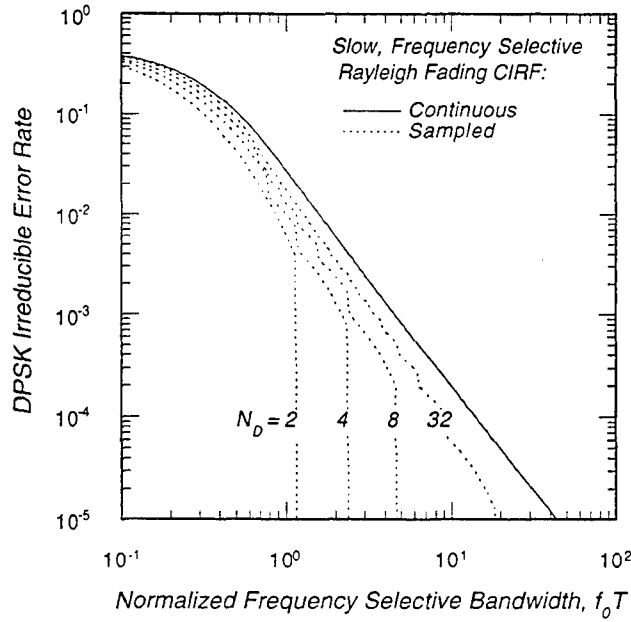


Figure C-6. DPSK irreducible channel bit error rate in slow, frequency selective fading with sampled CIRFs and $P_{\tau} = 0.975$.

Clearly there can be considerable difference between the irreducible DPSK demodulation error rate for sampled and continuous CIRFs depending on the value of $f_0 T$ and the number of delay samples per channel bit period. For $f_0 T = 1.0$ there is a factor of about 4.5 difference in the error rates for the $N_D = 2$ and continuous CIRF cases, but this difference shrinks to a factor of about 1.5 for $f_0 T = 0.2$.

Another feature of the curves is the discontinuities. The abrupt change in the irreducible error rate from zero to a finite value as the number of delay samples changes from 1 to 2 cannot be avoided. However, the discontinuities as N_{τ} varies from 2 to 3 to 4, for example, have the potential of producing discontinuous link performance results for weakly frequency selective fading channels.

The discontinuities are not caused by changes in N_{τ} *per se*, but rather are the result of the change in the total signal energy in the delay grid as that grid varies from $2\Delta\tau$ to $3\Delta\tau$, for example. This suggests that increasing the minimum energy in the grid from 0.975 to a larger value, say 0.999, can eliminate the discontinuities. This suggestion is confirmed by the results in Figure C-7 where the irreducible DPSK error

rate is plotted for the larger value of P_{τ} . These curves have a much smoother variation as $f_0 T$ decreases than do the corresponding curves in Figure C-6.

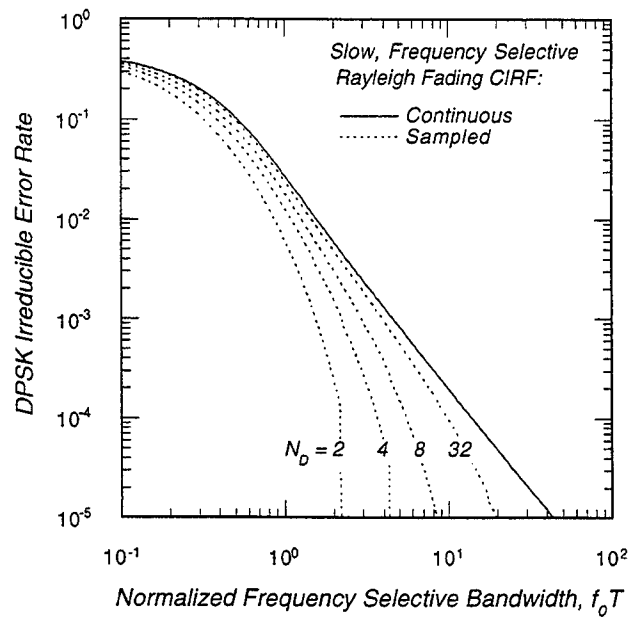


Figure C-7. DPSK irreducible channel bit error rate in slow, frequency selective fading with sampled CIRFs and $P_{\tau} = 0.999$.

APPENDIX D

DEMODULATION ERROR RATE FOR DPSK AND BFSK

Both differential phase-shift keying (DPSK) and binary frequency shift keying (BFSK) demodulation involve the comparison of two signal amplitudes. The purpose of this appendix is to calculate the probability that the amplitude of one voltage is greater than that of another where the two voltages are correlated, complex, zero-mean, and normally distributed random variables with different variances.

For differentially coherent DPSK demodulation, the decision metric is [Schwartz, Bennett, and Stein, 1966]

$$\hat{m} = \frac{1}{4}|Z_1 + Z_0| - \frac{1}{4}|Z_1 - Z_0|$$

where Z_0 and Z_1 are successive samples of the received signal voltage. If the transmitted modulation is unchanged from the 0 to 1 symbol period then $Z_1 + Z_0$ should have a larger amplitude than $Z_1 - Z_0$, and a demodulation error occurs if \hat{m} is negative. Conversely, if the transmitted modulation changes, then the amplitude of $Z_1 - Z_0$ should be larger than that of $Z_1 + Z_0$, and a demodulation error occurs if \hat{m} is positive. For BFSK, two tone filters are formed in the receiver corresponding to each of the two possible transmitted tones. The demodulation decision is formed by selecting the filter with the largest output amplitude.

For either DPSK or BFSK, the demodulation error rate is given by the probability that the amplitude of one voltage is greater than that of another voltage. To calculate this error rate for the case of Rayleigh fading, we need only to calculate the probability that $|w_1| \geq |w_2|$ where w_1 and w_2 are two complex, zero-mean, normally distributed random variables. A complication to this problem is introduced by the correlation between the two voltages. For both DPSK and BFSK this correlation is non-zero, and for the BFSK case this correlation is complex.

Consider w_1 and w_2 in terms of their real and imaginary parts,

$$\begin{aligned} w_1 &= x_1 + jy_1 \\ w_2 &= x_2 + jy_2 \end{aligned}$$

Because they are normally distributed, the second order statistics of w_1 and w_2 are completely determined by the mean values,

$$\langle x_1 \rangle = \langle x_2 \rangle = \langle y_1 \rangle = \langle y_2 \rangle = 0$$

variances,

$$\langle x_1^2 \rangle = \langle y_1^2 \rangle = \frac{1}{2} \sigma_1^2$$

$$\langle x_2^2 \rangle = \langle y_2^2 \rangle = \frac{1}{2} \sigma_2^2$$

and cross correlations,

$$\langle x_1 y_1 \rangle = \langle x_2 y_2 \rangle = 0$$

$$\langle x_1 x_2 \rangle = \langle y_1 y_2 \rangle = \frac{1}{2} \rho_R \sigma_1 \sigma_2 \quad ,$$

$$\langle x_1 y_2 \rangle = -\langle x_2 y_1 \rangle = \frac{1}{2} \rho_I \sigma_1 \sigma_2$$

where ρ_R and ρ_I denote the real and imaginary parts, respectively, of the normalized correlation coefficient. The first of these equations results because, for Rayleigh fading the real and imaginary parts of w_1 are uncorrelated as are the real and imaginary parts w_2 . The third equation reflects the fact that the two-frequency mutual coherence function is complex. Thus for BFSK modulation and frequency selective fading, the cross correlation of the outputs of the two tone filters is also complex. With these definitions it is easy to see that

$$\langle w_1^* w_1 \rangle = \sigma_1^2$$

$$\langle w_2^* w_2 \rangle = \sigma_2^2$$

$$\langle w_1 w_2 \rangle = 0$$

$$\langle w_1^* w_2 \rangle = \sigma_1 \sigma_2 (\rho_R + j \rho_I)$$

Thus the components of the complex voltages $\mathbf{w} = (x_1, y_1, x_2, y_2)$ are jointly normal with the covariance matrix

$$\mu = \frac{1}{2} \begin{bmatrix} \sigma_1^2 & 0 & \rho_R \sigma_1 \sigma_2 & \rho_I \sigma_1 \sigma_2 \\ 0 & \sigma_1^2 & -\rho_I \sigma_1 \sigma_2 & \rho_R \sigma_1 \sigma_2 \\ \rho_R \sigma_1 \sigma_2 & -\rho_I \sigma_1 \sigma_2 & \sigma_2^2 & 0 \\ \rho_I \sigma_1 \sigma_2 & \rho_R \sigma_1 \sigma_2 & 0 & \sigma_2^2 \end{bmatrix} ,$$

so the joint probability density function of \mathbf{w} is

$$f(x_1, y_1, x_2, y_2) = \frac{1}{\sqrt{(2\pi)^4 |\boldsymbol{\mu}|}} \exp\left[-\frac{1}{2} \mathbf{w} \cdot \boldsymbol{\mu}^{-1} \cdot \mathbf{w}^t\right] .$$

To compute the error probability we need the joint probability density function of the amplitudes of w_1 and w_2 . Changing to polar coordinates,

$$a_1 = \sqrt{x_1^2 + y_1^2} \quad \theta_1 = \tan^{-1}\left(\frac{y_1}{x_1}\right)$$

$$a_2 = \sqrt{x_2^2 + y_2^2} \quad \theta_2 = \tan^{-1}\left(\frac{y_2}{x_2}\right)$$

gives the following joint probability density function for the amplitudes and phases:

$$f(a_1, \theta_1, a_2, \theta_2) = \frac{1}{\pi^2 \sigma_1^2 \sigma_2^2 (1 - \rho_R^2 - \rho_I^2)} \times \exp\left\{-\frac{a_1^2 \sigma_2^2 + a_2^2 \sigma_1^2 + 2a_1 a_2 \sigma_1 \sigma_2 [\sin(\theta_1 - \theta_2) \rho_I - \cos(\theta_1 - \theta_2) \rho_R]}{\sigma_1^2 \sigma_2^2 (1 - \rho_R^2 - \rho_I^2)}\right\}$$

Integrating this expression over the range of the two phases ($0 \leq \theta_1 \leq 2\pi$, $0 \leq \theta_2 \leq 2\pi$) gives the joint probability density function of the two amplitudes:

$$f(a_1, a_2) = \frac{4a_1 a_2}{\sigma_1^2 \sigma_2^2 (1 - \rho^2)} \exp\left[-\frac{a_1^2 \sigma_2^2 + a_2^2 \sigma_1^2}{\sigma_1^2 \sigma_2^2 (1 - \rho^2)}\right] I_0\left[\frac{2\rho a_1 a_2}{\sigma_1 \sigma_2 (1 - \rho^2)}\right] ,$$

where $I_0(\cdot)$ is the modified Bessel function, and

$$\rho = \sqrt{\rho_R^2 + \rho_I^2} .$$

The DPSK or BFSK error rates are given by the probability that one amplitude is greater than another, so we arbitrarily set this equal to the probability that $a_1 > a_2$:

$$P(a_1 > a_2) = \int_0^\infty da_2 \int_{a_2}^\infty da_1 f(a_1, a_2) .$$

The a_1 integral can be written in terms of Marcum's Q -function [Marcum, 1960]:

$$P(a_1 > a_2) = \frac{2}{\sigma_2^2} \int_0^{\infty} a_2 \exp\left[-\frac{a_2^2}{\sigma_2^2}\right] Q\left[\frac{\sqrt{2}\rho a_2}{\sigma_2 \sqrt{1-\rho^2}}, \frac{\sqrt{2} a_2}{\sigma_1 \sqrt{1-\rho^2}}\right] da_2$$

where

$$Q(a, b) = \int_b^{\infty} x \exp\left[-\frac{1}{2}(a^2 + x^2)\right] I_0(ax) dx \quad .$$

The remaining integral in the expression for $P(a_1 > a_2)$ is given in Nuttall [1972]. Thus the probability that $a_1 > a_2$ is

$$P(a_1 > a_2) = \frac{1}{2} \left[1 - \frac{\sigma_2^2 - \sigma_1^2}{\sqrt{(\sigma_1^2 + \sigma_2^2)^2 - 4\sigma_1^2 \sigma_2^2 \rho^2}} \right] \quad .$$

APPENDIX E

DIFFERENTIAL PHASE-SHIFT KEYING WITH DIVERSITY COMBINING

A powerful mitigation technique for fading channels is having diversity in the received channel bits. Such diversity is obtained by transmitting the same data through independently fading channels, and a number of ways this can be achieved are described in *Bogusch* [1989]. Time diversity is easily obtained, for example, using block interleavers where the interleaver array is simply read out several times. Multiple copies of each symbol, separated in time by an interval corresponding to the span of the interleaver, are then transmitted over the channel. Spatial diversity can be obtained, for example, by simultaneously sending the same data from multiple spatially separated transmitters to the same receiver location or by receiving the data from the same transmitter with multiple spatially separated antennas.

With either type of diversity, one can not simply sum the signal voltages from independently fading channels because such coherent combining does not improve the signal-to-noise ratio unless the carrier phase is tracked on each channel to a common reference. When phase tracking is not feasible, or if phase ambiguities are not resolved, the information from the diversity channels must be non-coherently combined (*i.e.*, quantities related to signal energy must be combined).

Differential phase-shift keying (DPSK) demodulation decision metrics are non-coherent quantities that can be combined to take advantage of diversity. For each channel, the DPSK decision metric can be written as [*Schwartz, Bennett, and Stein*, 1966]

$$\hat{m} = E_+ - E_- ,$$

where

$$\begin{aligned} E_+ &= \frac{T}{4} |Z_{k+1} + Z_k|^2 \\ E_- &= \frac{T}{4} |Z_{k+1} - Z_k|^2 , \end{aligned}$$

and where Z_k is the signal plus noise voltage sample during the k^{th} symbol period¹. If the transmitted phase of the $k + 1^{st}$ symbol is the same as that of the k^{th} symbol, then in slow fading or non-fading channels the phase of the signal components of Z_k and Z_{k+1} will also be the same, the signal contributions will add in $Z_{k+1} + Z_k$ but will cancel in $Z_{k+1} - Z_k$, and \hat{m} should be positive. A demodulation error then occurs when \hat{m} is negative. Conversely, if the transmitted phase of the $k + 1^{st}$ symbol is 180° out of phase with that of the k^{th} symbol, then $Z_{k+1} - Z_k$ should have a larger magnitude than does $Z_{k+1} + Z_k$, and \hat{m} should be negative. In this case, a demodulation error occurs when \hat{m} is positive.

If N_C copies of the decision metric are available, they can be added together to form a combined metric:

$$\hat{m} = \frac{1}{N_C} \sum_{i=1}^{N_C} \hat{m}_i \quad . \quad (E.1)$$

The idea here is that the channels with faded signals have small values of \hat{m}_i , which contribute little to the sum, so primarily channels with strong signals determine the value of \hat{m} .

Although this is a simple combining algorithm, there are some very important implementation details. Obviously, the k^{th} symbol for each channel must correspond to the same transmitted symbol. If spatial diversity is used, for example, then the decision metrics from each channel must be aligned to account for possible differences in the time-of-arrival between the channels. Also, in order for channels with weak signals to have relatively small values of $|\hat{m}_i|$, all channels must have the same average noise contribution to $|\hat{m}_i|$. This can be accomplished by using noise-based AGC circuits.

The leading factor of $1/N_C$ in the combining equation is there to rescale the sum back to the same dynamic range as the individual values. This is important if there is a soft-decision decoder following the demodulation process. Otherwise, the scale factor has no effect on the probability of demodulation errors, and it is ignored in subsequent developments of the demodulation error rate with diversity combining.

¹ This form of the DPSK metric is convenient for analytic calculations but it is not the form actually used in hardware or in COMLNK. In a digital receiver, the DPSK decision metric is formulated as

$$\hat{m} = I_k I_{k-1} + Q_k Q_{k-1}.$$

Calculation of the DPSK demodulation error rate with diversity combining as described in Equation (E.1) is not simple. To the authors' knowledge, it is not possible to compute the probability density function of \hat{m} in closed form for an arbitrary number of combined non-fading additive white Gaussian noise (AWGN) channels except for the special case where all channels have exactly the same average signal-to-noise ratio. This latter case was addressed by *Bello and Nelin* [1962b] more than 35 years ago. In this appendix we present new results for DPSK decision metric diversity combining of two and three non-fading or Rician fading channels with unequal signal-to-noise ratios. We assume that the fading is slow and non-frequency selective.

E.1 STATISTICS OF SINGLE-CHANNEL DPSK DECISION METRIC.

The starting point for the calculation of the DPSK error rate with diversity combining is determining the statistics (*i.e.*, the probability density function of \hat{m}) of the single-channel DPSK decision metric for non-fading channels. This function is then used to compute the error rate when two or three metrics are summed together. The resulting expressions are averaged over fading distributions to obtain results valid in slow fading.

We show in Appendix B that in non-frequency selective fading we can assume, without loss of generality, that the phase of the transmitted signal is unchanged between the k^{th} and $k + 1^{st}$ channel bit periods when calculating the demodulation error rate. Thus the signal voltage coherently adds in the expression for E_+ and cancels in the expression for E_- in the absence of propagation effects when we assume that the receiver is ideally tracking the signal time-of-arrival and frequency. We also show in Appendix B that the additive white Gaussian noise (AWGN) voltage contributions to E_+ and E_- are uncorrelated and thus independent. The probability distributions for the amplitude associated with E_+ and E_- are then Rician and Rayleigh, respectively. Thus the probability density functions $f_+(E_+)$ and $f_-(E_-)$ of the signal plus noise energy and the noise only energy, respectively, are

$$f_+(E_+) = \frac{1}{N_0/2} \exp\left[-\frac{E_+ + r^2 T}{N_0/2}\right] I_0\left[\frac{2\sqrt{r^2 T E_+}}{N_0/2}\right],$$

$$f_-(E_-) = \frac{1}{N_0/2} \exp\left[-\frac{E_-}{N_0/2}\right]$$

where $I_0(\cdot)$ is the modified Bessel function, N_0 is the one-sided noise spectral density, T is the channel bit period, which is also equal to the sample period of Z_k , and r is the amplitude of the received signal. Both of these probability density functions are zero for negative values of the argument.

The probability density function of the difference $\hat{m} = E_+ - E_-$ is then given in terms of the probability density functions of E_+ and E_- by the usual expression:

$$f(\hat{m}) = \begin{cases} \int_{\hat{m}}^{\infty} f_-(x - \hat{m}) f_+(x) dx & \hat{m} > 0 \\ \int_0^{\infty} f_-(x - \hat{m}) f_+(x) dx & \hat{m} \leq 0 \end{cases}.$$

Using integrals in *Nuttall* [1972] to evaluate these expressions, the probability density function of \hat{m} reduces to

$$f(\hat{m}) = \begin{cases} \frac{1}{N_0} \exp\left[\frac{2\hat{m} - E_{cb}}{N_0}\right] & \hat{m} \leq 0 \\ \frac{1}{N_0} \exp\left[\frac{2\hat{m} - E_{cb}}{N_0}\right] Q\left[\sqrt{2\frac{E_{cb}}{N_0}}, \sqrt{\frac{8\hat{m}}{N_0}}\right] & \hat{m} > 0 \end{cases}, \quad (\text{E.2})$$

where $E_{cb} = r^2 T$ is the channel bit energy, and $Q(\cdot, \cdot)$ is Marcum's Q -function [*Marcum*, 1960]:

$$Q(a, b) = \int_b^{\infty} x \exp\left[-\frac{1}{2}(x^2 + a^2)\right] I_0(ax) dx.$$

With our assumption that the transmitted modulation is unchanged between the k^{th} and $k + 1^{\text{st}}$ channel bit periods, the DPSK channel bit or demodulation error rate is equal to the probability that \hat{m} is negative:

$$P_e = \int_{-\infty}^0 f(\hat{m}) d\hat{m} = \frac{1}{2} \exp\left[-\frac{E_{cb}}{N_0}\right]$$

which is the familiar non-fading (AWGN) expression for a single channel.

In the developments below we need the cumulative distribution function of the single-channel DPSK decision metric:

$$F(\hat{m}) = \int_{-\infty}^{\hat{m}} f(x) dx .$$

Using integrals given in *Nuttall* [1972], this distribution function is

$$F(\hat{m}) = \begin{cases} \frac{1}{2} \exp \left[-\frac{E_{cb} - 2\hat{m}}{N_0} \right] & \hat{m} \leq 0 \\ 1 - Q \left[2\sqrt{\frac{E_{cb}}{N_0}}, \sqrt{\frac{4\hat{m}}{N_0}} \right] + \frac{1}{2} \exp \left[-\frac{E_{cb} - 2\hat{m}}{N_0} \right] Q \left[\sqrt{\frac{2E_{cb}}{N_0}}, \sqrt{\frac{8\hat{m}}{N_0}} \right] & \hat{m} > 0 \end{cases} . \quad (E.3)$$

E.2 NON-FADING DPSK DEMODULATION ERROR RATE WITH TWO-AND THREE-CHANNEL COMBINING.

When two DPSK decision metrics for exactly the same transmitted channel bit are available, the metrics can be added together:

$$\hat{m} = \hat{m}_1 + \hat{m}_2 .$$

Note that we have not renormalized the metrics because for our current purpose, which is to compute the probability that \hat{m} is negative given that the transmitted modulation is unchanged between the k^{th} and $k+1^{st}$ channel bit periods, the normalization is irrelevant (*i.e.*, the probability of demodulation error is independent of the normalization factor as long as the normalization is positive).

To calculate the demodulation error rate we assume that the receiver is ideally tracking signal time-of-arrival and frequency and that the AWGN of the two channels is uncorrelated and has the same average power. The most restrictive of these assumptions is that the noise power is the same for both channels, especially when spatial diversity is used and the two metrics come from two different receivers. However, the evaluation of the effects of different average noise powers is a problem for which COMLNK is the ideal analysis tool. Our purpose here is to develop expressions for an idealized case that can be used to validate the simulation and estimate the performance gain afforded by diversity combining.

Given unchanged transmitted modulation between the two channel bit periods, a formal expression for the probability of demodulation error is just

$$P_e = \int_{-\infty}^0 f(\hat{m}) d\hat{m} ,$$

where now $f(\hat{m})$ is the probability density function of the combined metric. The calculation of $f(\hat{m})$ is complicated and is also unnecessary because $f(\hat{m})$ can be written in terms of the probability density functions of the two separate decision metrics. For uncorrelated AWGN the two decision metrics are also independent so the expression for P_e can be rewritten as

$$P_e = \int_{-\infty}^0 d\hat{m} \int_{-\infty}^{\infty} dx f_1(\hat{m} - x) f_2(x) ,$$

where $f_1(\cdot)$ and $f_2(\cdot)$ are the probability density functions of the two individual decision metrics. Both of these functions are given by the expressions in Equation (E.2). After some rearrangement the demodulation error rate reduces to

$$P_e = \int_{-\infty}^{\infty} f_2(\hat{m}) F_1(-\hat{m}) d\hat{m} ,$$

where $F_1(\cdot)$ is the cumulative distribution function of the individual decision metrics. The probability density function of the DPSK decision metric, derived in the previous subsection, has a different functional form depending on the sign of the argument. Thus to evaluate the expression for P_e one more step is necessary:

$$P_e = \int_{-\infty}^0 f_{2,-}(\hat{m}) F_{1,+}(-\hat{m}) d\hat{m} + \int_0^{\infty} f_{2,+}(\hat{m}) F_{1,-}(-\hat{m}) d\hat{m} ,$$

where $f_{2,+}(\cdot)$ and $F_{1,+}(\cdot)$ and $f_{2,-}(\cdot)$ and $F_{1,-}(\cdot)$ are the probability density function and cumulative distribution function, respectively, for positive and negative arguments, respectively. The probability of error can now be evaluated directly from this last expression, again using integrals given in Nuttall [1972].

After considerable algebra, the non-fading, two-channel DPSK error rate is

$$P_e = \frac{1}{8} [4 + \gamma_1 + \gamma_2] e^{-(\gamma_1 + \gamma_2)} , \quad (\text{Two Channels, Non-Fading}) \quad (\text{E.4})$$

where γ_1 and γ_2 are the values of the channel bit energy-to-noise spectral density ratio (E_{cb} / N_0) for the two channels.

When three DPSK decision metrics for exactly the same transmitted channel bit are available, the combined metric is

$$\hat{m} = \hat{m}_1 + \hat{m}_2 + \hat{m}_3 \quad .$$

Given that the transmitted modulation is unchanged between the k^{th} and $k+1^{st}$ channel bit periods, the probability of a channel bit error is the probability that \hat{m} is negative:

$$P_e = \int_{-\infty}^0 dx \int_{-\infty}^{\infty} dy f_3(x-y) \int_{-\infty}^{\infty} dz f_2(y-z) f_1(z) \quad ,$$

where $f_1(\cdot)$, $f_2(\cdot)$, and $f_3(\cdot)$ are the probability density functions of the individual metrics. Each of these functions is given by the expressions in Equation (E.2). Note that the last integral in the expression for P_e is the probability density function of $\hat{m}_1 + \hat{m}_2$, the last two integrals are the probability density function of $\hat{m}_1 + \hat{m}_2 + \hat{m}_3$, and the first integral is the probability that $\hat{m}_1 + \hat{m}_2 + \hat{m}_3$ is negative. After some manipulation the error rate then becomes

$$P_e = \int_{-\infty}^{\infty} dx f_1(x) \int_{-\infty}^{\infty} dy f_2(y-x) F_3(-y) \quad ,$$

where, again, $F_3(\cdot)$ is the cumulative distribution of a single-channel decision metric given in Equation (E.3). Remembering that the probability density and cumulative distribution functions have different forms for positive and negative arguments, this expression expands to six terms:

$$P_e = P_{e,1} + P_{e,2} + P_{e,3} + P_{e,4} + P_{e,5} + P_{e,6} \quad ,$$

where

$$P_{e,1} = \int_{-\infty}^0 dx f_{1,-}(x) \int_{-\infty}^x dy f_{2,-}(y-x) F_{3,+}(-y)$$

$$P_{e,2} = \int_{-\infty}^0 dx f_{1,-}(x) \int_x^0 dy f_{2,+}(y-x) F_{3,+}(-y)$$

$$P_{e,3} = \int_{-\infty}^0 dx f_{1,-}(x) \int_0^{\infty} dy f_{2,+}(y-x) F_{3,-}(-y)$$

$$P_{e,4} = \int_0^{\infty} dx f_{1,+}(x) \int_{-\infty}^0 dy f_{2,-}(y-x) F_{3,+}(-y)$$

$$P_{e,5} = \int_0^{\infty} dx f_{1,+}(x) \int_0^x dy f_{2,-}(y-x) F_{3,-}(-y)$$

$$P_{e,6} = \int_0^{\infty} dx f_{1,+}(x) \int_x^{\infty} dy f_{2,+}(y-x) F_{3,-}(-y) .$$

Most of these terms are just plain tedious to compute, but with some persistence closed form expressions can be obtained for all six. Two integrals are needed that are not in *Nuttall* [1972], but can be derived from results therein. These are

$$\int_0^{\infty} x^3 e^{-x^2} Q(a, bx) dx = \frac{1}{2} - \frac{b^2 \left[(b^2 + 2)(b^2 + 4) + a^2 b^2 \right]}{2(b^2 + 2)^3} \exp \left[-\frac{a^2}{b^2 + 2} \right]$$

and

$$\int_0^{\infty} x^3 Q(a, bx) dx = 2 \frac{1 + a^2 + \frac{1}{8} a^4}{b^4} .$$

The non-fading (AWGN) demodulation error rate when three uncorrelated DPSK decisions metrics are combined is

$$P_e = \frac{1}{64} \left[(4 + \gamma_1 + \gamma_2 + \gamma_3)(8 + \gamma_1 + \gamma_2 + \gamma_3) \right] e^{-(\gamma_1 + \gamma_2 + \gamma_3)} ,$$

(Three Channels, Non-Fading)

where γ_1 , γ_2 , and γ_3 are the values of the channel bit energy-to-noise spectral density ratio for the three DPSK metrics.

The non-fading (AWGN) DPSK demodulation error rates with one-, two-, or three-channel combining of the decision metrics are plotted versus the single channel bit energy-to-noise spectral density ratio per channel in Figure E-1. It is assumed that all N_C channels have exactly the same value of E_{cb} / N_0 .

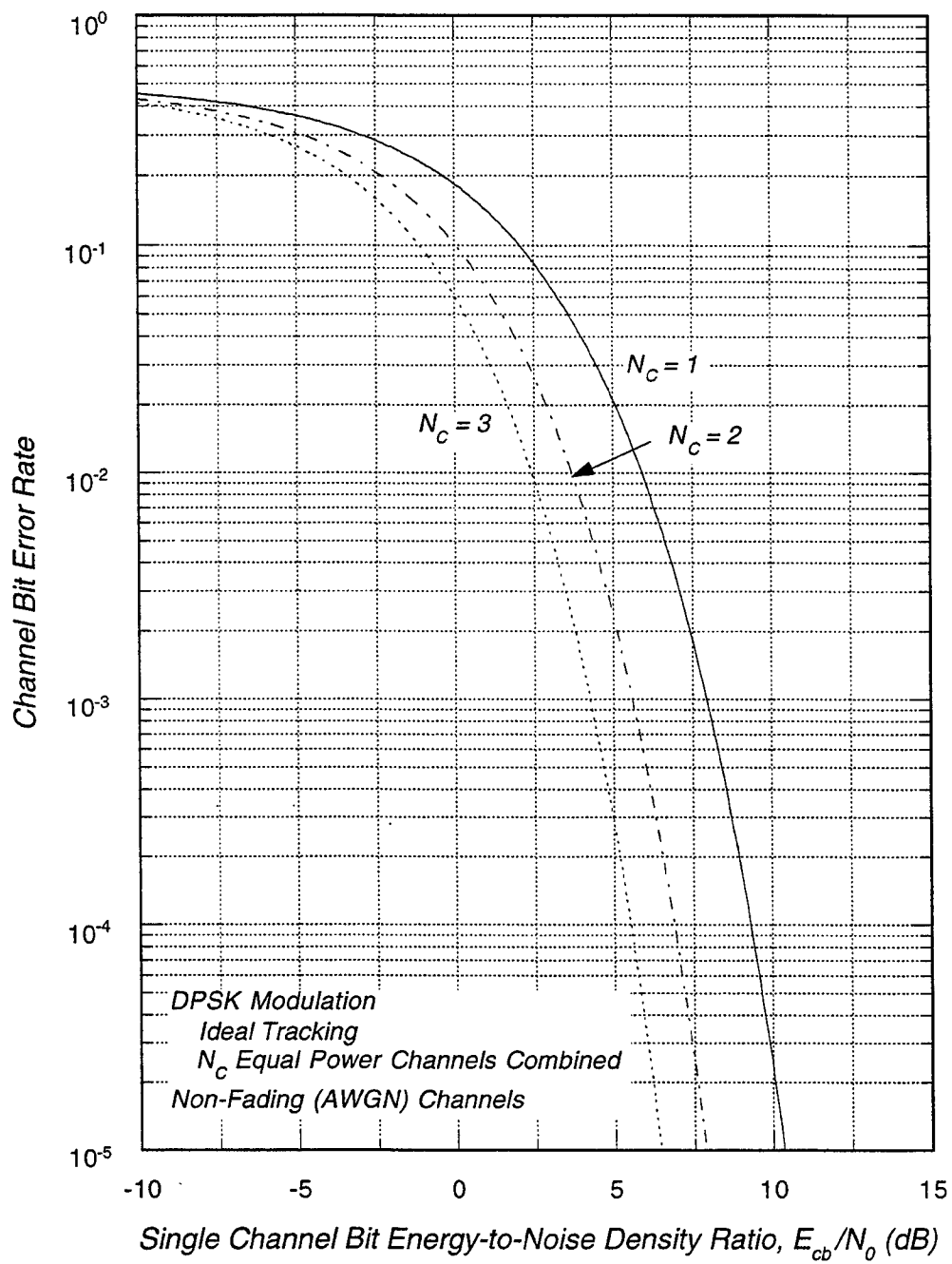


Figure E-1. Channel bit error rate versus single channel signal-to-noise ratio after combining DPSK decision metrics from N_C non-fading channels.

Note that we are plotting these curves versus the channel bit energy-to-noise spectral density ratio of a single channel. When the power in each channel is equal, as is the case here, the two-channel case has 3 dB more total power and the three-channel case has 4.8 dB more power than the single-channel case. Thus, if the diversity is obtained by repeating a user bit N_C times over the same channel and if the channel bit error rates are plotted versus user bit energy-to-noise spectral density ratio, where

$$E_{ub}/N_0 = N_C(E_{cb}/N_0) ,$$

then the two-channel curve must be shifted to the right by 3 dB and the three-channel curve must be shifted right by 4.8 dB. There is therefore a small penalty for time-diversity combining if the channel is not fading.

This penalty is the noncoherent combining loss that is illustrated in Figure E-2, where we re-plot the combined DPSK demodulation error rate versus E_{ub}/N_0 . Here the error rate increases as N_C increases because diversity combining only provides a gain when there is uncorrelated fading on each channel. When the channels are non-fading, as they are here, or when the fading on the multiple channels is highly correlated, one obtains a noncoherent combining *loss*.

E.3 SLOW FADING DPSK DEMODULATION ERROR RATE WITH TWO- AND THREE-CHANNEL COMBINING.

Of course the full advantage of diversity combining is realized in Rayleigh fading channels when the fading is uncorrelated from one channel to the next. For two-channel combining, we consider two cases. The first case is where there is uncorrelated Rician fading on both channels, and the second case is where there is correlated Rayleigh fading on the two channels. The first case illustrates how the advantage of combining increases as the fading channel statistics vary from non-fading to Rician fading to Rayleigh fading. The second case is interesting for either spatial or temporal diversity. For example, with spatial diversity the two metrics might come from receivers separated by a distance insufficient to completely decorrelate the fading channels. With temporal diversity, correlated fading occurs when the temporal separation of the channel bit pairs from which the metrics are formed is not large compared to the channel decorrelation time. The goal here is to illustrate how much correlation there can be in the channels before the advantage of diversity combining is lost. Finally, we compute the three-channel result for uncorrelated Rayleigh fading on all channels.

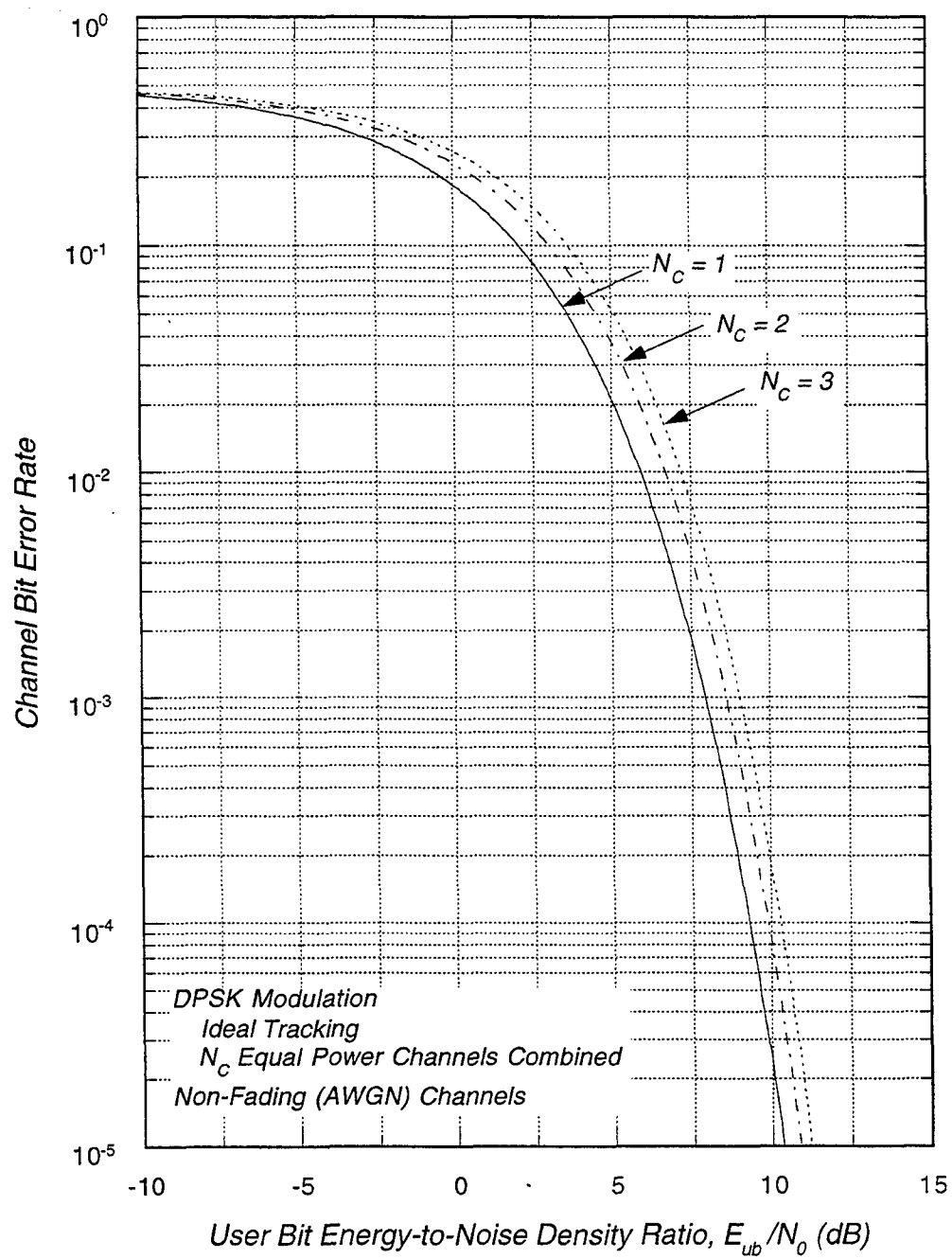


Figure E-2. Channel bit error rate versus total signal-to-noise ratio after combining DPSK decision metrics from N_c non-fading channels.

E.3.1 Two-Channel Case With Uncorrelated Slow Rician Fading.

In this subsection we consider the case of uncorrelated, slow Rician fading. Because the underlying statistics of the channel are normal, uncorrelated Rician fading is also independent. The average channel bit error rate is then given by averaging the non-fading expression over the two Rician distributions for the two channels:

$$\langle P_e \rangle = \int_0^\infty dS_1 f_{R,1}(S_1) \int_0^\infty dS_2 f_{R,2}(S_2) P_e(\gamma_1 S_1, \gamma_2 S_2) ,$$

where $f_{R,1}(\cdot)$ and $f_{R,2}(\cdot)$ are the probability density functions of Rician fading for the two channels. Both of these functions are given in Equation (2.2a) with S_0 set to unity. The quantity $P_e(\gamma_1 S_1, \gamma_2 S_2)$ is the two-channel non-fading result for the two E_{cb}/N_0 values equal to $\gamma_1 S_1$ and $\gamma_2 S_2$. In evaluating this expression we encounter the following expectations over the Rician distribution:

$$\begin{aligned} \langle e^{-\gamma S} \rangle &= \frac{1}{\gamma(1-R)+1} \exp \left[-\frac{\gamma R}{\gamma(1-R)+1} \right] \\ \langle S e^{-\gamma S} \rangle &= \frac{\gamma(1-R)^2 + 1}{[\gamma(1-R)+1]^3} \exp \left[-\frac{\gamma R}{\gamma(1-R)+1} \right] . \end{aligned}$$

The quantity R in these expectations is the ‘‘Rician index’’ which is defined in terms of the scintillation index S_4 of the channel:

$$R = \sqrt{1 - S_4^2} .$$

The second expectation requires an integral that is not directly in *Nuttall* [1972] or, to the authors’ knowledge, any other readily available integral table. The integral is²

$$\int_0^\infty x^3 e^{-ax^2} I_0(bx) dx = \frac{1}{2a^2} \left(1 + \frac{b^2}{4a} \right) \exp \left[\frac{b^2}{4a} \right] . \quad (\text{E.5})$$

The average two-channel bit error rate for uncorrelated Rician fading, in terms of the two expectations, is

² *Nuttall* [1972] gives a similar integral with x rather than x^3 in the integrand. This expression is obtained by differentiating the Nuttall result with respect to a .

$$\langle P_e \rangle = \frac{1}{2} \langle e^{-\gamma_1 S_1} \rangle \langle e^{-\gamma_2 S_2} \rangle + \frac{1}{8} \gamma_1 \langle S_1 e^{-\gamma_1 S_1} \rangle \langle e^{-\gamma_2 S_2} \rangle + \frac{1}{8} \gamma_2 \langle e^{-\gamma_1 S_1} \rangle \langle S_2 e^{-\gamma_2 S_2} \rangle$$

(Two Channels, Uncorrelated Rician Fading)

In the limit that both channels are non-fading, the Rician index of both is unity, the Rician probability density function acts as the delta function $\delta(S-1)$, both expectations are equal to $e^{-\gamma}$, and the non-fading limit of this expression is identical to the AWGN error rate in Equation (E.4).

When both channels are full Rayleigh fading the error rate reduces to

$$\langle P_e \rangle = \frac{6\gamma_1\gamma_2 + 5(\gamma_1 + \gamma_2) + 4}{8(\gamma_1 + 1)^2(\gamma_2 + 1)^2} \quad (E.6)$$

(Two Channels, Uncorrelated Rayleigh Fading)

It is interesting to consider this expression when one channel has a very small signal-to-noise ratio (say $\gamma_2 \approx 0$). The resulting error rate in the limit that the other signal-to-noise ratio is large is

$$\langle P_e \rangle \approx \frac{5}{8} \gamma_1^{-1} \quad (\gamma_1 \gg 1, \gamma_2 \approx 0)$$

If only the strong signal channel is used to form the DPSK decision metric then this limiting error rate is

$$\langle P_e \rangle \approx \frac{1}{2} \gamma_1^{-1} \quad (\gamma_1 \gg 1, \text{single channel})$$

Thus there is a small penalty for adding the contribution of a channel with a weak signal to the decision metric, as one would expect. Equivalently, there is a small benefit to not using the contribution from channels with weak signals if that condition can be recognized *a priori*.

The two-channel, Rician fading demodulation error rate is plotted in Figure E-3 versus the average single channel bit energy-to-noise density ratio without propagation effects. The values of E_{cb}/N_0 and S_4 are assumed to be the same in both channels. For comparison, the single-channel DPSK demodulation error rate curve is also plotted in the figure. As is the case for single-channel demodulation, Rician fading curves for 2-channel demodulation essentially vary from the non-fading to full Rayleigh fading curves as S_4 varies from 0.25 to 0.75 or so.

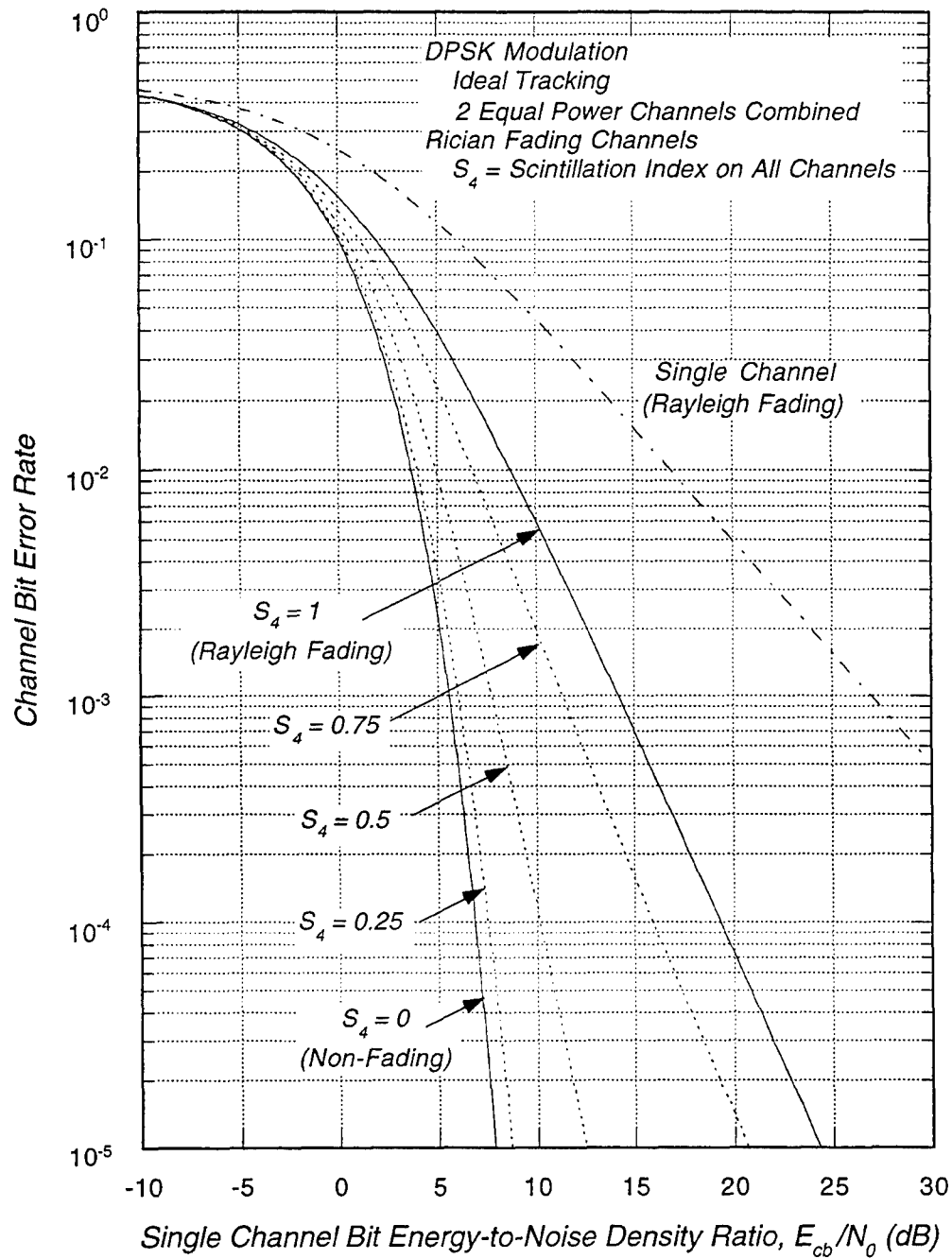


Figure E-3. Channel bit error rate after combining DPSK decision metrics from two Rician-fading channels.

E.3.2 Two-Channel Case With Correlated Slow Rayleigh Fading.

Now we consider the effects of correlated Rayleigh fading on the two channels. The noise in the two decision metrics is uncorrelated as before. The joint probability density function of correlated Rayleigh fading powers S_1 and S_2 is

$$f_p(S_1, S_2) = \frac{1}{1-\rho^2} \exp\left[-\frac{S_1 + S_2}{1-\rho^2}\right] I_0\left[\frac{2\rho\sqrt{S_1 S_2}}{1-\rho^2}\right],$$

where ρ is the correlation coefficient of the complex channel response function [Dana, 1995b]. The average error rate is then given by the double integral

$$\langle P_e \rangle = \int_0^\infty dS_1 \int_0^\infty dS_2 f_p(S_1, S_2) P_e(\gamma_1 S_1, \gamma_2 S_2).$$

After considerable algebra this expression reduces to

$$\langle P_e \rangle = \frac{6\gamma_1\gamma_2(1-\rho^2) + 5(\gamma_1 + \gamma_2) + 4}{8[\gamma_1\gamma_2(1-\rho^2) + \gamma_1 + \gamma_2 + 1]^2}.$$

(Two Channels, Correlated Rayleigh Fading)

In the limit of uncorrelated fading ($\rho = 0$) this expression reduces to that in Equation (E.6), as it should. The large signal-to-noise ratio limit of the uncorrelated Rayleigh fading expression is

$$\langle P_e \rangle \approx \frac{3}{4}(\gamma_1\gamma_2)^{-1} \quad (\rho = 0 \text{ and } \gamma_1 \gg 1, \gamma_2 \gg 1),$$

whereas in the limit of perfectly correlated fading ($\rho = 1$) and large values of the signal-to-noise ratio, the error rate is

$$\langle P_e \rangle \approx \frac{5}{8}(\gamma_1 + \gamma_2)^{-1} \quad (\rho = 1 \text{ and } \gamma_1 \gg 1, \gamma_2 \gg 1).$$

Clearly there can be a large error rate penalty for combining DPSK decision metrics from correlated fading channels relative to that obtained using metrics from uncorrelated fading channels. Still, combining two metrics with perfectly correlated Rayleigh fading but uncorrelated noise provides an approximate 5/8 reduction in the error rate over the single-channel value, at the expense of 3 dB more total power. Thus, there is still a noncoherent combining loss with correlated fading.

The two-channel DPSK demodulation error rate with correlated Rayleigh fading is plotted in Figure E-4 for several values of the channel correlation coefficient. Although there is a large penalty for combining decision metrics from two correlated fading channels, it is seen that the channels must be highly correlated to suffer the full penalty. Indeed, correlation coefficients greater than 0.75 are necessary for any significant degradation over the uncorrelated case.

Note, however, that there may be little advantage to diversity combining in coded systems. Given a good code with sufficient interleaving, channel bit error rates on the order of 0.1 can produce negligible decoded bit error rates. Figure E-4 shows only a small gain with uncorrelated fading in such cases. The major advantage of diversity combining may arise from relaxed interleaver requirements resulting from a shorter effective decorrelation time. This remains to be investigated.

E.3.3 Three-Channel Case With Uncorrelated Slow Rayleigh Fading.

In uncorrelated fading channels, the average three-channel combined error rate is computed from the expression

$$\begin{aligned} \langle P_e \rangle = & \frac{1}{2} \langle e^{-\gamma_1 S_1} \rangle \langle e^{-\gamma_2 S_2} \rangle \langle e^{-\gamma_3 S_3} \rangle + \frac{3}{16} \left[\gamma_1 \langle S_1 e^{-\gamma_1 S_1} \rangle \langle e^{-\gamma_2 S_2} \rangle \langle e^{-\gamma_3 S_3} \rangle + \right. \\ & + \gamma_2 \langle e^{-\gamma_1 S_1} \rangle \langle S_2 e^{-\gamma_2 S_2} \rangle \langle e^{-\gamma_3 S_3} \rangle + \gamma_3 \langle e^{-\gamma_1 S_1} \rangle \langle e^{-\gamma_2 S_2} \rangle \langle S_3 e^{-\gamma_3 S_3} \rangle \Big] \\ & + \frac{1}{32} \left[\gamma_1 \gamma_2 \langle S_1 e^{-\gamma_1 S_1} \rangle \langle S_2 e^{-\gamma_2 S_2} \rangle \langle e^{-\gamma_3 S_3} \rangle + \gamma_1 \gamma_3 \langle S_1 e^{-\gamma_1 S_1} \rangle \langle e^{-\gamma_2 S_2} \rangle \langle S_3 e^{-\gamma_3 S_3} \rangle \right. \\ & + \gamma_2 \gamma_3 \langle e^{-\gamma_1 S_1} \rangle \langle S_2 e^{-\gamma_2 S_2} \rangle \langle S_3 e^{-\gamma_3 S_3} \rangle \Big] + \frac{1}{64} \left[\gamma_1^2 \langle S_1^2 e^{-\gamma_1 S_1} \rangle \langle e^{-\gamma_2 S_2} \rangle \langle e^{-\gamma_3 S_3} \rangle + \right. \\ & + \gamma_2^2 \langle e^{-\gamma_1 S_1} \rangle \langle S_2^2 e^{-\gamma_2 S_2} \rangle \langle e^{-\gamma_3 S_3} \rangle + \gamma_3^2 \langle e^{-\gamma_1 S_1} \rangle \langle e^{-\gamma_2 S_2} \rangle \langle S_3^2 e^{-\gamma_3 S_3} \rangle \Big] \end{aligned}$$

This error rate can be evaluated for Rician fading using the following expectation:

$$\langle S^2 e^{-\gamma S} \rangle = \frac{2[\gamma(1-R)^2 + 1]^2 - R^2}{[\gamma(1-R) + 1]^5} \exp\left[-\frac{\gamma R}{\gamma(1-R) + 1}\right].$$

To calculate this expectation we have used the following integral derived by differentiating the expression in Equation (E.5) with respect to a :

$$\int_0^\infty x^5 e^{-ax^2} I_0(bx) dx = \frac{1}{a^3} \left(1 + \frac{b^2}{2a} + \frac{b^4}{32a^2} \right) \exp\left[\frac{b^2}{4a}\right].$$

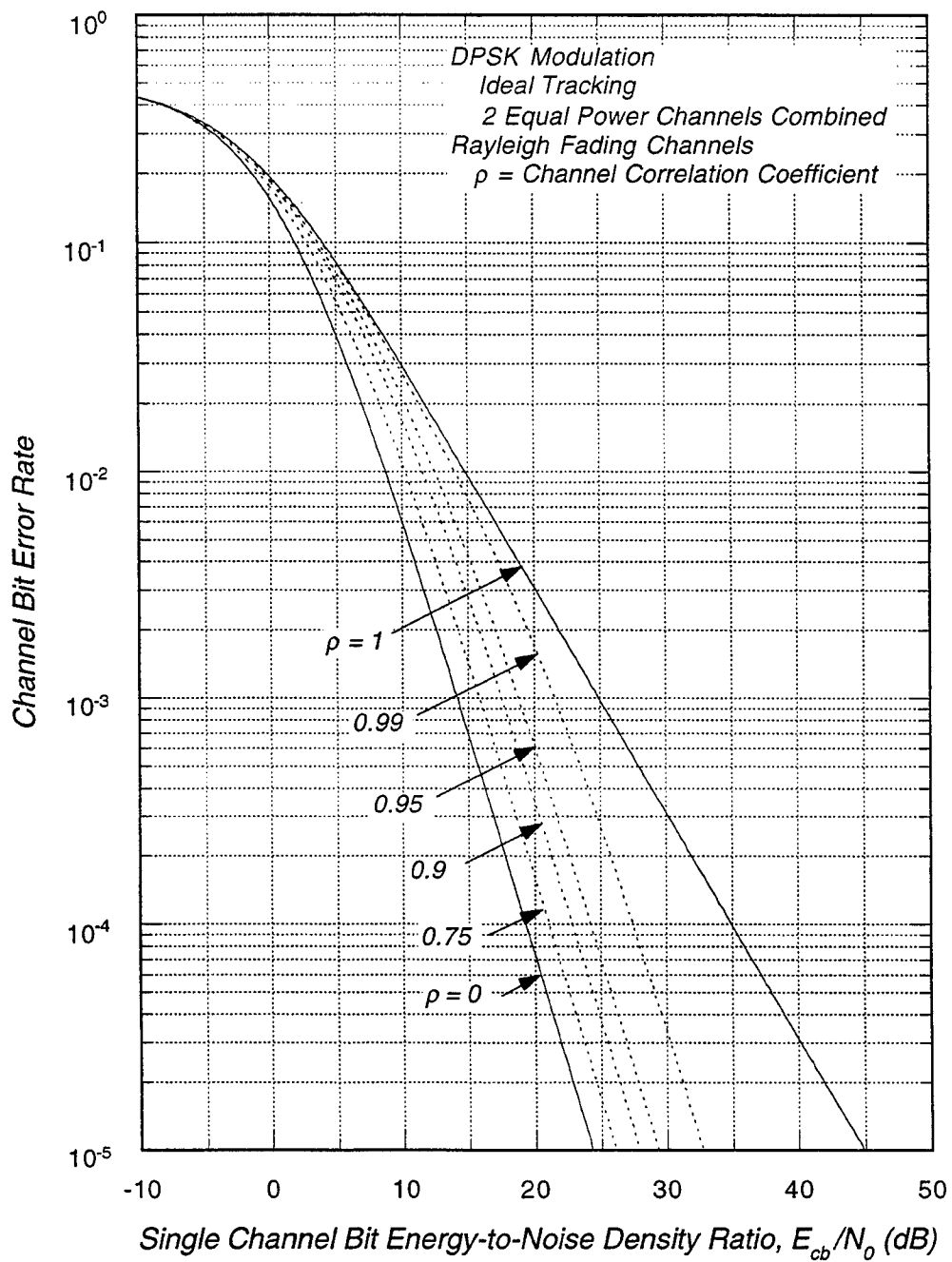


Figure E-4. Channel bit error rate after combining DPSK decision metrics from two correlated Rayleigh-fading channels.

Expressions for the lower-order moments are given in the previous subsection.

In the limit of Rayleigh fading on all three channels, the average demodulation error rate reduces to

$$\begin{aligned} \langle P_e \rangle = & \frac{1}{2(\gamma_1 + 1)(\gamma_2 + 1)(\gamma_3 + 1)} \\ & + \frac{21\gamma_1\gamma_2\gamma_3 + 13(\gamma_1\gamma_2 + \gamma_1\gamma_3 + \gamma_2\gamma_3) + 6(\gamma_1 + \gamma_2 + \gamma_3)}{32(\gamma_1 + 1)^2(\gamma_2 + 1)^2(\gamma_3 + 1)^2} \\ & + \frac{\gamma_1^2(\gamma_2 + 1)^2(\gamma_3 + 1)^2 + \gamma_2^2(\gamma_1 + 1)^2(\gamma_3 + 1)^2 + \gamma_3^2(\gamma_1 + 1)^2(\gamma_2 + 1)^2}{32(\gamma_1 + 1)^3(\gamma_2 + 1)^3(\gamma_3 + 1)^3} \end{aligned}$$

(Three Channels, Uncorrelated Rayleigh Fading)

The channel bit error rate from one-, two-, and three-channel combining of the DPSK decision metrics is plotted in Figure E-5 versus the single channel bit energy-to-noise spectral density ratio E_{cb}/N_0 , and in Figure E-6 versus the total user bit energy-to-noise spectral density ratio E_{ub}/N_0 . For comparison, the non-fading, single-channel error rate curve is also plotted in the figures.

The advantage of diversity combining of uncorrelated channels is evident from the error rate curves in Figure E-5 for the case where the multiple channels do not dilute the value of E_{cb}/N_0 per channel. In this case, combining two Rayleigh-fading decision metrics produces a demodulation error rate that is smaller than the single-channel non-fading value for error rates above about ten percent, and combining three Rayleigh-fading metrics results in a demodulation error rate that is smaller than the non-fading, single-channel value for error rates above about one percent.

The advantage of diversity combining is not so evident when the total user bit energy is divided among the channels, as illustrated in Figure E-6. In this case the multiple channel bit error rate with Rayleigh fading is about the same as that for a single channel with fading until the demodulation error rate is significantly below 10 percent, and the three-channel error rate curve is not much different than the two-channel curve until the demodulation error rate is well below one percent.

In either case, the advantage of diversity combining may be more evident in the bit error rate at the output of a decoder under slow fading conditions as the diversity combining helps to randomize the decoder input errors.

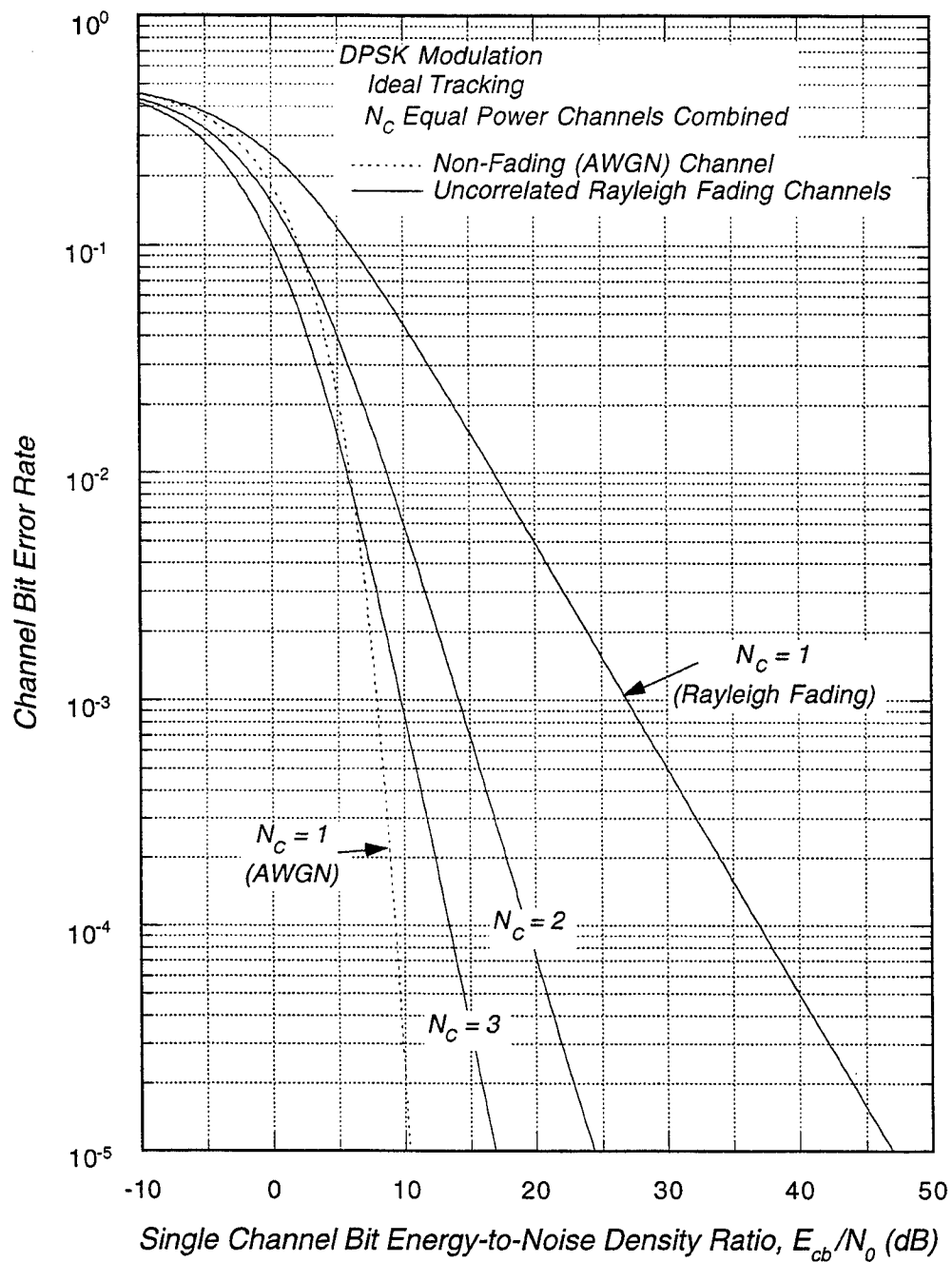


Figure E-5. Channel bit error rate after one-, two- and three-channel combining of DPSK decision metrics versus single channel signal-to-noise ratio E_{cb}/N_0 for uncorrelated Rayleigh fading.

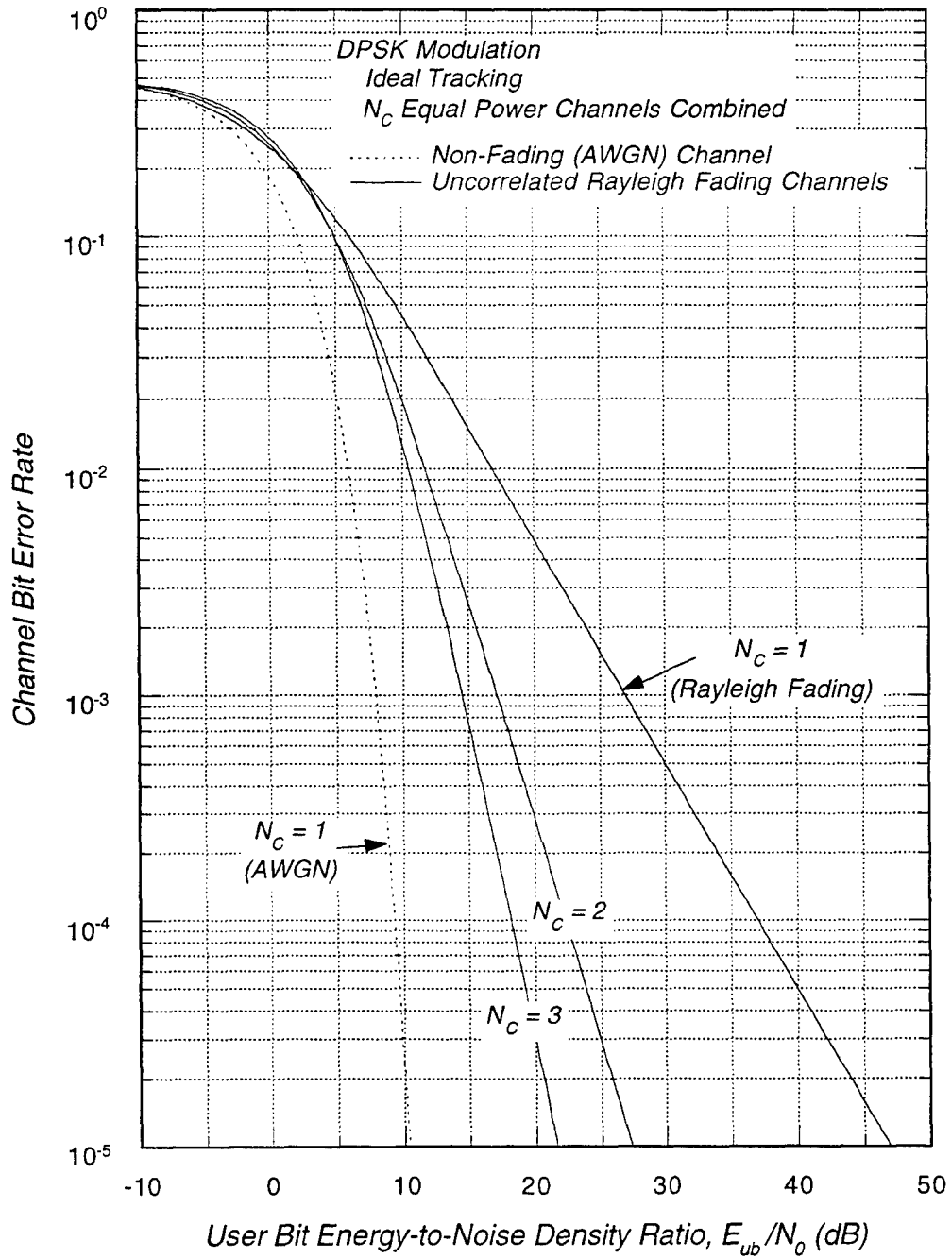


Figure E-6. Channel bit error rate after one-, two- and three-channel combining of DPSK decision metrics versus total user signal-to-noise ratio E_{ub}/N_0 for uncorrelated Rayleigh fading.

APPENDIX F

DEMODULATION PERFORMANCE OF NON-COHERENT M -ary FREQUENCY SHIFT KEYING IN FAST FADING

A functional block diagram of a non-coherent M -ary frequency shift keying (FSK) receiver is shown in Figure F-1. In such a receiver there are separate filters for each of the M possible transmitted tones. For non-coherent demodulation considered here, the filter with the largest output amplitude is selected to represent the transmitted tone. With suppressed-carrier tracking, the output of the selected filter is used in the automatic gain control (AGC), delay lock loop (DLL), and automatic frequency control (AFC) tracking loops. Thus the output of the demodulator is fed into the tracking loops in this block diagram. This is only one of several possible design configurations. Other implementations employ unmodulated sync symbols for tracking.

The block diagram is for a frequency hopped (FH) link. In this appendix we assume that the tracking loops are operating perfectly. That is, the receiver timing is aligned with the channel symbols, and the residual frequency error is small so any phase variation of the signal during a symbol is caused by the channel and the frequency offset between the tone and the carrier. With this assumption, frequency hopping and DLL performance only have an impact on the calculation of demodulation performance in frequency selective fading channels, which is discussed in Appendix G.

For orthogonal signaling, ideal time and frequency tracking, and slow or non-fading channels, the signal is completely canceled in all filters except the one corresponding to the transmitted tone. However, for fast fading the signal is not completely canceled in any of the M -ary filters because of the channel-imposed phase distortion. When this occurs, the output signal voltages of all of the filters are correlated, and it is not practical to calculate closed-form expressions for the demodulation error rate for general M -ary signaling. The one exception to this procedure is binary FSK (BFSK) modulation for which we can calculate an exact expression for the error rate. As suggested by *Rutherford* [1978]¹, we compute the mean power out of each filter, and calculate the demodulation error rate ignoring the correlation of the filter outputs. We will show that this procedure provides an upper limit to the demodulation error rate.

¹ *Rutherford* [1978] computed fast fading M -ary performance for channels with Gaussian Doppler spectra and assumed that the cross correlation coefficients are zero.

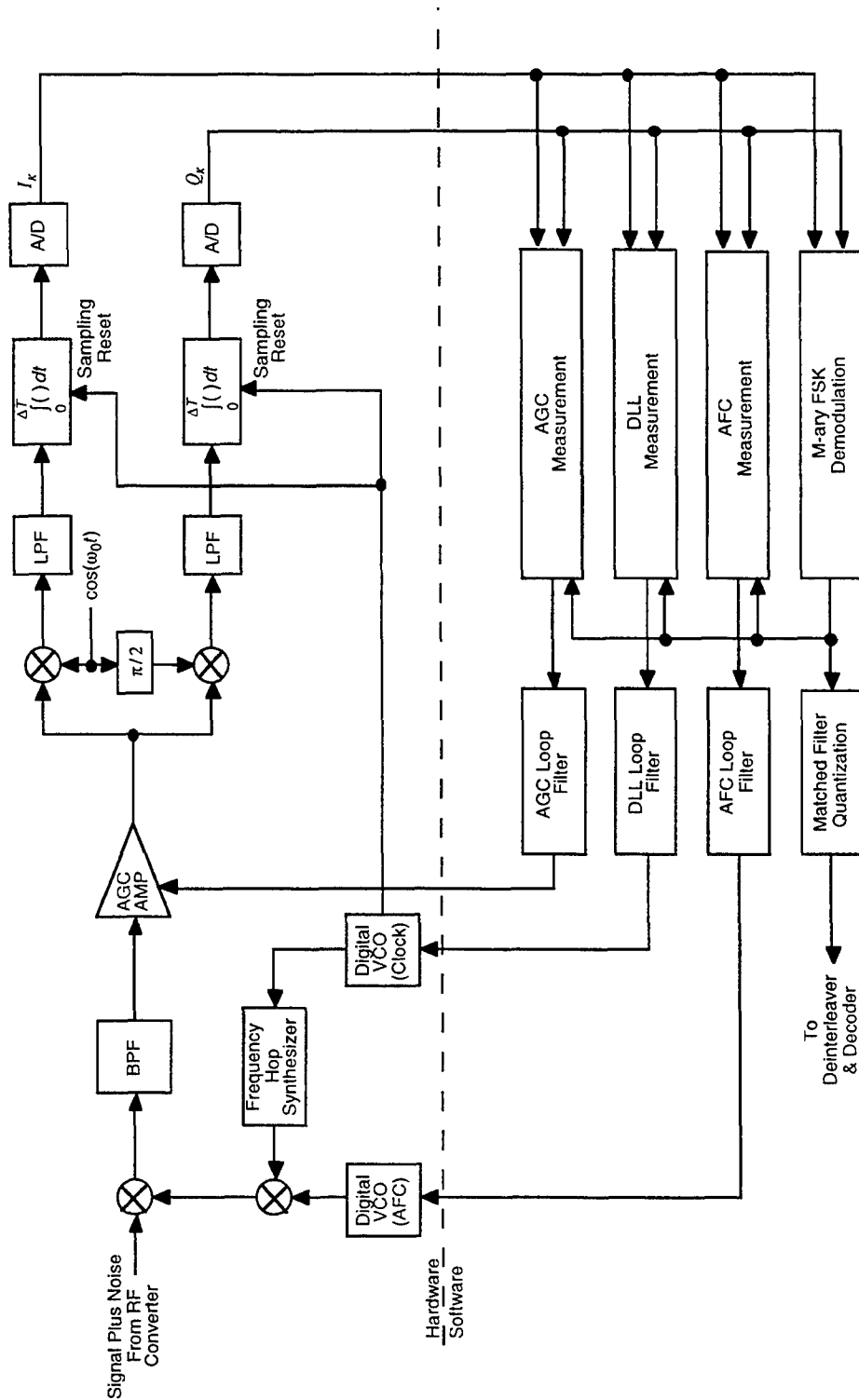


Figure F-1. Block diagram of an M-ary FSK receiver.

Some general results for FSK modulation are given in the first subsection of this appendix. Then the non-fading and slow fading M -ary FSK demodulation error rates are derived in Section F.2. BFSK demodulation error rates for fast, flat Rayleigh fading are developed in Section F.3 and are extended to the M -ary case in Section F.4. Because both COMLNK and modern digital receivers form the tone filters using discrete Fourier transforms (DFTs)², in section F.5 we investigate the effect of time sampling on the M -ary FSK error rate.

F.1 GENERAL FSK RESULTS.

In an M -ary FSK communications link, the transmitted signal during the k^{th} modulation period is

$$m(t) = \sum_k \exp[j(n_k \pi \Delta f)t] \Pi\left[\frac{t}{T} - k\right],$$

where Δf is the tone spacing and T is the symbol period (*i.e.*, the duration of a transmitted tone). The transmitted tone is determined by the value of n_k : $n_k = \pm 1$ for BFSK, $n_k = \pm 1, \pm 3$ for QFSK, $n_k = \pm 1, \pm 3, \pm 5, \pm 7$ for 8-ary FSK, and so on. The rectangular function $\Pi(\cdot)$ is defined as

$$\Pi(x) = \begin{cases} 1 & \text{if } |x| \leq \frac{1}{2} \\ 0 & \text{otherwise} \end{cases}.$$

Note that the exponential term in the expression for $m(t)$ represents a frequency offset in the transmitted signal, so the carrier frequency *per se* is never transmitted (unless sync symbol tracking is employed).

The received signal is the convolution of the channel impulse response function and the transmitted modulation:

$$u(t) = r \int_0^{\infty} m(t - \tau) h(t, \tau) d\tau,$$

² This is one implementation option. COMLNK also provides the option of multiple filters centered at the modulation offset frequencies of each of the M possible symbols. This configuration is well suited to large tone spacings and enables use of independent-tone signaling.

where r is the mean received signal amplitude. This signal is then processed in tone filters to determine which tone was transmitted. The output voltage of the i^{th} filter during the k^{th} symbol period is

$$Z_{i,k} = \frac{1}{T} \int_{(k-1/2)T}^{(k+1/2)T} [u(t) + n(t)] \exp[-j(i\pi\Delta f)t] dt .$$

There is one such filter for each of the possible n_k transmitted tones. The signal is demodulated by selecting filter with the largest output amplitude³.

The complex voltage $n(t)$ is additive white Gaussian noise (AWGN) with the usual properties:

$$\begin{aligned} \langle n(t) \rangle &= 0 \\ \langle n(t) n(t') \rangle &= 0 , \\ \langle n(t) n^*(t') \rangle &= N_0 \delta(t - t') \end{aligned}$$

where N_0 is the one-sided noise spectral density, and $\delta(\cdot)$ is the Dirac delta function. The second equation results because the real and imaginary parts of AWGN are uncorrelated. The noise contribution to the i^{th} tone filter output voltage is then

$$N_{i,k} = \frac{1}{T} \int_{(k-1/2)T}^{(k+1/2)T} n(t) \exp[-j(i\pi\Delta f)t] dt .$$

Because $n(t)$ is a complex, normally distributed random process with zero mean, $N_{i,k}$ is similarly distributed. To complete the description of the tone filter output noise, we need the variance and cross correlation of $N_{i,k}$. The noise cross correlation is

$$C_{i,i'}^N = \langle N_{i,k} N_{i',k}^* \rangle = \frac{1}{T^2} \int_{(k-1/2)T}^{(k+1/2)T} dt e^{-j(i\pi\Delta f)t} \int_{(k-1/2)T}^{(k+1/2)T} dt' e^{j(i'\pi\Delta f)t'} \langle n(t) n^*(t') \rangle .$$

³ This is true only for hard-decision demodulation, which is what is treated in this analysis. Coded systems often employ soft-decision demodulation, wherein the outputs of all M filters are used in subsequent processing.

AWGN is delta-correlated, so this expression reduces to

$$C_{i,i'}^N = \frac{N_0}{T} \frac{\sin\left[\frac{1}{2}\pi(i-i')\Delta f T\right]}{\frac{1}{2}\pi(i-i')\Delta f T} = \begin{cases} N_0/T & \text{if } i' = i \\ 0 & \text{otherwise} \end{cases}$$

for orthogonal signaling (*i.e.*, $\Delta f T = \text{positive integer}$ and $i - i' = \text{even integer}$ so the argument of the sine function is an integer $\times \pi$).

F.2 *M*-ary FSK IN NON-FADING AND SLOW FADING CHANNELS.

In a non-fading (AWGN) channel, the channel impulse response function imparts a simple phase rotation on the signal:

$$h(t, \tau) = e^{j\theta} \delta(\tau) ,$$

where the delta function indicates that the signal arrives with zero delay relative to its nominal time-of-arrival, and the phase θ varies slowly during the symbol period T assuming adequate frequency tracking in the receiver. The output voltages of the tone filters are then

$$Z_{i,k} = \frac{re^{j\theta}}{T} \int_{(k-1/2)T}^{(k+1/2)T} \exp[j\pi\Delta f(n_k - i)t] dt + N_{i,k} .$$

The *M*-ary FSK demodulation error rate in AWGN is then given by the probability that any of the filters that do not correspond to the transmitted tone have a larger output amplitude than that of the "correct filter". This problem reduces to computing the probability that any one of $M - 1$ uncorrelated, complex, zero mean, normally distributed random variables has a larger amplitude than another uncorrelated, normally distributed random variable with a non-zero mean. To compute this probability, we need the variances and cross correlation coefficients of the output voltages for the *M* tone filters.

Assuming that the receiver noise is uncorrelated with both the transmitted modulation and the channel fluctuations (if any), the cross correlation coefficients of the tone filter outputs are separable into signal and noise contributions:

$$C_{i,i'} = \langle Z_{i,k} Z_{i',k}^* \rangle = C_{i,i'}^S + C_{i,i'}^N ,$$

where $C_{i,i'}^N$ is given above. Without loss of generality, we assume that the i^{th} filter corresponds to the transmitted tone (i.e., $i = n_k$), and i' represents any filter. The signal contribution to the cross correlation coefficient is then

$$C_{i,i'}^S = \frac{r^2}{T^2} \int_{(k-1/2)T}^{(k+1/2)T} dt \int_{(k-1/2)T}^{(k+1/2)T} dt' e^{-j\pi(n_k-i')\Delta f t'} = \frac{r^2 \sin\left[\frac{1}{2}\pi\Delta f T(n_k - i')\right]}{\frac{1}{2}\pi\Delta f T(n_k - i')} .$$

In the limit that $i' = n_k$, this expression reduces to r^2 which is the signal energy out of the filter corresponding to the transmitted tone. The signal contribution to the output energy of the other filters is identically zero when the signaling is orthogonal:

$$\begin{aligned} \Delta f T &= \text{an integer} > 0 \\ n_k - i' &= \text{an even integer} \end{aligned} \quad (\text{orthogonal signaling}) ,$$

where the dimensionless quantity $\Delta f T$ is the normalized tone spacing.

The non-fading M -ary FSK demodulation error rate is now easy to compute. The output voltage of the i^{th} filter corresponding to the transmitted tone (in developments below we often refer to this as the "correct filter") is

$$Z_{i,k} = r e^{j\theta} + N_{i,k} ,$$

and the output voltages of the $M-1$ "other filters" are

$$Z_{i',k} = N_{i',k} ,$$

where $Z_{i',k}$ and $Z_{i'',k}$ ($i' \neq i''$) are uncorrelated and thus are independent, normally distributed random variables. The voltage $Z_{i,k}$ from the correct filter is a complex, zero mean random process plus a complex constant, so its signal plus noise ($S+N$) amplitude $a_1 = |Z_{i,k}|$ has a Rician probability density function:

$$f_{S+N}(a_1) = \frac{2a_1}{N_0/T} \exp\left[-\frac{a_1^2 + r^2}{N_0/T}\right] I_0\left[\frac{2ra_1}{N_0/T}\right] ,$$

where $I_0(\cdot)$ is the modified Bessel function. The voltages from the other $M-1$ tone filters are complex, zero mean random variables, so their amplitudes $a_l = |Z_{i',k}|$, comprised only of noise, have Rayleigh probability density functions:

$$f_N(a_l) = \frac{2a_l}{N_0/T} \exp\left[-\frac{a_l^2}{N_0/T}\right] \quad (l = 2, \dots, M) ,$$

where $f_N(\cdot)$ denotes the probability density function of the amplitude of any one of the noise-only filters. In a moment we need the cumulative distribution of any one of the noise-only amplitudes. This Rayleigh distribution has the familiar form

$$F_N(a) = \int_0^a f_N(a') da' = 1 - \exp\left[-\frac{a^2 T}{N_0}\right] .$$

It is easier to compute the probability that the correct filter is selected first and then subtract this probability from one to get the error rate. This is the probability that the maximum of the $M-1$ noise-only amplitudes is less than that of the correct tone filter with signal plus noise. The probability of selecting the correct tone filter is

$$P_c = \int_0^\infty da_1 f_{S+N}(a_1) \int_0^{a_1} da_0 f_{N,\max}(a_0) ,$$

where $f_{N,\max}(\cdot)$ is the probability density function of the largest of the $M-1$ noise-only amplitudes. The second integral (over a_0) is just the cumulative distribution of the maximum noise-only amplitude which is

$$F_{N,\max}(a) = [F_N(a)]^{M-1} .$$

The probability of correct demodulation is then

$$P_c = \int_0^\infty f_{S+N}(a) \left[1 - \exp(-a^2 T / N_0)\right]^{M-1} da .$$

This remaining integral is performed by expanding the term in square brackets in a binomial series:

$$\left[1 - e^{-x}\right]^{M-1} = \sum_{k=0}^{M-1} \binom{M-1}{k} (-1)^k e^{-kx} .$$

With this expansion, the probability of choosing the correct filter is

$$P_c = 1 - \sum_{k=1}^{M-1} \frac{(-1)^{k+1}}{k+1} \binom{M-1}{k} \exp\left[-\left(\frac{k}{k+1}\right) \frac{r^2 T}{N_0}\right] .$$

The second term on the right-hand-side of this equation is the probability that the filter with the largest amplitude does not correspond to the transmitted tone. This probability is equal to the M -ary symbol error rate.

For each transmitted symbol there are $\log_2 M$ channel bits. The average number of channel bits in error given a symbol error⁴ is $\frac{1}{2}M/(M-1)$. Thus the channel bit error rate P_e is related to M -ary symbol error rate by [Viterbi, 1966]

$$P_e = \frac{M/2}{M-1}(1 - P_c) \quad . \quad (\text{F.1})$$

In deriving this expression, it is assumed that every incorrect filter is equally likely to be chosen when a demodulation error occurs. This is the case here because the average noise energy out of each incorrect filter is the same. This is not the case in fast fading, however, where signal energy from the correct tone filter is spread preferentially into adjacent incorrect filters. Thus the expression in Equation (F.1) does not hold in general.

One more adjustment is necessary to transform from M -ary symbols to channel bits. The quantity r^2T/N_0 is the symbol energy-to-noise spectral density ratio. This is related to the channel bit energy-to-noise spectral density ratio (E_{cb}/N_0) by the number of channel bits per symbol (*i.e.*, $\log_2 M$):

$$\frac{E_{cb}}{N_0} = \frac{1}{\log_2 M} \frac{r^2T}{N_0} \quad .$$

With these transformations from symbols to channel bits, the M -ary FSK channel bit error rate for AWGN channels reduces to

$$P_e = \sum_{k=2}^M (-1)^k \frac{(M/2)(M-2)!}{k!(M-k)!} \exp \left[-\frac{(k-1)\log_2 M}{k} \frac{E_{cb}}{N_0} \right] \quad (M\text{-ary FSK, AWGN}) \quad .$$

⁴ This ratio is derived as follows. For any transmitted symbol, there are $M-1$ equally likely symbol errors in non-fading or slow fading channels. In each of the $\log_2 M$ bit positions there are exactly $M/2$ bits in error, when averaged over the ensemble of $M-1$ symbol errors, so the number of bit errors is $(M/2)\log_2 M$. The total number of bits contained in the $M-1$ symbols is $(M-1)\log_2 M$. The ratio is obtained by dividing the number of bit errors by the total number of bits.

For BFSK ($M = 2$) this expression reduces further to the familiar form

$$P_e = \frac{1}{2} \exp \left[-\frac{E_{cb}}{2N_0} \right] \quad (\text{BFSK, AWGN}) .$$

This formula is similar to that for DPSK demodulation except that 3 dB more signal power is needed with BFSK to achieve the same error rate. So why would one ever chose FSK modulation over DPSK modulation? One reason is that M -ary FSK demodulation in non-fading channels becomes more efficient as M increases (*i.e.*, a lower value of E_{cb} / N_0 is required for a given bit error rate). This is shown in Figure F-2 where the channel bit error rate is plotted for a few values of M (2, 4, 8, 16, and 32). The relative improvement decreases with increasing M , and there is about one dB advantage in 16-ary FSK relative to 8-ary FSK in AWGN. Also, 8-ary FSK is about one dB better than DPSK in AWGN. Thus 8-ary and 16-ary FSK have become the standard modulation techniques for some systems.

It will be seen that M -ary FSK demodulation performance degrades in fading channels as does the performance of all signalling techniques. First, for slow fading where the channel decorrelation time is much longer than the symbol period, the average demodulation error rate is given by averaging the AWGN expression over the fading distribution:

$$\langle P_e \rangle = \int_0^{\infty} P_e(\gamma S) f(S) dS$$

where γ is the channel bit energy-to-noise spectral density ratio in the absence of fading. The probability density function of Rician fading $f(S)$ is given in Equation (2.2a), and the resulting average M -ary channel bit error rate is

$$\langle P_e \rangle = \sum_{k=2}^M (-1)^k \frac{(M/2)(M-2)!}{k!(M-k)!} \frac{1}{1 + \gamma_k(1-R)} \exp \left[-\frac{\gamma_k R}{1 + \gamma_k(1-R)} \right] \quad (\text{Rician Fading})$$

where R is the "Rician index" defined in Equation (2.2b), and

$$\gamma_k = \frac{k-1}{k} \log_2 M \frac{E_{cb}}{N_0} .$$

The 8-ary FSK demodulation performance in slow Rician fading is plotted in Figure F-3 for several values of the scintillation index S_4 . These curves are nearly identical to those for DPSK modulation performance in Rician fading plotted in Figure B.5, and comments made about that figure apply here.

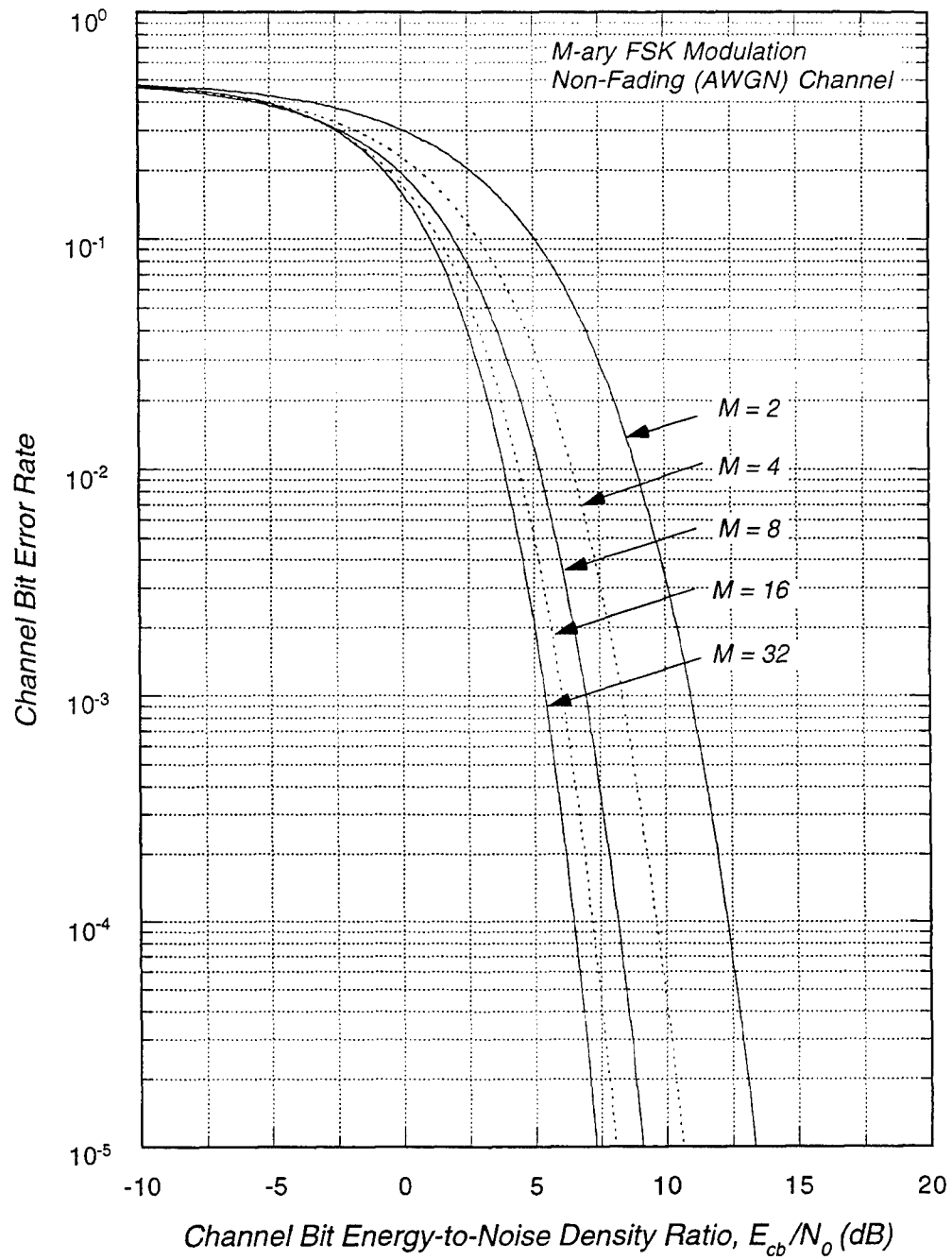


Figure F-2. M -ary FSK demodulation error rate for non-fading (AWGN) channels.

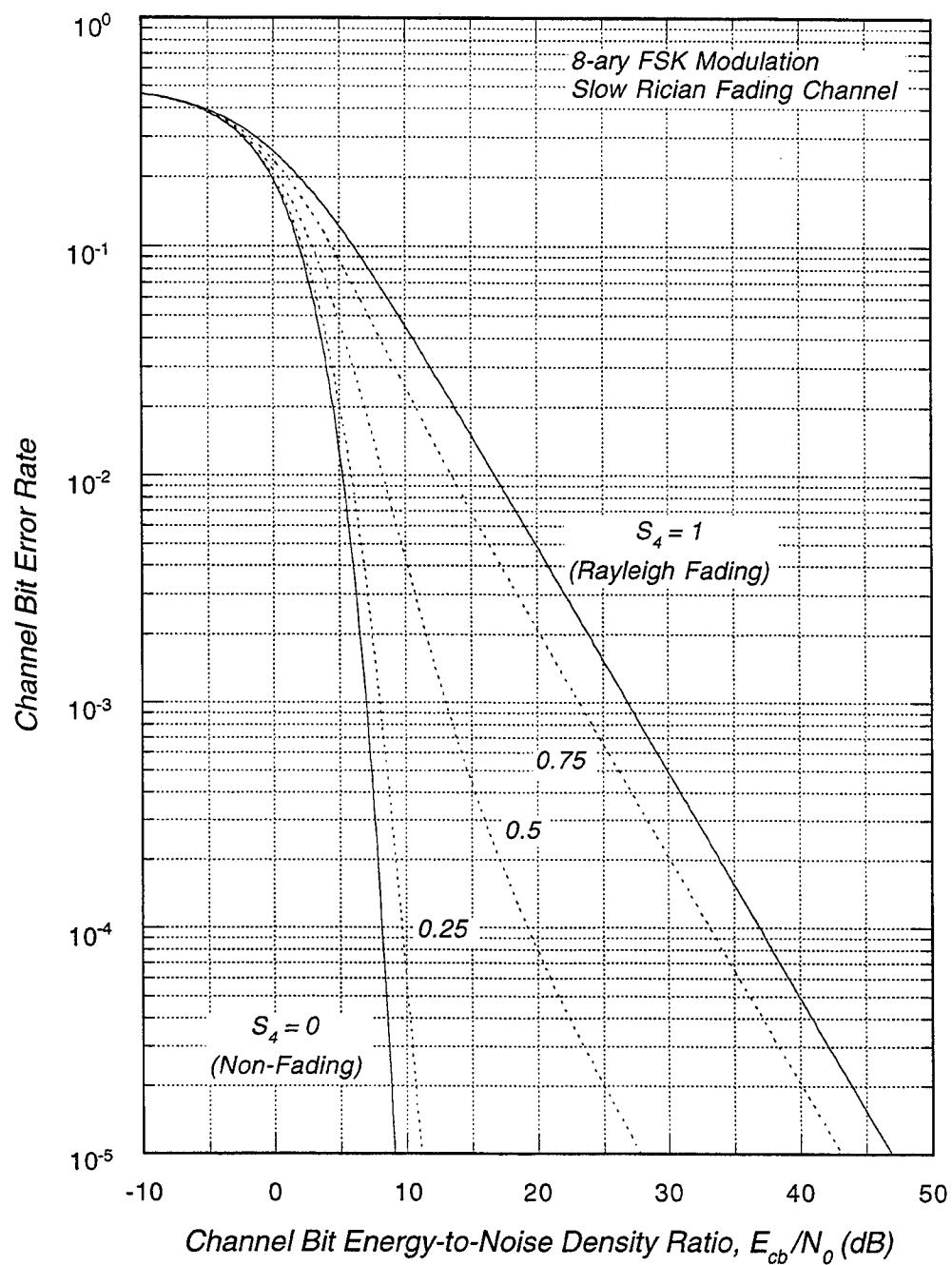


Figure F-3. 8-ary FSK demodulation error rate for slow Rician fading channels.

The real advantage of M -ary FSK over DPSK is seen in fast or frequency selective fading channels. The AWGN and slow fading demodulation error rates given above do not explicitly depend on two important properties of a transmitted FSK waveform: tone spacing and frequency hopping. The first of these provides a powerful mitigation technique for fast fading and the second for frequency selective fading. Neither is applicable to a DPSK waveform⁵, and the two together allow much more robust performance of FSK in severe fading channels than is possible with DPSK.

BFSK demodulation performance in fast fading is discussed in Section F.3 and is extended to M -ary FSK in Sections F.4 and F.5. BFSK performance in frequency selective fading is analyzed in Appendices G and H.

F.3 BFSK IN FAST FADING CHANNELS.

In a fast, flat fading channel, the channel impulse response function can be written as $h(t, \tau) = h(t)\delta(\tau)$, where the Delta function indicates that all of the signal arrives with zero delay relative to its nominal time-of-arrival, and $h(t)$ is referred to as the channel response function. For Rayleigh fading, $h(t)$ is a zero mean, normally distributed random variable.

Under the assumptions of perfect time and frequency tracking, the outputs of the two BFSK tone filters are

$$Z_{i,k} = \frac{r}{T} \int_{(k-1/2)T}^{(k+1/2)T} \exp[j\pi\Delta f(n_k - i)t] h(t) dt + N_{i,k} \quad ,$$

where r is the mean received signal amplitude. The BFSK demodulation error rate is then given by the probability that the filter corresponding to the transmitted tone has a smaller output amplitude than does the other filter.

For Rayleigh fading, this is just the probability that the variance of one complex, normally distributed random variable is smaller than that of another. The complication here is that these two variables are correlated, as we show in the developments below.

⁵ One can frequency hop DPSK waveforms, but the hop rate must be slow compared to the modulation rate so there are multiple DPSK symbols per hop. Frequency hopping provides a significant advantage to FSK demodulation in frequency selective fading channels because there can be just one symbol per hop.

The signal contribution to the output of the correct filter ($i = n_k$) is

$$S_1 = \frac{r}{T} \int_{(k-1/2)T}^{(k+1/2)T} h(t) dt , \quad (\text{F.2})$$

and the signal contribution to the output of the other filter ($i \neq n_k$) is

$$S_0 = \frac{r}{T} \int_{(k-1/2)T}^{(k+1/2)T} e^{\pm j(2\pi\Delta f)t} h(t) dt . \quad (\text{F.3})$$

The variance of S_1 is

$$\langle S_1 S_1^* \rangle = \frac{r^2}{T^2} \int_{(k-1/2)T}^{(k+1/2)T} dt \int_{(k-1/2)T}^{(k+1/2)T} dt' \langle h(t) h^*(t') \rangle .$$

For the stationary channels considered in this report, the autocorrelation of the channel response function is

$$\langle h(t) h^*(t') \rangle = \rho(t - t') ,$$

and the expression for the variance of S_1 collapses to a single integral:

$$\langle S_1 S_1^* \rangle = 2r^2 \int_0^1 \rho(T\xi)(1 - \xi) d\xi \equiv r^2 R_1 .$$

Similarly, the variance of S_0 is

$$\langle S_0 S_0^* \rangle = \frac{r^2}{T^2} \int_{(k-1/2)T}^{(k+1/2)T} dt \int_{(k-1/2)T}^{(k+1/2)T} dt' \langle h(t) h^*(t') \rangle \exp[\pm 2\pi j \Delta f (t - t')] ,$$

which, for stationary channels, reduces to

$$\langle S_0 S_0^* \rangle = 2r^2 \int_0^1 \rho(T\xi)(1 - \xi) \cos(\omega_M \xi) d\xi \equiv r^2 R_2 ,$$

where $\omega_M = 2\pi \Delta f T$. The cross correlation coefficient of S_0 and S_1 is

$$\langle S_1 S_0^* \rangle = \frac{r^2}{T^2} \int_{(k-1/2)T}^{(k+1/2)T} dt \int_{(k-1/2)T}^{(k+1/2)T} dt' \langle h(t) h^*(t') \rangle \exp(\mp 2\pi j \Delta f t') .$$

After some manipulation this reduces to

$$\langle S_1 S_0^* \rangle = \mp r^2 \frac{2(-1)^{\Delta f T}}{\omega_M} \int_0^1 \rho(T\xi) \sin(\omega_M \xi) d\xi \equiv r^2 R_3 .$$

With the inclusion of AWGN, the variance of the output voltage of the filter corresponding to the transmitted tone (σ_1^2), the variance of the output of the other filter (σ_0^2), and the cross correlation coefficient (C) are

$$\begin{aligned} \sigma_1^2 &= r^2 [R_1 + \gamma^{-1}] \\ \sigma_0^2 &= r^2 [R_2 + \gamma^{-1}] , \\ C &= r^2 R_3 \end{aligned} \quad (F.4)$$

where γ is the channel bit energy-to-noise spectral density ratio (E_{cb} / N_0). The cross correlation term goes as $r^2 R_3$ rather than $r^2 (R_3 + \gamma^{-1})$ because the noise out of the two filters is uncorrelated.

The BFSK demodulation error rate in fast, flat Rayleigh fading is then the probability that the output amplitude of the filter corresponding to the transmitted tone is less than that of the other filter. This probability is derived in Appendix D in terms of the variances and cross correlation coefficient. Writing this probability in terms of the R integrals defined above gives the following result:

$$\langle P_e \rangle = \frac{1}{2} \left[1 - \frac{R_1 - R_2}{\sqrt{(R_1 + R_2 + 2\gamma^{-1})^2 - 4R_3^2}} \right] \quad (\text{BFSK, Fast Rayleigh Fading}) .$$

Unfortunately, the R integrals cannot be written in closed form for the Gaussian Doppler frequency spectrum, but such closed form expressions are possible for the other spectra in given Chapter 2. Because the f^{-4} spectrum is the DSWA standard for flat fading [Wittwer, 1980], we give the R integrals for this case:

$$\begin{aligned}
R_1 &= \frac{2}{T_4^2} [2T_4 - 3 + (T_4 + 3)e^{-T_4}] \\
R_2 &= \frac{2 \{ 2T_4^5 - 3T_4^4 + 2\omega_M^2 (T_4^3 + 3T_4^2) + \omega_M^4 + [T_4^5 + 3T_4^4 - 6\omega_M^2 T_4^2 - \omega_M^4 (T_4 + 1)] e^{-T_4} \}}{(T_4^2 + \omega_M^2)^3} \\
R_3 &= 2(-1)^{\Delta f T} \frac{3T_4^2 + \omega_M^2 - [T_4^3 + 3T_4^2 + \omega_M^2 (T_4 + 1)] e^{-T_4}}{(T_4^2 + \omega_M^2)^2} , \tag{F.5}
\end{aligned}$$

where $\omega_M = 2\pi \Delta f T$, $T_4 = \alpha_4 T / \tau_0$, and α_4 ($\alpha_4 = 2.146193 \dots$) is a numerical constant defined in Section 2.1.

In the limit that the fading is slow ($T \ll \tau_0$), $R_1 = 1$, $R_2 = R_3 = 0$, and the BFSK demodulation error rate reduces to the familiar slow Rayleigh fading expression:

$$\langle P_e \rangle = (2 + \gamma)^{-1} \quad (\text{BFSK, Slow Rayleigh Fading}) .$$

BFSK channel bit error rate curves for several values of the ratio τ_0 / T_{cb} and for an f^{-4} Doppler frequency spectrum are plotted in Figure F-4 for minimum tone spacing ($\Delta f T = 1$) and in Figure F-5 for three times the minimum tone spacing ($\Delta f T = 3$). As is the case for DPSK demodulation, the BFSK curves exhibit an irreducible error rate which depends on the value of τ_0 / T_{cb} and the Doppler frequency spectrum. Unlike DPSK, the irreducible error rate can be lowered by a means other than increasing the channel bit rate (*i.e.*, increasing τ_0 / T_{cb} by decreasing T_{cb}), namely by increasing the tone spacing. For example, the irreducible error rate for $\tau_0 / T_{cb} = 1$ is about 0.07 for the minimum tone spacing but drops to 0.005 when the tone spacing is increased to $\Delta f T = 3$.

To summarize these results, the fast fading BFSK irreducible error rate ($\langle P_e \rangle$ with $\gamma \rightarrow \infty$) is shown in Figure F-6 versus the normalized decorrelation time τ_0 / T_{cb} for three tone spacings ($\Delta f T = 1, 3$, and 10) and for an f^{-4} Doppler frequency spectrum. Obviously, the irreducible error rate decreases as the tone spacing increases. The fading causes a Doppler frequency spread in the received signal, and some of the signal energy is spread from the correct filter to the other filter. The further the tones are separated in frequency, the less signal energy can be spread into the wrong filter.

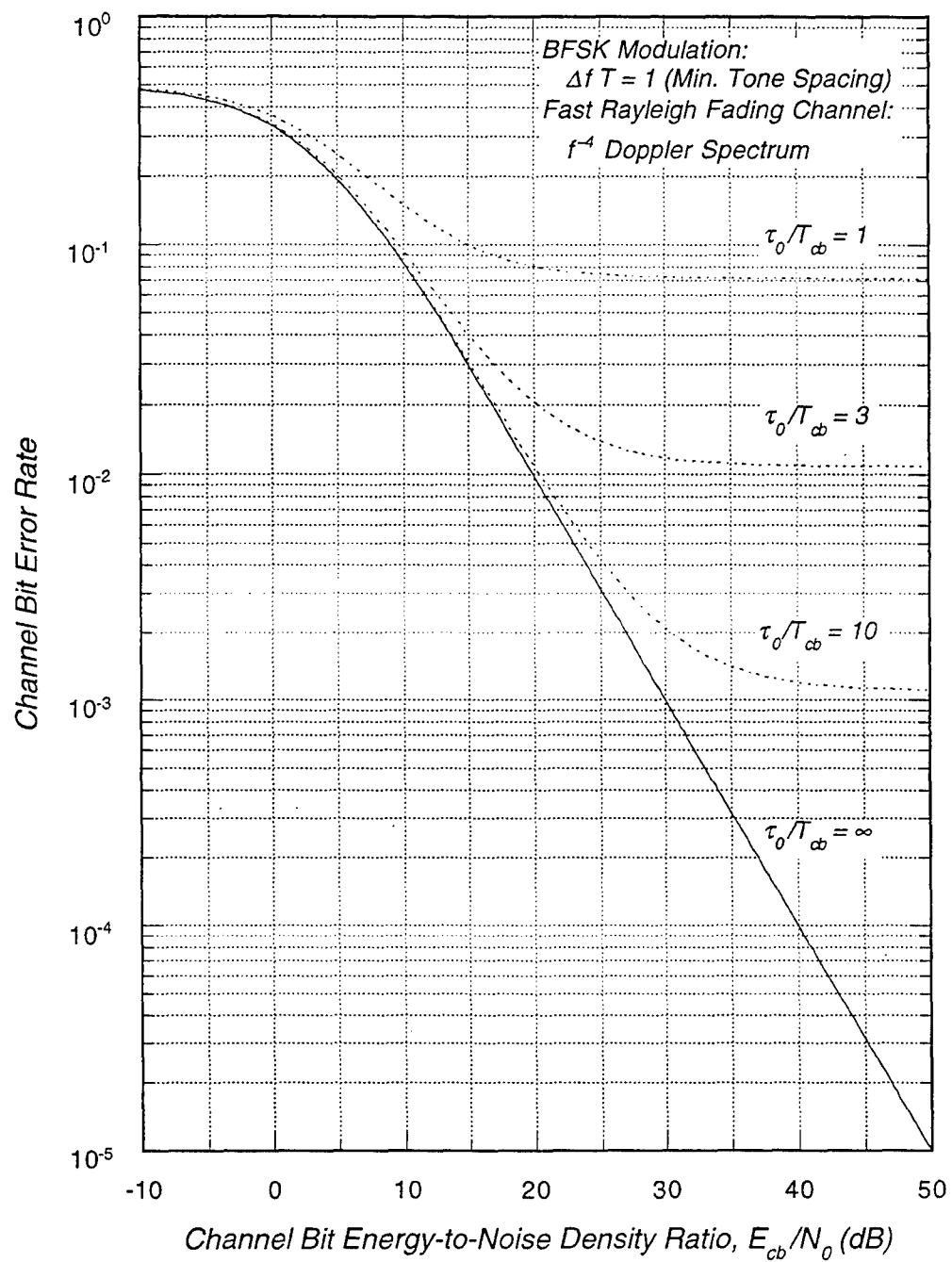


Figure F-4. BFSK demodulation error rate for minimum tone spacing in fast Rayleigh fading channels.

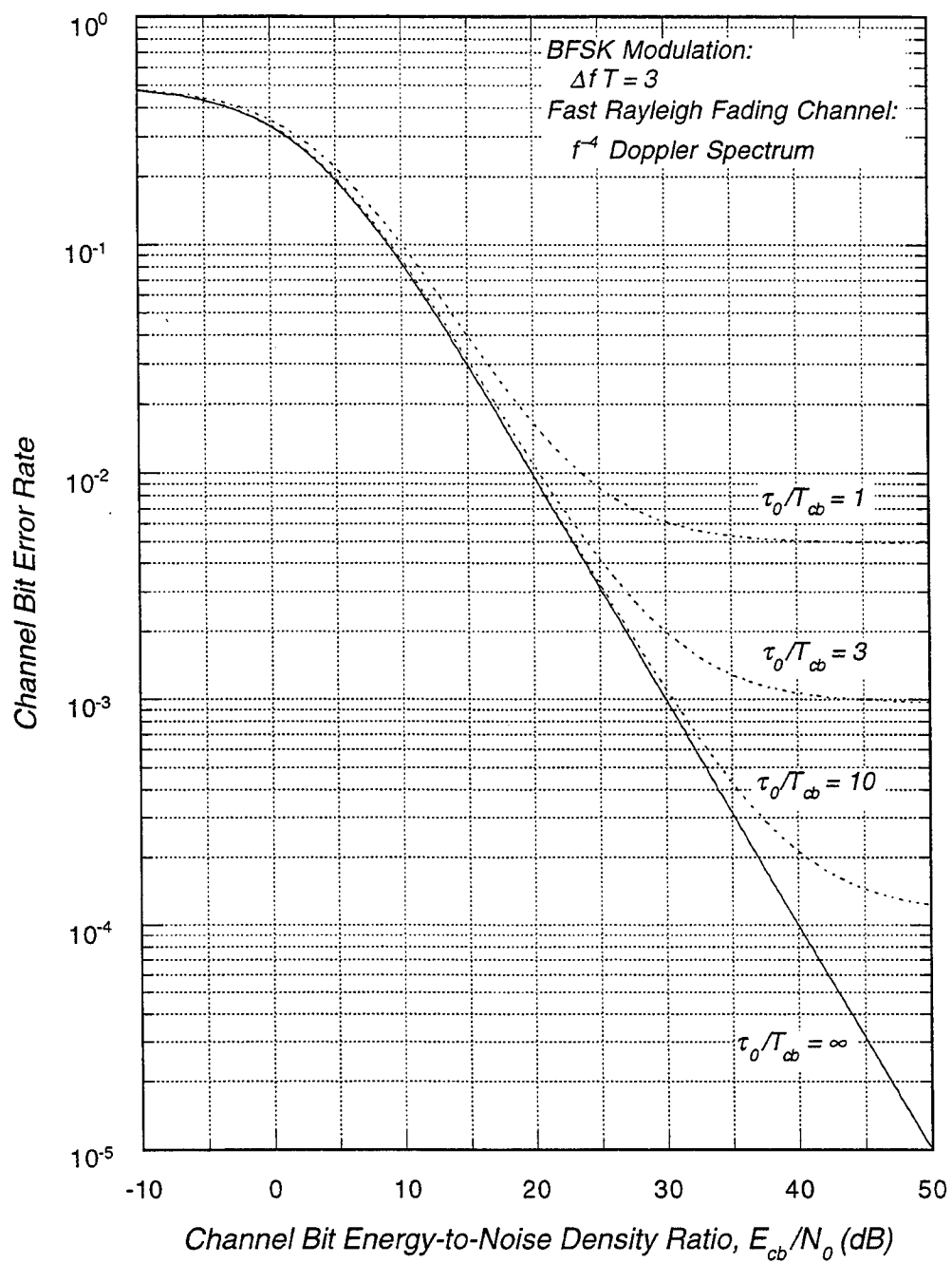


Figure F-5. BFSK demodulation error rate for three times minimum tone spacing in fast Rayleigh fading channels.

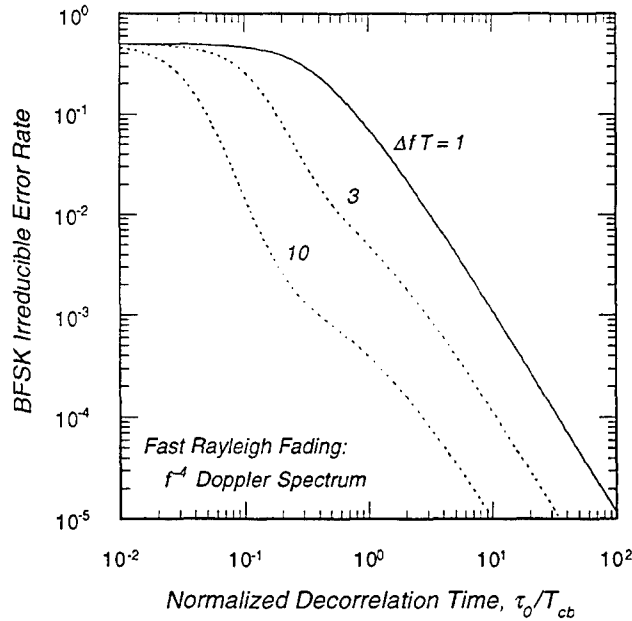


Figure F-6. Irreducible BFSK demodulation error rate for three tone spacings in fast Rayleigh fading channels.

An equivalent view of the Doppler frequency spread is obtained by considering the tone filter equations. In the correct filter [Eqn. (F.2)], the presence of the channel response function in the integrand reduces the signal energy at the output of the filter, primarily because of the random phase fluctuations contained in $h(t)$ prevent the signal vector from summing coherently during the integration period. In the other filter, there is a residual phase rotation that in the absence of fading has the effect of wrapping the signal vector around a circle $\Delta f T$ times. Thus for orthogonal signaling and no fading, the output of the other filter has no signal contribution because the signal vector is wrapped around to "bite its tail" during the integration period. With random phase perturbations caused by fading, the head does not end up exactly at the tail, and a signal contribution to the filter output results. Thus the fading causes a reduction in the signal energy out of the correct filter and an increase in the signal energy out of the other filter.

The effect of increasing the tone spacing is to decrease the effective integration period to $T_{cb} / (\Delta f T)$ because there are $\Delta f T$ complete phase rotations during the chan-

nel bit period. Thus, to first order, the effect of increasing tone spacing is to simply shift the $\Delta f T = 1$ irreducible error rate curve to the left by a factor of $\Delta f T$.

Of course this does not explain the odd change in the shape of the curves as $\Delta f T$ increases. This change is caused by the signal energy out of the other filter, as illustrated in Figure F-7 where the filter output signal energy is plotted versus τ_0 / T_{cb} . Obviously the signal energy out of the filter corresponding to the transmitted tone does not depend on the tone spacing, but the signal energy out of the other filter is very sensitive to this parameter. It is the behavior of the output signal energy of the other filter that causes the odd shape of the irreducible error rate curves.

Before leaving BFSK performance in fast fading there is one other point that we want to make. In principle this analysis can be extended to M -ary FSK demodulation. In fact we already have almost everything we need with the exception of the cross correlation of the outputs of filters that do not correspond to the transmitted tone. But it is these cross correlation terms that are the problem.

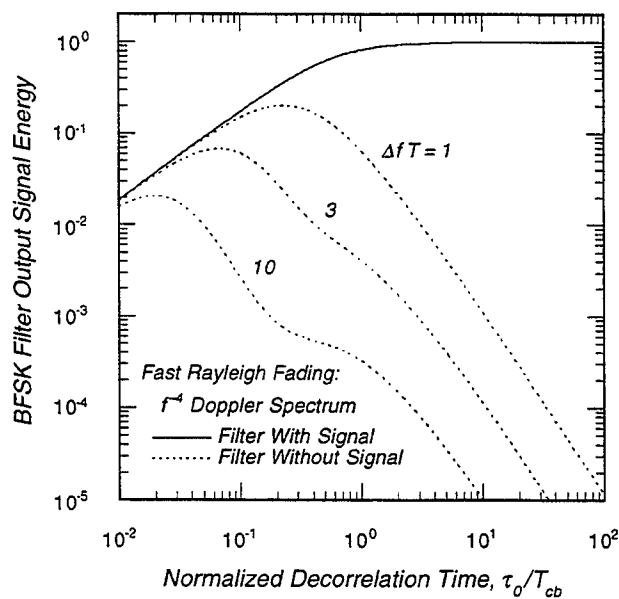


Figure F-7. BFSK filter output signal energy in fast Rayleigh fading channels.

F.4 *M*-ARY FSK IN CONTINUOUS FAST FADING CHANNELS.

In Rayleigh fading the outputs of all the M -ary filters are zero-mean, normally distributed random variables with non-zero correlation coefficients. Hence the calculation of the probability that one filter output amplitude is less than the maximum amplitude of all the other filters requires the calculation of the joint probability density function of M correlated Rayleigh amplitudes. This function must then be integrated over an M -dimensional space defined by $a_1 > \max(a_2, a_3, \dots, a_M)$. With the exception of the $M = 2$ case, for which an exact expression for the error rate is calculated in Appendix D, this may not be a tractable mathematical problem.

To estimate the fast fading M -ary FSK demodulation error rate we first assume Rayleigh fading so that the output signal plus noise voltages of all M filters are complex, zero mean, normally distributed random variables. We then compute the mean signal plus noise energy at the output of the filters and calculate the demodulation error rate with the approximation that the cross correlation between the filter outputs is negligible. To estimate the effect of this approximation, we compute the magnitude of a few cross correlation coefficients. We find that while the correlation between the correct filter and the other filters is indeed small, the correlation between the outputs of incorrect filters can be large and ignoring these terms does affect the calculated error rate. In this section we consider analog filters with continuous Fourier transforms. In Section F.5 we consider filters implemented with discrete Fourier transforms.

With this approximation, the M -ary FSK demodulation error rate problem reduces to finding the probability that the maximum amplitude of $M - 1$ uncorrelated, zero mean, normally distributed random variables is less than that of another zero mean, normally distributed random variable. As was the case for M -ary demodulation in non-fading channels, it is easier to compute the probability that the correct filter has the largest amplitude. This probability is

$$P_c = \int_0^{\infty} f_S(a) F_O(a) da \quad ,$$

where $f_S(\cdot)$ is the probability density function of the amplitude of the correct filter, and $F_O(\cdot)$ is the cumulative distribution of the amplitude of the other filters (*i.e.*, it is the probability that the largest amplitude of the other filters is less than the argument). For uncorrelated and hence independent filter outputs, $F_O(\cdot)$ reduces to the product of the cumulative distributions of the $M - 1$ filter output amplitudes:

$$F_O(a) = \prod_{\substack{i=1 \\ i \neq l}}^M F_{i,l}(a) ,$$

where $F_{i,l}(\cdot)$ is the cumulative distribution of output amplitude of the i^{th} filter given that the l^{th} filter is the correct one. This notation is necessary because the signal energy out of one of the other filters depends on how far away in frequency that filter is from the correct one.

We have already calculated the variance of the output voltages of the M filters, although a slight generalization is needed. These results are given in Equation (F.4). The required generalization is that the R_2 integral becomes

$$R_2(k) = 2 \int_0^1 \rho(T\xi)(1-\xi) \cos(k\omega_M \xi) d\xi , \quad (F.6)$$

where k is the distance of the other filter from the correct filter [$k = (i - l)/2$ where i and l are odd integers]. The formula for $R_2(k)$ for an f^{-4} Doppler spectrum is given by the R_2 expression in Equation (F.5) with ω_M replaced by $k\omega_M$. The R_1 integral, defined in Equation (F.4) for the output energy of the correct tone, remains the same. To simplify the notation, we rewrite the filter output variances as follows:

$$\begin{aligned} \mu_0 &= r^2 [R_1 + \gamma^{-1}] \\ \mu_k &= r^2 [R_2(k) + \gamma^{-1}] \end{aligned} ,$$

where we note that $R_2(0) = R_1$ so $\mu_0 = \mu_{k=0}$.

These equations define the diagonal elements of the filter covariance matrix. The off-diagonal elements are given by the filter cross correlation coefficient. Assuming that the n_0 tone is transmitted, the cross correlation coefficient of the filter output signal contributions is

$$C_{i,i'}^S = \langle S_i S_{i'}^* \rangle ,$$

where

$$S_i = \frac{r}{T} \int_{-T/2}^{T/2} h(t) \exp[-j\pi\Delta f(n_0 - i)t] dt .$$

We have already shown that the cross correlation of the noise is zero for orthogonal signaling. After some manipulation the cross correlation of the signal output reduces to

$$\begin{aligned} C_{i,i'}^S &= \frac{8r^2}{\omega_M(i-i')} \int_0^1 \rho(T\zeta) \sin\left[\frac{1}{4}\omega_M(i-i')(1-\zeta)\right] \cos\left\{\frac{1}{2}\omega_M\left[n_0 - \frac{1}{2}(i+i')\right]\zeta\right\} d\zeta \\ &\equiv r^2 R_4(n_0, i, i') \end{aligned}$$

In the limit that $i' = i$ this expression reduces further to

$$C_{i,i}^S = r^2 R_2(i) ,$$

which is equal to the expression above for μ_k ($k = i$) except that when $i' = i$ the noise variance is r^2 / γ rather than zero.

For an f^{-4} Doppler frequency spectrum, the R_4 function is given by the rather complicated expression

$$\begin{aligned} R_4(n_0, i, i') &= \frac{8(-1)^{AfT(i-i')}}{i-i'} \left\{ \frac{(n_0 - i') [12T_4^2 + \omega_M^2(n_0 - i')^2]}{[4T_4^2 + \omega_M^2(n_0 - i')^2]^2} - \frac{(n_0 - i) [12T_4^2 + \omega_M^2(n_0 - i)^2]}{[4T_4^2 + \omega_M^2(n_0 - i)^2]^2} \right. \\ &\quad - \frac{(n_0 - i') [4T_4^3 + 12T_4^2 + (1 + T_4)\omega_M^2(n_0 - i')^2] e^{-T_4}}{[4T_4^2 + \omega_M^2(n_0 - i')^2]^2} \\ &\quad \left. + \frac{(n_0 - i) [4T_4^3 + 12T_4^2 + (1 + T_4)\omega_M^2(n_0 - i)^2] e^{-T_4}}{[4T_4^2 + \omega_M^2(n_0 - i)^2]^2} \right\} \end{aligned}$$

Later we will evaluate this expression to assess the impact of neglecting the cross correlation coefficients in the error rate calculation.

The arithmetic of the M -ary FSK error rate problem is made easier by considering the probability distributions of the output energy (rather than the amplitude) because the energy has an exponential distribution when the amplitude is Rayleigh distributed. Thus the probability density function of the correct filter output energy is

$$f_S(x) = \frac{1}{\mu_0} \exp\left[-\frac{x}{\mu_0}\right] ,$$

and the cumulative distribution function of the output energy of the k^{th} other filter is

$$F_{O,k}(x) = 1 - \exp\left[-\frac{x}{\mu_k}\right] .$$

Now we are in a position to estimate the M -ary FSK fast fading demodulation error rate taking into account the mean output energy of each filter as a function of its distance from the correct filter.

As an example, the filters for an 8-ary FSK receiver are shown schematically in Figure F-8 where the horizontal line segments represent the 8 filters spaced evenly in frequency. The vertical arrows represent transmitted tones, and under each line segment is the corresponding value of k , the distance of the filter from the transmitted tone. There are only four cases, because the fifth case with the transmitted tone in the fifth position from the left is mathematically identical to case 4, the sixth case is mathematically identical to case 3, and so forth.

For case 1 the probability that the energy out of the correct filter is larger than that out of any of the other filters is

$$P_c = \int_0^{\infty} f_S(x) \prod_{k=1}^7 F_{O,k}(x) dx \quad . \quad (\text{Case 1})$$

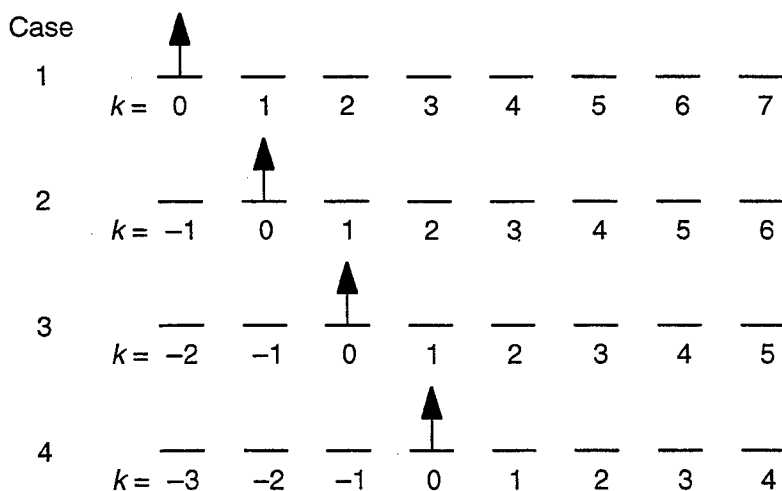


Figure F-8. 8-ary FSK tone filters.

For case 2 there are two filters with a distance of ± 1 from the transmitted tone, but one can see from Equation (F.6) that the output filter energy depends only on $|k|$. Thus for case 2 the probability that the correct filter has the maximum energy is

$$P_c = \int_0^{\infty} f_S(x) F_{O,1}(x) \prod_{k=1}^6 F_{O,k}(x) dx \quad (\text{Case 2})$$

Similarly, the probabilities of correct decision for cases 3 and 4 are

$$P_c = \int_0^{\infty} f_S(x) \prod_{k=1}^2 F_{O,k}(x) \prod_{k=1}^5 F_{O,k}(x) dx \quad (\text{Case 3})$$

$$P_c = \int_0^{\infty} f_S(x) \prod_{k=1}^3 F_{O,k}(x) \prod_{k=1}^4 F_{O,k}(x) dx \quad (\text{Case 4})$$

In general, the probability that the correct filter has the largest output energy is

$$P_c = \frac{2}{M} \sum_{l=0}^{M/2-1} \int_0^{\infty} f_S(x) \prod_{k=1}^l F_{O,k}(x) \prod_{k=1}^{M-l-1} F_{O,k}(x) dx \quad ,$$

assuming that the transmitted tone is uniformly distributed in the M possible positions. (The leading factor of $2/M$ in this equation is there because there are $M/2$ cases and each case is equally likely.) Subtracting this probability from unity gives the M -ary character error rate.

In fast fading the relationship between symbol error rate and the channel bit error rate is not given by the simple expression in Equation (F.1). In deriving that expression, it is assumed that when a demodulation error is made all incorrect tone filters are equally likely to be selected. This is only the case when all incorrect filters have equal output amplitudes on the average. When the channel bit error rate is less than 50 percent in fast fading, demodulation errors are most likely to be made by choosing a filter adjacent to the correct filter because these adjacent filters have the largest average output of all the incorrect filters. This changes the average number of channel bit errors per demodulation symbol error.

In the limit that only adjacent filters are chosen, we can compute the ratio of the channel bit error rate to the symbol error rate. For each of the $M-2$ interior filters,

there are two adjacent filters that can cause errors with equal probability. For the two end filters, there is only one adjacent filter that causes errors. Thus over the ensemble of M transmitted symbols, there are $2 + 2(M - 2) = 2M - 2$ equally likely symbol errors. The average number of channel bit errors per symbol error is found by counting the number of bit errors for each possibility and dividing by the total number of bits. It can be seen that the total number of bit errors, averaged over the ensemble of $2M - 2$ symbol errors, is given by⁶

$$2\log_2 M + 4\log_2(M/2) + 8\log_2(M/4) + \dots + M = \sum_{k=1}^{\log_2 M} 2^k \log_2(2^{1-k} M) .$$

The total number of bits contained in the $2M - 2$ symbols is $2(M - 1)\log_2 M$. Thus when only adjacent symbol errors are likely, we obtain the following relationship between channel bit error rate P_e and symbol error rate $1 - P_c$:

$$P_e = \frac{\sum_{k=1}^{\log_2 M} 2^{k-1} \log_2(2^{1-k} M)}{(M - 1)\log_2 M} (1 - P_c) .$$

A few examples illustrate the difference between the AWGN formula, $\frac{1}{2} M/(M - 1)$, and the expression given above for $P_e/(1 - P_c)$. For 8-ary FSK, the AWGN formula predicts this ratio to be $\frac{4}{7}$ or 0.57, whereas assuming adjacent filters cause all demodulation errors results in a value of $\frac{11}{21}$ or 0.52. This difference is even larger for 16-ary FSK where the AWGN formula predicts a ratio of $\frac{8}{15}$ or 0.53, whereas the adjacent filter assumption results in a ratio of $\frac{13}{30}$ or 0.43. Of course the ratio is 1 for BFSK, and one can show that it is $\frac{2}{3}$ for QFSK in either case. Thus for $M > 4$, use of the AWGN formula relating channel bit error rate to demodulation error rate will provide an upper bound to the channel bit error rate. To get around this analytic problem when comparing COMLNK results with theory, we will use demodulated symbol error rates rather than channel bit error rates for the 8-ary and 16-ary FSK cases.

For Rayleigh fading, all of the terms in the expression for correctly demodulating the M -ary FSK signal are of the form

⁶ There are 2 cases where all $\log_2 M$ bits are in error, there are 4 cases where $\log_2(M/2)$ bits are in error, there are 8 cases where $\log_2(M/4)$ bits are in error, and so on. Finally, there are M cases where there is only 1 bit in error.

$$P_M(\bar{v}_M) = \int_0^\infty e^{-x/v_0} \prod_{k=1}^{M-1} (1 - e^{-x/v_k}) dx \quad . \quad (F.7)$$

where $\bar{v}_M = \{v_0, v_1, \dots, v_{M-1}\}$. Dr. Scott Frasier of Mission Research Corporation [Frasier, 1996] pointed out that this integral can be written in terms of two similar integrals:

$$\begin{aligned} P_M(\bar{v}_M) &= \int_0^\infty e^{-x/v_0} \prod_{k=2}^{M-1} (1 - e^{-x/v_k}) dx - \int_0^\infty e^{-x(1/v_0 + 1/v_1)} \prod_{k=2}^{M-1} (1 - e^{-x/v_k}) dx \\ &= P_{M-1}(v_0, v_2, \dots, v_{M-1}) - P_{M-1}\left(\frac{v_0 v_1}{v_0 + v_1}, v_2, \dots, v_{M-1}\right) \end{aligned} \quad ,$$

where

$$P_2(v_0, v_1) = \frac{v_0^2}{v_0 + v_1} \quad .$$

Thus the integral in Equation (F.7) can be evaluated by recursion. The probability of selecting the correct tone filter is now evaluated as

$$P_c = \frac{2}{M} P_M(v_0, v_1, \dots, v_{M-1}) + \frac{2}{M} \sum_{l=1}^{M/2-1} P_M(v_0, v_1, \dots, v_{l-1}, v_0, \dots, v_{M-l-1}) \quad ,$$

where $v_k = \mu_k / \mu_0$ and $v_0 = 1$.

Before proceeding with M -ary FSK error rate results, we need to explore the effect of our approximation that the filter outputs are uncorrelated. Assuming a tone spacing of $\Delta f T = 3$, the filter output energy and cross correlation coefficients are plotted in Figures F-9 and F-10, respectively, versus decorrelation time normalized by the symbol period, τ_0/T . The output signal energy is plotted in the first of these figures for the correct filter ($i = n_0$), the two filters adjacent to the correct filter ($i = n_0 \pm 2$), and the next four filters closest to the correct one ($i = n_0 \pm 4$ and $i = n_0 \pm 6$). As expected, the adjacent filter has the largest average signal energy of all the other filters, and the average signal energy decreases as the distance $|n_0 - i|$ from the correct filter increases. When τ_0/T is less than 10^{-2} or so, the signal Doppler spread is so large that signal energy is spread almost uniformly, and all filters have about the same mean signal energy.

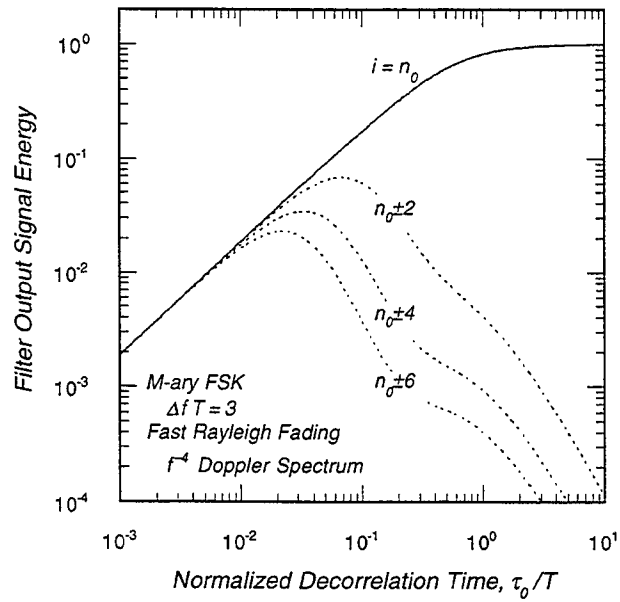


Figure F-9. FSK filter output signal energy in fast Rayleigh fading channels.

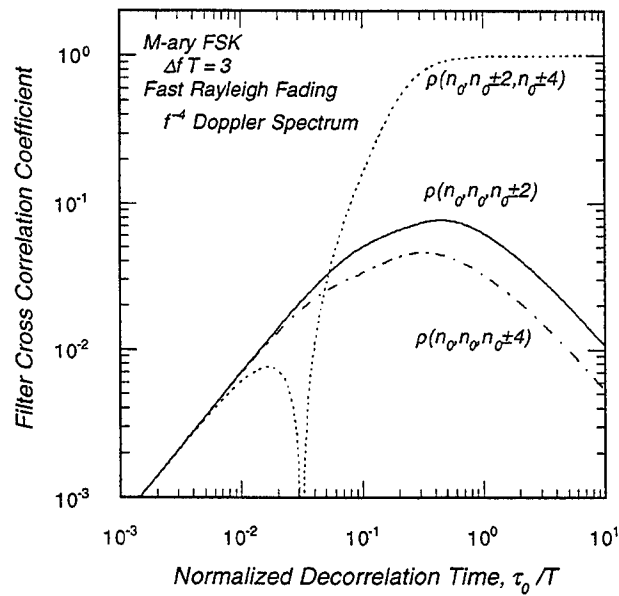


Figure F-10. FSK filter cross correlation coefficient in fast Rayleigh fading channels.

The cross correlation coefficient, plotted in Figure F-10, is given by

$$\rho(n_0, i, i') = \frac{|R_4(n_0, i, i')|}{\sqrt{R_2(n_0 - i)R_2(n_0 - i')}} ,$$

where $R_2(n_0 - i)$ is the output energy of the i^{th} filter (normalized to r^2) given that the n_0 tone is transmitted. We include the absolute value in this expression so that we can plot the correlation coefficient on a logarithmic scale. It is obvious in the plots of $\rho(n_0, i, i')$ where R_4 changes sign. The correlation between the correct filter output signal and that of the four closest filters, $\rho(n_0, n_0, n_0 \pm 2)$ and $\rho(n_0, n_0, n_0 \pm 4)$, is always small, peaking at a value less than $1/10$, so the other filter outputs are essentially uncorrelated with the correct filter output. The problem is that the correlation between two adjacent other filters, $\rho(n_0, n_0 \pm 2, n_0 \pm 4)$ for example, is large for $\tau_0/T > 1/10$.

When we neglect the correlation, we are essentially increasing the probability that one of those filters will have an output amplitude larger than that of the correct filter. Thus our theoretical results for $M > 2$ are an upper bound on the M -ary FSK demodulation error rate. For $\tau_0/T < 1/10$, the cross correlation coefficient is small, and our upper bound should be close to the true demodulation error rate. For $\tau_0/T > 10$, the mean energy of the other filters is very small compared to that of the correct filter, and again our upper bound should be close to the true value. It is for decorrelation times in the critical range $1/10 \leq \tau_0/T \leq 10$ where we will see the largest variation between our approximate theoretical results and measured error rates from COMLNK or actual hardware.

To illustrate the effects of fast Rayleigh fading on high-order frequency shift keying, we present calculated channel bit error rate results for 8-ary FSK. Keep in mind that these analytic results are upper bounds on true performance because the analysis ignores the effects of correlation between filters and also ignores the change in the relationship between symbol and bit error rates due to Doppler spreading.

The channel bit error rate for 8-ary FSK in fast Rayleigh fading is plotted in Figure F-11 for minimum tone spacing ($\Delta f T = 1$) and in Figure F-12 for three times minimum tone spacing ($\Delta f T = 3$). An f^{-4} Doppler frequency spectrum is used for these results. The fast fading curves are plotted for three values of the ratio of the channel decorrelation time to the channel bit period, where T_{cb} is related to the symbol period T by the expression $T_{cb} = T/\log_2 M$.

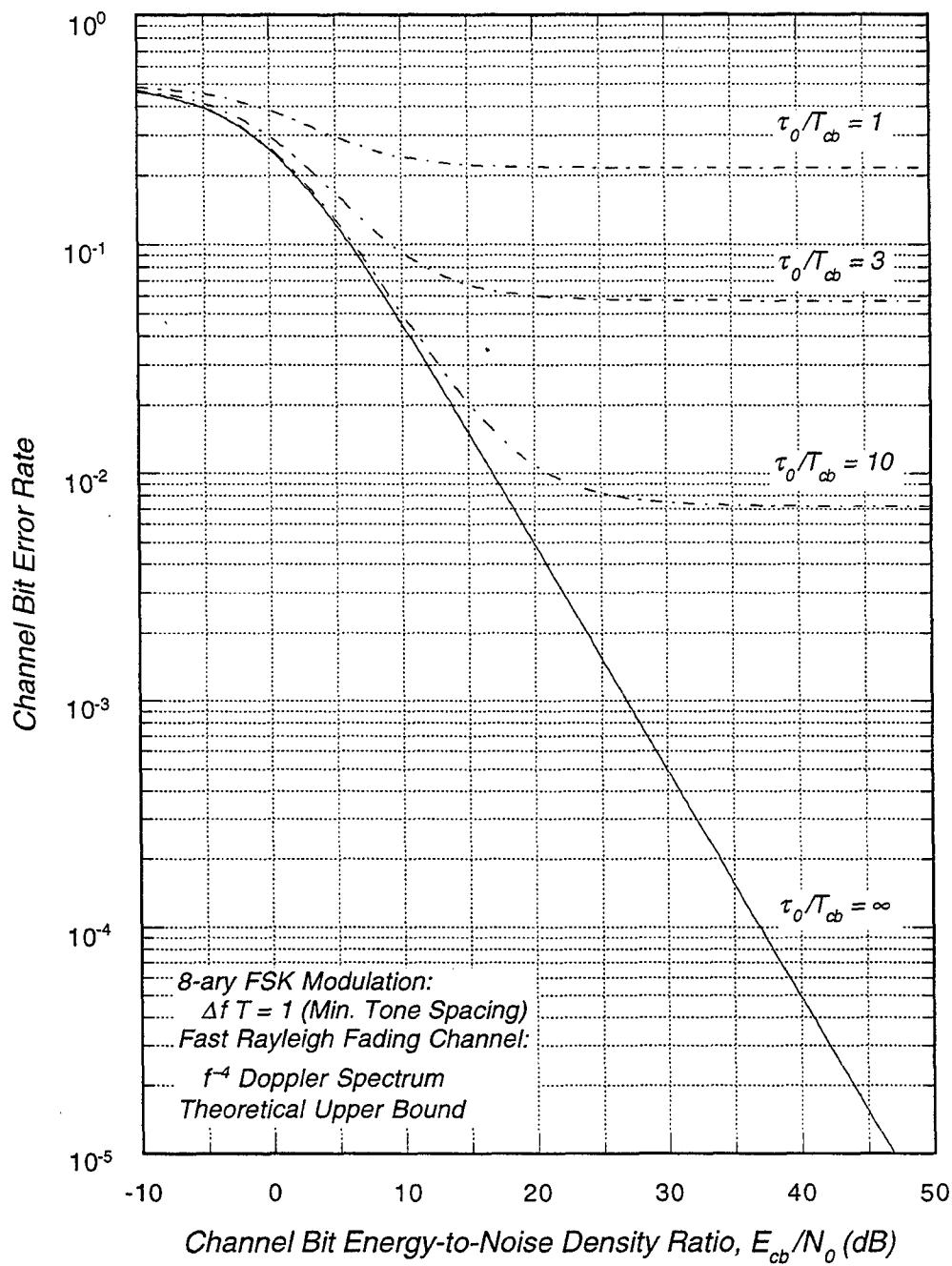


Figure F-11. 8-ary FSK demodulation error rate in fast Rayleigh fading channels for minimum tone spacing.

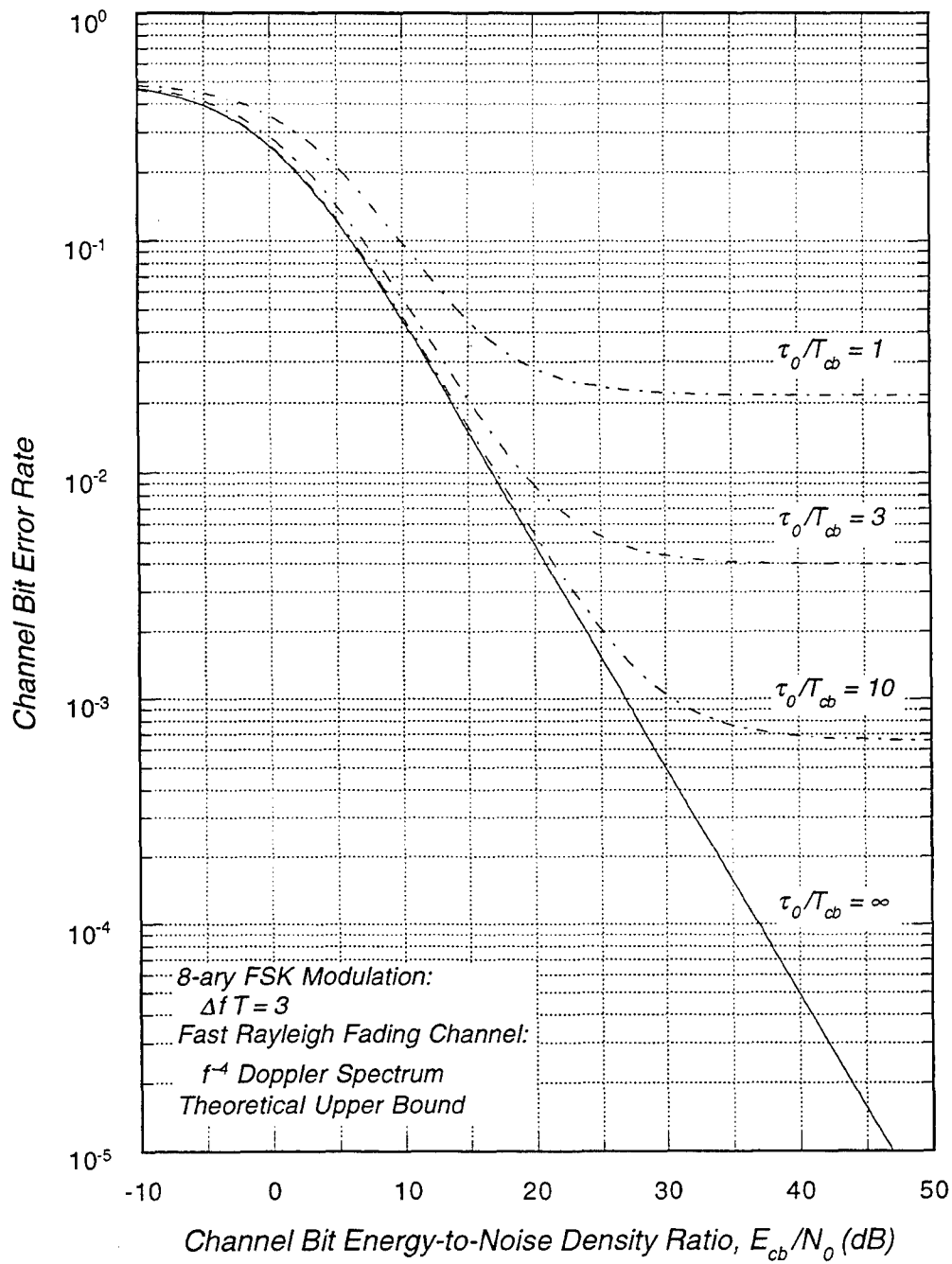


Figure F-12. 8-ary FSK demodulation error rate in fast Rayleigh fading channels for three times minimum tone spacing.

Each tone in 8-ary FSK, for example, represents 3 channel bits, so the channel bit period is one-third of the symbol period. The use of the ratio τ_0 / T_{cb} (rather than a ratio involving the symbol period T) and the channel bit energy-to-noise spectral density ratio E_{cb} / N_0 (rather than the symbol energy) allows a direct comparison of these fast fading curves to those presented earlier in this appendix for BFSK or in Appendix B for DPSK. All curves are for an equivalent channel bit rate.

The shift to the right in the $\tau_0 / T_{cb} = 1$ curve in Figure F-12 is caused by the loss in signal energy at the output of the correct filter due to channel phase fluctuations. This loss is 3.2 dB for $\tau_0 / T_{cb} = 1$ and the f^{-4} Doppler frequency spectrum. The irreducible error rate is caused by the presence of a signal component in the outputs of the other seven filters. By comparing curves in Figure F-11 with those in Figure F-12, one can see a significant reduction in the irreducible error rate as the tone spacing is increased.

A comparison of these results to those for BFSK shows what initially may be a surprising result: 8-ary FSK has a higher irreducible error rate for a fixed tone spacing and value of τ_0 / T_{cb} than does BFSK. For a constant channel bit rate, 8-ary FSK uses tones that are three times longer than used for BFSK and thus are three times closer in frequency for minimum tone spacing. Hence for a given decorrelation time, more signal energy is spread into adjacent filters with 8-ary FSK than with BFSK, and a higher irreducible error rate results.

This result is summarized in Figure F-13 where we plot the irreducible error rate for BFSK and 8-ary FSK for three values of the tone spacing. The BFSK results are the same as plotted in Figure F-6. By comparing the demodulation error rates of 8-ary FSK with $\Delta f T = 3$ to that of BFSK with $\Delta f T = 1$ we are comparing modulation formats with exactly the same frequency separation between the tones (Δf is the same in absolute units). For a fixed value of Δf , 8-ary FSK does have a lower irreducible demodulation error rate than does BFSK. The penalty in this case is that the 8-ary FSK waveform has a bandwidth that is about 2.6 times larger than that of BFSK.

F.5 M-ARY FSK IN SAMPLED FAST FADING CHANNELS.

Modern digital FSK receivers form tone filters by first sampling the signal and then performing discrete Fourier transforms (DFTs). This introduces an effect that is not in the previous analysis for the continuous case. This is the loss that results because the signal is sampled before the frequency shift $n_k \Delta f$ is removed.

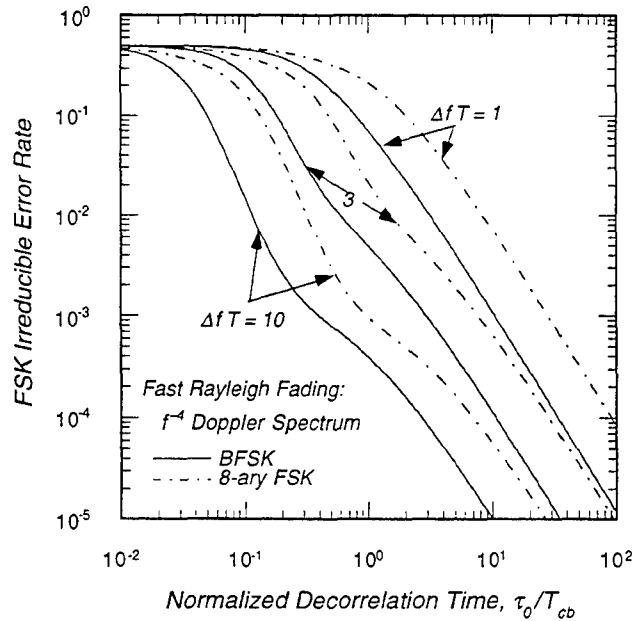


Figure F-13. Irreducible BFSK and 8-ary FSK demodulation error rates in fast Rayleigh fading channels.

Another motivation for this analysis is to investigate whether a portion of the Doppler frequency spectrum might be cut off in COMLNK because the simulation updates the channel at a rate slower than the demodulator A/D sample rate in most cases. The default channel update rate in COMLNK is $40/\tau_0$, which is based on the DSWA specification for time sampled channels [Wittwer, 1980; Dana, 1988]. This rate may be modified slightly in COMLNK so that the A/D sample rate is an integer multiple of the channel update rate (*i.e.*, so there are an integral number of A/D samples per channel update period).

While a channel update rate of $40/\tau_0$ is adequate to reproduce the temporal statistics of fades, we want to ensure that it is also adequate to represent the effect of Doppler spreading in FSK filters. The results below show that this channel update rate is indeed adequate as the irreducible error rate agrees closely with the results from the previous subsection for the continuous case.

To simplify this analysis slightly, we make two assumptions that limit the channel update period in our analysis: The number of A/D samples within the channel update

period and the number of channel updates within a modulation period are required to be integers. To do this we increase the number of channel updates per decorrelation time, starting at 40.

In the analysis, the channel update rate is limited to not exceed the A/D sampling rate. More rapid channel sampling would account for channel decorrelation within a single A/D sample. On the other extreme, the minimum channel update rate considered here is the FSK symbol rate. Less rapid channel sampling corresponds to slow fading with no appreciable Doppler spread.

The signal contribution to the k^{th} A/D sample that is used in the DFTs is

$$S_k = \frac{r}{\Delta t} \int_{k\Delta t}^{(k+1)\Delta t} m(t)h(t) dt \quad (-N_T/2 \leq k \leq N_T/2 - 1) ,$$

where $m(\cdot)$ is the transmitted tone and $h(\cdot)$ is the channel response. For fast, flat fading we only need to consider a single transmitted tone, so

$$m(t) = e^{j\pi n_0 \Delta f t} \Pi(t/T) ,$$

where $n_0 \Delta f$ is the tone frequency. To actually evaluate the expression for S_k in a simulation, it is assumed that the integral is separable into the product of two terms:

$$S_k \approx r \frac{1}{\Delta t} \int_{k\Delta t}^{(k+1)\Delta t} m(t) dt \frac{1}{\Delta t} \int_{k\Delta t}^{(k+1)\Delta t} h(t) dt .$$

The mean power of the first integral is less than unity because the received signal has a residual frequency of $n_0 \Delta f$ (assuming ideal frequency tracking) after downconversion to baseband. Thus there is a residual phase rotation of the signal during the sample period Δt . The second integral represents the effect of channel decorrelation during the signal sample period. Before proceeding with the FSK error rate, we need to investigate the statistics of these two terms.

F.5.1 Sampling Loss.

The first term in the expression for the A/D samples is denoted $\hat{S}(k\Delta t)$ where

$$\hat{S}(k\Delta t) = \frac{1}{\Delta t} \int_{k\Delta t}^{(k+1)\Delta t} m(t) dt .$$

After substituting the expression for the transmitted tone, the sampled signal is

$$\hat{S}(k\Delta t) = \exp\left[\frac{1}{2}jn_0\omega_M\left(k + \frac{1}{2}\right)/N_T\right] \frac{\sin\left[\frac{1}{4}n_0\omega_M/N_T\right]}{\left[\frac{1}{4}n_0\omega_M/N_T\right]},$$

where $\omega_M = 2\pi\Delta f T$ and the $k + \frac{1}{2}$ term in the exponential just shifts the time reference to the center of the samples. The mean power of $\hat{S}(k\Delta t)$, which is less than unity, gives the sampling loss assuming that the n_0 tone was transmitted. Assuming all tones are equally like to be transmitted, the average sampling loss is

$$L_S = \frac{2}{M} \sum_{i=1}^{M/2} \frac{\sin^2\left[\frac{1}{4}(2i-1)\omega_M/N_T\right]}{\left[\frac{1}{4}(2i-1)\omega_M/N_T\right]^2},$$

recognizing that the sampling loss is the same for $\pm n_0$. A table of sampling loss values for the minimum tone spacing ($\Delta f T = 1$) is given by *Bogusch* [1989] for a few values of M and N_T . The loss depends only on the ratio $\Delta f T/N_T$, so the sampling loss for other than the minimum tone spacing can be found from the table for some cases.

The average sampling loss is only meaningful for non-fading or slow fading channels where the demodulation error rate is independent of exactly which tone is transmitted. In fast fading, however, the demodulation error rate does depend on the transmitted tone, and the sampling loss per tone is applied for each transmitted tone.

F.5.2 Statistics of “Supersampled” Channels.

The second term in the expression for the A/D samples is denoted $\hat{h}(k\Delta t)$ where

$$\hat{h}(k\Delta t) = \frac{1}{\Delta t} \int_{k\Delta t}^{(k+1)\Delta t} h(t) dt.$$

When the decorrelation time is so small that it is necessary to perform multiple channel updates per A/D sample period, the channel in COMLNK is referred to as “supersampled.” The purpose of this subsection is to calculate the statistics of the supersampled channel.

Because the channel response function $h(t)$ for Rayleigh fading is a complex, zero-mean, normally distributed random process, the supersampled channel response $\hat{h}(k\Delta t)$ is similarly distributed, but with different second-order statistics. The auto-correlation function of $\hat{h}(k\Delta t)$, denoted C_c , is

$$C_c[(k-l)\Delta t] = \langle \hat{h}(k\Delta t) \hat{h}^*(l\Delta t) \rangle = \frac{1}{\Delta t^2} \int_{k\Delta t}^{(k+1)\Delta t} dt \int_{l\Delta t}^{(l+1)\Delta t} dt' \langle h(t) h^*(t') \rangle .$$

After some manipulation, this reduces to

$$C_c(K\Delta t) = \int_0^1 \{ \rho[(\zeta - K)\Delta t] + \rho[(\zeta + K)\Delta t] \} (1 - \zeta) d\zeta ,$$

where $K = k - l$ and $\rho(\cdot)$ is the temporal autocorrelation function of the channel response function. The supersampled autocorrelation evaluated at zero offset,

$$C_c(0) = 2 \int_0^1 \rho(\zeta\Delta t) (1 - \zeta) d\zeta$$

is the reduction in the signal energy within an A/D sample due to the decorrelation of the channel within that sample. An expression for $C_c(0)$, valid for a channel with an f^{-4} Doppler frequency spectrum, is given by the R_1 term in Equation (F.5), where for this case $T_4 = \alpha_4 T / N_T \tau_0$.

F.5.3 *M*-ary FSK Channel Bit Error Rate.

Calculation of the *M*-ary FSK channel bit error rate for time-sampled signals is essentially identical to the calculation for continuous signals. The only difference is in the formulas for the output signal energy of the filters. Once these values have been computed the error rate calculation is the same as outlined in Section F.4.

The signal contribution to the output of the n^{th} DFT filter, given that the n_0 tone was transmitted, is

$$S_D(n, n_0) = \frac{r}{N_T} \sum_{k=-N_T/2}^{N_T/2-1} \hat{S}(k\Delta t) \hat{h}(k\Delta t) \exp \left[-j\pi n \left(k + \frac{1}{2} \right) \Delta f \Delta t \right] .$$

There are M_1 A/D samples per channel update and M_2 channel updates per modulation period (so $M_1 M_2 = N_T$). After accounting for the difference in the A/D sample rate and the channel update rate, the signal contribution to the DFT output is

$$S_D(n, n_0) = r \sqrt{L_S(n_0)} \exp \left[\frac{j(n_0 - n) \omega_M}{4N_T} \right] \frac{1}{N_T} \sum_{l=0}^{M_2-1} \hat{h} \left[(-N_T/2 + lM_1) \Delta t \right] D(l, n_0, n) ,$$

where

$$L_S(n_0) = \frac{\sin^2 \left[\frac{1}{4} n_0 \omega_M / N_T \right]}{\left[\frac{1}{4} n_0 \omega_M / N_T \right]^2}$$

is the sampling loss when the n_0 tone is transmitted, and

$$D(l, n_0, n) = \sum_{k=-N_T/2+M_1}^{-N_T/2+(l+1)M_1-1} \exp \left[\frac{j(n_0 - n) \omega_M k}{2N_T} \right]$$

is the sum of the residual phase rotations within a DFT tone filter during the M_2 periods when the channel response function is constant.

The signal contribution to output energy of the DFT tone filters is

$$\begin{aligned} E(n_0, n) &= \langle S_D(n_0, n) S_D^*(n_0, n) \rangle \\ &= r^2 L_S(n_0) \frac{1}{N_T^2} \sum_{l=0}^{M_2-1} \sum_{l'=0}^{M_2-1} C_c[(l-l')M_1 \Delta t] D(l, n_0, n) D^*(l', n_0, n) \end{aligned}$$

After some manipulation, the contribution of the “ D ” terms to the double sum is

$$D(l, n_0, n) D^*(l', n_0, n) = \hat{S}_1(n_0, n) \hat{S}_1^*(n_0, n) (-1)^{\Delta f T} \exp \left\{ \frac{j \omega_M M_1 [(n_0 - n)(l - l')]}{2N_T} \right\},$$

where

$$\hat{S}_1(n_0, n) = \sum_{k=0}^{M_1-1} \exp \left[\frac{j(n_0 - n) \omega_M k}{2N_T} \right].$$

A closed form expression for this sum is

$$\hat{S}_1(n_0, n) = \begin{cases} \frac{1 - \exp \left[\frac{1}{2} j(n_0 - n) \omega_M M_1 / N_T \right]}{1 - \exp \left[\frac{1}{2} j(n_0 - n) \omega_M / N_T \right]} & \text{if } (n_0 - n) \Delta f T / N_T \neq \text{even integer} \\ M_1 & \text{otherwise} \end{cases}.$$

Using these relationships, the mean signal energy at the output of the n^{th} tone filter, given that the $n_0 \neq n$ tone is transmitted, is

$$E(n_0, n) = r^2 L_S(n_0) \frac{M_2 \sin^2 \left[\frac{1}{4} (n_0 - n) \omega_M M_1 / N_T \right]}{N_T^2 \sin^2 \left[\frac{1}{4} (n_0 - n) \omega_M / N_T \right]} \times \left\{ C_c(0) + 2 \sum_{k=1}^{M_2-1} C_c(k M_1 \Delta t) (1 - k / M_2) \cos \left[\frac{1}{2} (n_0 - n) \omega_M M_1 k / N_T \right] \right\},$$

and the mean signal energy at the output of the correct tone filter ($n = n_0$) is

$$E(n_0) = r^2 L_S(n_0) \frac{M_2 M_1^2}{N_T^2} \left\{ C_c(0) + 2 \sum_{k=1}^{M_2-1} C_c(k M_1 \Delta t) (1 - k / M_2) \right\}.$$

As we mentioned above, the difference between the M -ary FSK channel bit error rate in fast fading with continuous channel response functions and Fourier transforms and that obtained with A/D sampling and DFTs is small when the signal sampling rate is sufficient to unambiguously resolve the tone filters. To demonstrate this, we show in Figure F-14 the irreducible 8-ary FSK channel bit error rate as a function of the ratio τ_0 / T_{cb} for three values of the tone spacing. The solid and dashed lines in the figure are for the continuous case and the symbols indicate the error rate for the sampled case.

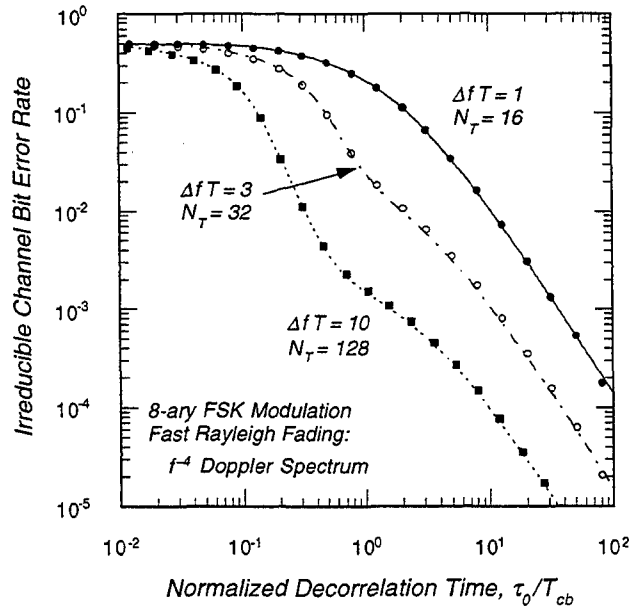


Figure F-14. 8-ary FSK channel bit error rate in fast Rayleigh fading channels for continuous and time-sampled cases.

The number of DFT points for each tone spacing is indicated in the figure, and the channel is sampled at least 40 times per τ_0 .

Clearly the results for the sampled case reproduce those for the continuous case. The only significant difference between the two cases is in the sampling loss (the continuous case has no sampling loss). The irreducible error rate is independent of that loss because it just reduces the signal amplitude of the A/D samples.

APPENDIX G

DEMODULATION PERFORMANCE OF BINARY FREQUENCY SHIFT-KEYING IN FREQUENCY SELECTIVE FADING WITH HOPPING

A functional block diagram of a frequency hopped, non-coherent binary frequency-shift keying (BFSK) receiver is shown in Figure G-1. There are two filters for either of the possible transmitted tones. For non-coherent hard-decision demodulation, the filter with the largest output amplitude is selected to represent the transmitted tone. With suppressed-carrier tracking, the output of the selected filter is used in the automatic gain control (AGC), delay lock loop (DLL), and automatic frequency control (AFC) tracking loops. Thus the demodulator output is fed back into the tracking loop measurements in this block diagram. This is only one of several possible design configurations. Other implementations employ unmodulated sync symbols for tracking, for example.

There are two fundamental characteristics of frequency selective fading that complicate the analysis of the FSK demodulation error rate. As pointed out in Section 2 of this report, the two-frequency mutual coherence function varies inversely with frequency difference. As a consequence, the correlation between the signal components at the filter outputs is not small as is sometimes the case for fast fading, and one is left with the problem of dealing with M mutually correlated random variables to compute the error rate. A further complication is that the two-frequency mutual coherence function is complex, so the cross correlation of the tone filter outputs is also complex. This effectively doubles the calculations necessary to compute the correlation coefficients. Thus analytic results are practical only in the case of BFSK modulation. As we will show, the BFSK case is sufficiently tedious mathematically that there is little incentive to attempt to develop analytic results for higher-order FSK signaling, although such results could, in principle, be obtained. Furthermore, the BFSK case is sufficient to achieve our goal of COMLNK validation. COMLNK, of course, readily handles much more complicated cases involving M -ary modulation and non-linear carrier tracking loop operation.

Frequency hopping provides two key advantages to an FSK communications link. The primary advantage of hopping is protection from jamming, whether hostile or inadvertent. A side benefit, if the hopping rate is equal to or larger than the modulation symbol rate, is protection from intersymbol interference in frequency selective fading channels.

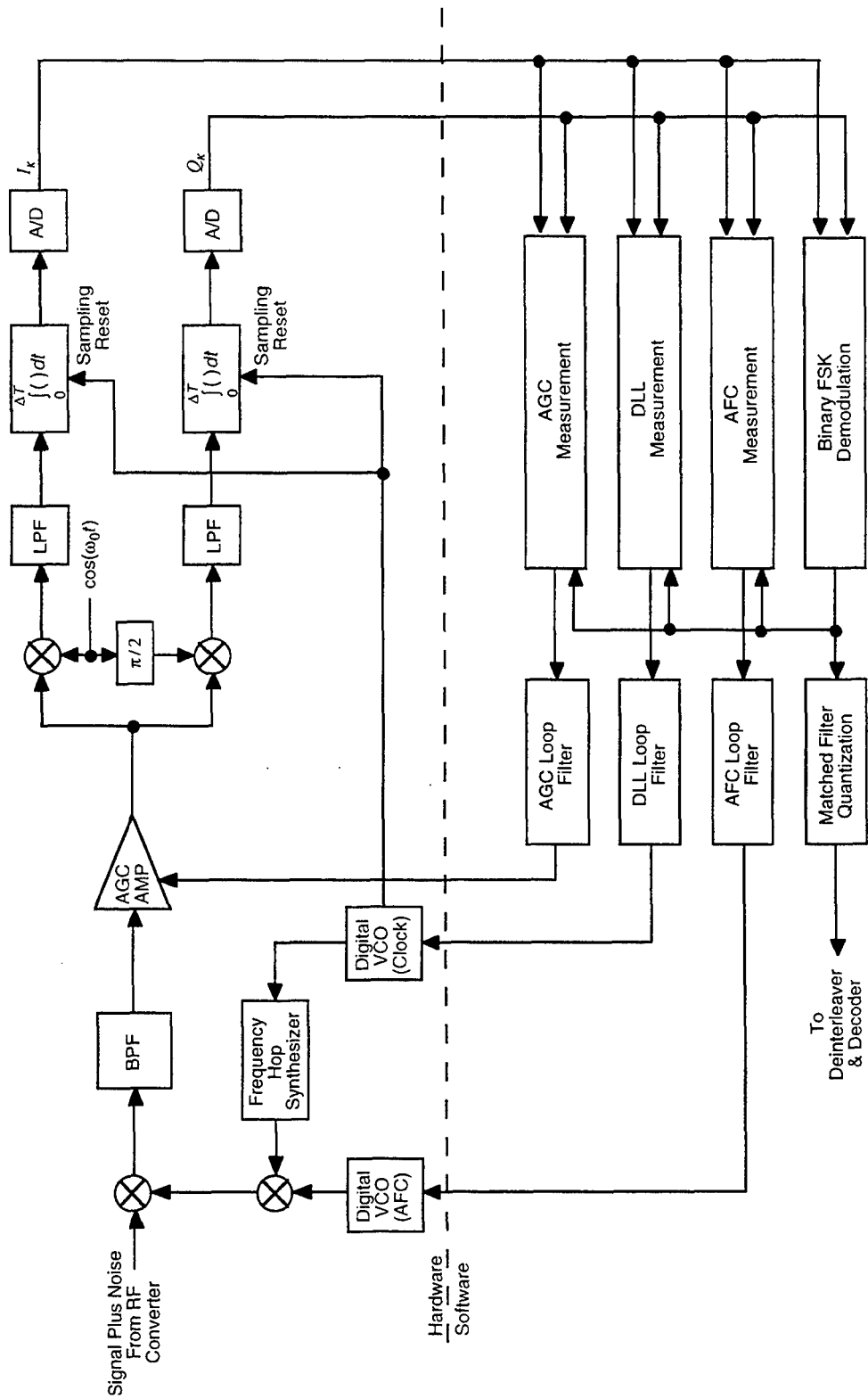


Figure G-1. Block diagram of a binary FSK receiver with frequency hopping.

In this appendix we will only consider the case where the hopping rate is equal to the symbol rate. If the hopping rate is faster than the symbol rate, then signal energy from multiple hops per symbol must be non-coherently combined. This would add considerable complexity to the analysis¹, although it is readily handled by COMLNK. If the hopping rate is slower than the symbol rate, then signal energy from previous symbols within a hop can interfere with the on-time symbol, and we consider the limiting case (no hopping) in Appendix H.

In Section G.1 of this appendix we give some general results for the BFSK signal with hopping and noise at the output of the tone filters for both continuous and sampled channel impulse response functions (CIRFs). In Section G.2 we investigate the performance of delay tracking in slow, frequency selective fading. Here we compute the ideal delay offset for both continuous and sampled CIRFs. The BFSK demodulation error rate with a fixed delay offset is then computed in Section G.3 for slow, frequency selective fading. Our results show that BFSK demodulation performance in frequency selective fading is very sensitive to the delay offset. Thus to compare simulation results with these theoretical developments we must turn the DLL in COMLNK off, and simulate demodulation performance at fixed values of the delay offset. In Section G.4 we calculate the BFSK error rate in fast, frequency selective fading assuming zero delay offset. Finally, in Section G.5 we discuss the effects of channel delay sampling on the BFSK demodulation error rate.

Even ignoring delay tracking, the BFSK demodulation error rate result for general time and frequency selective fading is extraordinarily tedious to calculate analytically and is only possible because of modern symbolic mathematics computer programs such as *Mathematica*® [Wolfram, 1996] used by the first-named author. To our knowledge these are new results that have not appeared elsewhere in the literature. Note that the tedious computation presented here is only associated with the theoretical analysis. The COMLNK digital simulation algorithms are quite straightforward.

G.1 GENERAL RESULTS FOR FSK WITH HOPPING.

In a binary FSK communications link, the transmitted signal during the k^{th} symbol period is

¹ Bogusch [1989] discusses 8-ary FSK non-coherent combining loss in AWGN and slow Rayleigh fading channels.

$$m(t) = \sum_k e^{j(\pi n_k \Delta f)t} \Pi\left[\frac{t}{T} - k\right] ,$$

where Δf is the tone spacing and T is the modulation period (or channel bit period for BFSK). The transmitted tone is determined by the value of n_k , where $n_k = \pm 1$ for BFSK. The rectangular function $\Pi(\cdot)$ is defined as

$$\Pi(x) = \begin{cases} 1 & \text{if } |x| \leq \frac{1}{2} \\ 0 & \text{otherwise} \end{cases} .$$

Here $m(t)$ represents a frequency offset in the transmitted signal, so the carrier frequency *per se* is never transmitted (unless sync symbol tracking is employed).

The received signal is the convolution of the channel impulse response function and the transmitted modulation. For a continuous CIRF the received signal is

$$u(t) = r \int_0^{\infty} m(t - \tau) h(t, \tau) d\tau ,$$

where r is the mean received signal amplitude. In slow fading developments later in this appendix, the CIRF does not vary during the modulation period, so $h(t, \tau)$ is replaced by $h(\tau)$ in this equation in this case. In either a simulation such as COMLNK or in a hardware channel simulator, the CIRF must be sampled in delay and time. The sampled CIRF version of the convolution equation is

$$u(t) = r \sum_{i=0}^{N_\tau-1} m(t - i\Delta\tau) h(t, i\Delta\tau) \Delta\tau ,$$

where $\Delta\tau$ is the delay sample size, and N_τ is the number of delay samples. In later developments we use $h_i(t)$ as a shorthand notation for $h(t, i\Delta\tau) \Delta\tau$.

The received signal is processed in filters to determine which tone was transmitted. The output voltage of the m^{th} filter ($m = \pm 1$) during the k^{th} symbol period is

$$Z_{m,k} = \frac{1}{T} \int_{(k-1/2)T+\tau_D}^{(k+1/2)T+\tau_D} [u(t) + n(t)] e^{-j(\pi m \Delta f)t} dt , \quad (\text{G.1})$$

where τ_D is the delay offset. The ideal value of τ_D is non-zero in frequency selective fading. The signal is demodulated by selecting the filter with the largest output amplitude².

When the signal is hopped so each symbol is transmitted at a different carrier frequency, signal energy from symbols other than the "on-time" symbol is severely attenuated by the receiver downconverter and band-pass filters. Ideally only energy from a single transmitted symbol is received during any sample period. Letting $k = 0$ represent the on-time symbol, the signal contribution to the filter output voltages [Equation (G.1)] is

$$S_m = r \int_0^{\infty} d\tau e^{-j(n_0 \pi \Delta f) \tau} \frac{1}{T} \int_{-T/2+\tau_D}^{T/2+\tau_D} dt h(t, \tau) e^{j\pi(n_0-m)\Delta f t} \Pi\left[\frac{t-\tau}{T}\right]$$

for a continuous CIRF and is

$$S_m = r \sum_{i=0}^{N_\tau-1} e^{-j(n_0 \pi \Delta f) i \Delta \tau} \frac{1}{T} \int_{-T/2+\tau_D}^{T/2+\tau_D} dt h_i(t) e^{j\pi(n_0-m)\Delta f t} \Pi\left[\frac{t-i\Delta\tau}{T}\right]$$

for a sampled CIRF.

The complex voltage $n(t)$ is additive white Gaussian noise (AWGN) with the usual properties:

$$\begin{aligned} \langle n(t) \rangle &= 0 \\ \langle n(t) n(t') \rangle &= 0, \\ \langle n(t) n^*(t') \rangle &= N_0 \delta(t - t') \end{aligned} \quad (G.2)$$

where N_0 is the one-sided noise spectral density, and $\delta(\cdot)$ is the Dirac delta function. The second equation results because the real and imaginary parts of AWGN are uncorrelated. The noise contribution to the filter output voltage is then

² Hard-decision demodulation is assumed here. In coded systems, soft-decision demodulation may be used, wherein all filter outputs are provided for subsequent processing.

$$N_{m,k} = \frac{1}{T} \int_{(k-1/2)T+\tau_D}^{(k+1/2)T+\tau_D} n(t) e^{-j(m\pi\Delta f)t} dt .$$

Because $n(t)$ is a complex, normally distributed random process with zero mean, $N_{m,k}$ is similarly distributed. Thus to complete the description of the filter output noise, we need the variance and cross correlation of $N_{m,k}$. The cross correlation is

$$C_{m,m'}^N = \langle N_{m,k} N_{m',k}^* \rangle = \frac{1}{T^2} \int_{(k-1/2)T+\tau_D}^{(k+1/2)T+\tau_D} dt e^{j\pi(n_k-m)\Delta f t'} \int_{(k-1/2)T+\tau_D}^{(k+1/2)T+\tau_D} dt' e^{-j\pi(n_k-m')\Delta f t'} \langle n(t) n^*(t') \rangle .$$

Because the noise $n(t)$ is delta-correlated, this expression reduces to

$$C_{m,m'}^N = \frac{N_0}{T} \exp[j\pi(m-m')\Delta f(kT+\tau_D)] \frac{\sin[\frac{1}{2}\pi(m-m')\Delta f T]}{\frac{1}{2}\pi(m-m')\Delta f T} = \frac{N_0}{T} \delta_{m,m'} \quad (\text{G.3})$$

for orthogonal signaling (*i.e.*, $\Delta f T = \text{positive integer}$) where $\delta_{m,m'}$ is the Kronecker delta-symbol:

$$\delta_{m,m'} = \begin{cases} 1 & \text{if } m = m' \\ 0 & \text{otherwise} \end{cases} .$$

G.2 IDEAL DELAY OFFSET.

In a frequency hopped FSK receiver, time tracking is done by generating early and late voltage samples at each hop position. The DLL then attempts to equalize the energy of these two samples. During the k^{th} symbol period, the early and late voltages at the output of the m^{th} tone filter are given by integrating the received voltage over the first and second halves of the tone period, respectively:

$$Z_E = \frac{1}{T} \int_{(k-1/2)T+\tau_D}^{kT+\tau_D} [u(t) + n(t)] \exp[-j(m\pi\Delta f)t] dt$$

$$Z_L = \frac{1}{T} \int_{kT+\tau_D}^{(k+1/2)T+\tau_D} [u(t) + n(t)] \exp[-j(m\pi\Delta f)t] dt .$$

The filter output voltage used for demodulation is just $Z_E + Z_L$. With one hop per symbol, we only need to consider these voltages for a single symbol, and the $k = 0$

symbol is a particularly convenient one. Now early and late sample energy can be evaluated for continuous and sampled channel impulse response functions.

Continuous CIRF: For this case the signal contributions to the early and late sample voltages from the filter corresponding to the transmitted tone are

$$S_E = r \int_0^{\infty} d\tau e^{-j(n_0 \pi \Delta f) \tau} \frac{1}{T} \int_{\tau_D - T/2}^{\tau_D} dt h(t, \tau) \Pi \left[\frac{t - \tau}{T} \right]$$

$$S_L = r \int_0^{\infty} d\tau e^{-j(n_0 \pi \Delta f) \tau} \frac{1}{T} \int_{\tau_D}^{\tau_D + T/2} dt h(t, \tau) \Pi \left[\frac{t - \tau}{T} \right] .$$

We assume for this calculation that the fading is slow compared to the modulation period ($\tau_0 / T \gg 1$), so the channel impulse response function is invariant over the period of the two time integrals. With this assumption the CIRF can be pulled out of the time integrals to give:

$$S_E = \frac{r}{2} \int_0^{\infty} h(\tau) e^{-j(n_0 \pi \Delta f) \tau} \Xi \left[\frac{2(\tau - \tau_D)}{T} + \frac{1}{2} \right] d\tau$$

$$S_L = \frac{r}{2} \int_0^{\infty} h(\tau) e^{-j(n_0 \pi \Delta f) \tau} \Xi \left[\frac{2(\tau - \tau_D)}{T} - \frac{1}{2} \right] d\tau$$

where $h(\tau)$ is the time-invariant channel impulse response function, and the trapezoid function $\Xi(\cdot)$ is defined as

$$\Xi(x) = \begin{cases} 1 & \text{if } |x| \leq \frac{1}{2} \\ \frac{3}{2} - |x| & \text{if } \frac{1}{2} \leq |x| \leq \frac{3}{2} \\ 0 & \text{otherwise} \end{cases} .$$

Similarly, the on-time signal voltage in slow fading, given by the integral of the received voltage over the entire symbol period T , is

$$S_O = r \int_0^{\infty} h(\tau) e^{-j(n_0 \pi \Delta f) \tau} \Lambda \left[\frac{\tau_D - \tau}{T} \right] d\tau ,$$

where Λ is the triangle function:

$$\Lambda(x) = \begin{cases} 1-|x| & \text{if } |x| \leq 1 \\ 0 & \text{otherwise} \end{cases} .$$

The average signal energy of the early, on-time, and late samples in frequency selective fading is obtained by making the usual assumptions that the CIRF is a zero-mean, complex normally distributed random process that is wide-sense stationary in frequency and thus has the following first and second order moments:

$$\begin{aligned} \langle h(\tau) \rangle &= \langle h(\tau) h(\tau') \rangle = 0 \\ \langle h(\tau) h^*(\tau') \rangle &= G(\tau) \delta(\tau - \tau') , \end{aligned} \quad (\text{G.4})$$

where $G(\tau)$ is the power impulse response function defined in Equation (2.8). We note that a phase-rotated CIRF such as

$$h(\tau) e^{-j(n_0 \pi \Delta f) \tau}$$

that appears in the equations for the signal voltages has exactly the same statistical properties as $h(\tau)$, so the phase term multiplying $h(\tau)$ can be ignored. With these statistical properties for the continuous CIRF, the average signal energy reduces to

$$\begin{aligned} \langle E_E \rangle &= \langle S_E S_E^* \rangle = \frac{r^2}{4} \int_0^{\infty} G(\tau) \Xi^2 \left[\frac{2(\tau - \tau_D)}{T} + \frac{1}{2} \right] d\tau \\ \langle E_O \rangle &= \langle S_O S_O^* \rangle = r^2 \int_0^{\infty} G(\tau) \Lambda^2 \left[\frac{\tau - \tau_D}{T} \right] d\tau \\ \langle E_L \rangle &= \langle S_L S_L^* \rangle = \frac{r^2}{4} \int_0^{\infty} G(\tau) \Xi^2 \left[\frac{2(\tau - \tau_D)}{T} - \frac{1}{2} \right] d\tau \end{aligned} \quad (\text{Continuous CIRF}) . \quad (\text{G.5})$$

These integrals can be done in closed form using the exponential form for the power impulse response function. The reader is spared the details.

Sampled CIRF: For a discrete (tapped delay line) channel impulse response function the expression for the early voltage becomes

$$S_E = \frac{r}{2} \sum_{i=0}^{N_\tau-1} h_i e^{-j(n_0 \pi \Delta f) i \Delta \tau} \Xi \left[\frac{2(i \Delta \tau - \tau_D)}{T} + \frac{1}{2} \right] .$$

Similar expressions hold for the on-time and late voltages. Equations similar to (G.4) hold for the sampled channel impulse response function:

$$\begin{aligned} \langle h_i \rangle &= \langle h_i h_{i'} \rangle = 0 \\ \langle h_i h_{i'}^* \rangle &= P_i \delta_{i,i'} \end{aligned} ,$$

where an expression for the mean power in each delay sample, P_i , is given in Equation (2.14). The integrals in Equations (G.5) are then replaced by a summation over discrete delays for the sampled CIRF case:

$$\begin{aligned} \langle E_E \rangle &= \frac{r^2}{4} \sum_{i=0}^{N_\tau-1} P_i \Xi^2 \left[\frac{2(i \Delta \tau - \tau_D)}{T} + \frac{1}{2} \right] \\ \langle E_O \rangle &= r^2 \sum_{i=0}^{N_\tau-1} P_i \Lambda^2 \left[\frac{i \Delta \tau - \tau_D}{T} \right] \quad (\text{Sampled CIRF}) . \\ \langle E_L \rangle &= \frac{r^2}{4} \sum_{i=0}^{N_\tau-1} P_i \Xi^2 \left[\frac{2(i \Delta \tau - \tau_D)}{T} - \frac{1}{2} \right] \end{aligned}$$

A delay lock loop attempts to adjust the receiver timing relative to the incoming signal until the average signal energy in the early sample is equal to that of the late sample. Thus we compute the ideal delay offset by solving the equation $\langle E_E \rangle = \langle E_L \rangle$ for τ_D . To see how this works in practice, it is useful to plot the early, on-time, and late energy for a few cases. In Figure G-2 we plot these quantities for the case where the frequency selective bandwidth is one-tenth of the symbol rate ($f_0 T = 0.1$) and the CIRF is continuous. The crossover point of the curves for the early and late energy gives the ideal delay offset, which for this case is $\tau_D / T = 0.49$ where $\tau_D = 0$ is the ideal offset for non-fading or flat fading channels. This is almost the same delay offset where the on-time energy is maximum³.

³ Solving the equation $\langle E_E \rangle = \langle E_L \rangle$ is not the same as maximizing $\langle E_O \rangle$.

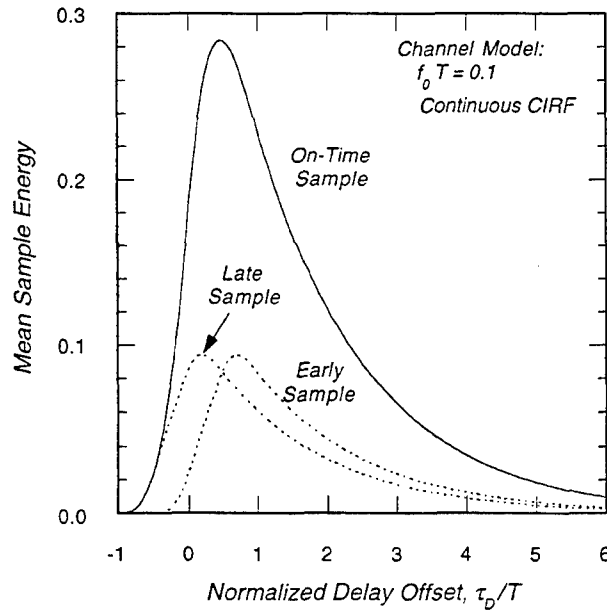


Figure G-2. Early, on-time, and late sample energy versus delay for a continuous CIRF.

When the CIRF is sampled in the delay domain, the early and late energy curves versus delay are not as well behaved, as illustrated in Figures G-3 and G-4 for CIRFs with two and four delay samples per symbol period, respectively. Again these curves are plotted for a normalized frequency selective bandwidth of one-tenth, and the early and late energy curves for a continuous CIRF are plotted also for comparison.

A local maximum occurs whenever the delay samples of the CIRF are aligned with the receiver's integration period. This is most pronounced in Figure G-3 where the early and late energy curves have local maxima for delays which are integer multiples of $T/2$. The crossover point of the sampled CIRF early and late energy curves is at $\tau_D/T = 0.31$, about one-fifth of a symbol period earlier than the crossover point for a continuous CIRF. The sampled CIRF curves for four samples per symbol period in Figure G-4 are somewhat better behaved, but clearly show a shift of the entire energy curve to earlier delays relative to the continuous CIRF curves. Thus the ideal delay offset also shifts to a smaller value.

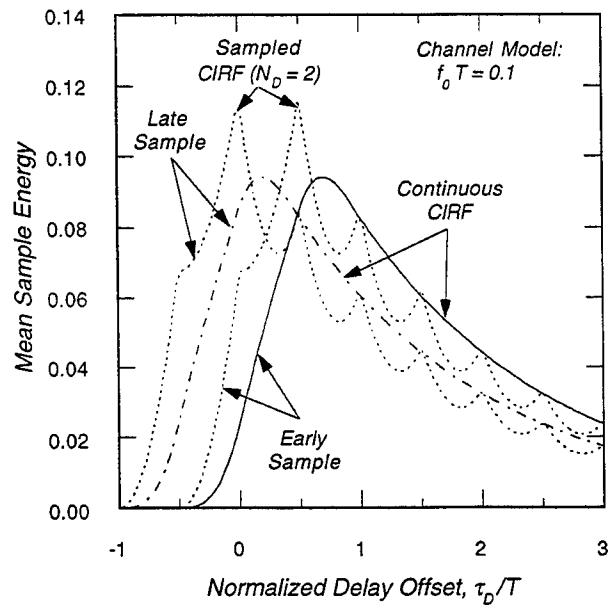


Figure G-3. Early and late sample energy versus delay for a sampled CIRF with two samples per symbol period.

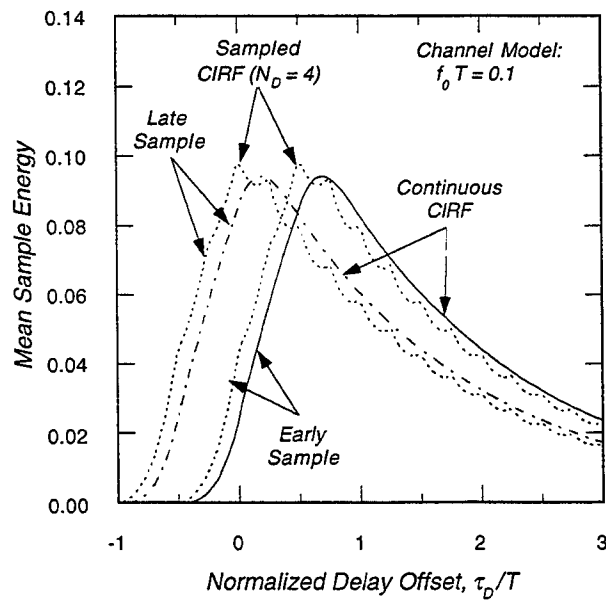


Figure G-4. Early and late sample energy versus delay for a sampled CIRF with four samples per symbol period.

The ideal delay offset versus the normalized frequency selective bandwidth $f_0 T$ is plotted in Figure G-5 for continuous CIRFs and sampled CIRFs with $N_D = 2, 4, 8,$ and 32 delay samples per symbol period. It is seen that a large number of delay samples per symbol is required to achieve close agreement between the sampled and continuous CIRF ideal delay offsets. However, this difference is of little practical significance for delay offsets less than one-tenth of a symbol period, and for $\tau_D / T \geq 0.1$ there are diminishing returns when more than four samples per symbol period are used. Thus we conclude that four channel samples per symbol period is probably sufficient for delay tracking in this case.

G.3 BFSK DEMODULATION ERROR RATE FOR SLOW, FREQUENCY SELECTIVE FADING WITH DELAY TRACKING.

As mentioned in the introduction to this appendix, the analytic expression for the BFSK error rate in time and frequency selective fading is quite complicated and adding the effects of delay tracking further exacerbates this problem. Thus we have chosen to develop analytic demodulation error rate expressions with non-zero delay offset only for slow, frequency selective fading and to develop such expressions with zero delay offset for fast, frequency selective fading. The first of these two cases is considered in this subsection.

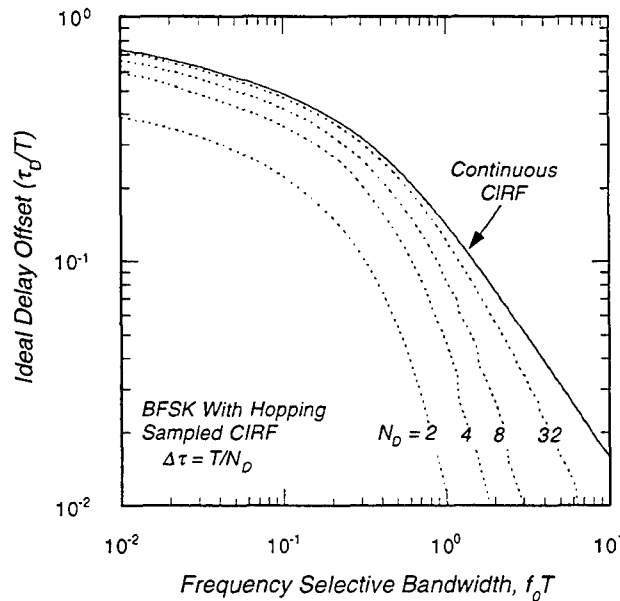


Figure G-5. Ideal delay offset for sampled and continuous CIRFs.

The output of the two BFSK tone filters is given by Equation (G.1). With frequency hopping, energy from symbols other than on-time symbol is attenuated by the downconversion and bandpass filtering processes in the front end of the receiver, so the transmitted signal can be written as

$$m(t) = e^{j(\pi n_0 \Delta f)t} \Pi\left[\frac{t}{T}\right],$$

where $n_0 = \pm 1$ is the transmitted tone. In slow fading, the voltage from the m^{th} tone filter is then

$$Z_m = \frac{r}{T} \int_{-T/2+\tau_D}^{T/2+\tau_D} dt e^{-j(m\pi\Delta f)t} \int_0^\infty d\tau h(\tau) e^{j(n_0\pi\Delta f)(t-\tau)} \Pi\left[\frac{t-\tau}{T}\right] + N_m.$$

This equation is easily extended to the case where the channel impulse response function is sampled by replacing the delay integral with a summation over the delay samples.

Without loss of generality, we assume that the $n_0 = +1$ tone is transmitted. By changing the order of integration, the voltage out of the filter corresponding to the transmitted tone can then be written as

$$Z_{+1} = r \int_0^\infty h(\tau) e^{-j(\pi\Delta f)\tau} \Lambda\left[\frac{\tau-\tau_D}{T}\right] d\tau + N_{+1}. \quad (\text{Continuous CIRF})$$

When the CIRF is sampled the output of this filter becomes

$$Z_{+1} = r \sum_{i=0}^{N_\tau-1} h_i e^{-j(\pi\Delta f)i\Delta\tau} \Lambda\left[\frac{i\Delta\tau-\tau_D}{T}\right] + N_{+1}. \quad (\text{Sampled CIRF})$$

Similarly, the voltage out of the other filter ($m = -1$) is

$$Z_{-1} = r C_M \int_0^\infty h(\tau) F(\tau, \tau_D) d\tau + N_{-1}, \quad (\text{Continuous CIRF})$$

$$Z_{-1} = r C_M \sum_{i=0}^{N_\tau-1} h_i F(i\Delta\tau, \tau_D) + N_{-1}, \quad (\text{Sampled CIRF})$$

where the coefficient C_M is defined as

$$C_M = \frac{(-1)^{\Delta f T}}{\omega_M} ,$$

and $\omega_M = 2\pi \Delta f T$ is the normalized tone spacing radian frequency. We assume that the tones are orthogonal, so $\Delta f T =$ an integer > 0 . The filter response is

$$F(\tau, \tau_D) = \pm j \times \begin{cases} e^{j(\pi \Delta f)(2\tau_D - \tau)} - e^{j(\pi \Delta f)\tau} & |\tau - \tau_D| \leq T \\ 0 & |\tau - \tau_D| > T \end{cases} ,$$

where the leading sign is plus for $\tau \leq \tau_D$ and is minus for $\tau > \tau_D$.

The demodulation error rate is computed from the mean energy at the outputs of the two filters and the voltage cross correlation coefficient. Using the properties of the continuous CIRF given in Equation (G.4) and the properties of the filter output noise given in Equation (G.3), the mean energy of the signal plus noise at the filter outputs are⁴

$$E_{+1} = \langle Z_{+1} Z_{+1}^* \rangle = r^2 \left\{ \int_0^\infty G(\tau) \Lambda^2 \left[\frac{\tau - \tau_D}{T} \right] d\tau + \frac{1}{\gamma} \right\} \quad (\text{Continuous CIRF})$$

$$E_{+1} = \langle Z_{+1} Z_{+1}^* \rangle = r^2 \left\{ \sum_{i=0}^{N_\tau-1} P_i \Lambda^2 \left[\frac{i\Delta\tau - \tau_D}{T} \right] + \frac{1}{\gamma} \right\} \quad (\text{Sampled CIRF})$$

and

$$E_{-1} = \langle Z_{-1} Z_{-1}^* \rangle = r^2 \left\{ \frac{4}{\omega_M^2} \int_0^\infty G(\tau) \sin^2 \left[\frac{\omega_M(\tau_D - \tau)}{2T} \right] d\tau + \frac{1}{\gamma} \right\} \quad |\tau - \tau_D| \leq T$$

(Continuous CIRF)

$$E_{-1} = \langle Z_{-1} Z_{-1}^* \rangle = r^2 \left\{ \frac{4}{\omega_M^2} \sum_{i=0}^{N_\tau-1} P_i \sin^2 \left[\frac{\omega_M(\tau_D - i\Delta\tau)}{2T} \right] + \frac{1}{\gamma} \right\} \quad |i\Delta\tau - \tau_D| \leq T ,$$

(Sampled CIRF)

⁴ The presence of ω_M in the denominator of the two expressions for E_{-1} indicates that one is not going to be able to set $\omega_M = 0$ to transform E_{-1} into E_{+1} .

where $\gamma = r^2 T / N_0$ is the mean channel bit energy-to-noise spectral density ratio. The cross correlation of the voltage out of the two filters is complex because, as discussed in Section 2, the two-frequency mutual coherence function for trans-ionospheric channels is complex. We show above that the noise out of the two filters is uncorrelated for orthogonal signaling, so only the signal contributes to the cross correlation coefficient. After some manipulation, the complex cross correlation coefficient is written in the form

$$C = \langle Z_{+1} Z_{-1}^* \rangle = 2r^2 \frac{(-1)^{\Delta f T + 1}}{\omega_M} \int_0^\infty G(\tau) \Lambda \left[\frac{\tau - \tau_D}{T} \right] \sin \left[\frac{\omega_M |\tau - \tau_D|}{2T} \right] e^{-j\frac{1}{2}\omega_M (\tau + \tau_D)/T} d\tau \quad .$$

(Continuous CIRF)

$$C = \langle Z_{+1} Z_{-1}^* \rangle = 2r^2 \frac{(-1)^{\Delta f T + 1}}{\omega_M} \sum_{i=0}^{N_i-1} P_i \Lambda \left[\frac{i\Delta\tau - \tau_D}{T} \right] \sin \left[\frac{\omega_M |i\Delta\tau - \tau_D|}{2T} \right] e^{-j\frac{1}{2}\omega_M (i\Delta\tau + \tau_D)/T} \quad .$$

(Sampled CIRF)

The integrals for the continuous CIRF case can be obtained in closed form for the exponential form of the power impulse response function. For the sampled CIRF case, the above expressions are evaluated numerically using Equation (2.14) for P_i . To simplify the results for the continuous CIRF case, we write the expressions for E_{+1} , E_{-1} , and C in terms of the normalized delay offset $\hat{\tau}_D = \tau_D / T$.

The mean signal plus noise energy at the output of the filter corresponding to the transmitted tone is then given by

$$E_{+1} = r^2 \left[\frac{1 + (1 - \lambda + \lambda \hat{\tau}_D)^2}{\lambda^2} - \frac{2e^{-\lambda(1-\hat{\tau}_D)}}{\lambda^2} + \frac{1}{\gamma} \right] \quad -1 \leq \hat{\tau}_D < 0$$

$$E_{+1} = r^2 \left[(\hat{\tau}_D - 1)^2 + \frac{2(1 + \lambda - \lambda \hat{\tau}_D)}{\lambda^2} - \frac{4e^{-\lambda \hat{\tau}_D}}{\lambda} - \frac{2e^{-\lambda(1+\hat{\tau}_D)}}{\lambda^2} + \frac{1}{\gamma} \right] \quad 0 \leq \hat{\tau}_D < 1$$

$$E_{+1} = r^2 \left[\frac{2[e^{-\lambda(\hat{\tau}_D-1)} - e^{-\lambda(\hat{\tau}_D+1)}]}{\lambda^2} - \frac{4e^{-\lambda \hat{\tau}_D}}{\lambda} + \frac{1}{\gamma} \right] \quad \hat{\tau}_D \geq 1$$

The mean signal plus noise energy of the output of the other filter is

$$E_{-1} = r^2 \left[\frac{2\lambda^2 \cos(\omega_M \hat{\tau}_D) + 2\omega_M \lambda \sin(\omega_M |\hat{\tau}_D|)}{\omega_M^2 (\lambda^2 + \omega_M^2)} - \frac{2}{\omega_M^2} - \frac{2e^{-\lambda(1+|\hat{\tau}_D|)}}{\lambda^2 + \omega_M^2} + \frac{1}{\gamma} \right] \quad -1 \leq \hat{\tau}_D \leq 1$$

$$E_{-1} = r^2 \left[\frac{2[e^{-\lambda(\hat{\tau}_D-1)} - e^{-\lambda(\hat{\tau}_D+1)}]}{\lambda^2 + \omega_M^2} + \frac{1}{\gamma} \right] \quad \hat{\tau}_D > 1$$

where again the tone spacing radian frequency is $\omega_M = 2\pi \Delta f T$. The cross correlation coefficient of the output voltages is complex, with real part C_R and imaginary part C_I :

$$C_R = r^2 \left\{ \frac{\lambda(\lambda^2 + \omega_M^2 - 2\lambda)}{(\lambda^2 + \omega_M^2)^2} - \frac{\lambda \hat{\tau}_D}{\lambda^2 + \omega_M^2} - \frac{(1 - \lambda + \lambda \hat{\tau}_D) \sin(\omega_M \hat{\tau}_D)}{\omega_M \lambda} \right. \\ \left. + \frac{[\omega_M(3\lambda^2 + \omega_M^2) \sin(\omega_M \hat{\tau}_D) + 2\lambda^3 \cos(\omega_M \hat{\tau}_D)] e^{-\lambda(1-\hat{\tau}_D)}}{\lambda(\lambda^2 + \omega_M^2)^2} \right\} \quad -1 \leq \hat{\tau}_D \leq 0$$

$$C_R = r^2 \left\{ -\frac{\lambda(\lambda^2 + \omega_M^2 + 2\lambda)}{(\lambda^2 + \omega_M^2)^2} + \frac{\lambda \hat{\tau}_D}{\lambda^2 + \omega_M^2} + \frac{(1 + \lambda - \lambda \hat{\tau}_D) \sin(\omega_M \hat{\tau}_D)}{\omega_M \lambda} \right. \\ \left. + \frac{2[\lambda \cos(\omega_M \hat{\tau}_D) - \omega_M \sin(\omega_M \hat{\tau}_D)] e^{-\lambda \hat{\tau}_D}}{\lambda^2 + \omega_M^2} \right. \\ \left. - \frac{[\omega_M(3\lambda^2 + \omega_M^2) \sin(\omega_M \hat{\tau}_D) - 2\lambda^3 \cos(\omega_M \hat{\tau}_D)] e^{-\lambda(1+\hat{\tau}_D)}}{\lambda(\lambda^2 + \omega_M^2)^2} \right\} \quad 0 \leq \hat{\tau}_D \leq 1$$

$$C_R = r^2 \left\{ \frac{2\lambda^2 \cos(\omega_M \hat{\tau}_D) [e^{-\lambda(\hat{\tau}_D+1)} - e^{-\lambda(\hat{\tau}_D-1)}]}{(\lambda^2 + \omega_M^2)^2} \right. \\ \left. - \frac{\omega_M(3\lambda^2 + \omega_M^2) \sin(\omega_M \hat{\tau}_D) [e^{-\lambda(\hat{\tau}_D+1)} - e^{-\lambda(\hat{\tau}_D-1)}]}{(\lambda^2 + \omega_M^2)^2 \lambda} \right. \\ \left. + \frac{2[\lambda \cos(\omega_M \hat{\tau}_D) - \omega_M \sin(\omega_M \hat{\tau}_D)] e^{-\lambda \hat{\tau}_D}}{\lambda^2 + \omega_M^2} \right\} \quad \hat{\tau}_D > 1$$

$$C_I = r^2 \left\{ \frac{\lambda [2\lambda^2 - (1+\lambda)(\lambda^2 + \omega_M^2)]}{\omega_M (\lambda^2 + \omega_M^2)^2} + \frac{\lambda^2 \hat{\tau}_D}{\omega_M (\lambda^2 + \omega_M^2)} - \frac{(1-\lambda + \lambda \hat{\tau}_D) \cos(\omega_M \hat{\tau}_D)}{\omega_M \lambda} \right. \\ \left. + \frac{[\omega_M (3\lambda^2 + \omega_M^2) \cos(\omega_M \hat{\tau}_D) - 2\lambda^3 \sin(\omega_M \hat{\tau}_D)] e^{-\lambda(1-\hat{\tau}_D)}}{\lambda (\lambda^2 + \omega_M^2)^2} \right\} \quad -1 \leq \hat{\tau}_D < 0$$

$$C_I = r^2 \left\{ \frac{\lambda [2\lambda^2 - (1-\lambda)(\lambda^2 + \omega_M^2)]}{\omega_M (\lambda^2 + \omega_M^2)^2} - \frac{\lambda^2 \hat{\tau}_D}{\omega_M (\lambda^2 + \omega_M^2)} - \frac{(1+\lambda - \lambda \hat{\tau}_D) \cos(\omega_M \hat{\tau}_D)}{\omega_M \lambda} \right. \\ \left. + \frac{2[\omega_M \cos(\omega_M \hat{\tau}_D) + \lambda \sin(\omega_M \hat{\tau}_D)] e^{-\lambda \hat{\tau}_D}}{\lambda^2 + \omega_M^2} \right. \\ \left. + \frac{[\omega_M (3\lambda^2 + \omega_M^2) \cos(\omega_M \hat{\tau}_D) + 2\lambda^3 \sin(\omega_M \hat{\tau}_D)] e^{-\lambda(1+\hat{\tau}_D)}}{\lambda (\lambda^2 + \omega_M^2)^2} \right\} \quad 0 \leq \hat{\tau}_D \leq 1$$

$$C_I = r^2 \left\{ \frac{\omega_M (3\lambda^2 + \omega_M^2) \cos(\omega_M \hat{\tau}_D) [e^{-\lambda(\hat{\tau}_D+1)} - e^{-\lambda(\hat{\tau}_D-1)}]}{\lambda (\lambda^2 + \omega_M^2)^2} \right. \\ \left. + \frac{2\lambda^2 \sin(\omega_M \hat{\tau}_D) [e^{-\lambda(\hat{\tau}_D+1)} - e^{-\lambda(\hat{\tau}_D-1)}]}{(\lambda^2 + \omega_M^2)^2} \right. \\ \left. + \frac{2[\omega_M \cos(\omega_M \hat{\tau}_D) + \lambda \sin(\omega_M \hat{\tau}_D)] e^{-\lambda \hat{\tau}_D}}{\lambda^2 + \omega_M^2} \right\} \quad \hat{\tau}_D > 1$$

The BFSK demodulation error rate is given in Appendix D with the substitutions $\sigma_1^2 = E_{-1}$, $\sigma_2^2 = E_{+1}$, and $\sigma_1^2 \sigma_2^2 \rho^2 = C_R^2 + C_I^2$. Thus the BFSK demodulation error rate with frequency hopping in slow, frequency selective Rayleigh fading is

$$\langle P_e \rangle = \frac{1}{2} \left[1 - \frac{E_{+1} - E_{-1}}{\sqrt{(E_{+1} + E_{-1})^2 - 4(C_R^2 + C_I^2)}} \right]. \quad (G.6)$$

As one might guess from the form of the equations for the filter output energy and the cross correlation coefficient, the demodulation error rate is quite sensitive to the delay tracking error. To illustrate this sensitivity, we plot the mean signal energy

and normalized correlation coefficient (ρ in the expression for $C_R^2 + C_I^2$) of the filter outputs versus delay offset in Figure G-6 for a case where the normalized frequency selective bandwidth $f_0 T$ is 0.1, the tone spacing $\Delta f T$ is 3, and the CIRF is continuous.

The same parameters for a sampled CIRF with two delay samples per symbol ($N_D = T / \Delta \tau = 2$) are plotted in Figure G-7. The corresponding irreducible error rates [*i.e.*, Equation (G.6) with $\gamma \rightarrow \infty$] versus delay offset are plotted in Figure G-8.

A number of observations are readily apparent from these results. First, the delay offset that maximizes the output signal energy of the filter corresponding to the transmitted tone *does not* necessarily correspond to the minimum BFSK demodulation error rate. Indeed, for the continuous CIRF case the minimum error rate occurs near $\tau_D = 0$ whereas the maximum energy occurs near $\tau_D = T/2$. Second, the irreducible error rate for the sampled CIRF case is zero for $\tau_D \leq -T/2$ because the normalized cross correlation coefficient is unity in this region. This is an artifact of the sampling (fortunately, the DLL, if operating near its ideal value, will keep the delay error positive). Third, the irreducible BFSK demodulation error rate is quite sensitive to the delay offset, especially when the CIRF is coarsely sampled. An active DLL, however, will tend to average over these delay offsets as the tracking error varies with time. For this reason, we turn the DLL off in COMLNK when generating simulation results to compare with these theoretical results. Therefore the comparisons have little practical significance other than for simulation verification.

The effect of delay tracking on BFSK performance is summarized in Figure G-9, where the irreducible BFSK demodulation error rate with the ideal delay offset (τ_D equal to the ideal value from Figure G-5) and with no offset ($\tau_D = 0$) is plotted versus normalized frequency selective bandwidth. While delay tracking does not minimize the error rate, it does reduce the irreducible error rate by a factor of about 2 for $f_0 T$ values greater than 2 or so. Below this value of $f_0 T$ however, delay tracking actually degrades BFSK demodulation performance slightly from the performance that could be obtained if the receiver could maintain time tracking at the position it should have in a benign environment ($\tau_D = 0$). Of course the possible presence of line-of-sight or total electron content dynamics or both force one to do delay tracking if the receiver is to have any chance of maintaining lock on the received signal. Furthermore, it must be emphasized that all results involving the irreducible error rate apply only when the signal-to-noise ratio is infinitely large, a condition that is rarely representative of actual practice.

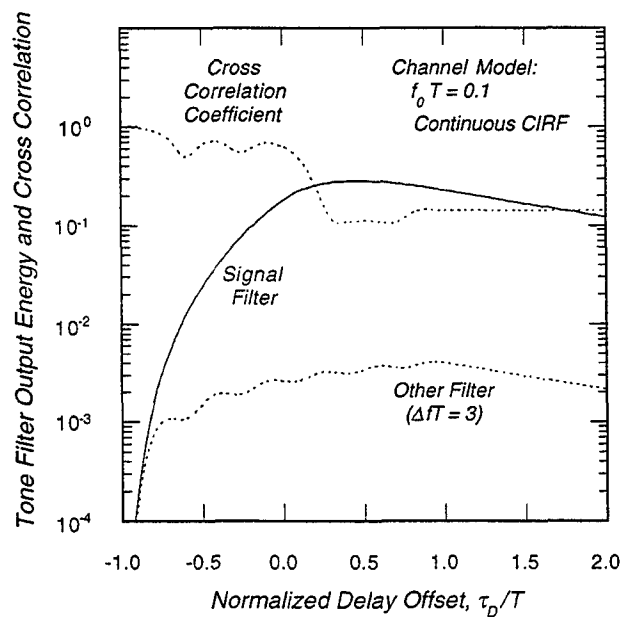


Figure G-6. Mean signal energy and cross correlation coefficient versus delay for a continuous CIRF, $f_0 T = 0.1$, and $\Delta f T = 3$.

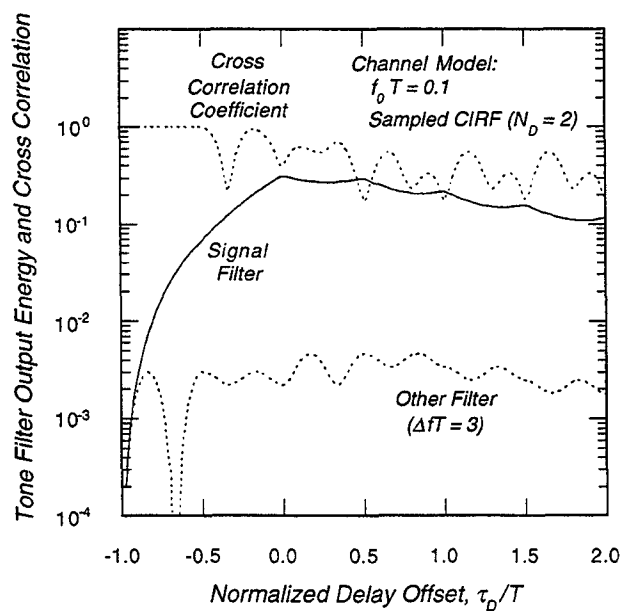


Figure G-7. Mean energy and cross correlation coefficient versus delay for a sampled CIRF ($N_D = 2$), $f_0 T = 0.1$, and $\Delta f T = 3$.

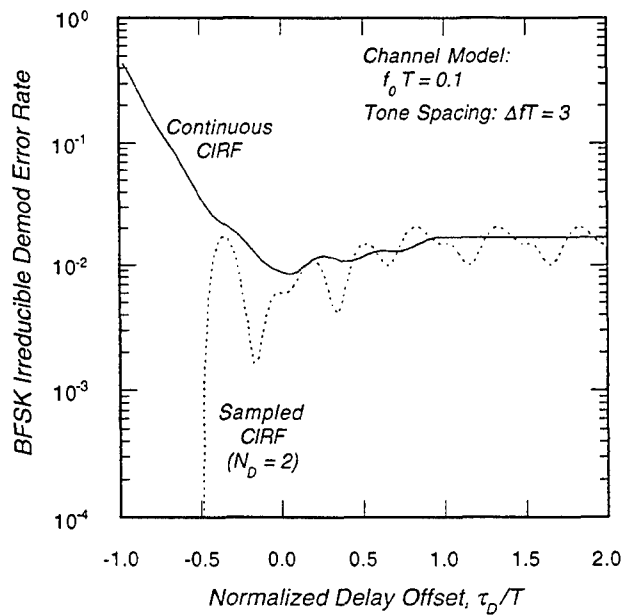


Figure G-8. BFSK irreducible demodulation error rate versus delay for continuous and sampled CIRFs, $f_0 T = 0.1$, and $\Delta f T = 3$.

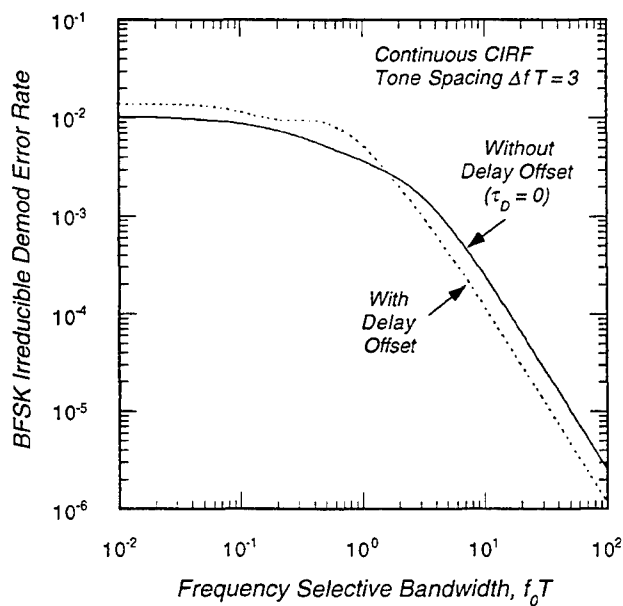


Figure G-9. BFSK irreducible demodulation error rate with frequency hopping and with and without delay offset.

It is interesting that the irreducible error rate of BFSK with hopping approaches a limit that is less than 50 percent in severe frequency selective fading ($f_0 T \rightarrow 0$). When the delay offset is zero, this asymptotic limit is

$$\langle P_e \rangle = \frac{1}{2} \left[1 - \frac{\omega_M^2 - 6}{\omega_M \sqrt{\omega_M^2 + 3}} \right] \quad (\gamma \rightarrow \infty, f_0 T \rightarrow 0, \tau_D = 0) ,$$

which is equal to 0.091 for minimum tone spacing ($\Delta f T = 1$), 0.011 for the $\Delta f T = 3$ case plotted in Figure G-9, and 9.5×10^{-4} for $\Delta f T = 10$.

The effect of tone spacing on the BFSK demodulation error rate in slow frequency selective fading with hopping is illustrated in Figure G-10 for a continuous CIRF where we plot the irreducible error rate for three values of $\Delta f T$. The delay offset is set to zero for these plots. For this case when $f_0 T$ is less than 1 or so, the demodulation irreducible error rate decreases by about a factor of 10 for each factor of 3 increase in the tone spacing.

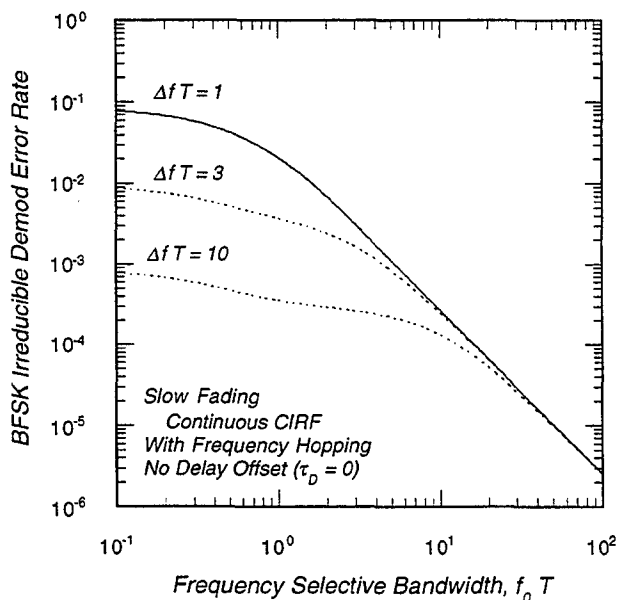


Figure G-10. BFSK irreducible demodulation error rate with frequency hopping for three tone spacings.

The ideal BFSK demodulation error rate in slow, frequency selective fading with frequency hopping and a continuous CIRF is plotted in Figure G-11 versus E_{cb}/N_0 for several values of $f_0 T$. For each case the ideal delay offset is given. At error rates above 5 percent or so, the effect of frequency selective fading is just to shift the error rate curves to the right by the loss in signal energy at the output of the filter corresponding to the transmitted tone. This loss in signal energy occurs because energy with times-of-arrival outside of the time interval $-T/2 + \tau_D \leq t \leq T/2 + \tau_D$ arrives when the receiver is set at a different carrier frequency. Energy from the on-time symbol that arrives early ($t < -T/2 + \tau_D$) arrives when the receiver is still at the carrier frequency of the previous symbol, and energy that arrives late ($t > T/2 + \tau_D$) arrives after the receiver has hopped to the carrier frequency of the next symbol. As the channel bit energy-to-noise density ratio increases, the curves approach an irreducible error rate determined by the amount of signal in the output of the wrong filter.

G.4 BFSK DEMODULATION ERROR RATE FOR FAST, FREQUENCY SELECTIVE FADING WITHOUT DELAY TRACKING.

As discussed above the expressions for the BFSK demodulation error rate in time and frequency selective fading are sufficiently complex that we have not included delay offset in this calculation. Thus the signal contribution to the tone filter outputs is

$$S_m = r \int_0^{\infty} d\tau e^{-j(n_0 \pi \Delta f) \tau} \frac{1}{T} \int_{-T/2}^{T/2} dt h(t, \tau) e^{j\pi(n_0 - m) \Delta f t} \Pi \left[\frac{t - \tau}{T} \right]$$

for the continuous CIRF case. The effect of the rectangular function in the equation for S_m is to change the lower limit of the time integral to $-T/2 + \tau$. The extension of this equation to the sampled CIRF case is straightforward. As before, delay integrals are replaced by sums over delay samples. We will not consider the sampled case further until we have derived expressions for the signal energy out of the two filters and the cross correlation coefficient.

To obtain the BFSK demodulation error rate in Rayleigh fading we need only to calculate the second order moments of S_m . In such fading, S_m is a complex, zero-mean, normally distributed random variable.

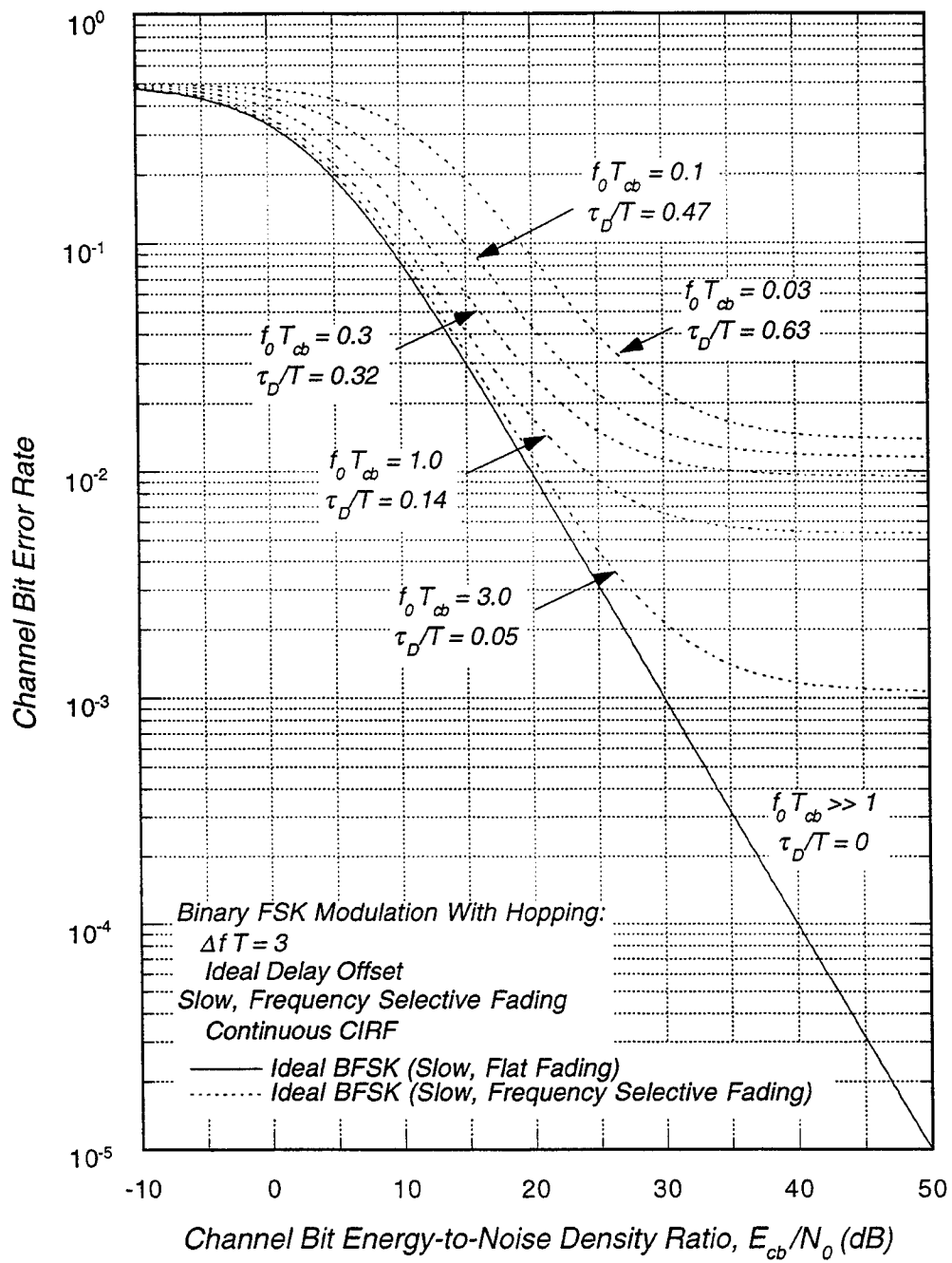


Figure G-11. BFSK demodulation error rate in slow, frequency selective fading with ideal delay offset.

G.4.1 Second Order Moments of S_m for Continuous CIRF Case.

Assuming, without loss of generality, that the $n_0 = +1$ tone was transmitted, the signal energy at the output of the filter corresponding to the transmitted tone is

$$E_{S,+1} = \langle S_{+1} S_{+1}^* \rangle = r^2 \int_0^T d\tau \int_0^T d\tau' e^{-j\pi\Delta f(\tau-\tau')} \frac{1}{T} \int_{-T/2+\tau}^{T/2} dt \frac{1}{T} \int_{-T/2+\tau'}^{T/2} dt' \langle h(t, \tau) h^*(t', \tau') \rangle .$$

For the turbulent model, the expectation of the channel impulse response function reduces to

$$\langle h(t, \tau) h^*(t', \tau') \rangle = G(\tau) \delta(\tau - \tau') \rho(t - t')$$

where the power impulse response function $G(\tau)$ is defined in Equation (2.8), and $\rho(t)$ is the temporal autocorrelation function of the fading. For simultaneous time and frequency selective fading we use the f^{-6} form for $\rho(t)$ defined in Section 2.

The number of time integrals can be reduced from two to one by the usual change to a difference variable. After changing to normalized delay ($\zeta = \tau/T$) and time ($\xi = t/T$) variables, the resulting expression for the signal energy out of the $m = +1$ tone filter is

$$E_{S,+1} = 2r^2 \int_0^1 TG(T\zeta) R_{+1}(\zeta) d\zeta ,$$

where the time integral $R_{+1}(\zeta)$ is

$$R_{+1}(\zeta) = \int_0^{1-\zeta} \rho(T\xi)(1-\zeta-\xi) d\xi .$$

We use this separation of the time and delay integrals to facilitate the extension of this and following expressions to the sampled CIRF case. The time integrals for both the sampled and continuous CIRF cases are the same, the only difference is whether or not the argument of the time integral is discrete or continuous. Thus $R_{+1}(\zeta)$ appears in the continuous CIRF expression for $E_{S,+1}$ and $R_{+1}(i\Delta\tau/T)$ appears in the sampled CIRF expression.

The signal energy at the output of the $m = -1$ tone filter is

$$E_{S,-1} = \langle S_{-1} S_{-1}^* \rangle = r^2 \int_0^T d\tau \int_0^T d\tau' e^{-j\pi\Delta f(\tau-\tau')} \frac{1}{T} \int_{-T/2+\tau}^{T/2} dt \frac{1}{T} \int_{-T/2+\tau'}^{T/2} dt' \\ \times e^{2\pi j \Delta f(t-t')} \langle h(t, \tau) h^*(t', \tau') \rangle$$

In a similar manner to that used to simplify the expression for $E_{S,+1}$, the expression for $E_{S,-1}$ reduces to the deceptively simple form

$$E_{S,-1} = 2r^2 \int_0^1 TG(T\zeta) R_{-1}(\zeta) d\zeta$$

where

$$R_{-1}(\zeta) = \int_0^{1-\zeta} \rho(T\xi) \cos(\omega_M \xi) (1 - \zeta - \xi) d\xi$$

The cross correlation coefficient between of signal contributions to the output of the two filters is

$$C = \langle S_{+1} S_{-1}^* \rangle = r^2 \int_0^T d\tau \int_0^T d\tau' e^{-j\pi\Delta f(\tau-\tau')} \\ \times \frac{1}{T} \int_{-T/2+\tau}^{T/2} dt \frac{1}{T} \int_{-T/2+\tau'}^{T/2} dt' e^{-j2\pi\Delta f t'} \langle h(t, \tau) h^*(t', \tau') \rangle$$

After considerable manipulation, the real (C_R) and imaginary (C_I) parts of this expression can be reduced to

$$C_R = -r^2 C_M \int_0^1 TG(T\zeta) R_{CR}(\zeta) d\zeta$$

$$C_I = r^2 C_M \int_0^1 TG(T\zeta) R_{CI}(\zeta) d\zeta$$

where the time integrals are

$$R_{CR}(\zeta) = [1 + \cos(\omega_M \zeta)] R_S(\zeta) + \sin(\omega_M \zeta) [R_p(\zeta) + R_C(\zeta)]$$

$$R_{CT}(\zeta) = [1 - \cos(\omega_M \zeta)] [R_p(\zeta) + R_C(\zeta)] + \sin(\omega_M \zeta) R_S(\zeta)$$

and where the integrals $R_S(\zeta)$, $R_C(\zeta)$, and $R_p(\zeta)$ are defined as

$$R_p(\zeta) = \int_0^{1-\zeta} \rho(T\xi) d\xi$$

$$R_S(\zeta) = \int_0^{1-\zeta} \rho(T\xi) \sin(\omega_M \xi) d\xi$$

$$R_C(\zeta) = \int_0^{1-\zeta} \rho(T\xi) \cos(\omega_M \xi) d\xi .$$

At this point we have formally solved the problem of the BFSK demodulation error rate in fast, frequency selective fading with no delay offset. To obtain an analytic answer, however, one must perform the indicated integrals. Therein lies the problem. For the f^{-6} form for the temporal autocorrelation function and the simple exponential form for the power impulse response function, the analytic expression for $E_{S,-1}$ has *more than 80 terms* unless care is taken to collect together similar factors. The expressions for C_R and C_I are even more unwieldy. Thus a symbolic mathematics program such as *Mathematica*® is necessary to have any hope of obtaining correct answers for these integrals.

The rest of this subsection is devoted to writing down the analytic results for the second order moments of S_m . These results are valid for the f^{-6} temporal autocorrelation function $\rho(t)$ and the exponential power impulse response function $G(\tau)$. For each moment we first calculate expressions for the time integrals because these are also used for the sampled CIRF case.

In normalized units, the power impulse response and temporal autocorrelation functions are

$$TG(T\xi) = \lambda e^{-\lambda \xi}$$

and

$$\rho(T\xi) = \left[1 + T_6 \xi + \frac{1}{3} (T_6 \xi)^2 \right] e^{-T_6 \xi}$$

where $\lambda = 2\pi f_0 T$, $T_6 = \alpha_6 T / \tau_0$, and α_6 is a numerical constant ($\alpha_6 = 2.904630\dots$) defined in Section 2.

Using the normalized temporal autocorrelation function, we get the following for the time integrals of $E_{S,+1}$ and $E_{S,-1}$:

$$R_{+1}(\zeta) = \frac{8(1-\zeta)T_6 - 15}{3T_6^2} + \left[\frac{T_6^2 + 7T_6 + 15}{3T_6^2} - \frac{2T_6 + 7}{3T_6} \zeta + \frac{1}{3} \zeta^2 \right] e^{-(1-\zeta)T_6}$$

$$R_{-1,1}(\zeta) = \frac{(1-\zeta)T_6}{T_6^2 + \omega_M^2} - \frac{[T_6 \cos(\omega_M \zeta) + \omega_M \sin(\omega_M \zeta)](1-\zeta)}{T_6^2 + \omega_M^2} e^{-(1-\zeta)T_6}$$

$$R_{-1,2}(\zeta) = \frac{[(1-\zeta)T_6 - 1](T_6^2 - \omega_M^2)}{(T_6^2 + \omega_M^2)^2} + \frac{A_1(\zeta) \cos(\omega_M \zeta) - B_1(\zeta) \sin(\omega_M \zeta)}{(T_6^2 + \omega_M^2)^2} e^{-(1-\zeta)T_6}$$

$$R_{-1,3}(\zeta) = \frac{2T_6^2[(1-\zeta)T_6 - 3](T_6^2 - 3\omega_M^2)}{3(T_6^2 + \omega_M^2)^3} - \frac{A_2(\zeta) \cos(\omega_M \zeta) + B_2(\zeta) \sin(\omega_M \zeta)}{3(T_6^2 + \omega_M^2)^3} e^{-(1-\zeta)T_6}$$

$$R_{-1,4}(\zeta) = -\frac{2T_6^2(T_6^4 - 6\omega_M^2 T_6^2 + \omega_M^4)}{(T_6^2 + \omega_M^2)^4} + \frac{A_3(\zeta) \cos(\omega_M \zeta) + B_3(\zeta) \sin(\omega_M \zeta)}{3(T_6^2 + \omega_M^2)^4} e^{-(1-\zeta)T_6}$$

where

$$A_1(\zeta) = [(1-\zeta)T_6 - 1] \left\{ \omega_M^2 [1 - (1-\zeta)T_6] - T_6^2 - (1-\zeta)T_6^3 \right\}$$

$$\begin{aligned} A_2(\zeta) = & T_6 \left\{ 6\omega_M^4(1-\zeta) + \omega_M^2 [18 - 5\omega_M^2(1-\zeta)^2] T_6 \right. \\ & - \omega_M^2 [6 - \omega_M^2(1-\zeta)^2] (1-\zeta) T_6^2 - 6[1 + \omega_M^2(1-\zeta)^2] T_6^3 \\ & \left. - 2[2 - \omega_M^2(1-\zeta)^2] (1-\zeta) T_6^4 - (1-\zeta)^2 T_6^5 + (1-\zeta)^3 T_6^6 \right\} \end{aligned}$$

$$\begin{aligned} A_3(\zeta) = & T_6^2 \left\{ 3\omega_M^2 [2 - \omega_M^2(1-\zeta)^2] - \omega_M^4 [18 - \omega_M^2(1-\zeta)^2] (1-\zeta) T_6 \right. \\ & - 3\omega_M^2 [12 + \omega_M^2(1-\zeta)^2] T_6^2 - 3\omega_M^2 [4 - \omega_M^2(1-\zeta)^2] (1-\zeta) T_6^3 \\ & + 3[2 + \omega_M^2(1-\zeta)^2] T_6^4 + 3[2 + \omega_M^2(1-\zeta)^2] (1-\zeta) T_6^5 \\ & \left. + 3(1-\zeta)^2 T_6^6 + (1-\zeta)^3 T_6^7 \right\} \end{aligned}$$

$$B_1(\zeta) = \omega_M [(1-\zeta)T_6 - 1] \left\{ \omega_M^2(1-\zeta) + 2T_6 + (1-\zeta)T_6^2 \right\}$$

$$\begin{aligned} B_2(\zeta) = & \omega_M T_6 \left\{ 3\omega_M^2 [2 - \omega_M^2(1-\zeta)^2] \right. \\ & - \omega_M^2 [14 - \omega_M^2(1-\zeta)^2] (1-\zeta) T_6 - 2[9 + \omega_M^2(1-\zeta)^2] T_6^2 \\ & \left. - 2[3 - \omega_M^2(1-\zeta)^2] (1-\zeta) T_6^3 + (1-\zeta)^2 T_6^4 + (1-\zeta)^3 T_6^5 \right\} \end{aligned}$$

$$\begin{aligned} B_3(\zeta) = & \omega_M T_6^2 \left\{ \omega_M^4 [6 - \omega_M^2(1-\zeta)^2] (1-\zeta) \right. \\ & + 6\omega_M^2 [4 - \omega_M^2(1-\zeta)^2] T_6 + 3\omega_M^2 [4 + \omega_M^2(1-\zeta)^2] (1-\zeta) T_6^2 \\ & + 3\omega_M^2 [2 + \omega_M^2(1-\zeta)^2] T_6^3 + 3[6 + \omega_M^2(1-\zeta)^2] (1-\zeta) T_6^4 \\ & \left. + 6(1-\zeta)^2 T_6^5 + (1-\zeta)^3 T_6^6 \right\} \end{aligned}$$

and

$$R_{-1}(\zeta) = R_{-1,1}(\zeta) + R_{-1,2}(\zeta) + R_{-1,3}(\zeta) + R_{-1,4}(\zeta) .$$

The time integrals for the real and imaginary parts of the cross correlation coefficient are

$$R_{CR,1}(\zeta) = \frac{\{-\omega_M [1 + \cos(\omega_M \zeta)] + \sin(\omega_M \zeta) T_6\} (1 - \zeta)^2 T_6^2}{3(T_6^2 + \omega_M^2)} e^{-(1-\zeta)T_6}$$

$$R_{CR,2}(\zeta) = -\frac{\omega_M (7T_6^2 + 3\omega_M^2) [1 + \cos(\omega_M \zeta)] (1 - \zeta) T_6}{3(T_6^2 + \omega_M^2)^2} e^{-(1-\zeta)T_6} \\ + \frac{(5T_6^2 + \omega_M^2) \sin(\omega_M \zeta) (1 - \zeta) T_6^2}{3(T_6^2 + \omega_M^2)^2} e^{-(1-\zeta)T_6}$$

$$R_{CR,3}(\zeta) = -\frac{\omega_M (15T_6^4 + 10\omega_M^2 T_6^2 + 3\omega_M^4) [1 + \cos(\omega_M \zeta)]}{3(T_6^2 + \omega_M^2)^3} [1 - e^{-(1-\zeta)T_6}] \\ + \frac{8 \sin(\omega_M \zeta) T_6^5}{3(T_6^2 + \omega_M^2)^3} [1 + e^{-(1-\zeta)T_6}]$$

$$R_{CI,1}(\zeta) = \frac{\{[1 - \cos(\omega_M \zeta)] T_6 - \omega_M \sin(\omega_M \zeta)\} (1 - \zeta)^2 T_6^2}{3(T_6^2 + \omega_M^2)} e^{-(1-\zeta)T_6}$$

$$R_{CI,2}(\zeta) = \frac{\omega_M (5T_6^2 + \omega_M^2) [1 - \cos(\omega_M \zeta)] (1 - \zeta) T_6^2}{3(T_6^2 + \omega_M^2)^2} e^{-(1-\zeta)T_6} \\ - \frac{\omega_M (7T_6^2 + 3\omega_M^2) \sin(\omega_M \zeta) (1 - \zeta) T_6}{3(T_6^2 + \omega_M^2)^2} e^{-(1-\zeta)T_6}$$

$$R_{CI,3}(\zeta) = \frac{8 [1 - \cos(\omega_M \zeta)] T_6^5}{3(T_6^2 + \omega_M^2)^3} e^{-(1-\zeta)T_6}$$

$$- \frac{\omega_M (15T_6^4 + 10\omega_M^2 T_6^2 + 3\omega_M^4) \sin(\omega_M \zeta)}{3(T_6^2 + \omega_M^2)^3} e^{-(1-\zeta)T_6}$$

$$R_{CI,4}(\zeta) = \frac{8 [1 - \cos(\omega_M \zeta)] T_6^5 + \omega_M (15T_6^4 + 10\omega_M^2 T_6^2 + 3\omega_M^4) \sin(\omega_M \zeta)}{3(T_6^2 + \omega_M^2)^3}$$

The time integrals for the complex cross correlation coefficient are then

$$R_{CR}(\zeta) = R_{CR,1}(\zeta) + R_{CR,2}(\zeta) + R_{CR,3}(\zeta)$$

$$R_{CI}(\zeta) = R_{CI,1}(\zeta) + R_{CI,2}(\zeta) + R_{CI,3}(\zeta) + R_{CI,4}(\zeta)$$

These integrals are then used to compute the delay integrals in the continuous CIRF case and the delay sums in the sampled CIRF case.

The signal energy out filter corresponding to the transmitted tone is then given by the expression

$$E_{S,+1} = \frac{16(\lambda - 1)T_6 - 30\lambda + 2(15\lambda + 8T_6)e^{-\lambda}}{3\lambda T_6^2}$$

$$+ \frac{2\lambda(T_6^2 + 7T_6 + 15)(e^{-T_6} - e^{-\lambda})}{3(\lambda - T_6)T_6^2}$$

$$- \frac{2\lambda(2T_6 + 7)[e^{-T_6} - (1 + \lambda - T_6)e^{-\lambda}]}{3(\lambda - T_6)^2 T_6}$$

$$+ \frac{2\lambda \{2e^{-T_6} - [2 + 2\lambda + \lambda^2 - 2(\lambda + 1)T_6 + T_6^2]e^{-\lambda}\}}{3(\lambda - T_6)^3}$$

The signal energy out of the other filter is an expression with a large number of terms. We find this expression easier to comprehend when it is broken into multiple terms (4), each with common denominators. These terms are:

$$E_{-1,1} = \frac{16(\lambda-1)T_6^5}{3\lambda(T_6^2 + \omega_M^2)^3} - \frac{2[T_6^5 + 5T_6^4 + 2(2 + \omega_M^2)T_6^3 + 6\omega_M^2 T_6^2 + \omega_M^4(T_6 + 1)](\lambda-1)T_6^2}{3\lambda(T_6^2 + \omega_M^2)^3} e^{-T_6}$$

$$E_{-1,2} = 2 \frac{-5T_6^6 + 15\omega_M^2 T_6^4 + 5\omega_M^4 T_6^2 + \omega_M^6}{(T_6^2 + \omega_M^2)^4} + 2 \frac{T_6^9 + 6T_6^8 + 3(5 + \omega_M^2)T_6^7 + 3(5 + 4\omega_M^2)T_6^6 + 3\omega_M^2(1 + \omega_M^2)T_6^5}{3(T_6^2 + \omega_M^2)^4} e^{-T_6}$$

$$E_{-1,3} = -\frac{2(T_6 - \lambda)(e^{-T_6} - e^{-\lambda})}{\lambda[(T_6 - \lambda)^2 + \omega_M^2]} + \frac{2[(T_6 - \lambda)^2 - \omega_M^2]T_6 e^{-\lambda}}{\lambda[(T_6 - \lambda)^2 + \omega_M^2]^2} - \frac{2\{T_6^3 + (1 - 3\lambda)T_6^2 + [\lambda(3\lambda - 2) + \omega_M^2]T_6 - \omega_M^2(\lambda + 1) + \lambda^2(1 - \lambda)\}T_6 e^{-T_6}}{\lambda[(T_6 - \lambda)^2 + \omega_M^2]^2}$$

$$E_{-1,4} = \frac{4(\lambda - T_6)[(T_6 - \lambda)^2 - 3\omega_M^2]T_6^2}{3\lambda[(T_6 - \lambda)^2 + \omega_M^2]^3} - \frac{2[T_6^5 - (5\lambda - 2)T_6^4]}{3\lambda[(T_6 - \lambda)^2 + \omega_M^2]^3} e^{-T_6} - \frac{4[(1 + \omega_M^2 - 4\lambda + 5\lambda^2)T_6^3 - \lambda(3 + 3\omega_M^2 - 6\lambda + 5\lambda^2)T_6^2]}{3\lambda[(T_6 - \lambda)^2 + \omega_M^2]^3} e^{-T_6} - \frac{2[\omega_M^4 + 6\omega_M^2(\lambda^2 - 1) + \lambda^2(6 - 8\lambda + 5\lambda^2)]T_6}{3\lambda[(T_6 - \lambda)^2 + \omega_M^2]^3} e^{-T_6} + 2 \frac{\lambda^3(2 - 2\lambda + \lambda^2) + 2\omega_M^2\lambda(\lambda^2 - 3) + \omega_M^4(\lambda + 2)}{3\lambda[(T_6 - \lambda)^2 + \omega_M^2]^3} e^{-T_6}$$

where

$$E_{S,-1} = E_{-1,1} + E_{-1,2} + E_{-1,3} + E_{-1,4} \quad .$$

Similarly, we organize the cross correlation coefficient into multiple terms with the same denominators. The real part C_R has 13 such terms:

$$C_{R,1} = S_M \frac{(1 - e^{-\lambda}) \lambda [\lambda (15T_6^4 + 10\omega_M^2 T_6^2 + 3\omega_M^4) + 8T_6^5]}{3(\lambda^2 + \omega_M^2)(T_6^2 + \omega_M^2)^3}$$

$$C_{R,2} = S_M \frac{(1 - e^{-\lambda})(15T_6^4 + 10\omega_M^2 T_6^2 + 3\omega_M^4)}{3(T_6^2 + \omega_M^2)^3}$$

$$C_{R,3} = S_M \frac{[8\lambda T_6^5 + \lambda(T_6 - \lambda)(15T_6^4 + 10\omega_M^2 T_6^2 + 3\omega_M^4)](e^{-T_6} - e^{-\lambda})}{3(T_6^2 + \omega_M^2)^3 [(T_6 - \lambda)^2 + \omega_M^2]}$$

$$C_{R,4} = S_M \frac{\lambda(15T_6^4 + 10\omega_M^2 T_6^2 + 3\omega_M^4)(e^{-T_6} - e^{-\lambda})}{3(T_6 - \lambda)(T_6^2 + \omega_M^2)^3}$$

$$C_{R,5} = -S_M \frac{\lambda T_6 (7T_6^2 + 3\omega_M^2) [e^{-\lambda} - (1 - \lambda + T_6)e^{-T_6}]}{3(T_6 - \lambda)^2 (T_6^2 + \omega_M^2)^2}$$

$$C_{R,6} = -S_M \frac{\lambda T_6^2 \{2e^{-\lambda} - [(T_6 - \lambda + 1)^2 + 1]e^{-T_6}\}}{3(T_6 - \lambda)^3 (T_6^2 + \omega_M^2)}$$

$$C_{R,7} = -S_M \frac{\lambda(T_6^2 + 5T_6 + 8)(e^{-T_6} - e^{-\lambda})}{3T_6 [(T_6 - \lambda)^2 + \omega_M^2]}$$

$$\begin{aligned}
C_{R,8} = & -S_M \frac{\left\{ \lambda T_6 \left[(T_6 - \lambda)^2 - \omega_M^2 \right] (7T_6^2 + 3\omega_M^2) + 2\lambda (T_6 - \lambda) T_6^2 (5T_6^2 + \omega_M^2) \right\} e^{-\lambda}}{3(T_6^2 + \omega_M^2)^2 \left[(T_6 - \lambda)^2 + \omega_M^2 \right]^2} \\
& + S_M \frac{\lambda T_6 \left\{ T_6^3 + (1 - 3\lambda) T_6^2 + [\omega_M^2 + \lambda(3\lambda - 2)] T_6 \right\} (7T_6^2 + 3\omega_M^2) e^{-T_6}}{3(T_6^2 + \omega_M^2)^2 \left[(T_6 - \lambda)^2 + \omega_M^2 \right]^2} \\
& - S_M \frac{\lambda T_6 [\omega_M^2 (\lambda + 1) + \lambda^2 (\lambda - 1)] (7T_6^2 + 3\omega_M^2) e^{-T_6}}{3(T_6^2 + \omega_M^2)^2 \left[(T_6 - \lambda)^2 + \omega_M^2 \right]^2} \\
& + S_M \frac{\lambda T_6^2 [T_6^2 - 2(\lambda - 1) T_6 + \lambda(\lambda - 2) + \omega_M^2] (5T_6^2 + \omega_M^2) e^{-T_6}}{3(T_6^2 + \omega_M^2)^2 \left[(T_6 - \lambda)^2 + \omega_M^2 \right]^2}
\end{aligned}$$

$$\begin{aligned}
C_{R,9} = & -S_M \frac{2\lambda T_6^2 (T_6 - \lambda) \left[(T_6 - \lambda)^2 - 3\omega_M^2 \right] e^{-\lambda}}{3(T_6^2 + \omega_M^2) \left[(T_6 - \lambda)^2 + \omega_M^2 \right]^3} \\
& + S_M \frac{\lambda T_6^2 \left\{ T_6^5 - (5\lambda - 2) T_6^4 + 2(1 + \omega_M^2 - 4\lambda + 5\lambda^2) T_6^3 \right\} e^{-T_6}}{3(T_6^2 + \omega_M^2) \left[(T_6 - \lambda)^2 + \omega_M^2 \right]^3} \\
& - S_M \frac{2\lambda (3 + 3\omega_M^2 - 6\lambda + 5\lambda^2) T_6^2 e^{-T_6}}{3(T_6^2 + \omega_M^2) \left[(T_6 - \lambda)^2 + \omega_M^2 \right]^3} \\
& + S_M \frac{\lambda [\omega_M^4 + 6\omega_M^2 (\lambda^2 - 1) + \lambda^2 (6 - 8\lambda + 5\lambda^2)] T_6 e^{-T_6}}{3(T_6^2 + \omega_M^2) \left[(T_6 - \lambda)^2 + \omega_M^2 \right]^3} \\
& - S_M \frac{\lambda [\omega_M^4 (\lambda + 2) + 2\omega_M^2 \lambda (\lambda^2 - 3) + \lambda^3 (2 - 2\lambda + \lambda^2)] T_6^2 e^{-T_6}}{3(T_6^2 + \omega_M^2) \left[(T_6 - \lambda)^2 + \omega_M^2 \right]^3}
\end{aligned}$$

$$C_{R,10} = S_M \frac{8\lambda (1 - e^{-\lambda})}{3T_6 (\lambda^2 + \omega_M^2)}$$

$$\begin{aligned}
C_{R,11} = & -S_M \frac{2\lambda T_6^3 [3(T_6 - \lambda)^2 - \omega_M^2] e^{-\lambda}}{3(T_6^2 + \omega_M^2) [(T_6 - \lambda)^2 + \omega_M^2]^3} \\
& + S_M \frac{\lambda T_6^3 \{T_6^4 - 4(\lambda - 1)T_6^3 + 2[\omega_M^2 + 3(\lambda - 1)^2]T_6^2\} e^{-T_6}}{3(T_6^2 + \omega_M^2) [(T_6 - \lambda)^2 + \omega_M^2]^3} \\
& - S_M \frac{4\lambda [\omega_M^2(\lambda - 1) + \lambda(3 - 3\lambda + \lambda^2)] T_6^4 e^{-T_6}}{3(T_6^2 + \omega_M^2) [(T_6 - \lambda)^2 + \omega_M^2]^3} \\
& + S_M \frac{\lambda [\omega_M^4 + 2\omega_M^2(\lambda^2 - 2\lambda - 1) + \lambda^2(6 - 4\lambda + \lambda^2)] T_6^3 e^{-T_6}}{3(T_6^2 + \omega_M^2) [(T_6 - \lambda)^2 + \omega_M^2]^3} \\
C_{R,12} = & -S_M \frac{2\lambda(T_6 - \lambda)(2T_6 + 5)}{3[(T_6 - \lambda)^2 + \omega_M^2]^2} e^{-T_6} \\
& - S_M \frac{\lambda(2T_6 + 5)[T_6^2 - 2(\lambda + 1)T_6 + \lambda^2 + 2\lambda + \omega_M^2]}{3[(T_6 - \lambda)^2 + \omega_M^2]^2} e^{-\lambda} \\
C_{R,13} = & -S_M \frac{2\lambda T_6 [3(T_6 - \lambda)^2 - \omega_M^2]}{3[(T_6 - \lambda)^2 + \omega_M^2]^3} e^{-T_6} \\
& + S_M \frac{\lambda T_6 \{T_6^4 - 4(\lambda + 1)T_6^3 + 2[\omega_M^2 + 3(\lambda + 1)^2]T_6^2\}}{3[(T_6 - \lambda)^2 + \omega_M^2]^3} e^{-\lambda} \\
& - S_M \frac{4\lambda [\omega_M^2(\lambda + 1) + \lambda(\lambda^2 + 3\lambda + 3)] T_6^2}{3[(T_6 - \lambda)^2 + \omega_M^2]^3} e^{-\lambda} \\
& + S_M \frac{\lambda [\omega_M^4 + 2\omega_M^2(\lambda^2 + 2\lambda - 1) + \lambda^2(\lambda^2 + 4\lambda + 6)] T_6}{3[(T_6 - \lambda)^2 + \omega_M^2]^3} e^{-\lambda}
\end{aligned}$$

where $S_M = (-1)^{\Delta_f T+1}$. The imaginary part has 16 terms:

$$C_{I,1} = -S_M \frac{[\lambda \omega_M^2 (15T_6^4 + 10\omega_M^2 T_6^2 + 3\omega_M^4) - 8\lambda^2 T_6^5](1 - e^{-\lambda})}{3\omega_M (\lambda^2 + \omega_M^2)(T_6^2 + \omega_M^2)^3}$$

$$C_{I,2} = -S_M \frac{8T_6^5(1 - e^{-\lambda})}{3\omega_M (T_6^2 + \omega_M^2)^3}$$

$$C_{I,3} = S_M \frac{[\omega_M^2 \lambda (15T_6^4 + 10\omega_M^2 T_6^2 + 3\omega_M^4) - 8\lambda (T_6 - \lambda) T_6^5](e^{-T_6} - e^{-\lambda})}{3\omega_M [(T_6 - \lambda)^2 + \omega_M^2](T_6^2 + \omega_M^2)^3}$$

$$C_{I,4} = -S_M \frac{8\lambda T_6^5 (e^{-\lambda} - e^{-T_6})}{3\omega_M (T_6 - \lambda)(T_6^2 + \omega_M^2)^3}$$

$$\begin{aligned} C_{I,5} = & S_M \frac{\lambda T_6^2 (5T_6^2 + \omega_M^2)[(T_6 - \lambda)^2 - \omega_M^2]}{3\omega_M (T_6^2 + \omega_M^2)^2 [(T_6 - \lambda)^2 + \omega_M^2]^2} e^{-\lambda} \\ & - S_M \frac{\lambda T_6^4 (5T_6^2 + \omega_M^2)[T_6 - (3\lambda - 1)]}{3\omega_M (T_6^2 + \omega_M^2)^2 [(T_6 - \lambda)^2 + \omega_M^2]^2} e^{-T_6} \\ & - S_M \frac{\lambda T_6^2 (5T_6^2 + \omega_M^2) \{ [\omega_M^2 + \lambda(3\lambda - 2)]T_6 - \omega_M^2(\lambda + 1) - \lambda^2(\lambda - 1) \}}{3\omega_M (T_6^2 + \omega_M^2)^2 [(T_6 - \lambda)^2 + \omega_M^2]^2} e^{-T_6} \end{aligned}$$

$$\begin{aligned} C_{I,6} = & -S_M \frac{2\omega_M \lambda T_6 (T_6 - \lambda)(7T_6^2 + 3\omega_M^2)}{3(T_6^2 + \omega_M^2)^2 [(T_6 - \lambda)^2 + \omega_M^2]^2} e^{-\lambda} \\ & + S_M \frac{\omega_M \lambda T_6 (7T_6^2 + 3\omega_M^2)[T_6^2 - 2(\lambda - 1)T_6 + \lambda(\lambda - 2) + \omega_M^2]}{3(T_6^2 + \omega_M^2)^2 [(T_6 - \lambda)^2 + \omega_M^2]^2} e^{-T_6} \end{aligned}$$

$$C_{I,7} = -S_M \frac{\lambda T_6^2 (5T_6^2 + \omega_M^2) [e^{-\lambda} - (1 - \lambda + T_6) e^{-T_6}]}{3\omega_M (T_6 - \lambda)^2 (T_6^2 + \omega_M^2)^2}$$

$$\begin{aligned} C_{I,8} = & S_M \frac{2\lambda (T_6 - \lambda) T_6^3 [(T_6 - \lambda)^2 - 3\omega_M^2]}{3\omega_M (T_6^2 + \omega_M^2) [(T_6 - \lambda)^2 + \omega_M^2]^3} e^{-\lambda} \\ & - S_M \frac{\lambda T_6^6 [T_6^2 - (5\lambda - 2)T_6 + 2(1 + \omega_M^2 - 4\lambda + 5\lambda^2)]}{3\omega_M (T_6^2 + \omega_M^2) [(T_6 - \lambda)^2 + \omega_M^2]^3} e^{-T_6} \\ & + S_M \frac{2\lambda^2 T_6^5 (3 + 3\omega_M^2 - 6\lambda + 5\lambda^2)}{3\omega_M (T_6^2 + \omega_M^2) [(T_6 - \lambda)^2 + \omega_M^2]^3} e^{-T_6} \\ & - S_M \frac{\lambda T_6^4 [\omega_M^4 + 6\omega_M^2 (\lambda^2 - 1) + \lambda^2 (5\lambda^2 - 8\lambda + 6)]}{3\omega_M (T_6^2 + \omega_M^2) [(T_6 - \lambda)^2 + \omega_M^2]^3} e^{-T_6} \\ & + S_M \frac{\lambda T_6^3 [\omega_M^4 (\lambda + 2) + 2\omega_M^2 (\lambda^2 - 3) + \lambda^3 (\lambda^2 - 2\lambda + 2)]}{3\omega_M (T_6^2 + \omega_M^2) [(T_6 - \lambda)^2 + \omega_M^2]^3} e^{-T_6} \end{aligned}$$

$$\begin{aligned} C_{I,9} = & -S_M \frac{2\omega_M \lambda T_6^2 [3(T_6 - \lambda)^2 - \omega_M^2]}{3(T_6^2 + \omega_M^2) [(T_6 - \lambda)^2 + \omega_M^2]^3} e^{-\lambda} \\ & + S_M \frac{\omega_M \lambda T_6^4 \{T_6^2 - 4(\lambda - 1)T_6 + 2[\omega_M^2 + 3(\lambda - 1)^2]\}}{3(T_6^2 + \omega_M^2) [(T_6 - \lambda)^2 + \omega_M^2]^3} e^{-T_6} \\ & - S_M \frac{4\omega_M \lambda T_6^3 [\omega_M^2 (\lambda - 1) + \lambda (\lambda^2 - 3\lambda + 3)]}{3(T_6^2 + \omega_M^2) [(T_6 - \lambda)^2 + \omega_M^2]^3} e^{-T_6} \\ & + S_M \frac{\omega_M \lambda T_6^2 [\omega_M^4 + \lambda^2 (\lambda^2 - 4\lambda + 6) + 2\omega_M^2 (\lambda^2 - 2\lambda - 1)]}{3(T_6^2 + \omega_M^2) [(T_6 - \lambda)^2 + \omega_M^2]^3} e^{-T_6} \end{aligned}$$

$$C_{I,10} = -S_M \frac{\lambda T_6^3 \left\{ e^{-\lambda} - \left[(T_6 - \lambda + 1)^2 + 1 \right] e^{-T_6} \right\}}{3\omega_M (T_6 - \lambda)^3 (T_6^2 + \omega_M^2)}$$

$$C_{I,11} = S_M \frac{\lambda (15T_6^2 - 21\lambda T_6 + 8\lambda^2)}{3\omega_M T_6 (T_6 - \lambda)^3} e^{-\lambda} \\ - S_M \frac{\lambda \left[T_6^4 - (2\lambda - 7)T_6^3 + (\lambda^2 - 12\lambda + 15)T_6^2 + \lambda(5\lambda - 21)T_6 + 8\lambda^2 \right]}{3\omega_M T_6 (T_6 - \lambda)^3} e^{-T_6}$$

$$C_{I,12} = S_M \frac{\lambda (T_6 - \lambda) (T_6^2 + 5T_6 + 8) (e^{-T_6} - e^{-\lambda})}{3\omega_M T_6 \left[(T_6 - \lambda)^2 + \omega_M^2 \right]}$$

$$C_{I,13} = S_M \frac{8\lambda^2 (1 - e^{-\lambda})}{3\omega_M T_6 (\lambda^2 + \omega_M^2)}$$

$$C_{I,14} = S_M \frac{\lambda (2T_6 + 5) \left[(T_6 - \lambda)^2 - \omega_M^2 \right]}{3\omega_M \left[(T_6 - \lambda)^2 + \omega_M^2 \right]^2} e^{-T_6} \\ + S_M \frac{\lambda (2T_6 + 5) \left\{ T_6^3 - (3\lambda + 1)T_6^2 + [\lambda(3\lambda + 2) + \omega_M^2]T_6 \right\}}{3\omega_M \left[(T_6 - \lambda)^2 + \omega_M^2 \right]^2} e^{-\lambda} \\ - S_M \frac{\lambda (2T_6 + 5) \left[\lambda^2 (\lambda + 1) + \omega_M^2 (\lambda - 1) \right]}{3\omega_M \left[(T_6 - \lambda)^2 + \omega_M^2 \right]^2} e^{-\lambda}$$

$$\begin{aligned}
C_{I,15} = & S_M \frac{2\lambda T_6 (T_6 - \lambda) \left[(T_6 - \lambda)^2 - 3\omega_M^2 \right]}{3\omega_M \left[(T_6 - \lambda)^2 + \omega_M^2 \right]^3} e^{-T_6} \\
& - S_M \frac{\lambda T_6^4 \left\{ T_6^2 - (5\lambda + 2)T_6 + [5\lambda^2 + 4\lambda + \omega_M^2 + 1] \right\}}{3\omega_M \left[(T_6 - \lambda)^2 + \omega_M^2 \right]^3} e^{-\lambda} \\
& + S_M \frac{2\lambda^2 T_6^3 (5\lambda^2 + 6\lambda + 3\omega_M^2 + 3)}{3\omega_M \left[(T_6 - \lambda)^2 + \omega_M^2 \right]^3} e^{-\lambda} \\
& - S_M \frac{\lambda T_6^2 \left[\lambda^2 (5\lambda^2 + 8\lambda + 6) + 6\omega_M^2 (\lambda^2 - 1) + \omega_M^4 \right]}{3\omega_M \left[(T_6 - \lambda)^2 + \omega_M^2 \right]^3} e^{-\lambda} \\
& + S_M \frac{\lambda T_6 \left[\lambda^3 (\lambda^2 + 2\lambda + 2) + 2\omega_M^2 \lambda (\lambda^2 - 3) + \omega_M^4 (\lambda - 2) \right]}{3\omega_M \left[(T_6 - \lambda)^2 + \omega_M^2 \right]^3} e^{-\lambda} \\
C_{I,16} = & -S_M \frac{8(1 - e^{-\lambda})}{3\omega_M T_6} .
\end{aligned}$$

G.4.2 Second Order Moments of S_m for Sampled CIRF Case.

The extension to the sampled CIRF case involves replacing the delay integrals with sums over the delay samples. Thus the signal contributions to the tone filter output energy are

$$E_{S,+1} = 2r^2 \sum_{i=0}^{N_D-1} P_i I_{+1}(i/N_D) . \quad (\text{Sampled CIRF})$$

$$E_{S,-1} = 2r^2 \sum_{i=0}^{N_D-1} P_i I_{-1}(i/N_D) . \quad (\text{Sampled CIRF})$$

where $N_D = T/\Delta\tau$ is the number of channel delay samples per symbol period. Similarly, the real and imaginary parts of the cross correlation coefficient are

$$C_R = -r^2 C_M \sum_{i=0}^{N_D-1} P_i I_{CR}(i/N_D) \quad (\text{Sampled CIRF})$$

$$C_I = r^2 C_M \sum_{i=0}^{N_D-1} P_i I_{CI}(i/N_D) \quad (\text{Sampled CIRF})$$

These expressions are evaluated numerically using the analytic expressions for the time integrals derived above.

G.4.3 BFSK Irreducible Demodulation Error Rate in Frequency Selective Fading With and Without CIRF Sampling.

The BFSK irreducible error rate is plotted in Figure G-12 for one slow fading ($\tau_0/T \gg 1$) and several fast fading ($\tau_0/T = 0.1$ to 10) channels. These results are for continuous CIRFs and no delay offset ($\tau_D = 0$). Three times the minimum tone spacing is used which provides considerable immunity to the effects of fast fading for values of τ_0/T greater than one. As pointed out in the previous subsection, the slow fading irreducible error rate approaches an asymptotic limit of 0.011 for small values of $f_0 T$. For $\tau_0/T \geq 1$, the effect of fast fading is essentially to add a small amount to the irreducible error rate determined by $f_0 T$. For $\tau_0/T < 1$, the irreducible error rate is essentially determined by the value of τ_0/T and is insensitive to the value of $f_0 T$.

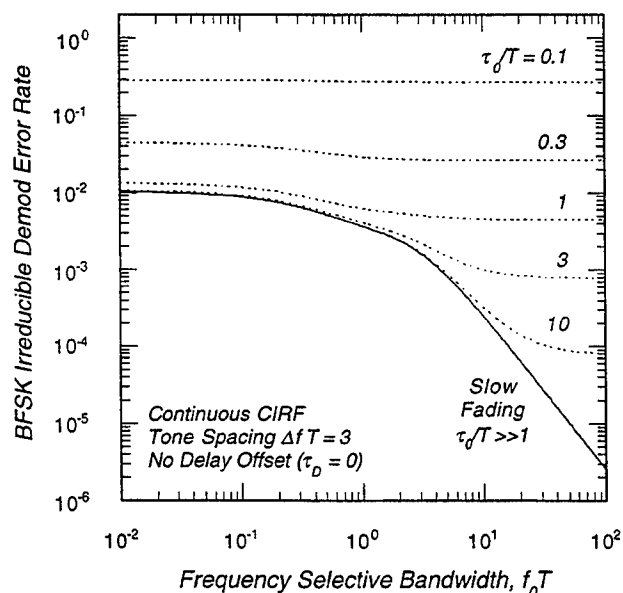


Figure G-12. BFSK irreducible demodulation error rate with frequency hopping in fast fading channels.

G.5 CIRF SAMPLING EFFECTS ON BFSK DEMOD ERROR RATE.

Finally, we investigate the effects of channel delay sampling on the BFSK demodulation error rate in frequency selective fading. As discussed above, sampling of the channel impulse response function in the delay domain is necessary to generate fading realizations for either hardware channel simulators or software simulations such as COMLNK. The only parameter of the sampling that we allow⁵ here is the number of delay samples per symbol period, N_D .

The BFSK irreducible error rate in slow, frequency selective fading is plotted versus normalized frequency selective bandwidth in Figure G-13 for continuous and sampled CIRFs. The tone spacing is three times the minimum for these results, and the delay offset is set to zero.

Clearly, the error rate curves are quite sensitive to the both the number of channel delay samples and the frequency selective bandwidth. This is understood by considering the total number of delay samples N_τ as a function of these two parameters. From Equation (2.13), with the total power P_τ in the sampled CIRF equal to the value (0.975) used in COMLNK⁶ and in these results, the number of delay samples is

$$N_\tau = 1 - \frac{\ln(1 - P_\tau)N_D}{2\pi f_0 T}.$$

When the second term on the right-hand-side of this formula is less than unity, the number of delay samples is unity, and the irreducible error rate is identically zero. For $N_D = 2$ and $P_\tau = 0.975$ this occurs when $f_0 T \geq 1.17$, and for $N_D = 64$ this occurs when $f_0 T \geq 37.7$. For values of $f_0 T$ that result in $N_\tau > 1$,

$$f_0 T < \frac{3.7N_D}{2\pi},$$

⁵ It has been demonstrated by *Reinking* [1995] that one can adjust the delay sample size and the power in the delay bins to allow the ideal delay offset with coarse sampling to approach the ideal value with a continuous CIRF. Presumably, one could do a similar thing with the error rate, but it is unlikely that one could match both the ideal delay offset and the BFSK error rate simultaneously. Furthermore, it is unreasonable to vary the channel model arbitrarily on the basis of minimizing or maximizing some measure of receiver performance.

⁶ *Dana* [1991] specifies the total signal power in the delay grid to be 0.975. It is now clear that a value closer to unity should be used, and a future version of COMLNK may employ a value of 0.999.

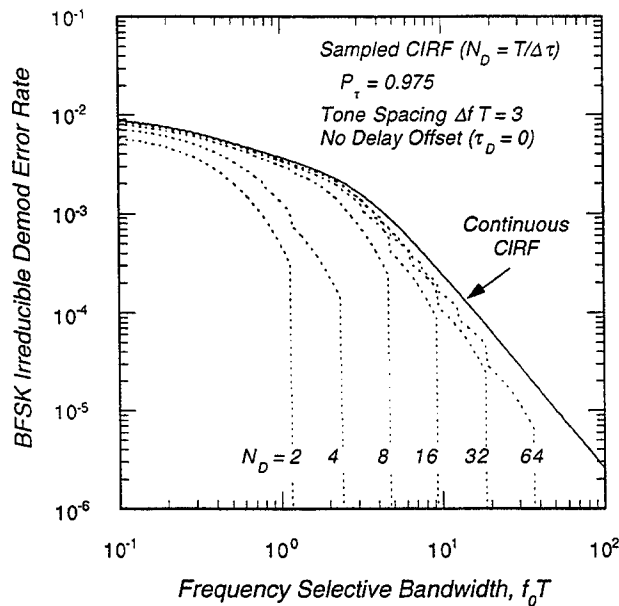


Figure G-13. BFSK irreducible demodulation error rate in sampled ($P_\tau = 0.975$) and continuous frequency selective fading.

the curves have a “stepped” appearance as N_τ varies from 2 to 3 to 4 and so on. Eventually, when $f_0 T$ is small enough that the number of delay samples becomes large, the steps smooth out, and the sampled CIRF BFSK irreducible error rate approaches the continuous CIRF curve.

Increasing the fraction of signal power in the delay grid, from 0.975 to say 0.999, can smooth out the steps. Using the formula above, this will increase the required number of delay samples by a factor of about 1.9 when $f_0 T$ is small. The advantage, however, is that the irreducible error rate is less sensitive to the exact number of delay samples, and the irreducible error rate curves are smoother as $f_0 T$ varies, as shown in Figure G-14.

When the tone spacing is three times the minimum value or larger, the irreducible BFSK error rate in slow, frequency selective fading is 0.0105 or less. The effect of delay sampling is to make this irreducible error rate even smaller. For demodulation error rates this small, a link that utilizes error correction coding and sufficient interleaving will have a user bit error rate of nearly zero. Thus for many applications the effects of channel delay sampling may be irrelevant to the user bit error rate.

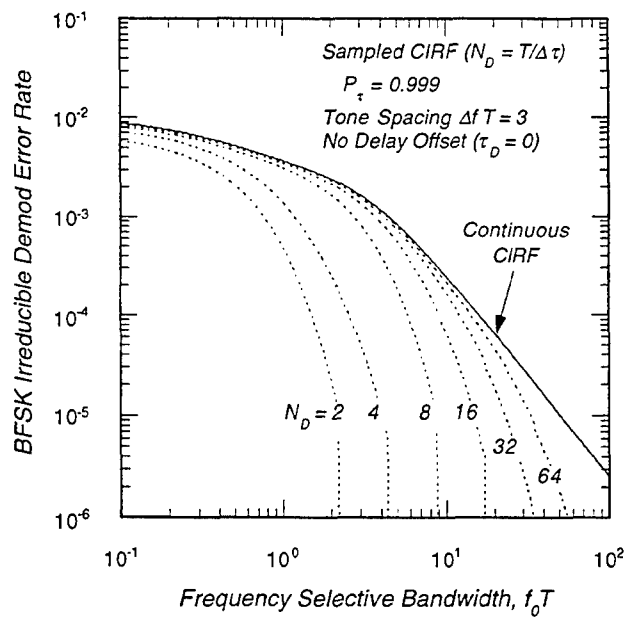


Figure G-14. BFSK irreducible demodulation error rate in sampled ($P_\tau = 0.999$) and continuous frequency selective fading.

APPENDIX H

DEMODULATION PERFORMANCE OF BINARY FREQUENCY SHIFT-KEYING IN FREQUENCY SELECTIVE FADING WITHOUT HOPPING

The frequency selective fading performance of a BFSK demodulator without frequency hopping is considered in this appendix. This case differs from the case with frequency hopping, considered in Appendix G, in that the front-end downconverter and bandpass filters of the receiver do not attenuate energy from previous symbols because all transmitted symbols have the same carrier frequency. Thus there is intersymbol interference (ISI) in a frequency selective channel.

A functional block diagram of a non-coherent binary frequency-shift keying (BFSK) receiver without frequency hopping is similar to that shown in Figure G-1. The block diagram in that figure is for BFSK with frequency hopping, although to turn the hopping off one only needs to set the number of allowed hop positions to one or otherwise disable the hop synthesizer.

We assume that the AGC and AFC tracking loops are operating perfectly and investigate the ideal delay offset in frequency selective fading. Our results show that this ideal offset is a small fraction of a symbol period in an unhopped system. Thus we ignore delay offset in developing expressions for the BFSK demodulation error rate.

In the next section of this appendix we give some general results for the BFSK signal and noise at the output of the tone filters in terms of the transmitted waveform. Then in Section H.2 we consider the ideal delay offset for this case. In Section H.3 we derive the demodulation error rate with and without sampling of the channel impulse response function (CIRF). The results for slow fading in this case are sufficiently complex that we have not attempted to extend them to the case of fast, frequency selective fading. This extension is straightforward, but the result would involve even more terms than the result for the case with hopping, which takes several pages to write down in Appendix G.

H.1 GENERAL BFSK RESULTS.

In a BFSK communications link, the transmitted signal during the k^{th} symbol is

$$m(t) = \sum_k e^{j(\pi n_k \Delta f)t} \Pi \left[\frac{t}{T} - k \right] ,$$

where Δf is the tone spacing and T is the symbol period. The transmitted tone is determined by the value of n_k , where $n_k = \pm 1$ for BFSK. The rectangular function $\Pi(\cdot)$ is defined as

$$\Pi(x) = \begin{cases} 1 & \text{if } |x| \leq \frac{1}{2} \\ 0 & \text{otherwise} \end{cases}.$$

Here $m(t)$ represents a frequency offset in the transmitted signal, so the carrier frequency *per se* is never transmitted, assuming that suppressed-carrier tracking is employed.

The received signal is the convolution of the channel impulse response function and the transmitted modulation. For a continuous CIRF, the received signal is

$$u(t) = r \int_0^{\infty} m(t - \tau) h(t, \tau) d\tau,$$

where r is the mean received signal amplitude. In slow fading the CIRF does not vary over the period of time that energy from a single transmitted symbol arrives at the receiver. Thus in slow fading $h(t, \tau)$ is replaced by $h(\tau)$ in this equation.

In either a simulation such as COMLNK or in a hardware channel simulator, the CIRF must be sampled in delay and time. The slow fading version of the convolution with a sampled CIRF is

$$u(t) = r \sum_{i=0}^{N_t-1} m(t - i\Delta\tau) h(i\Delta\tau) \Delta\tau,$$

where $\Delta\tau$ is the delay sample size, and N_t is the number of delay samples. In later developments we use h_i as a shorthand notation for $h(i\Delta\tau) \Delta\tau$.

The received signal is then processed in tone filters to determine which tone was transmitted. The output voltage of the m^{th} filter ($m = \pm 1$) during the k^{th} symbol period is

$$Z_{m,k} = \frac{1}{T} \int_{(k-1/2)T+\tau_D}^{(k+1/2)T+\tau_D} [u(t) + n(t)] e^{-j(\pi m \Delta f)t} dt, \quad (\text{H.1})$$

where τ_D is the delay offset that is non-zero in frequency selective fading. Hard-decision demodulation is performed by selecting the received symbol to be that corresponding to the filter with the largest output amplitude.

The complex voltage $n(t)$ is additive white Gaussian noise (AWGN) with the usual properties:

$$\begin{aligned}\langle n(t) \rangle &= 0 \\ \langle n(t)n(t') \rangle &= 0, \\ \langle n(t)n^*(t') \rangle &= N_0 \delta(t-t')\end{aligned}\quad (H.2)$$

where N_0 is the one-sided noise spectral density, and $\delta(\cdot)$ is the Dirac delta function. The second equation results because the real and imaginary parts of AWGN are uncorrelated. The noise contribution to the voltage out of the tone filters is then

$$N_{m,k} = \frac{1}{T} \int_{(k-1/2)T+\tau_D}^{(k+1/2)T+\tau_D} n(t) e^{-j(m\pi\Delta f)t} dt.$$

Because $n(t)$ is a complex, normally distributed random process with zero mean, $N_{m,k}$ is similarly distributed. Thus to complete the description of the tone filter output noise, we need the variance and cross correlation of $N_{m,k}$. The cross correlation is

$$C_{m,m'}^N = \langle N_{m,k} N_{m',k}^* \rangle = \frac{1}{T^2} \int_{(k-1/2)T+\tau_D}^{(k+1/2)T+\tau_D} dt e^{j\pi(n_k-m)\Delta f t'} \int_{(k-1/2)T+\tau_D}^{(k+1/2)T+\tau_D} dt' e^{-j\pi(n_k-m')\Delta f t'} \langle n(t)n^*(t') \rangle.$$

Because the noise $n(t)$ is delta-correlated, this expression reduces to

$$C_{m,m'}^N = \frac{N_0}{T} \exp[j\pi(m-m')\Delta f(kT+\tau_D)] \frac{\sin[\frac{1}{2}\pi(m-m')\Delta f T]}{\frac{1}{2}\pi(m-m')\Delta f T} = \frac{N_0}{T} \delta_{m,m'} \quad (H.3)$$

for orthogonal signaling (*i.e.*, for $\Delta f T =$ positive integer) where $\delta_{m,m'}$ is the Kronecker delta-symbol.

After some manipulation, the signal contribution to the output of the m^{th} filter in slow, frequency selective fading is

$$S_m = r \sum_{l=0}^{\infty} \int_{(l-1)T+\tau_D}^{(l+1)T+\tau_D} d\tau h(\tau) e^{-j(n_k-l)\pi\Delta f \tau} \frac{1}{T} \int_{-T/2+\tau_D}^{T/2+\tau_D} dt e^{-j(m-n_k-l)\pi\Delta f t} \Pi\left[\frac{t-\tau}{T} + l\right] \quad (H.4)$$

for the continuous CIRF case. We will consider the sampled CIRF case later, after we have investigated the effects of delay tracking. In further developments, we find that it is convenient to divide this signal into three parts, the on-time contribution from the k^{th} transmitted symbol and two contributions representing the ISI from previously transmitted symbols. The on-time signal contributions to the filter output voltages are given by the $l = 0$ term in Equation (H.4):

$$S_{O,m} = r \int_0^{T+\tau_D} d\tau h(\tau) e^{-j(n_k \pi \Delta f) \tau} \frac{1}{T} \int_{-T/2+\tau_D}^{T/2+\tau_D} dt e^{-j(m-n_k) \pi \Delta f t} \Pi\left[\frac{t-\tau}{T}\right] . \quad (\text{H.5})$$

The ISI contribution to the filter outputs is given by the $l \geq 1$ terms in Equation (H.4). After changing variables in the delay integral, we get

$$S_{l,m} = r \sum_{l=0}^{\infty} \int_{\tau_D}^{2T+\tau_D} d\tau h(\tau+lT) e^{-j(n_{k-l} \pi \Delta f)(\tau+lT)} \times \frac{1}{T} \int_{-T/2+\tau_D}^{T/2+\tau_D} dt e^{-j(m-n_{k-l}) \pi \Delta f t} \Pi\left[\frac{t-\tau}{T}+1\right] .$$

To aid in the evaluation of the filter cross correlation and output energy, the ISI contribution is divided into two parts, each with a delay integral over the range τ_D to $T + \tau_D$. These two terms are

$$S_{l,m}^1 = r \sum_{l=0}^{\infty} \int_{\tau_D}^{T+\tau_D} d\tau h(\tau+lT) e^{-j(n_{k-l} \pi \Delta f)(\tau+lT)} \frac{1}{T} \int_{-T/2+\tau_D}^{-T/2+\tau} dt e^{-j(m-n_{k-l}) \pi \Delta f t} \quad (\text{H.6})$$

$$S_{l,m}^2 = r \sum_{l=1}^{\infty} \int_{\tau_D}^{T+\tau_D} d\tau h(\tau+lT) e^{-j(n_{k-l} \pi \Delta f)(\tau+lT)} \frac{1}{T} \int_{-T/2+\tau}^{T/2+\tau_D} dt e^{-j(m-n_{k-l}) \pi \Delta f t} . \quad (\text{H.7})$$

The total signal contribution to the filter output is

$$S_m = S_{O,m} + S_{l,m}^1 + S_{l,m}^2 .$$

H.2 IDEAL DELAY OFFSET.

In an FSK receiver that does not use sync symbols, time tracking may be accomplished by generating early and late voltage samples from the first and second halves of

the modulation period. These samples are taken from the filter with the largest total output amplitude, which is the one chosen to correspond to the transmitted tone. The DLL then attempts to equalize the energy of these two samples. Rather than calculating the early and late samples, we are going to find the delay offset τ_D that maximizes the signal amplitude out of the correct filter. As we have shown previously, this should be close to, if not exactly equal to, the delay offset found by a DLL that equalizes the amplitude of the early and late samples. Ultimately, we are going to show that the delay that maximizes the output amplitude is a smaller fraction of the symbol period without frequency hopping than it is with hopping. We then use this as justification for ignoring delay in the error rate analysis. Thus we are not interested in the exact value of τ_D , but rather we want to show that τ_D/T is relatively small for this case.

Assuming that the receiver selects the output from the filter corresponding to the on-time transmitted tone (*i.e.*, the signal from the $m = n_k$ filter during the k^{th} symbol period), the on-time signal contribution to the correct filter is given by Equation (H.5). With $m = n_k$, the time integral in this equation is just the triangle function, so

$$S_{O,m} = r \int_0^{T+\tau_D} h(\tau) e^{-(n_k \pi \Delta f) \tau} \Lambda \left[\frac{\tau - \tau_D}{T} \right] d\tau \quad m = n_k, \quad (\text{H.8})$$

where

$$\Lambda(x) = \begin{cases} 1 - |x| & \text{if } |x| \leq 1 \\ 0 & \text{otherwise} \end{cases}$$

The ISI terms in Equations (H.6) and (H.7) contain contributions from previously transmitted symbols ($k - l$, $l \geq 1$) and thus have the same form for either the correct or the other filter.

The signal contribution to the energy at the output of the correct filter is

$$E_S = \langle S_m S_m^* \rangle = r^2 (E_O + E_I^1 + E_I^2 + C_{OI} + C_{II})$$

where the normalized¹ energy contributions are

¹ Normalized by the mean received signal energy in the absence of propagation effects, r^2 .

$$E_O = \frac{1}{r^2} \langle S_{O,m} S_{O,m}^* \rangle$$

$$E_I^1 = \frac{1}{r^2} \langle S_{I,m}^1 S_{I,m}^{1*} \rangle$$

$$E_I^2 = \frac{1}{r^2} \langle S_{I,m}^2 S_{I,m}^{2*} \rangle$$

$$C_{OI} = \frac{2}{r^2} \text{Re} \left[\langle S_{O,m} S_{I,m}^{1*} \rangle \right]$$

$$C_{II} = \frac{2}{r^2} \text{Re} \left[\langle S_{I,m}^1 S_{I,m}^{2*} \rangle \right] .$$

In evaluating these expectations, one gets expectations of the CIRF that reduce to

$$\langle h(\tau) h^*(\tau') \rangle = G(\tau) \delta(\tau - \tau') ,$$

where $G(\cdot)$ is the power impulse response function [Eqn. (2.8)], and $\delta(\cdot)$ is the Dirac delta function. The other two cross terms in the expression for the signal energy are then identically zero because the $S_{O,m}$ and $S_{I,m}^2$ terms have no overlapping regions in their delay integrals.

The signal energy out of the correct filter can now be computed using the delta-correlation property of the CIRF. The on-time contribution in normalized delay units ($\zeta = \tau/T$) is

$$E_O = \frac{1}{r^2} \langle S_{O,m} S_{O,m}^* \rangle = \int_0^{1+\hat{\tau}_D} T G(T\zeta) \Lambda^2(\zeta - \hat{\tau}_D) d\zeta .$$

where $\hat{\tau}_D = \tau_D/T$.

The ISI terms are a little more difficult to compute. For example, the signal energy of first ISI term is

$$\begin{aligned} E_I^1 = \frac{1}{r^2} \langle S_{I,m}^1 S_{I,m}^{1*} \rangle &= \sum_{l=0}^{\infty} \sum_{l'=0}^{\infty} \int_{\tau_D}^{T+\tau_D} d\tau \int_{\tau_D}^{T+\tau_D} d\tau' \langle h(\tau + lT) h^*(\tau' + l'T) \rangle \\ &\times \frac{1}{T} \int_{-T/2+\tau_D}^{-T/2+\tau} dt \frac{1}{T} \int_{-T/2+\tau_D}^{-T/2+\tau'} dt' \left\langle e^{j(n_{k-l-1}-m)\pi\Delta f t - j(n_{k-l'-1}-m)\pi\Delta f t' - jn_{k-l-1}\pi\Delta f(\tau+lT) + jn_{k-l'-1}\pi\Delta f(\tau'+l'T)} \right\rangle . \end{aligned}$$

We have made the physically reasonable assumption that the CIRF and the modulation are uncorrelated so that the expectations of the two can be factored into two terms. The expectation of the CIRF forces $\tau' = \tau$ and $l' = l$. The expectation of the phase term then reduces to

$$\left\langle e^{j(n_{k-l-1}-m)\pi\Delta f(t-t')} \right\rangle = \frac{1}{2} \left[1 + e^{\pm j2\pi\Delta f(t-t')} \right]$$

because, with equal probability, n_{k-l-1} is either equal m or it is not. In the latter case, $n_{k-l-1} - m = \pm 2$. The signal energy of the first ISI term then reduces to

$$E_I^1 = \frac{1}{2} \sum_{l=0}^{\infty} \int_{\hat{\tau}_D}^{1+\hat{\tau}_D} TG[T(\zeta+l)] \left\{ (\zeta - \hat{\tau}_D)^2 + \frac{4 \sin^2 \left[\frac{1}{2} \omega_M (\zeta - \hat{\tau}_D) \right]}{\omega_M^2} \right\} d\zeta ,$$

where $\omega_M = 2\pi\Delta f T$. Similarly, the energy of the second ISI term is

$$E_I^2 = \frac{1}{2} \sum_{l=1}^{\infty} \int_{\hat{\tau}_D}^{1+\hat{\tau}_D} TG[T(\zeta+l)] \left\{ (1-\zeta + \hat{\tau}_D)^2 + \frac{4 \sin^2 \left[\frac{1}{2} \omega_M (\zeta - \hat{\tau}_D) \right]}{\omega_M^2} \right\} d\zeta .$$

The on-time - ISI cross correlation term is

$$\begin{aligned} \frac{1}{r^2} \langle S_{O,m} S_{I,m}^* \rangle &= \sum_{l=0}^{\infty} \int_0^{T+\tau_D} d\tau \int_{\tau_D}^{T+\tau_D} d\tau' \langle h(\tau) h^*(\tau' + lT) \rangle \Lambda \left[\frac{\tau - \tau_D}{T} \right] \\ &\quad \times \frac{1}{T} \int_{-T/2+\tau_D}^{-T/2+\tau'} dt \left\langle e^{-j(n_{k-l-1}-m)\pi\Delta f t - jn_k\pi\Delta f \tau + jn_{k-l-1}\pi\Delta f(\tau' + lT)} \right\rangle \end{aligned}$$

The CIRF expectation again forces $\tau' = \tau$ and $l = 0$, and the phase expectation is

$$\left\langle e^{-j(n_{k-1}-m)\pi\Delta f t + j(n_{k-1}-n_k)\pi\Delta f \tau} \right\rangle = \frac{1}{2} \left[1 + e^{\pm j\pi\Delta f(t-\tau)} \right] .$$

The on-time-ISI cross correlation term is then

$$C_{OI} = 2 \int_{\hat{\tau}_D}^{1+\hat{\tau}_D} TG(T\zeta) \Lambda(\zeta - \hat{\tau}_D) \left\{ \zeta - \hat{\tau}_D - \frac{S_M}{\omega_M} \sin[\omega_M(\zeta - \hat{\tau}_D)] \right\} d\zeta ,$$

where $S_M = (-1)^{\Delta f T + 1}$.

The ISI cross correlation term is

$$\begin{aligned} \frac{1}{r^2} \langle S_l^1 S_l^{2*} \rangle &= \sum_{l=0}^{\infty} \sum_{l'=1}^{\infty} \int_{\tau_D}^{T+\tau_D} d\tau \int_{\tau_D}^{T+\tau_D} d\tau' \langle h(\tau + lT) h^*(\tau + l'T) \rangle \\ &\times \frac{1}{T} \int_{-T/2+\tau_D}^{-T/2+\tau} dt \frac{1}{T} \int_{-T/2+\tau'}^{T/2+\tau_D} dt' \left\langle e^{-jn_{k-l-1}\pi\Delta f(\tau+lT) + jn_{k-l'}\pi\Delta f(\tau'+l'T) + j(n_{k-l-1}-m)\pi\Delta ft - j(n_{k-l'}-m)\pi\Delta ft'} \right\rangle \end{aligned}$$

Once again the CIRF expectation forces $\tau' = \tau$ and $l' = l$, so the phase expectation is

$$\left\langle e^{-j(n_{k-l-1}-n_{k-l})\pi\Delta f(\tau+lT) + j(n_{k-l-1}-m)\pi\Delta ft - j(n_{k-l}-m)\pi\Delta ft'} \right\rangle.$$

At this point it is convenient to pick a value for the transmitted tone, and we select $n_k = m = +1$. The mean signal energy out of the correct filter is in fact independent of the choice for n_k , but one has to evaluate the ISI cross correlation for both choices to demonstrate this. The phase expectation depends on n_{k-l} and n_{k-l-1} . Assuming that the transmitted modulation is uncorrelated from symbol-to-symbol, there are four equally likely possibilities:

n_{k-l} Value	n_{k-l-1} Value	Probability of Occurrence
+1	+1	$\frac{1}{4}$
+1	-1	$\frac{1}{4}$
-1	+1	$\frac{1}{4}$
-1	-1	$\frac{1}{4}$

The phase expectation is then given by the expression

$$\begin{aligned} &\left\langle e^{-j(n_{k-l-1}-n_{k-l})\pi\Delta f(\tau+lT) + j(n_{k-l-1}-m)\pi\Delta ft - j(n_{k-l}-m)\pi\Delta ft'} \right\rangle \\ &= \frac{1}{4} \left[1 + e^{-2\pi j\Delta f(\tau+lT) + 2\pi j\Delta ft'} + e^{2\pi j\Delta f(\tau+lT) - 2\pi j\Delta ft} + e^{-2\pi j\Delta f(t-t')} \right] \end{aligned}$$

The time integrals in the ISI cross correlation term can now be done in closed form with the result

$$C_{II} = \frac{1}{2} \sum_{l=1}^{\infty} \int_{\hat{\tau}_D}^{1+\hat{\tau}_D} d\tau TG[T(\zeta+l)] \left\{ (\zeta - \hat{\tau}_D)(1 + \hat{\tau}_D - \zeta) - \frac{4 \sin^2 \left[\frac{1}{2} \omega_M (\zeta - \hat{\tau}_D) \right]}{\omega_M^2} \right. \\ \left. - \frac{S_M}{\omega_M} [1 - 2(\zeta - \hat{\tau}_D)] \sin[\omega_M (\zeta - \hat{\tau}_D)] \right\}$$

For the exponential form of the power impulse response function given in Equation (2.8), the sums in the above expression can be done directly:

$$\sum_{l=1}^{\infty} TG[T(\zeta + lT)] = \lambda e^{-\lambda \zeta} S_0 ,$$

where $\lambda = 2\pi f_0 T$ and

$$S_0 = \sum_{l=1}^{\infty} e^{-\lambda l} = \frac{e^{-\lambda}}{1 - e^{-\lambda}} . \quad (\text{H.9})$$

The delay integrals can now be done analytically, and the signal energy out of the correct filter, as a function of the normalized delay error $\hat{\tau}_D$ and frequency selective bandwidth λ , can be calculated. Writing the signal energy in two terms

$$E_S = r^2 (E_{S,1} + E_{S,2}) ,$$

the second of which is proportional to S_0 , we get following:

$$E_{S,1} = \frac{(\lambda \hat{\tau}_D)^2 - 2\lambda(\lambda + 1)\hat{\tau}_D + \lambda^2 + 2\lambda + 2}{\lambda^2} - \frac{3\lambda + 1}{\lambda^2} e^{-\lambda \hat{\tau}_D} + \frac{1 - e^{-\lambda}}{\lambda^2 + \omega_M^2} e^{-\lambda \hat{\tau}_D} \\ - \frac{\lambda^2 + 2}{2\lambda^2} e^{-\lambda(\hat{\tau}_D + 1)} - \frac{2S_M \lambda^2}{(\lambda^2 + \omega_M^2)^2} e^{-\lambda(\hat{\tau}_D + 1)} - \frac{S_M \lambda [\lambda(\lambda - 2) + \omega_M^2]}{(\lambda^2 + \omega_M^2)^2} e^{-\lambda \hat{\tau}_D} , \quad (\text{H.10})$$

$$E_{S,2} = S_0 \left\{ \frac{\lambda^2 - \lambda + 2}{2\lambda^2} e^{-\lambda \hat{\tau}_D} - \frac{\lambda^2 + \lambda + 2}{2\lambda^2} e^{-\lambda(\hat{\tau}_D+1)} + \frac{1 - e^{-\lambda}}{\lambda^2 + \omega_M^2} e^{-\lambda \hat{\tau}_D} \right. \\ \left. - \frac{S_M \lambda [\lambda(\lambda - 4) + \omega_M^2]}{2(\lambda^2 + \omega_M^2)^2} e^{-\lambda \hat{\tau}_D} - \frac{S_M \lambda [\lambda(\lambda + 4) + \omega_M^2]}{2(\lambda^2 + \omega_M^2)^2} e^{-\lambda(\hat{\tau}_D+1)} \right\}, \quad (\text{H.11})$$

where, again, $\omega_M = 2\pi \Delta f T$ and $S_M = (-1)^{\Delta f T + 1}$. Note that the flat fading limit ($\lambda \rightarrow \infty$) of $E_{S,1} + E_{S,2}$ is unity.

Rather than developing similar expressions for the early and late signal energy out of the correct filter so that we can find the ideal delay offset, we are going to approximate the delay offset by that which maximizes the above expression. This delay is plotted in Figure H-1 versus normalized frequency selective bandwidth, $f_0 T$. For comparison, the delay offset that maximizes the signal energy out of the correct filter of a BFSK demodulator with frequency hopping is also plotted in the figure. Both of these curves are for a continuous CIRF, and for the case without hopping, the tone spacing $\Delta f T$ is two². The delay that maximizes the output energy of the unhopped signal approaches one-third of a symbol period as $f_0 T$ approaches zero.

However, we will show that the irreducible error rate for this case is below 10 percent only for $f_0 T \geq 0.3$, and in this range the ideal delay offset is less than 0.13. In further developments of the BFSK demodulation error rate for this case, we will assume that the delay offset is zero to simplify somewhat the resulting expressions for the signal energy out of the other filter and the cross correlation coefficient.

H.3 DEMODULATION ERROR RATE WITH CONTINUOUS CIRFS.

To calculate the BFSK demodulation error rate we need the second order statistics of the signal contributions to the outputs of the two filters (*i.e.*, the two output amplitudes and the cross correlation coefficient). Equations (H.5), (H.6) and (H.7) are used to compute these statistics. The signal energy out of the correct filter is already given by the two terms in Equations (H.10) and (H.11) evaluated at $\hat{\tau}_D = 0$. Rather

² Here the signal energy out of the correct filter depends on the tone spacing because the ISI contains contributions, with equal probability, from both possible transmitted symbols. In the hopped case, the output energy of the correct filter is independent of the tone spacing. The reason for choosing $\Delta f T = 2$ for these results will be apparent later in this appendix.

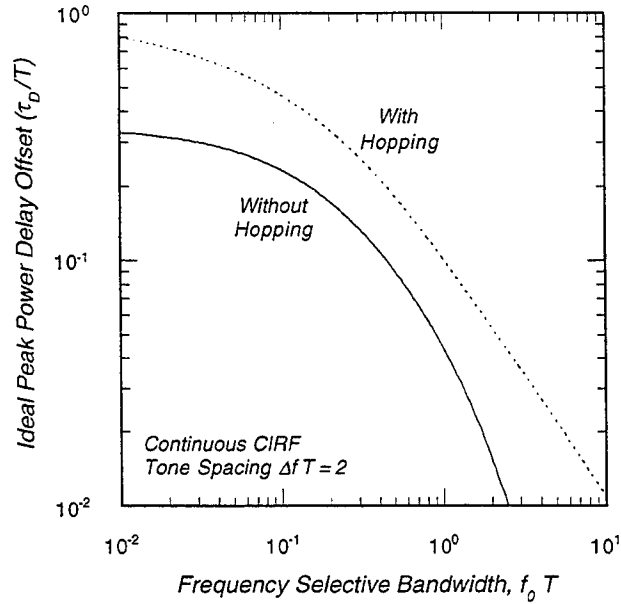


Figure H-1. Ideal delay offset that maximizes the correct filter output amplitude for BFSK modulation with and without hopping.

than just writing this expression down, we find it convenient to express the signal energy and cross correlation coefficient in terms of integrals over delay. These integrals can then be transformed to sums to get the second order statistics for the case where the channel impulse response function is sampled in the delay domain. It is also convenient, although not absolutely necessary, to choose a value for the on-time transmitted symbol, and we choose $n_k = +1$. The demodulation error rate is independent of this choice.

With our choice for the on-time transmitted symbol, the normalized signal energy out of the correct filter ($m = n_k = +1$) is

$$\begin{aligned}
 E_{+1} &= \frac{1}{r^2} \left\langle \left| S_{O,+1} + S_{I,+1}^1 + S_{I,+1}^2 \right|^2 \right\rangle \\
 &= \frac{1}{r^2} \left\{ \langle S_{O,+1} S_{O,+1}^* \rangle + 2 \operatorname{Re} \left[\langle S_{O,+1} S_{I,+1}^{1*} \rangle \right] \right. \\
 &\quad \left. + \langle S_{I,+1}^1 S_{I,+1}^{1*} \rangle + \langle S_{I,+1}^2 S_{I,+1}^{2*} \rangle + 2 \operatorname{Re} \left[\langle S_{I,+1}^1 S_{I,+1}^{2*} \rangle \right] \right\}
 \end{aligned}$$

Cross terms of the form

$$\langle S_{O,+1} S_{I,+1}^2 \rangle$$

are identically zero because there is no overlap in the delay integrals of the two terms. Each of the terms in the expression for E_{+1} is given by expressions in the previous section with $\hat{\tau}_D = 0$. The signal energy out of the correct filter is then given by

$$E_{+1} = R_0 - R_1 + \frac{1}{2} R_2 + R_{S,1} + \frac{1}{2} R_{S,2} - R_{S,3} + \frac{1}{2} S_0 (R_0 - R_1 + R_2 + R_{S,1} + R_{S,2} - 2R_{S,3}) \quad (\text{H.12})$$

where S_0 is given by Equation (H.9). The R integrals are defined as

$$R_0 = \int_0^1 TG(T\zeta) d\zeta = 1 - e^{-\lambda}$$

$$R_1 = \int_0^1 TG(T\zeta) \zeta d\zeta = \frac{1 - (\lambda + 1)e^{-\lambda}}{\lambda}$$

$$R_2 = \int_0^1 TG(T\zeta) \zeta^2 d\zeta = \frac{2 - (\lambda^2 + 2\lambda + 2)e^{-\lambda}}{\lambda^2}$$

$$R_{S,1} = -\frac{S_M}{\omega_M} \int_0^1 TG(T\zeta) \sin(\omega_M \zeta) d\zeta = -\frac{S_M \lambda (1 - e^{-\lambda})}{\lambda^2 + \omega_M^2}$$

$$R_{S,2} = \frac{4}{\omega_M^2} \int_0^1 TG(T\zeta) \sin^2 \left[\frac{1}{2} \omega_M \zeta \right] d\zeta = \frac{2(1 - e^{-\lambda})}{\lambda^2 + \omega_M^2}$$

$$R_{S,3} = -\frac{S_M}{\omega_M} \int_0^1 TG(T\zeta) \zeta \sin(\omega_M \zeta) d\zeta = -\frac{S_M \lambda [2\lambda(1 - e^{-\lambda}) - (\lambda^2 + \omega_M^2)e^{-\lambda}]}{(\lambda^2 + \omega_M^2)^2}$$

$$\begin{aligned} R_{S,4} &= -\frac{S_M}{\omega_M} \int_0^1 TG(T\zeta) (1 - 2\zeta) \sin^2 \left[\frac{1}{2} \omega_M \zeta \right] d\zeta \\ &= -\frac{S_M \omega_M [\lambda(\lambda^2 + \omega_M^2)(1 + e^{-\lambda}) - 2(3\lambda^2 + \omega_M^2)(1 - e^{-\lambda})]}{2\lambda(\lambda^2 + \omega_M^2)^2} \end{aligned}$$

$$R_{S,5} = \int_0^1 TG(T\zeta) \zeta(1-\zeta) \sin(\omega_M \zeta) d\zeta$$

$$= \frac{2\lambda \omega_M \left[\lambda(\lambda^2 + \omega_M^2)(1 + e^{-\lambda}) - (3\lambda^2 - \omega_M^2)(1 - e^{-\lambda}) \right]}{(\lambda^2 + \omega_M^2)^3}$$

$$R_C = \int_0^1 TG(T\zeta) \zeta(1-\zeta) \cos(\omega_M \zeta) d\zeta$$

$$= \frac{\lambda(\lambda^4 - \omega_M^4)(1 + e^{-\lambda}) - 2\lambda^2(\lambda^2 - 3\omega_M^2)(1 - e^{-\lambda})}{(\lambda^2 + \omega_M^2)^3}$$

Closed form expressions for these integrals are obtained using the exponential power impulse response function [Eqn. (2.8)]. The latter three integrals will be used in subsequent expressions.

The normalized signal energy at the output of the other filter ($m = -1$) is

$$E_{-1} = \frac{1}{r^2} \left\langle |S_{O,-1} + S_{I,-1}^1 + S_{I,-1}^2|^2 \right\rangle$$

$$= \frac{1}{r^2} \left\{ \left\langle S_{O,-1} S_{O,-1}^* \right\rangle + 2 \operatorname{Re} \left[\left\langle S_{O,-1} S_{I,-1}^{1*} \right\rangle \right] \right.$$

$$\left. + \left\langle S_{I,-1}^1 S_{I,-1}^{1*} \right\rangle + \left\langle S_{I,-1}^2 S_{I,-1}^{2*} \right\rangle + 2 \operatorname{Re} \left[\left\langle S_{I,-1}^1 S_{I,-1}^{2*} \right\rangle \right] \right\}$$

Terms from ISI only (those on the last line of this expression) are equal to the corresponding terms in the expression for E_{+1} :

$$\left\langle S_{I,-1}^1 S_{I,-1}^{1*} \right\rangle = \left\langle S_{I,+1}^1 S_{I,+1}^{1*} \right\rangle$$

$$\left\langle S_{I,-1}^2 S_{I,-1}^{2*} \right\rangle = \left\langle S_{I,+1}^2 S_{I,+1}^{2*} \right\rangle$$

$$2 \operatorname{Re} \left[\left\langle S_{I,-1}^1 S_{I,-1}^{2*} \right\rangle \right] = 2 \operatorname{Re} \left[\left\langle S_{I,+1}^1 S_{I,+1}^{2*} \right\rangle \right]$$

because these terms only depend on previously transmitted symbols, and are independent of the on-time symbol. Thus the first two terms in the second expression for E_{-1} (those on the middle line) must be evaluated.

The on-time signal energy is

$$E_{O,-1} = \frac{1}{r^2} \langle S_{O,-1} S_{O,-1}^* \rangle$$

$$= \int_0^T d\tau \int_0^T d\tau' \langle h(\tau) h^*(\tau') \rangle e^{-j\pi\Delta f(\tau-\tau')} \frac{1}{T} \int_{-T/2+\tau}^{T/2} dt \frac{1}{T} \int_{-T/2+\tau'}^{T/2} dt' e^{2\pi j\Delta f(t-t')} .$$

The CIRF expectation forces $\tau' = \tau$, so this expression collapses to

$$E_{O,-1} = \frac{4}{\omega_M^2} \int_0^1 TG(T\zeta) \sin^2 \left[\frac{1}{2} \omega_M \zeta \right] d\zeta = R_{S,2} .$$

The on-time ISI cross correlation term for the other filter is

$$\frac{1}{r^2} \langle S_{O,-1} S_{I,-1}^{1*} \rangle = \sum_{l=0}^{\infty} \int_0^T d\tau \int_0^T d\tau' \langle h(\tau) h^*(\tau + lT) \rangle$$

$$\times \frac{1}{T} \int_{-T/2+\tau}^{T/2} dt \frac{1}{T} \int_{-T/2}^{-T/2+\tau'} dt' \langle e^{-j\pi\Delta f\tau + j\pi n_{k-l-1}\Delta f(\tau'+lT) + 2\pi j\Delta ft - j\pi(1+n_{k-l-1})\Delta ft'} \rangle .$$

Again the CIRF expectation forces $\tau' = \tau$ and $l = 0$. The phase expectation then reduces to

$$\langle e^{-j\pi(1-n_{k-1})\Delta f\tau + 2\pi j\Delta ft - j\pi(1+n_{k-1})\Delta ft'} \rangle = \frac{1}{2} \left[e^{2\pi j\Delta f(t-t')} + e^{-2\pi j\Delta f(\tau-t)} \right] .$$

The cross correlation coefficient for this case reduces to

$$C_{OI,-1} = \frac{2}{r^2} \text{Re} \left[\langle S_{O,-1} S_{I,-1}^{1*} \rangle \right]$$

$$= - \int_0^1 TG(T\zeta) \left[\frac{4}{\omega_M^2} \sin^2 \left(\frac{1}{2} \omega_M \zeta \right) - \frac{S_M}{\omega_M} \zeta \sin(\omega_M \zeta) \right] d\zeta = R_{S,2} + R_{S,3} .$$

Combining terms gives the following for the signal energy at the output of the other filter:

$$E_{-1} = \frac{1}{2} (R_2 + R_{S,2} - 2R_{S,3}) + \frac{1}{2} S_0 (R_0 - R_1 + R_2 + R_{S,1} + R_{S,2} - 2R_{S,3}) . \quad (\text{H.13})$$

All that is left to do to calculate the BFSK demodulation error rate is to compute the cross correlation coefficient of the outputs of the two filters. Expanded out in terms of the three components of the output signal, this cross correlation is

$$C = \frac{1}{r^2} \langle S_{+1} S_{-1}^* \rangle = \frac{1}{r^2} \left\{ \langle S_{O,+1} S_{O,-1}^* \rangle + \langle S_{O,+1} S_{I,-1}^{1*} \rangle + \langle S_{O,+1} S_{I,-1}^{2*} \rangle \right. \\ \left. + \langle S_{I,+1}^1 S_{O,-1}^* \rangle + \langle S_{I,+1}^1 S_{I,-1}^{1*} \rangle + \langle S_{I,+1}^1 S_{I,-1}^{2*} \rangle \right. \\ \left. + \langle S_{I,+1}^2 S_{O,-1}^* \rangle + \langle S_{I,+1}^2 S_{I,-1}^{1*} \rangle + \langle S_{I,+1}^2 S_{I,-1}^{2*} \rangle \right\}$$

Two of these terms are zero because there is no overlap in the delay integrals, so

$$\langle S_{O,+1} S_{I,-1}^{2*} \rangle = \langle S_{I,+1}^2 S_{O,-1}^* \rangle = 0$$

This leaves *only* seven terms to evaluate, each of which can be complex. These terms are reduced in exactly the same way as the energy terms. Expectations of the CIRF reduce the number of delay integrals from two to one, and expectations with the on-time component eliminate all terms with $l \geq 1$. Expectations of the modulation involving just one transmitted symbol reduce to two terms, and expectations of the modulation involving two transmitted symbols reduce to four terms. The reader is spared the tedious details. After considerable algebra, the real (C_R) and imaginary (C_I) parts of C can be reduced to

$$C_R = \frac{1}{2}(1 + S_0) [R_C - R_{S,1} - R_{S,2} + 2R_{S,3}] \\ C_I = \frac{1}{2}(1 + S_0) [2R_{S,4} - R_{S,5}] \quad (\text{H.14})$$

The BFSK demodulation error rate without frequency hopping is given by the expression in Appendix D with the substitutions

$$\sigma_1^2 = r^2 [E_{-1} + \gamma^{-1}] \\ \sigma_2^2 = r^2 [E_{+1} + \gamma^{-1}] , \quad (\text{H.15}) \\ \sigma_1^2 \sigma_2^2 \rho^2 = r^2 (C_R^2 + C_I^2)$$

where $\gamma = r^2 T / N_0$ is the symbol (or bit for BFSK) energy-to-noise spectral density ratio. Thus the BFSK demodulation error rate in slow, frequency selective Rayleigh fading is

$$\langle P_e \rangle = \frac{1}{2} - \frac{E_{+1} - E_{-1}}{2\sqrt{(E_{+1} + E_{-1} + 2\gamma^{-1})^2 - 4(C_R^2 + C_I^2)}} \quad (\text{H.16})$$

The BFSK irreducible demodulation error rate without frequency hopping [Equation (H.16) with $\gamma \rightarrow \infty$] in slow, frequency selective fading channels with continuous CIRFs is compared to the value with hopping from Appendix G in Figure H-2. Without hopping, the ISI drives the irreducible error rate to 50 percent for small values of the normalized frequency selective bandwidth, $f_0 T$, whereas the irreducible error rate with hopping approaches about 0.02 in this limit for $\Delta f T = 2$ tone spacing.

For values of $f_0 T \geq 3$ and $\Delta f T = 2$ the irreducible error rate without hopping is less than that with hopping. These curves do not cross, however, if we compare the irreducible error rates with three times the minimum tone spacing. This suggests that there is a significant variation in the irreducible error rate with tone spacing for BFSK without hopping.

Because the expressions for the BFSK error rate depend on the tone spacing in a rather complicated way, it is instructive to plot the irreducible error rate for various values of the normalized tone spacing $\Delta f T$. These plots are in Figure H-3 for $\Delta f T$ in the range 1–10. Surprisingly, the irreducible error rate depends, in a significant way, on whether or not the normalized tone spacing is even or odd, and there is an optimum tone spacing which is twice the minimum tone spacing.

A word of caution is necessary. Based on our results for sampled CIRFs presented in the next section, the rich behavior of unhopped BFSK demodulation performance with tone spacing in frequency selective fading depends on having an infinite bandwidth. Because real transmitters and receivers are band-limited, it is unlikely that an actual system will have performance that is this sensitive to the value of the tone spacing. We address this in more detail at the end of this appendix.

The BFSK channel bit error rate without hopping for the optimum tone spacing ($\Delta f T = 2$) and for slow, frequency selective fading with continuous CIRFs is plotted in Figure H-4 versus E_{cb} / N_0 for several values of $f_0 T_{cb}$.

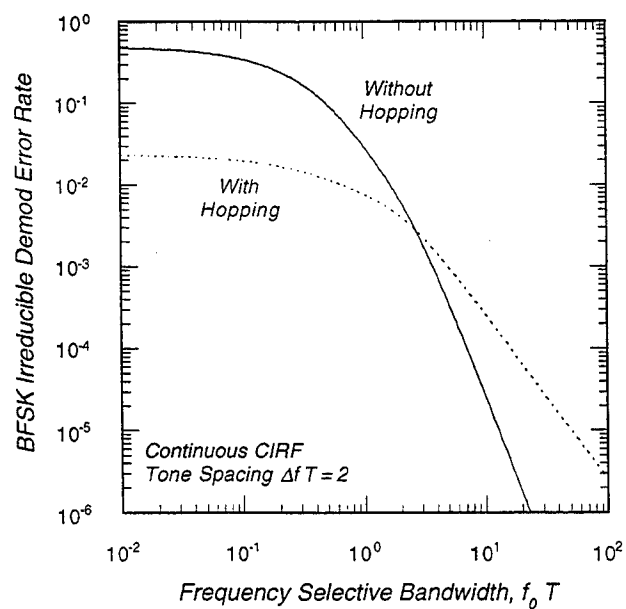


Figure H-2. BFSK irreducible demodulation error rate in slow, frequency selective fading with and without hopping.

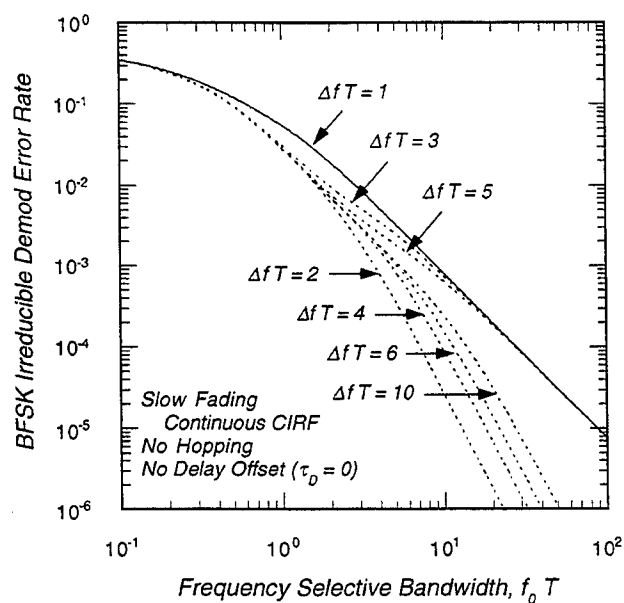


Figure H-3. BFSK irreducible demodulation error rate without hopping for several tone spacings in slow, frequency selective fading.

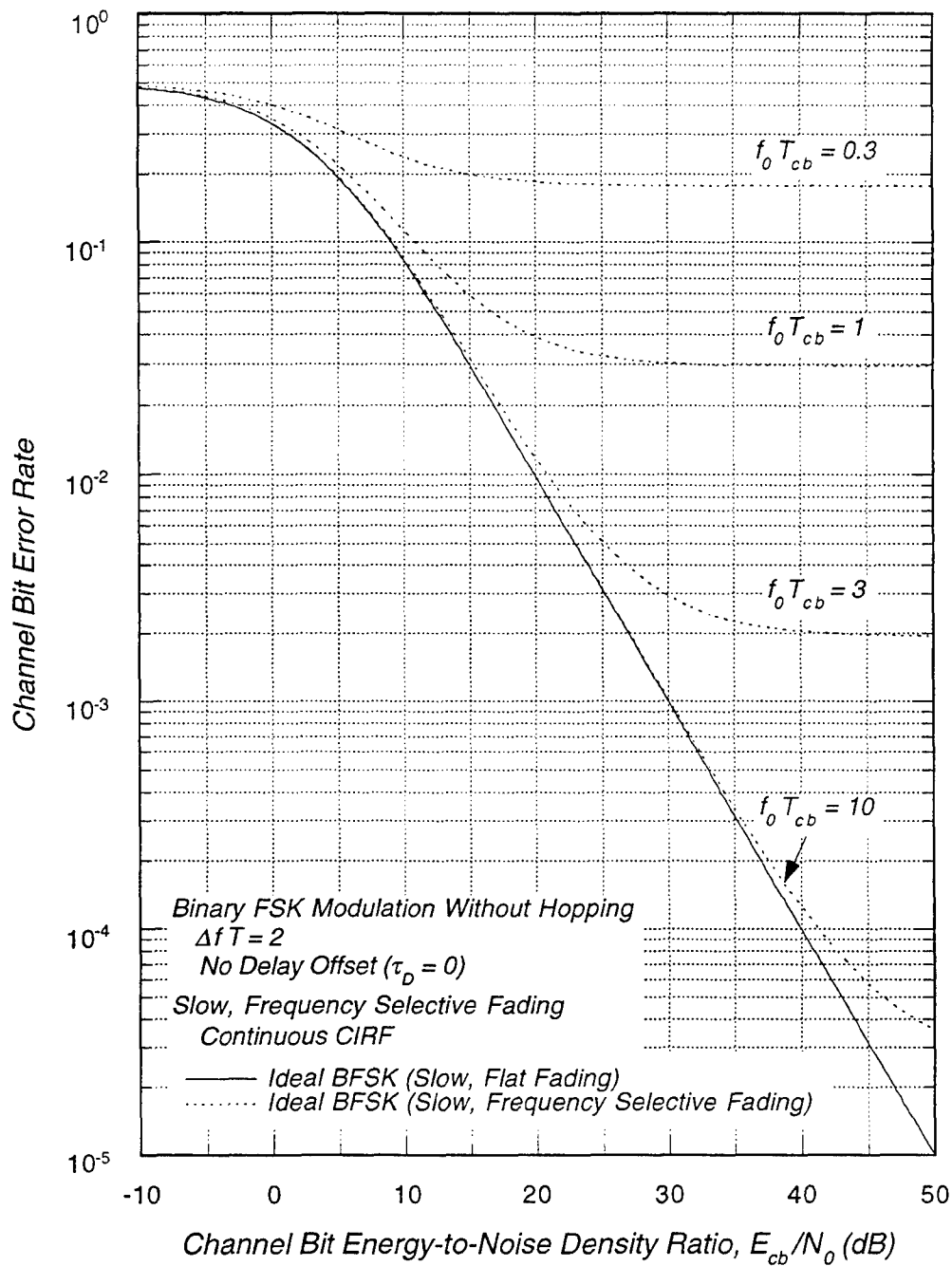


Figure H-4. BFSK channel bit error rate without hopping for the optimum tone spacing in slow, frequency selective fading.

H.4 DEMODULATION ERROR RATE WITH SAMPLED CIRFS.

When the channel impulse response function is sampled in the delay domain, as it must be in software simulations or in hardware channel simulators, the on-time signal contribution to the output of the tone filters when the delay offset is zero is

$$S_{O,m} = r \sum_{i=0}^{N_D-1} h_i e^{-j(n_k \pi \Delta f) i \Delta \tau} \frac{1}{T} \int_{-T/2}^{T/2} dt e^{-j(m-n_k) \pi \Delta f t} \Pi \left[\frac{t - i \Delta \tau}{T} \right],$$

where N_D is the number of channel delay samples per modulation symbol period. Similarly, the ISI contributions are

$$S_{I,m}^1 = r \sum_{l=0}^{\infty} \sum_{i=0}^{N_D-1} h_{i+lN_D} e^{-j(n_{k-l-1} \pi \Delta f)(i \Delta \tau + lT)} \frac{1}{T} \int_{-T/2}^{-T/2+i \Delta \tau} dt e^{-j(m-n_{k-l-1}) \pi \Delta f t}$$

$$S_{I,m}^2 = r \sum_{l=1}^{\infty} \sum_{i=0}^{N_D-1} h_{i+lN_D} e^{-j(n_{k-l} \pi \Delta f)(i \Delta \tau + lT)} \frac{1}{T} \int_{-T/2+i \Delta \tau}^{T/2} dt e^{-j(m-n_{k-l}) \pi \Delta f t}.$$

The time integrals in these expressions have exactly the same form as they have for the continuous CIRF case. The expressions written down in the previous subsection for the second order moments of the tone filter outputs are valid here when the delay integrals are replaced by delay sums. Equations (H.12), (H.13), and (H.14) still hold, with some modification described below, where

$$R_0 = \sum_{i=0}^{N_D-1} P_i$$

$$R_1 = \sum_{i=0}^{N_D-1} P_i (i / N_D)$$

$$R_2 = \sum_{i=0}^{N_D-1} P_i (i / N_D)^2$$

$$R_{S,1} = -\frac{S_M}{\omega_M} \sum_{i=0}^{N_D-1} P_i \sin[\omega_M (i / N_D)]$$

$$\begin{aligned}
R_{S,2} &= \frac{4}{\omega_M^2} \sum_{i=0}^{N_D-1} P_i \sin^2 \left[\frac{1}{2} \omega_M (i / N_D) \right] \\
R_{S,3} &= -\frac{S_M}{\omega_M} \sum_{i=0}^{N_D-1} P_i (i / N_D) \sin [\omega_M (i / N_D)] \\
R_{S,4} &= -\frac{S_M}{\omega_M} \sum_{i=0}^{N_D-1} P_i [1 - 2(i / N_D)] \sin^2 \left[\frac{1}{2} \omega_M (i / N_D) \right] \\
R_{S,5} &= \sum_{i=0}^{N_D-1} P_i (i / N_D) [1 - (i / N_D)] \sin [\omega_M (i / N_D)] \\
R_C &= \sum_{i=0}^{N_D-1} P_i (i / N_D) [1 - (i / N_D)] \cos [\omega_M (i / N_D)] ,
\end{aligned}$$

for sampled CIRFs. The upper limit in the delay sums, $N_D - 1$, in these expressions is replaced by $N_\tau - 1$ when $N_\tau < N_D$. Equivalently, one could evaluate these expressions by setting $P_i = 0$ for $i \geq N_\tau$.

The mean power of the sampled CIRF in each delay bin (P_i) in terms of the normalized frequency selective bandwidth ($\lambda = 2\pi f_0 T$) and the number of delay samples per symbol period is [Equation (2.14)]:

$$P_i = \left(1 - e^{-\lambda / N_D}\right) e^{-i\lambda / N_D} ,$$

and the total number of channel delay samples is

$$N_\tau = 1 - \frac{\ln(1 - P_\tau) N_D}{\lambda} , \quad (\text{H.17})$$

where P_τ is the fraction of signal energy in the sampled delay grid. The current DSWA specification for P_τ is 0.975 [Dana, 1991].

The modification mentioned above is necessary because with a sampled CIRF there are not an infinite number of delayed symbols in the ISI. The ISI contributions to the second order moments have the form

$$E_X = \sum_{l=1}^{\infty} \sum_{i=0}^{N_D-1} P_{i+lN_D} R_X(i / N_D)$$

where $R_X(i/N_D)$ is one of the delay sums. Because the sampled CIRF has an exponential fall-off for P_i ,

$$P_{i+lN_D} = e^{-l\lambda} P_i ,$$

and the ISI sum can be separated from the sum over the delay:

$$E_X = \left[\sum_{l=1}^{N_\tau/N_D-1} e^{-l\lambda} \right] \left[\sum_{i=0}^{N_D-1} P_i R_X(i/N_D) \right] ,$$

where N_τ/N_D is the number of delayed symbol periods in the sampled CIRF. There are two cases. When $N_\tau \leq N_D$, only energy from the immediately preceding symbol contributes to the energy received during the on-time symbol period, and

$$E_X = 0 \quad N_\tau < N_D .$$

When $N_\tau \geq N_D$,

$$E_X = \left[\sum_{l=1}^{N_\tau/N_D-1} e^{-l\lambda} \right] \left[\sum_{i=0}^{N_D-1} P_i R_X(i/N_D) \right] + e^{-\lambda N_{\tau D}} \left[\sum_{i=0}^{N_{\tau D}-1} P_i R_X(i/N_D) \right] \quad N_\tau \geq N_D ,$$

where $N_{\tau D}$ is the remainder of N_τ divided by N_D . The second term in this expression is evaluated only if $N_{\tau D} > 0$.

The BFSK irreducible error rate for $\Delta f T = 2$ in slow, frequency selective fading without hopping and with a sampled CIRF is plotted in Figure H-5 for several values of the number of channel delay samples per symbol period and for the current specification for total signal power in the delay grid, $P_\tau = 0.975$. For comparison, the irreducible error rate when the CIRF is continuous is also plotted in the figure.

As was the case for BFSK with hopping, the error rate curves are quite sensitive to the both the value of N_D and the frequency selective bandwidth. This is understood by considering the total number of delay samples N_τ as a function of these two parameters given in Equation (H.17). When the second term on the right-hand-side of this equation is less than unity, the number of delay samples is unity, and the irreducible error rate is identically zero. For $N_D = 2$ this occurs when $f_0 T \geq 1.17$, and for $N_D = 16$ this occurs when $f_0 T \geq 9.4$. For values of $f_0 T$ that result in $N_\tau > 1$, the curves have a "stepped" appearance as N_τ varies from 2 to 3 to 4 and so on. Eventually, when $f_0 T$ is small enough that the number of delay samples becomes large, the

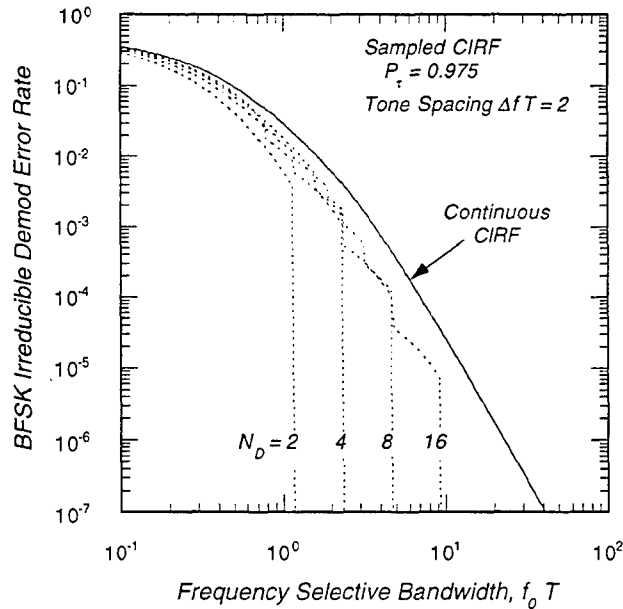


Figure H-5. BFSK irreducible demodulation error rate in slow, frequency selective fading with sampled CIRFs and $P_t = 0.975$.

steps smooth out, and the sampled CIRF irreducible error rate approaches the continuous CIRF curve.

The stepped behavior for small values of N_t can be smoothed out by increasing the fraction of signal power in the delay grid from 0.975 to 0.999. The resulting BFSK irreducible error rate is plotted in Figure H-6. On the basis of these results and similar ones in Appendix G, the value of P_t in COMLNK may be increased to 0.999 in a future version of the code.

Another effect of sampling the channel impulse response function in delay is that the signal spectrum is effectively truncated. To demonstrate this, we present a few general results for the output of a matched filter when the CIRF is sampled. The point of this digression is to show the effect of sampling and bandlimiting on the irreducible error rate plotted in Figure H-3. In discussing the results in this figure, we state that the rich behavior of the error rate with tone spacing depends on having a transmitted signal and a receiver with an essentially infinite bandwidth. We demonstrate this in the developments that follow.

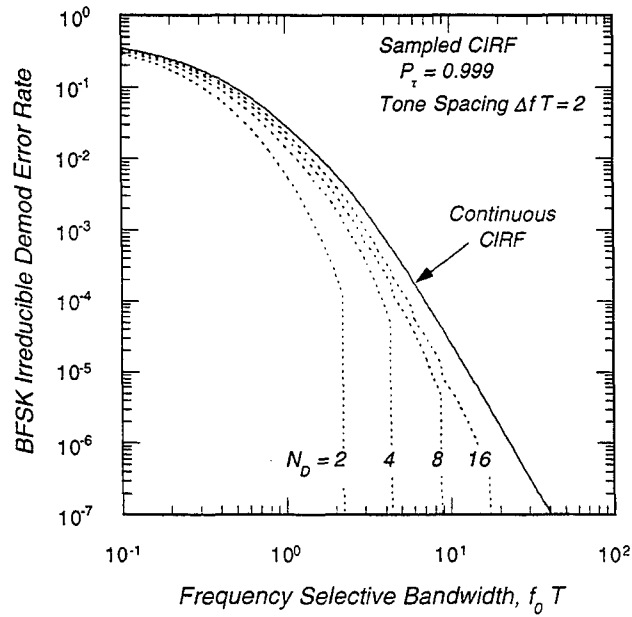


Figure H-6. BFSK irreducible demodulation error rate in slow, frequency selective fading with sampled CIRFs and $P_\tau = 0.999$.

Consider a transmitted rectangular pulse with a frequency spectrum $M(\omega)$. This signal then propagates through a channel with a continuous CIRF for the moment. In the frequency domain, the channel transfer function (*i.e.*, the frequency spectrum of the fading) is the Fourier transform of the CIRF:

$$H(\omega) = \int_0^{\infty} h(\tau) e^{-j\omega\tau} d\tau .$$

For the purposes of this calculation we consider the channel to be slow fading so we have suppressed the time dependence of the CIRF and $H(\omega)$. The signal contribution to the output of a matched filter is then given by the inverse Fourier transform:

$$S(\tau) = \int_{-\infty}^{\infty} |M(\omega)|^2 H(t, \omega) e^{j\omega\tau} \frac{d\omega}{2\pi} ,$$

where τ in this equation is the offset of the receiver's delay tracking loop. For a single transmitted rectangular pulse of duration T , the combined signal and matched filter spectrum is

$$|M(\omega)|^2 = T \frac{\sin^2\left(\frac{1}{2}T\omega\right)}{\left(\frac{1}{2}T\omega\right)^2} .$$

When the CIRF is sampled these two Fourier transforms are discrete. The frequency sample size $\Delta\omega$ is related to the sampled delay grid size $\Delta\tau$ and the number of frequency samples:

$$\Delta\omega = \frac{2\pi}{N_F \Delta\tau} ,$$

where $1/\Delta\tau$ is the unambiguous bandwidth represented by the sampled CIRF. The expression above just divides this bandwidth into N_F frequency bins and converts frequency in Hertz to frequency in radians. The sampled channel transfer function is the discrete Fourier transform (DFT) of the sampled CIRF, $h_i = h(i\Delta\tau)\Delta\tau$. Thus

$$H(k\Delta\omega) = \sum_{i=0}^{N_F-1} h_i \exp(-2\pi j i k / N_F) \quad (-N_F/2 \leq k \leq N_F/2 - 1) ,$$

and the signal contribution to the output of the matched filter is

$$S(\tau) = \frac{N_D}{N_F} \sum_{k=-N_F/2}^{N_F/2-1} \frac{\sin^2(\pi N_D k / N_F)}{(\pi N_D k / N_F)^2} H(k\Delta\omega) \exp[2\pi j k (\tau / \Delta\tau) / N_F] ,$$

where $N_D = T / \Delta\tau$ is the number of delay samples per modulation period. The unambiguous radian frequency bandwidth represented by the sampled channel transfer function and this DFT is

$$-\frac{\pi}{\Delta\tau} \leq k\Delta\omega < \frac{\pi}{\Delta\tau} .$$

For the minimum number of delay samples per modulation period ($N_D = 2$), the frequency bandwidth of the DFT extends between the first nulls in the $\sin x / x$ spectrum of the signal (*i.e.*, $-\pi \leq \pi N_D k / N_F < +\pi$), and the rest of the sidelobe structure of the signal is cut off. As N_D is increased, more-and-more of the sidelobe structure of the signal is included in the DFT. Thus the primary effect of increasing N_D is to include more of the signal spectrum sidelobes.

The BFSK irreducible error rate without hopping for sampled, slow fading channels is plotted in Figures H-7 and H-8 for 2 and 64 delay samples per modulation period, respectively, and for normalized tone spacings of 1, 2, and 3. The total signal power in the delay grid is set at 0.999 for these results. Note that the abscissa is different in the two plots.

For $N_D = 2$, the rich behavior of the irreducible error rate with tone spacing is not evident as the plots for the three tone spacings fall essentially on top of each other. The irreducible error rate for this case is zero for $f_0 T \geq 2.2$ because the number of delay samples is unity for f_0 in this range. We expect that similar curves would result if the irreducible error rate were to be calculated for a continuous CIRF when the transmitted signal spectrum is attenuated outside of the first nulls. The irreducible error rates plotted in Figure H-8 for $N_D = 64$ are similar to the corresponding curves in Figure H-3 for a continuous CIRF because in this case most of the sidelobe structure of the transmitted signal is included in the DFT.

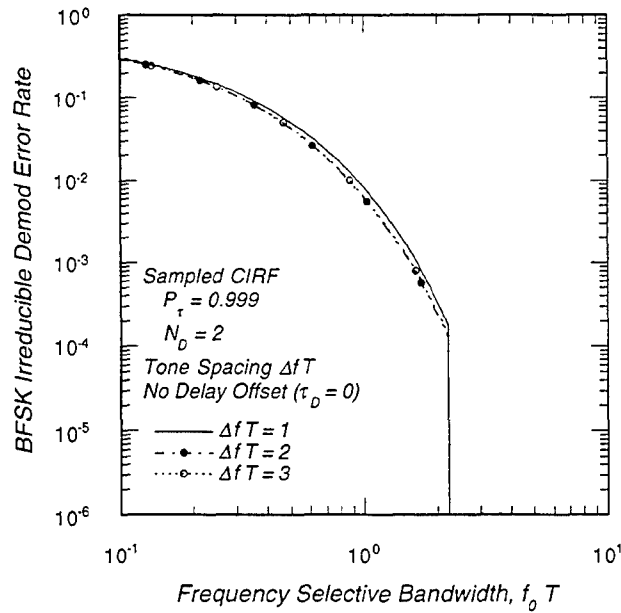


Figure H-7. BFSK irreducible demodulation error rate in slow, frequency selective fading for sampled CIRFs with $N_D = 2$.

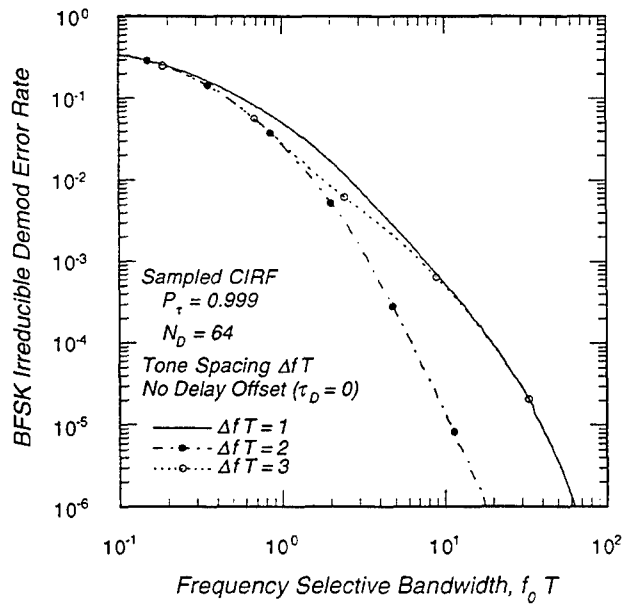


Figure H-8. BFSK irreducible demodulation error rate in slow, frequency selective fading for sampled CIRFs with $N_D = 64$.

DISTRIBUTION LIST

DEPARTMENT OF DEFENSE

BALLISTIC MISSILE DEFENSE OFFICE
7100 DEFENSE PENTAGON
WASHINGTON, DC 20301-7100
ATTN: TRB, DR L. PIERRE

DEFENSE ADVANCED RESEARCH
PROJECTS AGENCY
3701 NORTH FAIRFAX DRIVE
ARLINGTON, VA 22203-1714
ATTN: CHIEF SCIENTIST

DEFENSE TECHNICAL INFORMATION CENTER
8725 JOHN J. KINGMAN ROAD, SUITE 0944
FORT BELVOIR, VA 22060-6218
ATTN: DTIC/OCF

DEFENSE THREAT REDUCTION AGENCY
6801 TELEGRAPH ROAD
ALEXANDRIA, VA 22310-3398
ATTN: CP
ATTN: CPWCT
ATTN: CPWP, DR. K. SCHWARTZ
ATTN: CPWP, R. KEHLET
ATTN: CPWT, L. WITTWER
ATTN: CPWT, W. ZIMMERS
ATTN: NSSA
ATTN: NSSA, W. SUMMA

DIRECTOR
DISA
TECHNICAL RESOURCES CENTER
7010 DEFENSE PENTAGON
WASHINGTON, DC 20301-7010
ATTN: JNGO

DIRECTOR
STRATEGIC & SPACE SYSTEMS
3090 DEFENSE PENTAGON
WASHINGTON, DC 20301
ATTN: DR G. SCHNEITER

US NUCLEAR COMMAND & CONTROL
SYS SUPPORT STAFF
SKYLINE #3, SUITE 500
5201 LEESBURG PIKE
FALLS CHURCH, VA 22041-3202
ATTN: LIBRARY

DEPARTMENT OF DEFENSE CONTRACTORS

INSTITUTE FOR DEFENSE ANALYSES
1801 N. BEAUREGARD STREET
CONTROL & DISTRIBUTION
ALEXANDRIA, VA 22311
ATTN: H. WOLFHARD

ITT INDUSTRIES
ITT SYSTEMS CORPORATION
ATTN: AODTRA/DASIAC
1680 TEXAS STREET, SE
KIRTLAND AFB, NM 87117-5669
ATTN: DASIAC
ATTN: DASIAC/DARE
ATTN: R. RUTHERFORD

ITT SYSTEMS CORPORATION
2560 HUNTINGTON AVENUE
ALEXANDRIA, VA 22303
ATTN: C. WOODHOUSE

LOCKHEED MARTIN CORPORATION
3251 HANOVER ST.
PALO ALTO, CA 94304-1187
ATTN: J. KUMER

LOGICON RDA
2100 WASHINGTON BOULEVARD
ARLINGTON, VA 22204-5706
ATTN: D. CARLSON

MISSION RESEARCH CORPORATION
P. O. BOX 1257
HUNTSVILLE, AL 35807
ATTN: B. BAUER

MISSION RESEARCH CORPORATION
P. O. BOX 2256
ATASCADERO, CA 93423-2256
ATTN: R. L. BOGUSCH

MISSION RESEARCH CORPORATION
P. O. BOX 7957
NASHUA, NH 03060
ATTN: R. ARMSTRONG
ATTN: W. WHITE

MISSION RESEARCH CORPORATION
P. O. BOX 51203
PACIFIC GROVE, CA 93950-6203
ATTN: D. KNEPP
ATTN: J. REINKING

MISSION RESEARCH CORPORATION
P. O. BOX 542
NEWINGTON, VA 22122-0542
ATTN: B. WORTMAN

MISSION RESEARCH CORPORATION
P. O. DRAWER 719
SANTA BARBARA, CA 93102-0719
ATTN: B. R. MILNER
ATTN: B. SAWYER
ATTN: D. LANDMAN
ATTN: D. SOWLE
ATTN: F. GUIGLIANO
ATTN: R. BIGONI
ATTN: R. DANA
ATTN: R. HENDRICK
ATTN: S. GUTSCHE
ATTN: TECHNICAL LIBRARY

MITRE CORPORATION
1150 ACADEMY PARK LOOP #212
COLORADO SPRINGS, CO 80910
ATTN: G. COMPARETTO

PACIFIC-SIERRA RESEARCH CORPORATION
WASHINGTON OPERATIONS
1400 KEY BOULEVARD, SUITE 700
ARLINGTON, VA 22209
ATTN: M. ALLERDING

PHOTON RESEARCH ASSOCIATES
WASHINGTON DIVISION
1911 N. FORT MYER DRIVE, SUITE 408
ATTN: D. BURWELL

PHYSICAL SCIENCES, INC.
20 NEW ENGLAND BUSINESS CENTER
ANDOVER, MA 01810
ATTN: G. CALEDONIA

SCIENCE APPLICATIONS INT'L CORPORATION
2111 EISENHOWER AVENUE, SUITE 303
ALEXANDRIA, VA 22314
ATTN: J. COCKAYNE, SUITE 205

SCIENCE APPLICATIONS INT'L CORPORATION
10260 CAMPUS POINT DRIVE
SAN DIEGO, CA 92121-1578
ATTN: B. LEE
ATTN: D. SACHS

SCIENCE APPLICATIONS INT'L CORPORATION
P. O. BOX 1303
MCLEAN, VA 22102
ATTN: E. HYMAN
ATTN: T. LOVERN

SPARTA INC.
4901 CORPORATE DRIVE, SUITE 102
HUNTSVILLE, AL 35805
ATTN: C. HARPER

TELEDYNE BROWN ENGINEERING
P. O. BOX 070007
HUNTSVILLE, AL 35807-7007
ATTN: J. FORD
ATTN: J. WOLFSBERGER, JR.
ATTN: N. PASSINO
ATTN: R. E. LEWIS/MS-50

THE AEROSPACE CORPORATION
P. O. BOX 92957
LOS ANGELES, CA 90009-2957
ATTN: DR J. M. STRAUS, M2/264
ATTN: G. LIGHT, M5/643
ATTN: M. ROLENZ

TOYON RESEARCH CORPORATION
75 AERO CAMINO, SUITE A
GOLETA, CA 93117-3139
ATTN: JISE

TRW INC.
SPACE & ELECTRONICS GROUP
ONE SPACE PARK
REDONDO BEACH, CA 90278-1078
ATTN: T.I.C., S/1930

TRW SPACE & DEFENSE
HUNTSVILLE OPERATIONS
213 WYNN DRIVE
HUNTSVILLE, AL 35805
ATTN: W. L. JOHNSON

VISIDYNE, INC.
P. O. BOX 1399
GOLETA, CA 93116-1399
ATTN: J. CARPENTER
ATTN: J. DEVORE
ATTN: J. JORDANO
ATTN: J. THOMPSON
ATTN: T. L. STEPHENS
ATTN: W. SCHLUETER

DEPARTMENT OF ENERGY

SANDIA NATIONAL LABORATORIES

ATTN: MAIL SERVICES

P. O. BOX 5800

ALBUQUERQUE, NM 87185-0459

ATTN: G. CABLE, MS 0977

ATTN: TECHNICAL LIBRARY, MS 0899

DEPARTMENT OF THE AIR FORCE

AFIWC/MSO

102 HALL BOULEVARD, SUITE 315

SAN ANTONIO, TX 78243-7016

ATTN: SAVC

AFIWC/MSO

102 HALL BOULEVARD, SUITE 315

SAN ANTONIO, TX 78243-7016

ATTN: SAZ

AIR FORCE FOR STUDIES & ANALYSIS

1570 AIR FORCE PENTAGON

WASHINGTON, DC 20330-1570

ATTN: SATI, ROOM 1D363

AIR UNIVERSITY LIBRARY

600 CHENNAULT CIRCLE

BUILDING 1405, ROOM 160

MAXWELL AFB, AL 36112-6424

ATTN: AUL-LSE

NATIONAL TEST FACILITY/ENC

ATTN: DATA MANAGEMENT OFFICE

730 IRWEN AVENUE

FALCON AFB, CO 80912-7300

ATTN: NTF/EN, MAJ VAN FOSSON

HEADQUARTERS

US STRATEGIC COMMAND

901 SAC BOULEVARD

OFFUTT AFB, NE 68113-6580

ATTN: DTRA LIAISON

ATTN: J5

ATTN: J61

US ARMY NATIONAL GROUND

INTELLIGENCE CENTER

220 7TH STREET, NE

CHARLOTTESVILLE, VA 22901-5396

ATTN: IAFSTC-RMT

DEPARTMENT OF THE ARMY

COMMANDER

US ARMY ENGINEERING &

SUPPORT CENTER

P. O. BOX 1600

HUNTSVILLE, AL 35807-4301

ATTN: P. J. KISS

US ARMY RESEARCH LAB

AMSRL-SL-CS E3331

5101 HOADLEY RD.

ABERDEEN PROVING GROUND, MD 21010-5423

ATTN: SLCBR-SS-T, TECHNICAL LIBRARY

COMMANDER

US ARMY SPACE & STRATEGIC

DEFENSE COMMAND

CSSD-TC-SR

P. O. BOX 1500

HUNTSVILLE, AL 35807-3801

ATTN: B. CARRUTH

US ARMY THAAD PROJECT OFFICE

P. O. BOX 1500

HUNTSVILLE, AL 35807-3801

ATTN: CSSD-GR-S, W DICKINSON

ATTN: SFAE-MD-NMDR-E,

C. KIRCHNRE

ATTN: SFAE-MD-THA-S-PC, CAROL EVANS

DEPARTMENT OF THE NAVY

NAVAL RESEARCH LABORATORY

4555 OVERLOOK AVENUE, SW

WASHINGTON, DC 20375-5000

ATTN: CODE 7604, H. HECKATHORN

OTHER GOVERNMENT

CENTRAL INTELLIGENCE AGENCY

WASHINGTON, DC 20505

ATTN: ORD/E P G, DR D. CRESS

ATTN: OSWR/SSD FOR, L. BERG



Defense Threat Reduction Agency
8725 John J. Kingman Road, MS 6201
Fort Belvoir, VA 22060-6201

SEP 12 2001

MEMORANDUM FOR PRINTING AND REPRODUCTION BRANCH (ADSR)

SUBJECT: The printing of, **DSWA-TR-98-61**, "Digital Communications in Fading Channels:
COMLNK Validation"

Referenced subject report was printed with missing text in Block 3 of the Standard Form 298. The report has been determined to be Unclassified. The text should appear as follows:

Technical

961001 - 980630

Request you distribute an errata with adhesive backing for easy installation. A distribution list and labels have been provided for your use. Your point-of-contact in this office is Miss Suzie Ballif, (703) 767-4725.

Sincerely,

Linda M. Powell
Chief, Administrative Services
Division

Technical 961001 - 980630

Technical 961001 - 980630